MECHANICS OF SEDIMENT TRANSPORT AND BEDROCK EROSION IN STEEP LANDSCAPES

Thesis by
Joel Simon Scheingross

In Partial Fulfillment of the Requirements for the Degree
of
Doctor of Philosophy

CALIFORNIA INSTITUTE OF TECHNOLOGY
Pasadena, California
2016
(Defended August 31, 2015)

ACKNOWLEDGEMENTS

This thesis would not have been possible without the help, support, guidance, and friendship of countless individuals. First and foremost, I'd like to thank my advisor, Michael Lamb. Mike – thanks for encouraging me to pursue geomorphology when we were at Berkeley together and for twisting my arm to start as a grad student at Caltech even though I didn't feel quite ready at the time. Beyond the fundamentals of geomorphology, I hope I've picked up a bit of your good taste in developing research problems, as well as your mastery of scientific communication and storytelling. Thanks for believing in me, constantly pushing me to do my best, and always making time to chat no matter how hectic your schedule got. It's been fun, challenging, and ultimately rewarding. I'm looking forward to continued collaboration in the future.

My path to Caltech began first at UC Berkeley where Sean Schoville introduced me to the scientific research process. Bill Dietrich opened my eyes to the dynamic landscape we live in while graciously advising me through my first geomorphology research experience, and he continues to be a welcome source of advice and support. At Caltech, Jean-Philippe Avouac, Mark Simons, Andy Thompson, and Pablo Ampuero have made for a supportive and insightful thesis committee. I've benefitted from countless conversations with other faculty, most notable Woody Fischer, Victor Tsai, Michael Gurnis, John Grotzinger, and Joe Kirschvink. Sabbatical visits to Caltech from Jeremy Venditti, Joshua West, and Sergio Fagherazzi offered me new and fresh perspectives in geomorphology and beyond.

I've been fortunate to have many great collaborators who have contributed in various ways to the content within. I am gratefully indebted to Brian Fuller whose patience, guidance, and ingenuity was critical to all the experimental work presented in this thesis, and who braved rattlesnakes and poison oak in our effort to install a waterfall plunge-pool sediment monitoring station at the start of four years of awful drought. Brent Minchew tirelessly processed radar data which made Chapter 1 possible, Ben Mackey sparked my interest in earthflows and provided thoughtful guidance on landslides and more, Eric Winchell endured my company for the two summers of fieldwork and countless rain storms that led to Chapter 2, and Fanny Brun made tedious measurement of sediment concentration for Chapter 3, all the while providing fine cheeses, delicious chocolate, and great company. While our co-authored work is not presented in this thesis, Roman DiBiase has been a great friend, officemate, collaborator, and climbing partner, and his perspective was invaluable throughout my time at Caltech. I am greatly appreciative of the undergraduate and high school students I've had the pleasure to work with; Daniel Lo, Khadijah Omerdin, Juliane Preimesberge, Gheorghe Schreiber, and Conor O'Toole all worked hard while never complaining, and have made meaningful contributions to this thesis.

Countless friends and colleagues have shaped my thinking about the mechanics of steep landscapes. Jeff Prancevic deserves to be at the top of this list for his patience and willingness to discuss the most intricate aspects of sediment transport mechanics, for always offering great suggestions, and for his enduring friendship. For almost a decade, Jonathan Perkins and Marisa Palucis have been my go-to sources to nerd out about geology and geomorphology with. Vamsi

Ganti, Ajay Limaye, Luca Maltesta, Florent Gimbert, Mathieu Lapotre, Isaac Larsen, Adam Booth, Austin Chadwick, Alistair Hayden, Ryan Ewing, and Phairot Chatanantavet have been great lab mates and friends, whose perspectives and insights are always appreciated. The administrative staff within GPS, and at Caltech as a whole, has made logistics a breeze. Janice Grancich deserves extra special thanks in this regard.

My perspective on science, life, and more has evolved over countless coffees and lunches with Daniel Stolper, while Paul Magyar has seen me through five years of (mostly) ups and (occasional) downs over our kitchen table (hi Paul – I know you'll be the first to read this when it goes online). Jeff Marlow, Alison Piasecki, Megan Newcombe, Erika Swanson, and Jennifer Shechet have been great friends since day one. I've been fortunate to spend time in the mountains (on foot, bike, and dangling from a rope) with Pratyush Tiwary, Patrick Sanan, Daven Quinn, Hamik Mukelyan, Chirranjeevi Gopal, Tucker Jones, Elisabeth Krause, Dan & Danielle Bower, Sebastian Kopf, Katie Snell, Lauren Montemayor, and, last but certainly not least, Elle Chimiak. Thanks for giving me encouragement to get out of the lab, and for the opportunities to let my mind rest while my body suffered.

Finally, I would not where I am today without the love and support of my family. Mom and Dad, Evan and Daniella (and Riley!), Poppop and Grandma, and Bubby – thanks for everything and more.

ABSTRACT

Erosion is concentrated in steep landscapes such that, despite accounting for only a small fraction of Earth's total surface area, these areas regulate the flux of sediment to downstream basins, and their rugged morphology records transient changes (or lack thereof) in geologic and climatic forcing. Steep landscapes are geomorphically active; large sediment fluxes and rapid landscape evolution rates can create or destroy habitat for humans and wildlife alike, and landslides, debris flows, and floods common in mountainous areas represent a persistent natural and structural hazard. Despite the central role that steep landscapes play in the geosciences and in landscape management, the processes controlling their evolution have been poorly studied compared to lower-gradient areas. This thesis focuses on the basic mechanics of sediment transport and bedrock incision in steep landscapes, as these are the fundamental processes which set the pace and style of landscape evolution. Chapter 1 examines the spatial distribution of slow-moving landslides; these landslides can dominate sediment fluxes to river networks, but the controls on their occurrence are poorly understood. Using a case-study along the San Andreas Fault, California, I show that slow-moving landslides preferentially occur near the fault, suggesting a rock-strength control on landslide distribution. Chapter 2 provides the first field-measurements of incipient sediment motion in streams steeper than 14% and shows a large influence of slope-dependent flow hydraulics and grain-scale roughness on particle motion. Chapter 3 presents experimental evidence for bedrock erosion by suspended sediment, suggesting that, in contrast to prevailing theoretical predictions, suspension-regime transport in steep streams can be the dominant erosion agent. Steep streams are often characterized by the presence of waterfalls and bedrock steps which can have locally high rates of erosion; Chapters 4 and 5 present newly developed, experimentally validated theory on sediment transport through and bedrock erosion in waterfall plunge pools. Finally, Chapter 6 explores the formation of a bedrock slot canyon where interactions between sediment transport and bedrock incision lead to the formation of upstream-propagating bedrock step-pools and waterfalls.

TABLE OF CONTENTS

Introduction

Erosion of bedrock shapes the surface of Earth and other planets, creating steep landscapes which awe the public, from snow-capped mountain peaks to raging waterfalls to deeply incised canyons. Understanding the controls on the formation and evolution of these landscapes lies at the heart of the geosciences. Landscapes adjust their rate and style of erosion in response to changes in climate, tectonics, and sea-level (e.g., Anderson and Anderson, 2010; Whipple et al., 2013), such that surface morphology and landscape features can be used to infer the past environmental history on Earth, Mars, and other planets (e.g., Baker and Milton, 1974; Bull, 1991; Perron et al., 2006).

As landscapes steepen, their rates of erosion tend to increase (e.g., Gilbert, 1877; DiBiase et al., 2010), such that the majority of erosion on Earth is concentrated in mountain ranges and other areas of high relief (Milliman and Syvitski, 1992; Larsen et al., 2014). High relief in these mountainous areas allow steep landscapes to record changes in base-level and climate through, for example, the formation of upstream propagating waterfalls (e.g., Gilbert, 1907; Seidl et al., 1994; Seidl et al., 1996; Crosby and Whipple, 2006; Lamb et al., 2007; Mackey et al., 2014) (Fig. 0.1) and successive river terraces (Bull, 1991; Hancock et al., 1999; Fuller et al., 2009). Steep landscapes also set the flux of sediment to basins downstream, such that interpretations of environmental signals in sedimentary records benefit from a detailed understanding of the erosional processes upstream (e.g., Romans et al., in press).

Over shorter timescales, sediment transport and erosion in steep landscapes have important implications for environmental management. Sediment fluxes from upstream

set the rate at which man-made dams fill with sediment and require dredging, and the magnitude and grain-size distribution of sediment delivered by steep channels can aid in both the building and destruction of habitat in riparian areas (e.g., Lisle, 1989; Buffington et al., 2004; Montgomery, 2004). Landslides, debris flows, and floods are common in steep landscapes, and understanding the controls on their occurrence is critical to natural hazards prevention (e.g., Cannon et al., 2009; Petley, 2012).

Given the critical role steep landscapes play in both short and long-term geologic processes, it is surprising that the main processes responsible for shaping steep landscapes remain poorly studied compared to lower-gradient portions of landscapes. This thesis attempts to address this knowledge gap through a detailed study of the mechanics of sediment transport and bedrock erosion in steep landscapes. The thesis is organized following the path of sediment from mountain ridges to channels downstream. I begin on hillslopes where sediment is delivered to rivers below, and then cover first the transport of sediment in steep channels, followed by the bedrock erosion which results from transported sediment, with an emphasis on sediment transport and erosion mechanics at waterfalls.

Chapter 1 focuses on slow-moving landslides, which can be the primary source of sediment to rivers (Kelsey, 1978; Roering et al., 2009), but for which the controls on occurrence are poorly understand. Through a detailed case-study, I show that slow-moving landslides preferentially form in areas of reduced rock strength proximal to fault zones, and provide a conceptual model for prediction of slow-moving landslide occurrence throughout landscapes.

Chapter 2 provides a detailed overview on the controls of initial motion of sediment in steep streams. The presence of large cobbles and boulders, low flow depth to roughness ratios, and large-woody debris cause the sediment transport laws developed in lower-gradient streams to break down when applied to steep channels (e.g., Lamb et al., 2008b; Yager et al., 2012; Prancevic and Lamb, 2015). Over three years of field monitoring, I collected and analyzed data to determine the competing influences of flow hydraulics and grain-scale roughness on sediment motion in steep streams, and provide a framework to incorporate these effects in sediment transport predictions.

Sediment transport produces erosion via bedrock abrasion from impacting particles. This erosion is often maximized during large floods in steep channels (e.g., Stark et al., 2010; Cook et al., 2012) when high shear stresses can lead to the transport of sediment in suspension. However, commonly used bedrock-abrasion models (e.g., Sklar and Dietrich, 2004) assume erosion rates drop to zero during particle suspension, leading to counter-intuitive predictions of decreasing erosion rates with increasing flood magnitude. In Chapter 3, I performed controlled laboratory experiments documenting bedrock incision from suspended sediment. The experimental results agree with a recently-developed theoretical model (Lamb et al., 2008a), and suggest that suspension-regime erosion can dominate bedrock incision in steep streams and in large floods.

Waterfalls are common in steep streams, and can retreat upstream at rates which outpace standard fluvial incision by orders of magnitude (Mackey et al., 2014), thus providing the dominant erosion mechanism across many steep landscapes. Chapters 4 and 5 cover the mechanics of waterfall sediment transport and erosion, which have intrigued geomorphologists for over a century (Gilbert, 1890; Holland and Pickup, 1976;

Young, 1985; Crosby and Whipple, 2006; Haviv et al., 2010), but for which little progress in terms of mechanistic understanding has been made. Erosion and upstream retreat of waterfalls requires, at minimum, the transport of sediment away from the waterfall base, such that sediment transport may represent the rate-limiting step in waterfall erosion. In Chapter 4, I developed a theory to predict sediment transport through waterfall plunge-pools and performed controlled laboratory experiments testing and calibrating the model. Chapter 5 combines this waterfall plunge-pool sediment-transport model with an existing bedrock-abrasion model (Lamb et al., 2008a), modified to make appropriate for plunge-pools. This model is validated by laboratory experiments eroding plunge pools into artificial bedrock, and allows predictions of relative rates of plunge-pool vertical-incision versus lateral-waterfall-retreat.

Finally, Chapter 6 represents a synthesis of the previous work by examining the competing influences of sediment transport at steep slopes, suspension erosion, and waterfall plunge-pool retreat on bedrock-channel morphology and erosion. Chapter 6 explores the development of a deeply incised slot canyon in a controlled laboratory flume tilted to 19.5% channel slope, showing plunge pools and waterfalls can form autogenically through internal dynamics between sediment transport, flow hydraulics, and evolving bedrock topography, and that these features can dominate total channel lowering.

The work presented in this thesis offers new tools to predict bedrock erosion in steep landscapes, and allows for comparison with existing bedrock erosion models which fail to incorporate waterfalls and suspension-erosion processes. For example, most landscape evolution models ignore waterfall processes, instead predicting that increases

in uplift can create steepened channel sections (knickzones) which retreat by standard fluvial erosion processes (Fig 0.2A) (e.g., Egholm et al., 2013). Applying existing fluvial incision models to these steepened channel sections give competing results with stream-power style models (e.g., Howard, 1994; Whipple and Tucker, 1999) predicting erosion rates increase with increasing slope while the most widely-used process-based model (Sklar and Dietrich, 2004) predicts erosion rates decrease with increasing slope due to the onset of sediment suspension (e.g., Wobus et al., 2006; Crosby et al., 2007). For knickzones formed by successive waterfalls (Fig. 0.2B), our waterfall-erosion model generally predicts increased rates of waterfall retreat compared to models designed for lower-gradient rivers. This implies that the presence of waterfalls can enhance the rate of transmission of changes in base-level to upstream catchments. Thus, when using the morphology of steep landscapes to invert for timing of changes in geologic or climatic forcing (e.g. Fig. 0.1), accounting for waterfall erosion processes should yield earlier estimates of the timing of base-level change relative to lower-gradient river incision models.

The progress made in this thesis highlights many opportunities for future research. The waterfall erosion work presented in Chapters 4-6 focuses exclusively on waterfalls with bedrock plunge-pools; however, not all waterfalls display plunge-pools, and additional waterfall-erosion mechanisms exist such as a toppling of bedrock columns (e.g., Young, 1985; Weissel and Seidl, 1997; Lamb and Dietrich, 2009). Furthermore, it is not straightforward to scale-up the reach-scale erosional processes covered in this thesis to long-profile evolution models which have waterfalls separated by lower-gradient river reaches. Doing this requires mechanistic theory describing the controls on the

formation of waterfalls and spacing between waterfalls in steep rivers. Despite progress made in Chapter 6 addressing these questions, such detailed theory does not yet exist and remains a ripe question for future work.

References

Anderson, R. S., and S. P. Anderson (2010), *Geomorphology: The mechanics and chemistry of landscapes*, Cambridge University Press, Cambridge.

Baker, V. R., and D. J. Milton (1974), Erosion by Catastrophic Floods on Mars and Earth, *Icarus*, *23*(1), 27-41, doi:Doi 10.1016/0019-1035(74)90101-8.

Buffington, J. M., D. R. Montgomery, and H. M. Greenberg (2004), Basin-scale availability of salmonid spawning gravel as influenced by channel type and hydraulic roughness in mountain catchments, *Canadian Journal of Fisheries and Aquatic Sciences*, *61*(11), 2085-2096, doi:10.1139/f04-141.

Bull, W. B. (1991), *Geomorphic response to climate change*, Oxford University Press, New York.

Cannon, S. H., J. E. Geartner, M. G. Rupert, J. A. Michael, D. R. Staley, and B. B. Worstell (2009), Emergency asssessment of postfire debris-flow hazards for the 2009 Station Fire, San Gabriel Mountains, Southern California, *U.S. Geological Survey Open-File Report 2009-1227*.

Cook, K. L., J. M. Turowski, and N. Hovius (2012), A demonstration of the importance of bedload transport for fluvial bedrock erosion and knickpoint propagation, *Earth Surface Processes and Landforms*, *38*(7), 683-695, doi:doi: 10.1002/esp.3313.

Crosby, B. T., and K. X. Whipple (2006), Knickpoint initiation and distribution within fluvial networks: 236 waterfalls in the Waipaoa River, North Island, New Zealand, *Geomorphology*, *82*(1-2), 16-38, doi:10.1016/j.geomorph.2005.08.023.

Crosby, B. T., K. X. Whipple, N. M. Gasparini, and C. W. Wobus (2007), Formation of fluvial hanging valleys: Theory and simulation, *Journal of Geophysical Research-Earth Surface*, *112*(F3), doi:10.1029/2006jf000566.

DiBiase, R. A., K. X. Whipple, A. M. Heimsath, and W. B. Ouimet (2010), Landscape form and millennial erosion rates in the San Gabriel Mountains, CA, *Earth and Planetary Science Letters*, *289*(1-2), 134-144, doi:10.1016/j.epsl.2009.10.036.

Egholm, D., M. Knudsen, and M. Sandiford (2013), Lifespan of mountain ranges scaled by feedbacks betwween landsliding and erosion by rivers, *Nature*, *498*, 475-478, doi:doi:10.1038/nature12218.

Fuller, T. K., L. A. Perg, J. K. Willenbring, and K. Lepper (2009), Field evidence for climate-driven changes in sediment supply leading to strath terrace formation, *Geology*, *37*(5), 467-470, doi:10.1130/g25487a.1.

Gilbert, G. K. (1877), *Report on the Geology of the Henry Mountains: Geographical and Geological Survey of the Rocky Mountain Region*, 160 pp., U.S. Government Print Office, Washington, D.C.

Gilbert, G. K. (1890), The history of the Niagara River, extracted from the sixth annual report to the commissioners of the state reservation at Niagara, Albany, NY.

Gilbert, G. K. (1907), The rate of recession of Niagara Falls, *US Geological Survey Bulletin*, *306*, 1-31.

Hancock, G. S., R. S. Anderson, O. A. Chadwick, and R. C. Finkel (1999), Dating fluvial terraces with Be-10 and Al-26 profiles: application to the Wind River, Wyoming, *Geomorphology*, *27*(1-2), 41-60, doi:Doi 10.1016/S0169-555x(98)00089-0.

Haviv, I., Y. Enzel, K. X. Whipple, E. Zilberman, A. Matmon, J. Stone, and K. L. Fifield (2010), Evolution of vertical knickpoints (waterfalls) with resistant caprock: Insights from numerical modeling, *Journal of Geophysical Research-Earth Surface*, *115*, doi:10.1029/2008jf001187.

Holland, W. N., and G. Pickup (1976), Flume study of knickpoint development in stratified sediment, *Geological Society of America Bulletin*, *87*(1), 76-82, doi:10.1130/0016-7606(1976)87<76:fsokdi>2.0.co;2.

Howard, A. D. (1994), A detachment-limited model of drainage-basin evolution, *Water Resources Research*, *30*(7), 2261-2285, doi:10.1029/94wr00757.

Kelsey, H. M. (1978), Earthflows in Franciscan Melange, Van Duzen River Basin, California, *Geology*, *6*(6), 361-364, doi:10.1130/0091-7613(1978)6<361:eifmvd>2.0.co;2.

Lamb, M. P., and W. E. Dietrich (2009), The persistence of waterfalls in fractured rock, *Geological Society of America Bulletin*, *121*(7-8), 1123-1134, doi:10.1130/b26482.1.

Lamb, M. P., W. E. Dietrich, and L. S. Sklar (2008a), A model for fluvial bedrock incision by impacting suspended and bed load sediment, *Journal of Geophysical Research-Earth Surface*, *113*(F3), doi:10.1029/2007jf000915.

Lamb, M. P., W. E. Dietrich, and J. G. Venditti (2008b), Is the critical Shields stress for incipient sediment motion dependent on channel-bed slope?, *Journal of Geophysical Research-Earth Surface*, *113*(F2), doi:10.1029/2007jf000831.

Lamb, M. P., A. D. Howard, W. E. Dietrich, and J. T. Perron (2007), Formation of amphitheater-headed valleys by waterfall erosion after large-scale slumping on Hawai'i, *Geological Society of America Bulletin*, *119*(7-8), 805-822, doi:10.1130/b25986.1.

Larsen, I. J., D. R. Montgomery, and H. M. Greenberg (2014), The contribution of mountains to global denudation, *Geology*, *42*(6), 527-530, doi:10.1130/G35136.1.

Lisle, T. E. (1989), Sediment transport and resulting deposition in spawning gravels, north coastal California, *Water Resources Research*, *25*(6), 1303-1319.

Mackey, B. H., J. S. Scheingross, M. P. Lamb, and K. A. Farley (2014), Knickpoint formation, rapid propagation, and landscape response following coastal cliff retreat at the last interglacial sea-level highstand: Kaua'i, Hawai'i, *Geological Society of America Bulletin*, *126*(7-8), 925-942, doi:10.1130/b30930.1.

Milliman, J. D., and J. P. M. Syvitski (1992), Geomorphic tectonic control of sediment discharge to the ocean: The importance of small mountainous rivers, *Journal of Geology*, *100*(5), 525-544.

Montgomery, D. R. (2004), Geology, geomorphology, and the restoration ecology of salmon, *GSA Today*, *14*(11), 4-12.

Perron, J. T., M. P. Lamb, C. D. Koven, I. Y. Fung, E. Yager, and M. Adamkovics (2006), Valley formation and methane precipitation rates on Titan, *Journal of Geophysical Research-Planets*, *111*(E11), doi:10.1029/2005je002602.

Petley, D. (2012), Global patterns of loss of life from landslides, *Geology*, *40*(10), 927-930, doi:10.1130/G33217.1.

Prancevic, J. P., and M. P. Lamb (2015), Unraveling bed slope from relative roughness in initial sediment motion, *Journal of Geophysical Research-Earth Surface*, *120*(3), 474-489, doi:10.1002/2014jf003323.

Roering, J. J., L. L. Stimely, B. H. Mackey, and D. A. Schmidt (2009), Using DInSAR, airborne LiDAR, and archival air photos to quantify landsliding and sediment transport, *Geophysical Research Letters*, *36*, doi:10.1029/2009gl040374.

Romans, B. W., S. Castelltort, J. A. Covault, A. Fildani, and J. P. Walsh (in press), Environmental signal propagation in sedimentary systems across timescales, *Earth Science Reviews*, doi:10.1016/j.earscirev.2015.07.012.

Seidl, M. A., W. E. Dietrich, and J. W. Kirchner (1994), Longitudinal profile development into bedrock - an analysis of Hawaiian channels, *Journal of Geology*, *102*(4), 457-474.

Seidl, M. A., J. K. Weissel, and L. F. Pratson (1996), The kinematics and pattern of escarpment retreat across the rifted continental margin of SE Australia, *Basin Research*, *8*(3), 301-316, doi:10.1046/j.1365-2117.1996.00266.x.

Sklar, L. S., and W. E. Dietrich (2004), A mechanistic model for river incision into bedrock by saltating bed load, *Water Resources Research*, *40*(6), doi:10.1029/2003wr002496.

Stark, C. P., J. R. Barbour, Y. S. Hayakawa, T. Hattanji, N. Hovius, H. Chen, C.-W. Lin, M.-J. Horng, K.-Q. Xu, and Y. Fukahata (2010), The Climatic Signature of Incised River Meanders, *Science*, *327*(5972), 1497-1501, doi:10.1126/science.1184406.

Weissel, J. K., and M. A. Seidl (1997), Influence of rock strength properties on escarpment retreat across passive continental margins, *Geology*, *25*(7), 631-634, doi:10.1130/0091-7613(1997)025<0631:iorspo>2.3.co;2.

Whipple, K. X., R. A. DiBiase, and B. T. Crosby (2013), Bedrock Rivers, in *Treatise on Geomorphology*, edited by J. Shroder, Jr. and E. E. Wohl, Academic Press, San Diego, doi:10.1016/B978-0-12-374739-6.00254-2.

Whipple, K. X., and G. E. Tucker (1999), Dynamics of the stream-power river incision model: Implications for height limits of mountain ranges, landscape response timescales, and research needs, *Journal of Geophysical Research-Solid Earth*, *104*(B8), 17661-17674, doi:10.1029/1999jb900120.

Wobus, C. W., B. T. Crosby, and K. X. Whipple (2006), Hanging valleys in fluvial systems: Controls on occurrence and implications for landscape evolution, *Journal of Geophysical Research-Earth Surface*, *111*(F2), doi:10.1029/2005jf000406.

Yager, E. M., W. E. Dietrich, J. W. Kirchner, and B. W. McArdell (2012), Prediction of sediment transport in step-pool channels, *Water Resources Research*, *48*, doi:10.1029/2011WR010829.

Young, R. (1985), Waterfalls: Form and process, *Zeitschrift fur Geomorphologie*(Supplementband 55), 81-95.

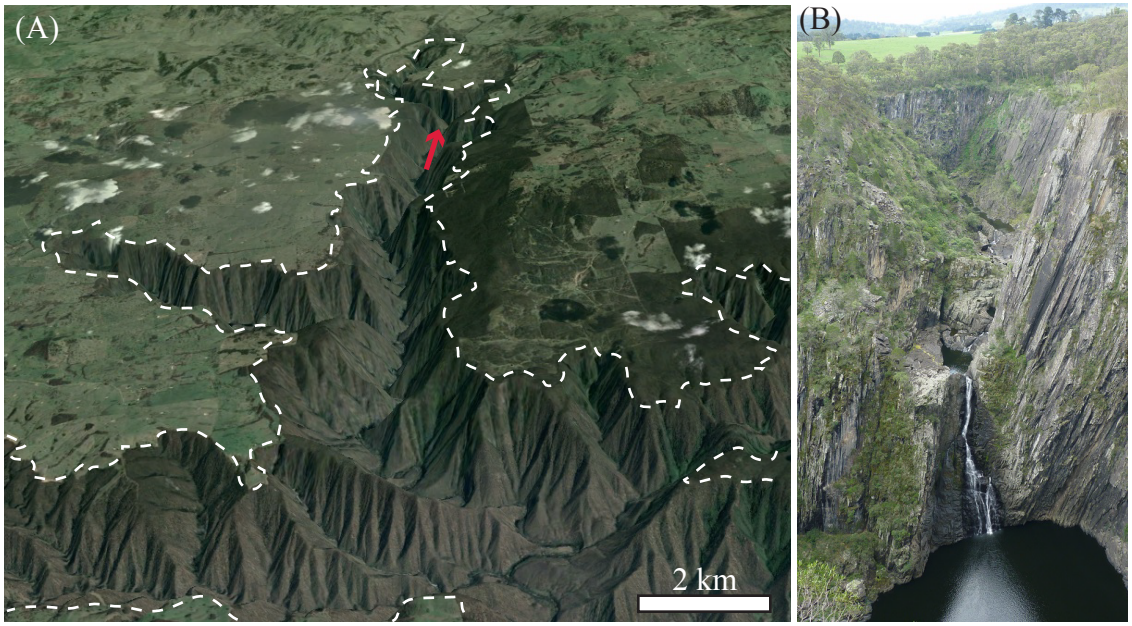

Figure 0.1: (A) Google Earth perspective view of Apsley River, southeast Australia. The high-relief, dissected landscape in the lower portion of the image is eroding headward into the low-relief landscape above following rifting along the Australian continental margin ~ 85 Ma [e.g., Seidl et al., 1996]. White-dashed line marks transition between the transient-landscape below and relict landscape above. (B) The head of the Apsley River canyon features a series of waterfalls. Red arrow in (A) notes orientation of photograph (B). Photo credit: Brian Piper, released under CC BY-NC-ND 2.0.

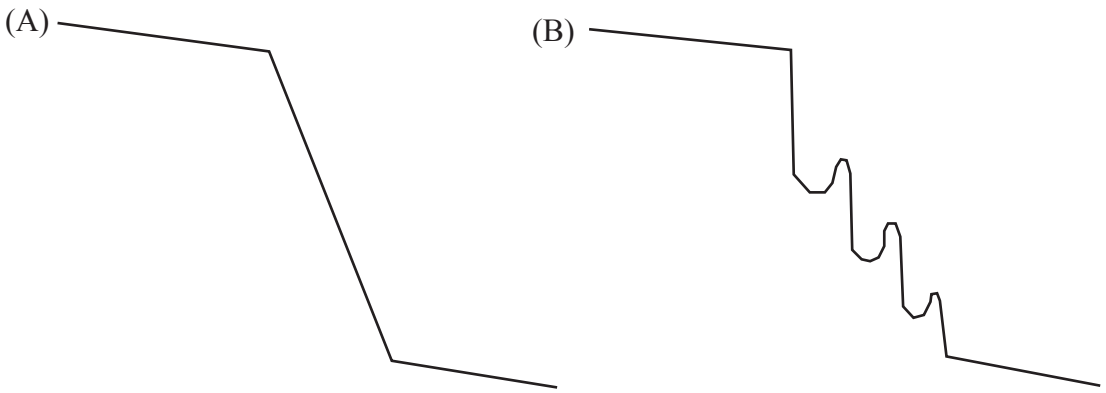

Figure 0.2: (A) Example of knickzone modeled as steepened river section without the presence of waterfalls. (B) Example of knickzone modeled as a series of waterfalls.

Chapter 1

FAULT-ZONE CONTROLS ON THE SPATIAL DISTRIBUTION OF SLOW-MOVING LANDSLIDES

Joel S. Scheingross[1], Brent M. Minchew[2], Benjamin H. Mackey[1,3], Mark Simons[2], Michael P. Lamb[1], Scott Hensley[4]

[1] Division of Geological and Planetary Sciences, California Institute of Technology, Pasadena, CA, 91125, USA
[2] Seismological Laboratory, Division of Geological and Planetary Sciences, California Institute of Technology, Pasadena, CA, 91125, USA
[3] Now at Department of Geological Sciences, University of Canterbury, Christchurch, New Zealand
[4] Jet Propulsion Laboratory, California Institute of Technology, Pasadena, CA, 91109, USA

* Adapted from Scheingross, Joel S., et al. “Fault-zone controls on the spatial distribution of slow-moving landslides.” Geological Society of America Bulletin, V. 125, no. 3/4, p. 473-489 (2013)
DOI: 10.1130/B30719.1

1.1 Abstract

Slow-moving landslides (earthflows) can dominate hillslope sediment flux and landscape erosion in hilly terrain with mechanically weak, fine-grained rock. Controls on the occurrence of slow-moving landslides are poorly constrained, and need to be understood for landscape evolution models, sediment budgets, and infrastructure and hazards planning. Here we use airborne interferometric synthetic aperture radar (InSAR) to document 150 previously unidentified active earthflows along the central, creeping portion of the San Andreas Fault, California, USA. The earthflows move seasonally in response to winter rainfall, occur on hillslopes at ~20-40% gradients (less than typically associated with rapid, catastrophic landslides), and have similar morphological characteristics to earthflows in different climatic and tectonic settings. Although our data extend up to 10 km from the fault trace, approximately 75% of detected landslides occur within 2 km of the active fault. Topographic, precipitation, and rock type metrics alone are not enough to explain the observed spatial distribution of earthflows. Instead, we hypothesize that earthflows cluster near the creeping San Andreas Fault because of a fault-induced zone of reduced bulk-rock strength that increases hillslope susceptibility to failure. In addition, similar lithology, topography, and climate exist north of the creeping section of the fault, yet earthflows there are rare. This may be due to large-magnitude earthquakes episodically triggering co-seismic rapid landslides, which preferentially remove weak rock from the fault damage zone. Our analysis suggests the necessary conditions for earthflow formation in central California include some combination of reduced rock strength, fine-grained sedimentary rock, threshold precipitation and relief, and possibly the absence of large-magnitude earthquakes. These conditions likely hold for earthflow development in other areas, and our

work suggests local variations in rock strength and seismicity, such as those associated with fault zones, need to be accounted for to accurately predict earthflow occurrence.

1.2 Introduction

In areas of weak, fine-grained bedrock with low to moderate hillslope gradients, slow-moving landslides can be the primary drivers of hillslope lowering and the dominant source of sediment to river networks (Kelsey, 1978; Schwab et al., 2008; Roering et al., 2009; Mackey and Roering, 2011). The transport of sediment from hillslopes to river networks via slow-moving landslides has direct implications for fluvial erosion and river-profile evolution (e.g., Kelsey, 1978; Korup, 2006), sedimentation engineering and loading (e.g., Brown and Ritter, 1971), and aquatic habitat (e.g. Lisle, 1989; Montgomery, 2004). Furthermore, slow-moving landslides can damage roads and structures (e.g., Putnam and Sharp, 1940), and pose further hazards to property and life via mobilization into debris flows (Reid et al., 2003).

We use the terms slow-moving landslides and earthflows interchangeably to refer to active hillslope mass failures involving non-turbulent downslope movement of hillslope material, typically at rates of millimeters to meters per year (Cruden and Varnes, 1996). These landslides can exceed 5 m in depth, deform via a combination of basal sliding and internal deformation, can be continually active for periods of years to centuries, and are distinct from rapid, catastrophic landslides that occur over periods of seconds to minutes (e.g., Kelsey, 1978; Bovis and Jones, 1992; Coe et al., 2003; Mackey and Roering, 2011). Earthflow thickness is commonly assumed to extend to near the base of the zone of weathered bedrock (e.g., Swanson and Swanston, 1977; Trotter, 1993; Booth and Roering,

2011), resulting in transport of both weathered bedrock and soil. Since earthflows require readily available material to transport, the bedrock weathering rate may limit earthflow activity (Mackey and Roering, 2011).

While the kinematics and mechanics of individual earthflows have been studied for over 70 years (e.g., Putnam and Sharp, 1940; Hutchinson and Bhandari, 1971; Kelsey, 1978; Keefer and Johnson, 1983; Iverson and Major, 1987; Angeli et al., 1996; Schulz et al., 2009), the controls on the spatial distribution of active earthflows are still poorly understood. In comparison, the spatial distribution of large catastrophic landslides has been widely shown to depend on uplift rates, climate, lithology, topography, rock structure, and seismicity (e.g., Keefer, 1984; Gabet et al., 2004; Roering et al., 2005). Similarly, the locations of smaller shallow landslides frequently correlate with soil depth, drainage area, convergent topography, intense precipitation, and removal of vegetation (e.g., Montgomery and Dietrich, 1994; Dietrich et al., 1995; Montgomery et al., 2000; Schmidt et al., 2001). Although slow-moving landslides are known to preferentially occur in Mediterranean-type climates with moderate hillslope gradients and mechanically weak sedimentary rock (e.g., Kelsey, 1978; Keefer and Johnson, 1983), there are numerous landscapes with these environmental conditions where active earthflows are not present, as well as mountainous areas with more extreme climates which feature active earthflows (e.g., Angeli et al., 1996; Leprince et al., 2008; Schulz et al., 2009). Where earthflows do occur, they tend to cluster spatially (e.g., Kelsey, 1978; Keefer and Johnson, 1983), suggesting some combination of environmental factors is required for extensive earthflow activity (Mackey and Roering, 2011). Understanding the controls on the spatial distribution of slow-moving landslides is needed to assess their contribution to erosion and landscape morphology, which in turn are

essential inputs to landscape evolution modeling (e.g., Tucker and Hancock, 2010), geomorphic transport laws (Dietrich et al., 2003), and hazard analysis (e.g., Radbruch-Hall et al., 1982).

The spatial distribution of earthflows may be influenced by a number of geologic, biologic, climatic, and topographic factors including, but not limited to, rock type, rock strength, bedrock fracture density, bedrock weathering rate, uplift rate, vegetation type and density, precipitation rate and intensity, hillslope azimuthal orientation (i.e., topographic aspect), and hillslope gradient (Kelsey, 1978; Keefer and Johnson, 1983; Bovis, 1985; Iverson, 1985; Zhang et al., 1993; Mackey and Roering, 2011). The majority of these variables have not been explored in a systematic way, and, in most cases, it is difficult to link earthflow distribution to a certain process. For example, several studies note a preference for earthflow occurrence on south facing hillslopes (e.g., Putnam and Sharp, 1940; Kelsey, 1978; Mackey and Roering, 2011), but there are competing explanations for this dependency including the lack of deep-rooted vegetation (Kelsey, 1978) and desiccation cracking (McSaveney and Griffiths, 1987; Mackey and Roering, 2011).

Here, we focus on two possible controls on the spatial distribution of slow-moving landslides that have not been previously explored: the influence of fault zone damage and large-magnitude earthquakes. Discrete seismic events along faults create a near-fault zone of fractured and pulverized rock (e.g., Chester and Logan, 1986; Ben-Zion and Sammis, 2003; Dor et al., 2006; Mitchell et al., 2011; Savage and Brodsky, 2011). The width of this damage zone varies, but can range from intense fracturing at the meter to hundreds-of-meter scale centered on the fault trace, with less intense fracturing extending several kilometers from the fault at the Earth surface (e.g., Fialko et al., 2002; Ma, 2008; Finzi et

al., 2009; Savage and Brodsky, 2011). Fault damage zones influence erosional processes (Wechsler et al., 2009), and one hypothesis we explore herein is that these zones may be favorable for slow-moving landslides due to reduced bulk-rock strength and the presence of bedrock fractures. However, an alternate hypothesis is that rapid, catastrophic landslides, which commonly occur following large earthquakes (e.g., Lawson, 1908; Keefer, 1984; Malamud et al., 2004), may preferentially remove fractured and weathered rock from the fault damage zone (e.g., Parker et al., 2011), leaving behind stronger bedrock in which earthflow formation is minimized.

To test these two competing hypotheses for fault zone controls on the spatial distribution of earthflows, we investigated the central portion of the San Andreas Fault (SAF) in central California, where fault zone damage can be isolated from large co-seismic landslides due to the presence of a "creeping" section of the fault that lacks large earthquakes. We use airborne interferometric synthetic aperture radar (InSAR) to map slow-moving landslides along the creeping section of the central SAF (Fig. 1.1), and compare these results to 1) earthflows in northern California, which occur in a similar lithology, but under different climatic and tectonic conditions (Mackey and Roering, 2011), and 2) earthflows (or a lack thereof) along the locked section of the central SAF. We begin by providing a description of the study area and the methods employed in processing and analyzing the airborne InSAR data. Next we present results on the morphologic characteristics of the earthflow population; seasonal changes in earthflow activity; the observed spatial distribution of active landslides in relationship to geologic, climatic, and topographic variables; and comparison to earthflows in northern California. Finally, we explore the role of reduced rock strength in the SAF damage zone as a possible mechanism

for the observed earthflow spatial distribution, and compare earthflow distributions in the creeping versus locked sections of the SAF to examine the influence of large-magnitude earthquakes.

1.3 Study area

The region bounding the creeping section of the San Andreas Fault in central California provides an ideal location to investigate the influence of fault damage zones and seismicity on the spatial distribution of earthflows. The area is subject to a common tectonic history and features many previously unmapped slope failures with morphologies characteristic of slow-moving landslides. The landslides occur dominantly along a narrow zone running parallel to the SAF, thus providing a long, linear swath ideal for spatial analysis (cf. Hilley and Arrowsmith, 2008). We examine the spatial distribution of active earthflows over a ~145-km-long by 22-km-wide swath parallel to (and approximately centered on) the creeping segment of the San Andreas Fault (Fig. 1.1).

The SAF is a right-lateral strike-slip fault and is divided into locked sections that exhibit stick-slip behavior due to large-magnitude earthquakes, and a creeping section that exhibits near continuous deformation. The creeping section of the San Andreas Fault extends north-northwest from Parkfield, CA to San Juan Bautista, CA and creeps at a rate of ~3 cm/yr (Savage and Burford, 1973; Burford and Harsh, 1980; Titus et al., 2005; Roladone et al., 2008; Ryder and Bürgmann, 2008) (Fig. 1.1). North and south of the creeping section, the fault is locked and generates relatively large-magnitude earthquakes, while within the creeping section there are small (M_w<4) but frequent earthquakes (e.g., Nadeau and McEvilly, 2004).

Rock type southwest of the creeping section of the SAF consists of marine sandstones, mudstones, and shales dominantly from the Pancho Rico, Santa Margarita, and Monterey Formations. Lithology northeast of the fault consists of Franciscan mélange, serpentinite, marine sandstone of the Etchegoin Formation, and shales of the Monterey, Gravelly Flat, and Panoche Formations (Dibblee, 2005; 2006; 2007a-j). The area southwest of the fault is characterized by low-relief rolling hills (up to ~200 meters ridge to valley relief), while the area northeast of the fault is steeper and of higher relief (up to ~900 m ridge to valley relief), which may be due to more competent bedrock. Average annual precipitation, as measured by rain gauges, ranges from approximately 225 – 500 mm/yr in the study area, with higher average annual levels of precipitation northeast of the SAF (Western Regional Climate Center).

At the southern and northern extent of the San Andreas Fault creeping section, seismic data sets show the presence of a low velocity zone up to ~6 km wide at the surface, with a wider damage zone on the northeastern side of the fault (e.g., Thurber et al., 1997; Li et al., 2004; Lewis et al., 2007). This asymmetry is likely due to lithology differences on either side of the fault that induce preferential propagation directions for seismic waves (e.g., Ben-Zion and Shi, 2005; Dor et al., 2008). Electromagnetic imaging in the creeping section shows areas of low-resistivity overlapping with low seismic velocity zones (Unsworth et al., 1999; Bedrosian et al., 2004). Both low seismic velocity and low resistivity have been inferred to represent high bedrock fracture density, which acts to reduce bulk-rock strength (Bedrosian et al., 2004; Clarke and Burbank, 2010). A fault damage zone likely exists throughout the creeping section of the SAF, as measurements of fault offset features suggest the SAF has experienced 300 – 320 km of cumulative

displacement (compared to the approximately 150 km length of the creeping zone), ensuring that material currently in the creeping section has previously passed through locked portions of the fault subject to stick-slip behavior (Huffman, 1972; Matthews, 1976; Graham et al., 1989; Revenaugh and Reasoner, 1997).

1.4 Airborne InSAR acquisition and processing

We mapped active earthflows using InSAR data that were acquired by the Uninhabited Aerial Vehicle Synthetic Aperture Radar (UAVSAR) system, which is operated by NASA's Jet Propulsion Laboratory, and are publicly available from the Alaska Satellite Facility (*http://uavsar.jpl.nasa.gov/*). UAVSAR is a left-looking, L-band (24-cm wavelength, 1.25 GHz), fully polarimetric, repeat-pass-capable SAR system that, at the time of data collection, was flown aboard a NASA Gulfstream III aircraft. The system is capable of collecting data with a 1.9 m range (cross-track) and 0.8 m azimuth (along-track) resolution (Hensley et al., 2009b). The use of an airborne platform distinguishes UAVSAR from more conventional spaceborne SAR systems (e.g., ALOS, ERS, etc.), which typically provide greater spatial coverage at the expense of coarser resolution, fixed flight tracks, and fixed repeat-pass times.

Compared to data acquired from satellites, random aircraft motions complicate the processing task, and are, to a significant degree, accounted for using data from UAVSAR's native differential GPS system and inertial navigation unit, which operate in conjunction with the precision autopilot system. The centimeter-scale residual motion between aircraft repeat passes (i.e., residual interferometric baseline) that is uncompensated for using onboard metrology data is estimated from the imagery registration information between the

two InSAR passes to generate geodetically useful data (Hensley et al., 2009a). Small residuals can remain after this process, but because UAVSAR maintains a very small baseline (typically less than 2 m) interferometric noise (decorrelation) is primarily due to temporal variations in the study area.

UAVSAR data are geo-located and typically averaged over a 3 x 12 (range x azimuth) pixel window prior to public distribution to give a usable resolution of 5.7 m in range and 9.6 m in azimuth. Unwrapped interferograms are available with the UAVSAR repeat-pass interferometry (RPI) data, but we chose to unwrap the interferograms ourselves using the Statistical-Cost, Network-Flow Algorithm for Phase Unwrapping (SNAPHU) (Chen and Zebker, 2000;2001;2002) software suite, because the high relief in the study area yields branches of low interferometric correlation (high noise) which can cause the standard unwrapping algorithm used in the UAVSAR processing chain to neglect large portions of usable data. We filtered the interferograms using the Goldstein-Werner filtering method (filtering exponent = 0.5, filtering window = 3 x 3, and interferometric correlation estimation window = 5 x 5) (Goldstein and Werner, 1998) prior to unwrapping with SNAPHU and we excluded data that have interferometric correlation values less than 0.3 (Rosen et al., 2000; Simons and Rosen, 2007).

1.5 Earthflow morphology and bulk characteristics

1.5.1 Methods

Even with high resolution imagery and topographic data, it can be difficult to differentiate between active and dormant earthflows which can retain morphological signatures of movement long after flowing has ceased (Mackey et al., 2009; Mackey and

Roering, 2011). To objectively identify active features, we mapped landslides within the spatial extent of UAVSAR line 14003 (heading 140˚ from north), which runs parallel to the creeping section of the SAF (Fig. 1.1, Table 1). We also used ~1 m^2 resolution aerial photographs (Bing Maps, *http://www.bing.com/maps/*) which are accurately orthorectified within ESRI ArcMap 10, and a 10 m resolution (National Elevation Dataset, *http://ned.usgs.gov/*) digital elevation model (DEM) with vertical accuracy of 2.4 meters (Gesch et al., 2002; Gesch, 2007). Because InSAR measurements are only sensitive to the component of motion along the radar line-of-sight (LOS), we examined an additional 30 interferograms generated from UAVSAR flight lines that were flown perpendicular to the SAF (Table 1). We note that the majority of active landslides documented herein are observable in the interferograms formed from UAVSAR flight line 14003. The high resolution of airborne InSAR and ability to fly at any desired heading allows documentation of deformation on small active earthflows (> 50 m in width). The data set includes three different lines-of-sight covering different lengths of time (~0.5 years to almost 2 years repeat pass time).

We identified active landslides as areas that showed a departure from the background interferogram phase and were coincident with morphometric features (observed in high-resolution aerial images) indicative of slow-moving landslides (e.g., lateral margins, pressure ridges, and hummocky terrain (Kelsey, 1978; Cruden and Varnes, 1996; McKean and Roering, 2004; Booth et al., 2009; Mackey and Roering, 2011)). To minimize false-positives in active landslide classification, we required both characteristic earthflow terrain in aerial images and motion revealed by InSAR for identification. Field reconnaissance of InSAR-identified earthflows revealed deformed roads and active highway maintenance as

additional evidence of recent activity (Fig. 1.2). The majority of identified earthflows exhibited increased velocity during winter months as is commonly observed for slow-moving landslides (discussed below), suggesting that InSAR detected true landslide motion. Finally, we note the absence of large landslide scars within the study area, suggesting that the earthflows are not related to rapid, catastrophic landslides.

1.5.2 Earthflow slope distribution

We identified a total of 150 slow-moving landslides that were active within the study region between May 2010 and July 2011. These landslides vary in active width from ~50 to 1,500 m, active length from ~100 to 2,500 m, active area from ~0.005 to 2 km^2, and show a lognormal distribution of areal extent (Fig. 1.3). Mean earthflow slope (defined as the mean of all slope values calculated on a pixel by pixel basis within an earthflow) is limited to a narrow range (0.32 ± 0.1; mean $\pm$ 1 sigma standard deviation) (Fig. 1.4A). We interpret the narrow slope distribution of earthflows to suggest slow-moving landslides may regulate hillslope gradients and create threshold hillslopes (e.g., Carson and Petley, 1970; Burbank et al., 1996; Mackey and Roering, 2011). That is, when hillslopes exceed a threshold angle, gravitational stresses become large enough to induce earthflow activity; earthflows then advect material downslope until the hillslope gradient falls below a threshold angle and movement ceases due to the reduction in gravitational stress. This finding is significant as threshold hillslopes are typically associated with rapid landsliding (e.g., Burbank et al., 1996; Larsen and Montgomery, 2012) which limit hillslope gradients to slopes of approximately 0.6 (~30°) (e.g., Roering et al., 2001; Binnie et al., 2007; Ouimet et al., 2009), compared to earthflows which appear to limit hillslopes to much lower gradients (i.e., slopes of ~0.3).

A complication to the threshold hillslope hypothesis above is our observation of earthflow slope varying inversely with landslide areal extent (Fig. 1.3). Assuming earthflow area scales with landslide thickness, as has been shown for rapid-landslides (e.g., Larsen et al., 2010), thicker earthflows failing at lower slopes suggests earthflows initiate movement at a threshold basal shear stress rather than a threshold slope. However, this is a second order effect in our study area, as mean earthflow slope decreases by a factor of approximately one third over two orders of magnitude change in landslide areal extent.

We compared the slope distributions of earthflows in this study to another population of 122 slow-moving landslides within the Eel River watershed in northern California (Mackey and Roering, 2011). The Eel River watershed has similar lithology to our study site (most earthflows occur in Franciscan Complex mélange), with ~2-3 times greater annual average precipitation rates, and slightly higher vegetation densities (Mackey and Roering, 2011). Both populations of earthflows show narrow distributions of mean earthflow slope, and have statistically indistinguishable mean slope distributions (p = 0.62 in a two-sample t-test at 5% confidence level, Fig. 1.4B). The observation of earthflow populations in distinct climates and tectonic regimes with indistinguishable hillslope gradient distributions further supports the idea that earthflows set threshold hillslopes.

1.5.3 Earthflow aspect distribution

Earthflows along the SAF occur dominantly on southwest facing slopes of ~170 – 250° aspect (Fig. 1.4C). The aspect dependence could be influenced by the distribution of slopes adjacent to the SAF, where earthflows are most common; however, southwest facing hillslopes only account for one third of the terrain immediately adjacent to the SAF compared to the approximately two thirds of earthflows with average aspects of 170-250°

(Fig. 1.4). Additionally, although the southwest aspect of earthflows matches the radar LOS of the line 14003 interferogram, the observed aspect dependence should not be an artifact of limited radar LOS diversity as we mapped landslides using interferograms with three different LOS directions, thereby eliminating bias due to a single imaging geometry. Southwest aspect dependence could arise due to increased solar insolation on south facing hillslopes which induces desiccation cracks facilitating water flow to the earthflow failure plane (McSaveney and Griffiths, 1987; Mackey and Roering, 2011), or due to an absence of deep-rooted vegetation on south facing hillslopes which increases hillslope susceptibility to rapid-landslides (e.g., Montgomery et al., 2000; Schmidt et al., 2001; Roering et al., 2003) and has been argued to apply to earthflows (Kelsey, 1978; Zhang et al., 1993). We note that southwest hillslopes observed here lack trees or other deep-rooted vegetation (both on stable and active terrain), and the southwest aspect dependence of earthflows is more pronounced than that found by Mackey and Roering (2011) (Fig. 1.4D). This may be due to more systematic variation in vegetation with aspect in our study area compared to Mackey and Roering (2011), who found no systematic difference in vegetation cover between hillslope directions in their study area, and would thus suggest that both lack of deep-rooting vegetation and increased solar insolation are important factors for predicting earthflow spatial distribution. Interestingly, Beaty (1956) noted a preference for earthflows on north facing hillslopes near Berkeley, CA, and argued that reduced solar insolation on north facing hillslopes allowed increased moisture retention. In our study area, we see no preference for earthflows on north facing hillslopes, suggesting that vegetation and solar insolation-induced desiccation cracking may be more important in controlling earthflow spatial distribution than moisture retention.

1.6 Earthflow velocities

1.6.1 Methods

The study area is characterized by an increase in precipitation during winter months (Fig. 1.5), and comparison between the May 11, 2010 – November 16, 2010 line 14003 interferogram (hereafter referred to as the "summer interferogram") and the November 16, 2010 – July 12, 2011 line 14003 interferogram (hereafter referred to as the "winter interferogram", see Table 1 for full interferogram identifications) allowed us to document changes in earthflow activity, spatial extent, and velocity between a relatively dry and a relatively wet period.

LOS velocities for individual earthflows were calculated for the fault-parallel interferograms by locally subtracting the mean phase value of the area around the landslide from the unwrapped interferogram. Since InSAR only measures LOS velocity, we do not know true downslope earthflow velocities. However, the majority of landslides are oriented at similar angles with respect to the radar LOS direction, thus allowing meaningful relative comparison of LOS velocities between earthflows.

In order to examine the total number of earthflows that showed an increase in LOS velocity, we compared the distribution of the ratio v_w/v_s, where v_w and v_s are the median LOS velocities of a given landslide in the winter and summer interferogram, respectively. We excluded all areas with interferometric correlation of less than 0.3 in our analysis of velocity and defined a value, a^*, representing the fraction of a given earthflow area with interferometric correlation values greater than 0.3; for example, a value of $a^* = 0.9$ means 90% of the pixels within the earthflow areal extent have interferometric correlation > 0.3.

1.6.2 Seasonal controls on earthflow velocity and areal extent

Comparisons between the winter and summer interferograms showed that both landslide velocity and areal extent tend to increase in the wetter (i.e., winter) period (cf. Calabro et al., 2010). For example, a seasonal increase in individual earthflow activity is clearly illustrated for a large landslide in the study area where we observed that the winter interferogram showed downslope movement in many portions of the earthflow not active in the summer interferogram, as well as 25-200% increase in LOS velocity relative to the summer interferogram (Fig. 1.6).

We found that approximately 75% of earthflows showed an increase in median velocity ($v_w/v_s > 1$) between the summer and winter interferograms, with many landslides more than doubling velocity, and a maximum rate of increase of velocity of $v_w/v_s = 10.2$ (Fig. 1.7A). The calculated increase in median velocity was not particularly sensitive to values of a^*, except at very high a^* values where low sample size may have introduced error (Fig. 1.7B). We also note that when examining the 90^{th} LOS velocity percentile, greater than 80% of earthflows are interpreted to have increased in velocity in the winter interferogram, and there is a slightly stronger dependence on a^* (Fig. 1.7C).

We interpret the observed increase in velocity and earthflow areal extent in the winter interferogram as due to winter precipitation that increased pore-water pressure within earthflows (e.g., Iverson and Major, 1987; Schulz et al., 2009). Seasonal, precipitation-driven increases in earthflow velocity have been well documented for several individual and small groups of earthflows (e.g., Putnam and Sharp, 1940; Angeli et al., 1996; Coe et al., 2003; van Asch, 2005; Calabro et al., 2010), but no study, to our knowledge, has documented such behavior across an entire study area. The increase in

areal extent of active earthflows in the wet period suggests the possibility of a yield strength, whereby portions of an individual landslide can switch between active and inactive.

1.7 Spatial distribution of earthflows

1.7.1 Methods

In order to examine controls on the spatial distribution of active earthflows along the creeping section of the SAF we divided the study area into sets of evenly spaced SAF-parallel and SAF-perpendicular swaths for which we calculated zonal statistics of earthflow activity, topographic metrics, precipitation metrics, and rock type. This analysis was designed to test for confounding variables that may explain the distribution of earthflows independent of the association with the SAF. The fault-perpendicular swaths are 4 km (along-fault) by 12 km (cross-fault) and extend along the full ~145 km length of the study area (Fig 8A). The fault-parallel swaths are 1 km (cross-fault) by 75 km (along-fault) extending approximately from Parkfield, CA to Bitterwater, CA (Fig. 1.8B). Both sets of swaths were selected so that the majority of active landslides would be included within the swaths, but small enough so that landslide-prone areas and landslide absent areas were not included within a single swath. For each swath segment we calculated the percent of terrain that was actively deforming, the mean hillslope gradient (from the 10 m NED DEM), the fraction of southwest facing hillslopes, the total precipitation over the study period (May 2010 - July 2011, estimated for 4x4 km grid cells by a spatial climatic interpolation (PRISM Climate Group, Oregon State University)), maximum predicted seven-day rainfall intensity for a two-year recurrence interval period (estimated for ~0.9 x 0.9 km grid cells by

a spatial climatic interpolation (Perica, 2011)), and the fraction of the dominant regional rock types (sandstone, mudstone, shale, and Franciscan mélange) exposed within each swath segment. Lithology was mapped by digitizing major units in 13 geologic maps along the SAF (Dibblee, 2005;2006;2007a-j); each unit was characterized by its dominant lithology.

In addition to the above variables, we also compared measures of seismicity to earthflow occurrence within swaths along the creeping section of the SAF in order to investigate if an anti-correlation exists between large-magnitude earthquakes and earthflow activity as suggested above. We used peak ground acceleration (PGA) as a ground motion variable to represent seismicity because catastrophic landslide spatial density following large earthquakes has been shown to scale with PGA (Meunier et al., 2007; Meunier et al., 2008). We calculated PGA at 1 km^2 grid cells for all 3576 earthquakes (M_w>0.5) which occurred between May 11, 2010 and July 12, 2011 within our study area (the time frame corresponding to line 14003 interferograms which were used in landslide mapping), as well as for 42731 earthquakes which occurred during a 20-year period from January 1, 1991 – December 31, 2010. The 20-year dataset has 33 earthquakes with $M_w \geq 4$, including the 2004 Parkfield Earthquake (M_w=6.0). We obtained earthquake magnitudes and locations from the Northern California Earthquake Data Center (*http://quake.geo.berkeley.edu/*), and calculated PGA with a generic attenuation law (Boore and Atkinson, 2007) using average shear-wave velocity values between 0 and 30 m depth (V_s30) provided by the United States Geological Survey at ~1 km^2 grid cells which define our PGA grid (*http://earthquake-.usgs.gov/hazards/apps/vs30/*). While no attenuation law exists which is calibrated for low-

magnitude earthquakes (M_w<~5.0), the Boore and Atkinson (2007) model produces PGA values that decay with distance from the source, so that the general trends in PGA across the study area should hold, even if the exact PGA values are inaccurate. For both sets of earthquakes, we computed the median PGA (across all earthquakes) at each grid cell and the single maximum PGA value achieved at a grid cell over the study period to compare with earthflow distribution. We chose to use maximum and median PGA in order to investigate the relative influence of single, large events versus small, frequent events, respectively.

1.7.2 Cross-fault earthflow spatial distribution

Active earthflows in the study area are most densely concentrated within a ~2 km zone on either side of the SAF between Parkfield, CA and Bitterwater, CA (Fig. 1.1). Approximately 60% of landslides occur within 1 km of the fault (~75% occur within 2 km of the SAF), and the earthflows are slightly preferentially distributed east of the SAF (Fig. 1.9). This distribution may be a result of a larger fraction of southwest facing slopes being present east of the fault or from asymmetric damage zones along the fault (e.g., Dor et al., 2006; Lewis et al., 2007; Mitchell et al., 2011). North of Bitterwater we observe nearly all earthflows are northeast of the SAF (Fig. 1.8A), coincident with geophysical surveys that show relatively weak, fractured rock (Thurber et al., 1997; Bedrosian et al., 2004).

Zonal swath mapping parallel to the SAF allows examination of the influence of changes in topographic and climatic conditions on earthflow spatial distribution in relation to distance from the SAF. Within our fault-parallel swaths, the percent of active terrain (i.e., the percent of area occupied by earthflows within a given swath) peaks at ~7% along the SAF, and ranges from 0-3% away from the SAF (Fig. 1.10A). Median topographic

slope (over the entire area within the swath) is anti-correlated with percent of active terrain, dropping to ~0.27 along the SAF, and ranging between ~0.34 – 0.38 away from the fault (Fig. 1.10B). Topographic relief is small southwest of the SAF (< ~300 m), increasing to maximum values of ~750 m northeast of the SAF (Fig. 1.10C). The percent of swath area with southwest facing hillslopes is similar to the percent of active terrain, with a peak at ~35% near the fault, and dropping to ~22% (the expected value if hillslope aspect is evenly distributed) away from the SAF (Fig. 1.10D). Annual precipitation and maximum expected seven-day rainfall intensity both show a steady increase from southwest to northeast (Fig. 1.10E). The distribution of the fraction of Franciscan Complex (dominantly mélange) exposed in a swath is similar to the distribution of the percent of active terrain, but there is no obvious visual correlation between other lithologies and active terrain (Fig. 1.10F).

We interpret none of the above metrics as sufficient to fully explain the observed cross-fault spatial distribution of earthflows. As earthflows likely suppress the development of steeper slopes (discussed above), mean hillslope gradient in earthflow dominated areas is partially set by earthflows themselves. Thus we discount the anti-correlation between topographic slope and earthflow activity (Fig. 1.10A,B). Hillslope aspect does not appear to be a sufficient condition to explain earthflow spatial distribution. If availability of southwest facing aspects limits earthflow development we would expect only a slight reduction in earthflow spatial density away from the SAF where ~20% of the landscape has southwest facing hillslopes, not a drop to almost 0% active terrain. Threshold values of relief and precipitation are likely necessary for earthflow activity, but not sufficient conditions for earthflow generation, as we observe onset of earthflows coincident with increases in relief, annual precipitation, and rainfall intensity. However, we note that relief

and precipitation are correlated in nature, and, furthermore, the precipitation interpolations used here employ elevation as a predictor of rainfall, thus limiting our ability to determine the influences of relief and precipitation independently. Finally, earthflows occur in several different rock types which exist throughout the study area, thus lithology does not appear to be restricting earthflow extent to areas near the SAF.

We suggest that the extent of the reduced rock strength and bedrock fracturing within the fault damage zone is a primary control on the cross-fault spatial distribution of earthflows in our study area. The high density of earthflows within 2 km of the SAF is within the range of general theoretical predictions and geophysical measurements for fault damage zones widths (Thurber et al., 1997; Fialko et al., 2002; Bedrosian et al., 2004; Ma, 2008; Finzi et al., 2009), and no other morphometric or climatic variable we analyzed is sufficient to explain the cross-fault earthflow spatial distribution. Reduced rock strength and high fracture density within the fault damage zone should exist along the entire length of the SAF and its splays. Therefore, if fault damage is the determining factor affecting the presence of earthflows, we would expect to see earthflow activity outside of the creeping zone.

1.7.3 Along-fault earthflow spatial distribution

In the along-fault direction, the highest spatial density of earthflows occurs between Parkfield, CA and Bitterwater, CA; only one active earthflow was mapped south of Parkfield (Figs. 1.1, 1.8, and 1.10G). North of Bitterwater, earthflows decrease in spatial density and are mostly northeast of the SAF (with some crossing the Calaveras-Paicines fault system) (Figs. 1.1 and 1.8). Zonal swath mapping in the study area perpendicular to the SAF shows median topographic slope is lowest south of Parkfield, is consistently

between 0.30 – 0.40 for ~100 km north of Parkfield, and falls to ~0.22 at the northeastern extent of the study area (Fig. 1.10H). Maximum topographic relief is smallest south of Parkfield, increases to ~750 m at ~50 km north of Parkfield, and then slowly decreases (Fig. 1.10I). The fraction of terrain with southwest facing aspects is scattered between ~20 – 30%, but is generally above what is expected for an equal distribution of aspects (~22%, Fig. 1.10J). Annual precipitation and rainfall intensity have similar distributions to the percent of active terrain, with lows on the southwestern and northeastern extent of the creeping section, and peaks between Parkfield and Bitterwater (Fig. 1.10K). There is no visual correlation between the distribution of rock type and percent of active terrain (Fig. 1.10L). As with the fault-parallel swaths above, topographic slope, hillslope aspect, precipitation, and lithology do not appear to individually exert a strong control on the spatial distribution of earthflows.

1.7.4 Seismic controls on earthflow spatial distribution within the creeping SAF

The abrupt increase in earthflow occurrence coincident with the beginning of the creeping section of the San Andreas Fault suggests that earthflow spatial distribution may be influenced by the lack of large-magnitude earthquakes in the study area. We use the fault-perpendicular swaths to test for correlation between spatial density of earthflows and seismic ground motion. There is no visual correlation of earthflow occurrence with either maximum or median PGA in both the 20-year (1991 – 2011) and 427 day (May 2010 – July 2011) sets of earthquakes (Fig. 1.11). In fact, there is a slight anti-correlation between earthflow occurrence and maximum PGA for the 20-year period (Fig. 1.11B,D). Anti-correlation between maximum PGA and earthflow occurrence is consistent with our hypothesis that co-seismic landslides produced by large-magnitude earthquakes remove

weak material on hillslopes, effectively limiting earthflow source material. If co-seismic landslides are on average 1 meter deep and the weathering rate of bedrock averages 0.5 mm/yr (DeLong et al., 2012), a large earthquake could suppress earthflow development for a period of up to 2000 years (i.e., 1 m / 0.5 mm yr^{-1}), if not longer. Under such conditions, earthquake data sets extending hundreds to thousands of years would be needed to fully capture the relationship between seismic ground-motion and earthflow spatial distribution.

1.8 Discussion

1.8.1 Mechanisms for fault damage controls on earthflow activity

We argue that the presence of a fault damage zone is the primary control on the cross-fault distribution of earthflows within the creeping section of the SAF, and could increase earthflow activity in three ways. First, through decreasing mechanical rock strength and thus increasing susceptibility towards hillslope failure (e.g., Molnar et al., 2007; Clarke and Burbank, 2010). Second, through creating bedrock fractures which act as conduits for groundwater and rain flow. Fractures extending to the surface can aid in the rapid delivery of rain water to the landslide failure plane and has been suggested as a mechanism to increase pore-water pressure resulting in landslide movement (McSaveney and Griffiths, 1987; Coe et al., 2003). Third, through higher rates of weathering due to increased fracture density (e.g., Molnar et al., 2007). Water and biological organisms, which enter bedrock through fractures, enhance weathering via hydrolysis of minerals and root-development (Graham et al., 2010). As earthflow failure surfaces are commonly near the base of the zone of highly weathered bedrock (e.g., Swanson and Swanston, 1977; Trotter, 1993; Booth and Roering, 2011), this process can produce increased availability of

earthflow source material and thicker earthflow deposits, thus driving earthflow activity via increased gravitational stresses. Increased weathering rates may be particularly important as earthflows have been argued to undergo long periods of inactivity while waiting for weathering processes to renew sufficient source material for movement to re-initiate (Mackey and Roering, 2011). The availability of readily transportable material may be especially high for earthflows that cross or have heads abutting the SAF (22% of earthflows within our study area, Fig. 1.1B). For these earthflows, the creeping motion of the fault may drive landslide activity via lateral advection of material into the earthflow sediment source zone at rates faster than background weathering processes. That is, motion along the SAF could potentially supply source material to earthflows faster than earthflow movement depletes the available supply.

1.8.2 Do large-magnitude earthquakes suppress earthflow development?

We showed a potential anti-correlation between earthflows and maximum PGA within the creeping section of the SAF and further investigate the hypothesis that large-magnitude earthquakes inhibit earthflow development by comparing the spatial distribution of earthflows in the creeping versus northern locked section of the SAF and its major splays (the Hayward and Calaveras faults). North of the creeping section, the SAF passes through the Santa Cruz Mountains, eventually entering the Pacific Ocean ~10 km south of San Francisco, CA. Earthflows in the Santa Cruz Mountains exist (Wieczorek et al., 2007), but are rare, and the area has a high density of rapid-landslides as opposed to earthflows (Nolan and Marron, 1985). Similarly, earthflows are not common within the fault damage zone of the Calaveras or Hayward faults. Keefer and Johnson (1983) summarized literature and conducted extensive aerial and ground-based reconnaissance to identify areas of high

earthflow spatial density over a large portion of the San Francisco Bay area, including the entire lengths of the Calaveras and Hayward faults. Comparing mapping by Keefer and Johnson (1983) with earthflows identified in this study shows earthflows are more continuously distributed along the creeping section of the SAF than along the Calaveras and Hayward faults (Fig. 1.12). While Keefer and Johnson (1983) mapped an area of high earthflow density at the northern extent of the Calaveras and Hayward faults, earthflows here extend distances up to 12 km from the fault, suggesting factors besides fault zone damage are influencing the earthflow spatial distribution.

Both the Santa Cruz Mountains and the areas adjacent to the Calaveras and Hayward faults feature abundant exposure of Franciscan mélange and other lithologies which have been documented to host earthflows (Jennings and Burnett, 1961; Rogers, 1966), suggesting rock type does not limit earthflow occurrence north of the creeping section. To investigate the controls of relief, hillslope gradient, aspect, and annual precipitation on earthflow spatial distribution, we performed a swath analysis similar to that presented above for the area extending ~2 km on either side of the SAF from the Transverse Ranges to the San Francisco Peninsula. These swaths showed that relief, slope, and aspect are similar between the northern locked and creeping sections of the SAF, although annual precipitation is higher in the former.

Given the similarity in lithology, topography, and climate between the northern locked and creeping sections of the SAF, we expect an equal spatial distribution of earthflows within the fault damage zones of both areas. The lack of earthflows within the fault damage zone north of the creeping section may be controlled by large-magnitude earthquakes which induce co-seismic landslides. The Santa Cruz Mountains experienced

many co-seismic landslides during the 1906 San Francisco Earthquake (M_w=7.9) and the 1989 Loma Prieta Earthquake (M_w=6.9) (Lawson, 1908; Keefer, 2000). Similarly, paleoseismology on the Hayward Fault shows large-magnitude earthquakes have a recurrence interval of ~160 years, with the last earthquake in 1868 (M_w=6.8) (Lienkaemper et al., 2010), and that there have been 13 M_w>5 earthquakes on the Calaveras Fault in the past 150 years (Oppenheimer et al., 1990; Manaker et al., 2003). Co-seismic landslides associated with these large-magnitude earthquakes may preferentially remove weathered and fractured bedrock from hillslopes, thus limiting the availability of source material for earthflow transport, and suppressing earthflow development. This last point is difficult to unambiguously prove as climatic, topographic, and geologic conditions vary when moving from the creeping to the locked sections of the SAF (Fig. 1.13). For example, heavy rainfall associated with an El Niño year (1997-1998) produced a large number of rapid landslides in the Santa Cruz Mountains (Baum et al., 1999), suggesting that rainfall-induced shallow-landsliding may also limit earthflow source material. Similarly, Keefer and Johnson (1983) show areas of high earthflow density outside of the fault damage zone, perhaps driven by increased regional precipitation in the San Francisco Bay area which could allow earthflow development despite increased rock strength. Ultimately, the competing influences of topography, climate, lithology, rock strength, and seismicity all can affect earthflow spatial distribution.

Comparing earthflow distribution between the creeping and southern-locked sections of the SAF is difficult. At the southern extent of the creeping section, co-seismic, rapid landslides have been documented for the 1966 and 2004 Parkfield Earthquakes (both M_w=6.0) (Brown et al., 1967; Rymer et al., 2006). Unfortunately, despite observing the

southern extent of our mapped earthflows coincident with the onset of co-seismic landslides, we are unable to test the anti-correlation of earthflows and seismicity in this region. Our swath analysis showed relief, hillslope gradient, and precipitation decrease south of the creeping section of the SAF, as the SAF enters a broad, low relief valley (Fig. 1.13). Thus, topography and climate in the southern locked section is not suitable for the generation of earthflows, regardless of the degree of seismicity.

We interpret the observed earthflow spatial distribution within the creeping section of the SAF to be a unique case where low regional precipitation and the absence of large-magnitude earthquakes limits the spatial distribution of slow-moving landslides to the reduced rock strength and high fracture density fault damage zone, thus allowing a test of rock strength and bedrock fracture controls on earthflow spatial distribution. It is possible that under changing environmental conditions (for example, increased precipitation) earthflows could become more frequent in areas outside of the fault damage zone of the creeping SAF. In such a scenario, earthflows within the fault damage zone may occur at lower slopes due to decreased rock strength.

We find that faulting introduces competing influences that can both promote and suppress the occurrence of slow-moving landslides through reduced rock strength and large-magnitude earthquakes, respectively. These processes should be accounted for in the development of landscape evolution models and geomorphic transport laws, which incorporate earthflow processes. Future work on the relative influences of tectonics, climate, topography, and lithology is needed to develop a robust model to predict the spatial distribution of earthflows, similar to previous work for shallow-landslides (e.g., Montgomery and Dietrich, 1994; Dietrich et al., 1995).

1.9 CONCLUSIONS

We use a combination of airborne InSAR and high-resolution aerial images to map the occurrence and extent of active, slow-moving landslides in a ~145 by 22 km swath centered on the creeping portion of the San Andreas Fault, CA. The majority of mapped landslides show high interferometric correlation and display seasonal increases in line-of-sight velocity corresponding to periods of increased precipitation. The earthflows occur dominantly with mean hillslope gradients near 0.32, suggesting slow-moving landslides create threshold hillslopes at slope angles significantly lower than commonly assumed for rapid-landslides. We find a strong association between earthflow occurrence and distance from the SAF, with ~75% of mapped landslides occurring within 2 km of the fault trace. This zone corresponds to theoretical predictions and field measurements of the surficial extent of the San Andreas Fault damage zone. The observed spatial distribution of earthflows cannot be explained by topographic metrics, rock type, or climate alone. Instead, we suggest the extent of the fault damage zone locally controls the spatial distribution of earthflows along the creeping section of the SAF. The fault damage zone features fractured and pulverized rock which reduces bulk-rock strength, increases bedrock permeability, and may increase bedrock weathering rates (and hence, earthflow thickness), all of which promote earthflow activity. Earthflows occur at lower spatial densities north of the creeping section, perhaps as a result of large-magnitude earthquakes inducing co-seismic landslides that suppress earthflow development via removal of earthflow source material from hillslopes. We suggest that reduced rock strength, bedrock fracturing, threshold precipitation and relief, fine-grained rock, and possibly the absence of large-magnitude

earthquakes are necessary conditions for earthflow development in central California. None of these variables alone are sufficient for earthflow formation, but in certain cases a single variable can exert a strong control.

1.10 ACKNOWLEDGEMENTS

We benefitted from fruitful discussions with Jean-Philippe Avouac, Jean-Paul Ampuero, and Piyush Agram. Eric Fielding, Yang Zheng, and Brian Hawkins helped facilitate UAVSAR data access. The Keck Institute for Space Studies provided funding for this study through the Advanced Earth Surface Observation Project. JSS was partially supported by a NSF Graduate Research Fellowship. We thank three anonymous reviewers for insightful comments that improved the structure and clarity of this manuscript.

1.11 REFERENCES

Angeli, M. G., Gasparetto, P., Menotti, R. M., Pasuto, A., and Silvano, S., 1996, A visco-plastic model for slope analysis applied to a mudslide in Cortina d'Ampezzo, Italy: Quarterly Journal of Engineering Geology, v. 29, p. 233-240.

Baum, R. L., Schuster, R. L., and Godt, J. W., 1999, Map showing locations of damaging landslides in Santa Cruz County, California, Resulting From 1997-98 El Niño rainstorms: USGS Miscelleneous Field Studies MF-2325-D.

Beaty, C. B., 1956, Landslides and slope exposure: Journal of Geology, v. 64, no. 1, p. 70-74.

Bedrosian, P. A., Unsworth, M. J., Egbert, G. D., and Thurber, C. H., 2004, Geophysical images of the creeping segment of the San Andreas Fault: implications for the role of crustal fluids in the earthquake process: Tectonophysics, v. 385, no. 1-4, p. 137-158.

Ben-Zion, Y., and Sammis, C. G., 2003, Characterization of fault zones: Pure and Applied Geophysics, v. 160, no. 3-4, p. 677-715.

Ben-Zion, Y., and Shi, Z. Q., 2005, Dynamic rupture on a material interface with spontaneous generation of plastic strain in the bulk: Earth and Planetary Science Letters, v. 236, no. 1-2, p. 486-496.

Binnie, S. A., Phillips, W. M., Summerfield, M. A., and Fifield, L. K., 2007, Tectonic uplift, threshold hillslopes, and denudation rates in a developing mountain range: Geology, v. 35, no. 8, p. 743-746.

Boore, D. M., and Atkinson, G. M., 2007, Boore-Atkinson NGA ground motion relations for the geometric mean horiztonal component of peak and spectral ground motion parameters: Pacific Earthquake Engineering Research Center.

Booth, A. M., and Roering, J. J., 2011, A 1-D mechanistic model for the evolution of earthflow-prone hillslopes: Journal of Geophysical Research-Earth Surface, v. 116.

Booth, A. M., Roering, J. J., and Perron, J. T., 2009, Automated landslide mapping using spectral analysis and high-resolution topographic data: Puget Sound lowlands, Washington, and Portland Hills, Oregon: Geomorphology, v. 109, no. 3-4, p. 132-147.

Bovis, M. J., 1985, Earthflows in the interior plateau, southwest British Columbia: Canadian Geotechnical Journal, v. 22, no. 3, p. 313-334.

Bovis, M. J., and Jones, P., 1992, Holocene history of earthflow mass movements in south-central British Columbia – the influence of hydroclimatic changes: Canadian Journal of Earth Sciences, v. 29, no. 8, p. 1746-1755.

Brown, R. D., Vedder, J. G., Wallace, R. E., Roth, E. F., Yerkes, R. F., Castle, R. O., Waananen, A. O., Page, R. W., and Eaton, J. P., 1967, The Parkfield-Cholame California, Earthquakes of June-August 1966-Surface Geology Effects, Water-Resources Aspects, and Preliminary Seismic Data: USGS Professional Paper 579.

Brown, W.M., and Ritter, J.R., 1971, Sediment transport and turbity in the Eel River basin, California: U.S. Geological Survey Water-Supply Paper 1986, 67 p.

Burbank, D. W., Leland, J., Fielding, E., Anderson, R. S., Brozovic, N., Reid, M. R., and Duncan, C., 1996, Bedrock incision, rock uplift and threshold hillslopes in the northwestern Himalayas: Nature, v. 379, no. 6565, p. 505-510.

Burford, R. O., and Harsh, P. W., 1980, Slip on the San Andreas Fault in central California from alignment array surveys: Bulletin of the Seismological Society of America, v. 70, no. 4, p. 1233-1261.

Calabro, M. D., Schmidt, D. A., and Roering, J. J., 2010, An examination of seasonal deformation at the Portuguese Bend landslide, southern California, using radar interferometry: Journal of Geophysical Research-Earth Surface, v. 115.

Carson, M. A., and Petley, D. J., 1970, The existence of threshold hillslopes in the denudation of the landscape: Transactions of the Institute of British Geographers, v. 49.

Chen, C. W., and Zebker, H. A., 2000, Network approaches to two-dimensional phase unwrapping: intractability and two new algorithms: Journal of the Optical Society of America A-Optics Image Science and Vision, v. 17, no. 3, p. 401-414.

-, 2001, Two-dimensional phase unwrapping with use of statistical models for cost functions in nonlinear optimization: Journal of the Optical Society of America A-Optics Image Science and Vision, v. 18, no. 2, p. 338-351.

-, 2002, Phase unwrapping for large SAR interferograms: Statistical segmentation and generalized network models: Ieee Transactions on Geoscience and Remote Sensing, v. 40, no. 8, p. 1709-1719.

Chester, F. M., and Logan, J. M., 1986, Implications for mechanical-properties of brittle faults from observations of the Punchbowl Fault Zone, California: Pure and Applied Geophysics, v. 124, no. 1-2, p. 79-106.

Clarke, B. A., and Burbank, D. W., 2010, Bedrock fracturing, threshold hillslopes, and limits to the magnitude of bedrock landslides: Earth and Planetary Science Letters, v. 297, no. 3-4, p. 577-586.

Coe, J. A., Ellis, W. L., Godt, J. W., Savage, W. Z., Savage, J. E., Michael, J. A., Kibler, J. D., Powers, P. S., Lidke, D. J., and Debray, S., 2003, Seasonal movement of the Slumgullion landslide determined from Global Positioning System surveys and field instrumentation, July 1998-March 2002: Engineering Geology, v. 68, no. 1-2, p. 67-101.

Cruden, D. M., and Varnes, D. J., 1996, Landslide types and processes, *in* Turner, A. K., and Schuster, R. L., eds., Landslides: Investigation and Mitigation: Washington, D.C., National Academy Press, p. 36-71.

DeLong, S. B., Prentice, C. S., Hilley, G. E., and Ebert, Y., 2012, Multitemporal ALSM change detection, sediment delivery, and process mapping at an active earthflow: Earth Surface Processes and Landforms, v. 37, no. 3, p. 262-272.

Dibblee, T. W., 2005, Geologic map of the Parkfield quadrangle, Fresno & Monterey Counties, California Santa Barbara Museum of Natural History, scale 1:24:000, 1 sheet.

-, 2006, Geologic map of the Smith Mountain quadrangle, Monterey and Fresno Counties, California Santa Barbara Museum of Natural History, scale 1:24:000, 1 sheet.

-, 2007a, Geologic map of the Bickmore Canyon quadrangle, Monterey and San Benito counties, California Santa Barbara Museum of Natural History, scale 1:24:000, 1 sheet.

-, 2007b, Geologic map of the Cherry Peak quadrangle, San Benito County, California Santa Barbara Museum of Natural History, scale 1:24:000, 1 sheet.

-, 2007c, Geologic map of the Hepsedam Peak quadrangle, Monterey and San Benito counties, California Santa Barbara Museum of Natural History, scale 1:24:000, 1 sheet.

-, 2007d, Geologic map of the Lonoak quadrangle, Monterey and San Benito counties, California Santa Barbara Museum of Natural History, scale 1:24:000, 1 sheet.

-, 2007e, Geologic map of the Monarch Peak quadrangle, Monterey and San Benito counties, California Santa Barbara Museum of Natural History, scale 1:24:000, 1 sheet.

-, 2007f, Geologic map of the Priest Valley quadrangle, San Benito, Monterey and Fresno counties, California Santa Barbara Museum of Natural History, scale 1:24:000, 1 sheet.

-, 2007g, Geologic map of the Rock Spring Peak quadrangle, San Benito County, California Santa Barbara Museum of Natural History, scale 1:24:000, 1 sheet.
-, 2007h, Geologic map of the San Benito Mountain quadrangle, Fresno, Monterey and San Benito counties, California Santa Barbara Museum of Natural History, scale 1:24:000, 1 sheet.
-, 2007i, Geologic map of the Slack Canyon quadrangle, Monterey and Fresno counties, California Santa Barbara Museum of Natural History, scale 1:24:000, 1 sheet.
-, 2007j, Geologic map of the Stockdale Mountain quadrangle, Monterey County, California Santa Barbara Museum of Natural History, scale 1:24:000, 1 sheet.
Dietrich, W. E., Bellugi, D. G., Sklar, L. S., Stock, J. D., Heimsath, A. M., and Roering, J. J., 2003, Geomorphic Transport Laws for Predicting Landscape From and Dynamics, *in* Wilcock, P. R., and Iverson, R., eds., Prediction in Geomorphology: Washington DC, American Geophysical Union.
Dietrich, W. E., Reiss, R., Hsu, M. L., and Montgomery, D. R., 1995, A process-based model for colluvial soil depth and shallow landsliding using digital elevation data: Hydrological Processes, v. 9, no. 3-4, p. 383-400.
Dor, O., Ben-Zion, Y., Rockwell, T. K., and Brune, J., 2006, Pulverized rocks in the Mojave section of the San Andreas Fault Zone: Earth and Planetary Science Letters, v. 245, no. 3-4, p. 642-654.
Dor, O., Yildirim, C., Rockwell, T. K., Ben-Zion, Y., Emre, O., Sisk, M., and Duman, T. Y., 2008, Geological and geomorphologic asymmetry across the rupture zones of the 1943 and 1944 earthquakes on the North Anatolian Fault: possible signals for preferred earthquake propagation direction: Geophysical Journal International, v. 173, no. 2, p. 483-504.
Fialko, Y., Sandwell, D., Agnew, D., Simons, M., Shearer, P., and Minster, B., 2002, Deformation on nearby faults induced by the 1999 Hector Mine earthquake: Science, v. 297, no. 5588, p. 1858-1862.
Finzi, Y., Hearn, E. H., Ben-Zion, Y., and Lyakhovsky, V., 2009, Structural properties and deformation patterns of evolving strike-slip faults: numerical simulations incorporating damage rheology: Pure and Applied Geophysics, v. 166, no. 10-11, p. 1537-1573.
Gabet, E. J., Burbank, D. W., Putkonen, J. K., Pratt-Sitaula, B. A., and Ojha, T., 2004, Rainfall thresholds for landsliding in the Himalayas of Nepal: Geomorphology, v. 63, no. 3-4, p. 131-143.
Gesch, D., Oimoen, M., Greenlee, S., Nelson, C., Steuck, M., and Tyler, D., 2002, The National Elevation Dataset: Photogrammetric Engineering and Remote Sensing, v. 68, no. 1, p. 5-+.
Gesch, D. B., 2007, The National Elevation Dataset, *in* Maune, D., ed., Digital elevation model technologies and applications: the DEM users manual: Bethesda, American Society for Photogrammetry and Remote Sensing, p. 99-118.
Goldstein, R. M., and Werner, C. L., 1998, Radar interferogram filtering for geophysical applications: Geophysical Research Letters, v. 25, no. 21, p. 4035-4038.
Graham, R. C., Rossi, A. M., and Hubbert, K. R., 2010, Rock to regolith conversion: producing hospitable substrates for terrestrial ecosystems: GSA Today, v. 20, no. 2, p. 4-9.
Graham, S. A., Stanley, R. G., Bent, J. V., and Carter, J. B., 1989, Oligocene and miocene paleogeography of central California and displacement along the San Andreas Fault: Geological Society of America Bulletin, v. 101, no. 5, p. 711-730.
Hensley, S., Michel, T., Simard, M., Jones, C., Muellerschoen, R., Le, C., Zebker, H., and Chapman, B., 2009, Residual motion estimation for UAVSAR: implications of an electronically scanned array, *in* Proceedings 2009 IEEE Radar Conference, Pasadena, CA, May 04-08 2009a, p. 450-454.
Hensley, S., Zebker, H., Jones, C., Michel, T., Muellerschoen, R., and Chapman, B., 2009b, First deformation results using the NASA/JPL UAVSAR instrument, 2nd Annual Asia Pacific SAR Conference: Xian, China.
Hilley, G. E., and Arrowsmith, J. R., 2008, Geomorphic response to uplift along the Dragon's Back pressure ridge, Carrizo Plain, California: Geology, v. 36, no. 5, p. 367-370.
Huffman, O. F., 1972, Lateral displacement of upper Miocene rocks and Neogene history of offset along San Andreas Fault in central California: Geological Society of America Bulletin, v. 83, no. 10, p. 2913-2946.
Hutchinson, J. N., and Bhandari, R. K., 1971, Undrained loading, a fundamental mechanism of mudflows and other mass movements: Geotechnique, v. 21, no. 4, p. 353-358.
Iverson, R. M., 1985, A constitutive equation for mass-movement behavior: Journal of Geology, v. 93, no. 2, p. 143-160.

Iverson, R. M., and Major, J. J., 1987, Rainfall, groundwater-flow, and seasonal movement at Minor Creek Landslide, northwestern California - physical interpretation of empirical relations: Geological Society of America Bulletin, v. 99, no. 4, p. 579-594.

Jennings, C. W., and Burnett, J. L., compilers, 1961, Geologic Map of California: San Francisco Sheet: Sate of California Department of Natural Resources, scale 1:250,000, 1 sheet.

Keefer, D. K., 1984, Landslides caused by earthquakes: Geological Society of America Bulletin, v. 95, no. 4, p. 406-421.

-, 2000, Statistical analysis of an earthquake-induced landslide distribution - the 1989 Loma Prieta, California event: Engineering Geology, v. 58, p. 231-249.

Keefer, D. K., and Johnson, A. M., 1983, Earth flows: morphology, mobilization and movement: USGS Professional Paper 1264.

Kelsey, H. M., 1978, Earthflows in Franciscan Melange, Van Duzen River basin, California: Geology, v. 6, no. 6, p. 361-364.

Korup, O., 2006, Rock-slope failure and the river long profile: Geology, v. 34, no. 1, p. 45-48.

Larsen, I. J., and Montgomery, D. R., 2012, Landslide erosion coupled to tectonics and river incision: Nature Geoscience, v. 5, no. 7, p. 468-473.

Larsen, I. J., Montgomery, D. R., and Korup, O., 2010, Landslide erosion controlled by hillslope material: Nature Geoscience, v. 3, no. 4, p. 247-251.

Lawson, A., 1908, The California Earthquake of April 18, 1906: Report of the State Earthquake Investigation Commission.

Leprince, S., Berthier, E., Ayoub, F., Delacourt, C., and Avouac, J. P., 2008, Monitoring Earth surface dynamics with optical imagery: EOS Transactions, American Geophysical Union, v. 89.

Lewis, M. A., Ben-Zion, Y., and McGuire, J. J., 2007, Imaging the deep structure of the San Andreas Fault south of Hollister with joint analysis of fault zone head and direct P arrivals: Geophysical Journal International, v. 169, no. 3, p. 1028-1042.

Li, Y. G., Vidale, J. E., and Cochran, E. S., 2004, Low-velocity damaged structure of the San Andreas Fault at Parkfield from fault zone trapped waves: Geophysical Research Letters, v. 31, no. 12.

Lienkaemper, J. J., Williams, P. L., and Guilderson, T. P., 2010, Evidence for a twelfth large earthquake on the southern hayward fault in the past 1900 years: Bulletin of the Seismological Society of America, v. 100, no. 5A, p. 2024-2034.

Lisle, T. E., 1989, Sediment transport and resulting deposition in spawning gravels, north coastal California, Water Resources Research, v. 25, no. 6, p.1303-1319.

Ma, S., 2008, A physical model for widespread near-surface and fault zone damage induced by earthquakes: Geochemistry Geophysics Geosystems, v. 9.

Mackey, B. H., and Roering, J. J., 2011, Sediment yield, spatial characteristics, and the long-term evolution of active earthflows determined from airborne LiDAR and historical aerial photographs, Eel River, California: Geological Society of America Bulletin, v. 123, no. 7-8, p. 1560-1576.

Mackey, B. H., Roering, J. J., and McKean, J. A., 2009, Long-term kinematics and sediment flux of an active earthflow, Eel River, California: Geology, v. 37, no. 9, p. 803-806.

Malamud, B. D., Turcotte, D. L., Guzzetti, F., and Reichenbach, P., 2004a, Landslide inventories and their statistical properties: Earth Surface Processes and Landforms, v. 29, no. 6, p. 687-711.

-, 2004b, Landslides, earthquakes, and erosion: Earth and Planetary Science Letters, v. 229, no. 1-2, p. 45-59.

Manaker, D. M., Bürgmann, R., Prescott, W. H., and Langbein, J., 2003, Distribution of interseismic slip rates and the potential for significant earthquakes on the Calaveras fault, central California: Journal of Geophysical Research-Solid Earth, v. 108, no. B6.

Matthews, V., 1976, Correlation of Pinnacles and Neenach Volcanic Formations and their bearing on San Andreas Fault problem: AAPG Bulletin-American Association of Petroleum Geologists, v. 60, no. 12, p. 2128-2141.

McKean, J., and Roering, J., 2004, Objective landslide detection and surface morphology mapping using high-resolution airborne laser altimetry: Geomorphology, v. 57, no. 3-4, p. 331-351.

McSaveney, M. J., and Griffiths, G. A., 1987, Drought, rain, and movement of a recurrent earthflow complex in New-Zealand: Geology, v. 15, no. 7, p. 643-646.

Meunier, P., Hovius, N., and Haines, A. J., 2007, Regional patterns of earthquake-triggered landslides and their relation to ground motion: Geophysical Research Letters, v. 34, no. 20.

Meunier, P., Hovius, N., and Haines, J. A., 2008, Topographic site effects and the location of earthquake induced landslides: Earth and Planetary Science Letters, v. 275, no. 3-4, p. 221-232.

Mitchell, T. M., Ben-Zion, Y., and Shimamoto, T., 2011, Pulverized fault rocks and damage asymmetry along the Arima-Takatsuki Tectonic Line, Japan: Earth and Planetary Science Letters, v. 308, no. 3-4, p. 284-297.

Molnar, P., Anderson, R. S., and Anderson, S. P., 2007, Tectonics, fracturing of rock, and erosion: Journal of Geophysical Research-Earth Surface, v. 112, no. F3.

Montgomery, D. R., 2004, Geology, geomorphology, and the restoration ecology of salmon, GSA Today, v. 14, no. 11, p. 4-12.

Montgomery, D. R., and Dietrich, W. E., 1994, A physically-based model for the topographic control on shallow landsliding: Water Resources Research, v. 30, no. 4, p. 1153-1171.

Montgomery, D. R., Schmidt, K. M., Greenberg, H. M., and Dietrich, W. E., 2000, Forest clearing and regional landsliding: Geology, v. 28, no. 4, p. 311-314.

Nadeau, R. M., and McEvilly, T. V., 2004, Periodic pulsing of characteristic microearthquakes on the San Andreas Fault: Science, v. 303, no. 5655, p. 220-222.

National Elevation Dataset, United States Geological Survey: http://ned.usgs.gov/, (accessed December 2011).

Nolan, K. M., and Marron, D. C., 1985, Contrast in stream-channel response to major storms in two mountainous areas of California: Geology, v. 13, no. 2, p. 135-138.

Oppenheimer, D. H., Bakun, W. H., and Lindh, A. G., 1990, Slip partitioning of the Calaveras Fault, California, and prospects for future earthquakes: Journal of Geophysical Research-Solid Earth and Planets, v. 95, no. B6, p. 8483-8498.

Ouimet, W. B., Whipple, K. X., and Granger, D. E., 2009, Beyond threshold hillslopes: Channel adjustment to base-level fall in tectonically active mountain ranges: Geology, v. 37, no. 7, p. 579-582.

Parker, R. N., Densmore, A. L., Rosser, N. J., de Michele, M., Li, Y., Huang, R., Whadcoat, S., and Petley, D. N., 2011, Mass wasting triggered by the 2008 Wenchuan earthquake is greater than orogenic growth: Nature Geoscience, v. 4, no. 7, p. 449-452.

Percia, S., Dietz, S., Heim, S., Hiner, L., Maitaria, K., Martin, D., Pavlovic, S., Ishani, R., Trypaluk, C., Unruh, D., Yan, F., Yekta, M., Zhao, T., Bonnin, G., Brewer, D., Chen, L., Parzybok, T., and Yarchoan, J., 2011, NOAA atlas 14 precipitation-frequency atlas of the United States, California, v. 6, version 2.0, NOAA, National Weather Service, Silver Spring, MD, http://hdsc.nws.noaa.gov/hdsc/pfds/pfds_gis.html, (accessed July 2012).

PRISM Climate Group, Oregon State University: http://prism.oregonstate.edu, (accessed December 2011).

Putnam, W. C., and Sharp, R. P., 1940, Landslides and earthflows near Ventura, Southern California: Geographical Review, v. 30, no. 4.

Radbruch-Hall, D. H., Colton, R. B., Davies, W. E., Lucchitta, I., Skipp, B. A., and Varnes, D. J., 1982, Landslide overview map of the conterminous United States: USGS Professional Paper 1183.

Revenaugh, J., and Reasoner, C., 1997, Cumulative offset of the San Andreas fault in central California: A seismic approach: Geology, v. 25, no. 2, p. 123-126.

Reid, M. E., Brien, D. L., LaHusen, R. G., Roering, J. J., de la Fuente, J., and Ellen, S. D., 2003, Debris-flow initiation from large, slow-moving landslides: Debris-Flow Hazards Mitigation: Mechanics, Prediction, and Assessment, Vols 1 and 2.

Roering, J. J., Kirchner, J. W., and Dietrich, W. E., 2005, Characterizing structural and lithologic controls on deep-seated landsliding: Implications for topographic relief and landscape evolution in the Oregon Coast Range, USA: Geological Society of America Bulletin, v. 117, no. 5-6, p. 654-668.

Roering, J. J., Kirchner, J. W., Sklar, L. S., and Dietrich, W. E., 2001, Hillslope evolution by nonlinear creep and landsliding: An experimental study: Geology, v. 29, no. 2, p. 143-146.

Roering, J. J., Stimely, L. L., Mackey, B. H., and Schmidt, D. A., 2009, Using DInSAR, airborne LiDAR, and archival air photos to quantify landsliding and sediment transport: Geophysical Research Letters, v. 36.

Roering, J. J., Schmidt, K. M., Stock, J. D., Dietrich, W. E., and Montgomery, D. R., 2003, Shallow landsliding, root reinforcement, and the spatial distribution of trees in the Oregon Coast Range: Canadian Geotechnical Journal, v. 40, no. 2, p. 237-253.

Rogers, T. H., compiler, 1966, Geologic Map of California: San Jose Sheet: Sate of California Department of Natural Resources, scale 1:250,000, 1 sheet.

Rolandone, F., Bürgmann, R., Agnew, D. C., Johanson, I. A., Templeton, D. C., d'Alessio, M. A., Titus, S. J., DeMets, C., and Tikoff, B., 2008, Aseismic slip and fault-normal strain along the central creeping section of the San Andreas fault: Geophysical Research Letters, v. 35, no. 14.

Rosen, P. A., Hensley, S., Joughin, I. R., Li, F. K., Madsen, S. N., Rodriguez, E., and Goldstein, R. M., 2000, Synthetic aperture radar interferometry - Invited paper: Proceedings of the Ieee, v. 88, no. 3, p. 333-382.

Ryder, I., and Bürgmann, R., 2008, Spatial variations in slip deficit on the central San Andreas Fault from InSAR: Geophysical Journal International, v. 175, no. 3, p. 837-852.

Rymer, M. J., Tinsley, J. C., III, Treiman, J. A., Arrowsmith, J. R., Clahan, K. B., Rosinski, A. M., Bryant, W. A., Snyder, H. A., Fuis, G. S., Toke, N. A., and Bawden, G. W., 2006, Surface fault slip associated with the 2004 Parkfield, California, earthquake: Bulletin of the Seismological Society of America, v. 96, no. 4, p. S11-S27.

Savage, H. M., and Brodsky, E. E., 2011, Collateral damage: Evolution with displacement of fracture distribution and secondary fault strands in fault damage zones: Journal of Geophysical Research-Solid Earth, v. 116.

Savage, J. C., and Burford, R. O., 1973, Geodetic determination of relative plate motion in central California: Journal of Geophysical Research, v. 78, no. 5, p. 832-845.

Schmidt, K. M., Roering, J. J., Stock, J. D., Dietrich, W. E., Montgomery, D. R., and Schaub, T., 2001, The variability of root cohesion as an influence on shallow landslide susceptibility in the Oregon Coast Range: Canadian Geotechnical Journal, v. 38, no. 5.

Schulz, W. H., McKenna, J. P., Kibler, J. D., and Biavati, G., 2009, Relations between hydrology and velocity of a continuously moving landslide-evidence of pore-pressure feedback regulating landslide motion?: Landslides, v. 6, no. 3, p. 181-190.

Schwab, M., Rieke-Zapp, D., Schneider, H., Liniger, M., and Schlunegger, F., 2008, Landsliding and sediment flux in the Central Swiss Alps: A photogrammetric study of the Schimbrig landslide, Entlebuch: Geomorphology, v. 97, no. 3-4, p. 392-406.

Simons, M., and Rosen, P. A., 2007, Interferometric Synthetic Aperture Radar Geodesy, *in* Schubert, G., ed., Treatise on Geophysics, Volume 3, Elsevier, p. 391-446.

Swanson, F. J., and Swanston, D. N., 1977, Complex mass-movement terrains in the western Cascade Range, Oregon, Reviews in Engineering Geology, Volume 3, Geological Society of America, p. 113-124.

Thurber, C., Roecker, S., Ellsworth, W., Chen, Y., Lutter, W., and Sessions, R., 1997, Two-dimensional seismic image of the San Andreas fault in the northern Gabilan range, central California: Evidence for fluids in the fault zone: Geophysical Research Letters, v. 24, no. 13, p. 1591-1594.

Titus, S. J., DeMets, C., and Tikoff, B., 2005, New slip rate estimates for the creeping segment of the San Andreas fault, California: Geology, v. 33, no. 3, p. 205-208.

Trotter, C. M., 1993, Weathering and regolith properties at an earthflow site: Quarterly Journal of Engineering Geology, v. 26, no. 3, p. 163-178.

Tucker, G. E., and Hancock, G. R., 2010, Modelling landscape evolution: Earth Surface Processes and Landforms, v. 35, no. 1, p. 28-50.

Unsworth, M., Egbert, G., and Booker, J., 1999, High-resolution electromagnetic imaging of the San Andreas fault in central California: Journal of Geophysical Research-Solid Earth, v. 104, no. B1, p. 1131-1150.

van Asch, T. W. J., 2005, Modelling the hysteresis in the velocity pattern of slow-moving earth flows: the role of excess pore pressure: Earth Surface Processes and Landforms, v. 30, no. 4, p. 403-411.

Wechsler, N., Rockwell, T. K., and Ben-Zion, Y., 2009, Application of high resolution DEM data to detect rock damage from geomorphic signals along the central San Jacinto Fault: Geomorphology, v. 113, no. 1-2, p. 82-96.

Western Regional Climate Center, 1986, NOAA Cooperative Stations: http://www.wrcc.dri.edu/climatedata/climsum/ (accessed December 2011).

Wieczorek, G. F., Reid, M. E., Jodicke, W., Pearson, C., and Wilcox, G., 2007, Rainfall and seasonal movement of the Weeks Creek landslide, San Mateo County, California: U.S. Geological Survey Data Series 278.

Zhang, X. B., Phillips, C., and Marden, M., 1993, A comparison of earthflow movement mechanisms on forested and grassed slopes, Raukumara Peninsula, North Island, New-Zealand: Geomorphology, v. 6, no. 2, p. 175-187.

TABLE 1: UAVSAR INTERGEROGRAMS USED IN THIS STUDY

Line ID	Heading (°)*	Start Date	End Date	Days Elapsed	Full Interfeorgram ID†
San Andreas Fault parallel interferograms					
14003	140	17-Nov-09	16-Nov-10	363	SanAnd_14003_09091-005_10081-014_0363d_s01_L090_01
14003	140	11-May-10	16-Nov-10	189	SanAnd_14003_10037-011_10081-014_0189d_s01_L090_01
14003	140	16-Nov-10	12-Jul-11	238	SanAnd_14003_10081-014_11048-021_0238d_s01_L090_01
14003	140	11-May-10	12-Jul-11	427	SanAnd_14003_10037-011_11048-021_0427d_s01_L090_01
San Andreas Fault perpendicular interferograms					
05008	50	26-Oct-09	18-Nov-10	363	SanAnd_05008_09085-004_10082-012_0388d_s01_L090_01
05008	50	26-Oct-09	13-Jul-11	189	SanAnd_05008_09085-004_11049-009_0625d_s01_L090_01
05008	50	23-Feb-09	3-May-10	238	SanAnd_05008_09008-005_10034-003_0434d_s01_L090_01
05010	50	3-May-10	21-Apr-11	427	SanAnd_05010_10034-005_11015-009_0353d_s01_L090_01
05010	50	26-Oct-09	18-Nov-10	387	SanAnd_05010_09085-006_10082-010_0387d_s01_L090_01
05010	50	23-Feb-09	3-May-10	434	SanAnd_05010_09008-003_10034-005_0434d_s01_L090_01
05010	50	23-Feb-09	18-Nov-10	633	SanAnd_05010_09008-003_10082-010_0633d_s01_L090_01
05012	50	3-May-10	21-Apr-11	353	SanAnd_05012_10034-007_11015-007_0353d_s01_L090_01
05012	50	26-Oct-09	18-Nov-10	387	SanAnd_05012_09085-008_10082-008_0387d_s01_L090_01
05014	50	18-Nov-10	21-Apr-11	154	SanAnd_05014_10082-006_11015-005_0154d_s01_L090_01
05014	50	26-Oct-09	18-Nov-10	387	SanAnd_05014_09085-010_10082-006_0387d_s01_L090_01
05016	50	18-Nov-10	21-Apr-11	154	SanAnd_05016_10082-004_11015-003_0154d_s01_L090_01
05016	50	26-Oct-09	18-Nov-10	387	SanAnd_05016_09085-012_10082-004_0387d_s01_L090_01
05016	50	26-Oct-09	21-Apr-11	541	SanAnd_05016_09085-012_11015-003_0541d_s01_L090_01
05016	50	20-Feb-09	18-Nov-10	635	SanAnd_05016_09007-018_10082-004_0635d_s01_L090_01
05018	50	18-Nov-10	21-Apr-11	154	SanAnd_05018_10082-002_11015-001_0154d_s01_L090_01
05018	50	13-Nov-09	18-Nov-10	370	SanAnd_05018_09089-001_10082-002_0370d_s01_L090_02
05020	50	13-Nov-09	18-Nov-10	370	SanAnd_05020_09089-003_10082-000_0370d_s01_L090_01
05022	50	13-Nov-09	16-Nov-10	367	SanAnd_05022_09089-005_10081-001_0367d_s01_L090_01
05022	50	13-Nov-09	12-May-11	544	SanAnd_05022_09089-005_11027-010_0544d_s01_L090_01
05024	50	13-Nov-09	16-Nov-10	367	SanAnd_05024_09089-007_10081-003_0367d_s01_L090_01
23009	230	3-May-10	21-Apr-11	353	SanAnd_23009_10034-004_11015-010_0353d_s01_L090_01
23011	230	3-May-10	21-Apr-11	353	SanAnd_23011_10034-006_11015-008_0353d_s01_L090_01
23011	230	26-Oct-09	18-Nov-10	387	SanAnd_23011_09085-007_10082-009_0387d_s01_L090_01
23013	230	18-Nov-10	21-Apr-11	154	SanAnd_23013_10082-007_11015-006_0154d_s01_L090_01
23013	230	26-Oct-09	18-Nov-10	387	SanAnd_23013_09085-009_10082-007_0387d_s01_L090_01
23015	230	18-Nov-10	21-Apr-11	154	SanAnd_23015_10082-005_11015-004_0154d_s01_L090_01
23015	230	26-Oct-09	18-Nov-10	387	SanAnd_23015_09085-011_10082-005_0387d_s01_L090_01
23017	230	13-Nov-09	18-Nov-10	370	SanAnd_23017_09089-000_10082-003_0370d_s01_L090_01
23019	230	13-Nov-09	18-Nov-10	370	SanAnd_23019_09089-002_10082-001_0370d_s01_L090_01

*Heading is aircraft flight direction in degrees from north

†Full interferogram ID refers to the NASA Jet Propulsion Lab identification code as listed at http://uavsar.jpl.nasa.gov/

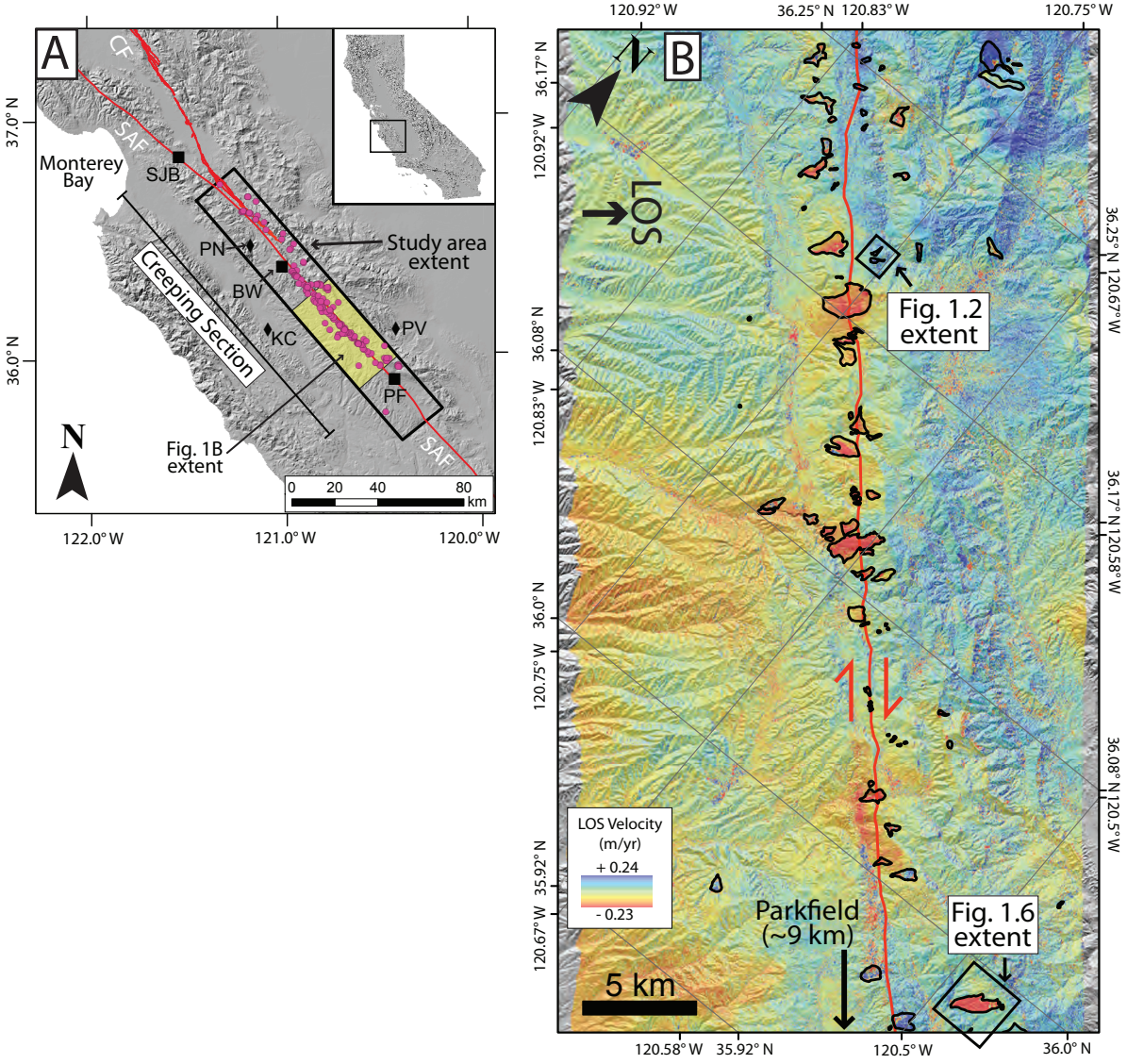

Figure 1.1: (A) Location map showing the study area including active earthflows (pink dots), the San Andreas Fault (SAF) and Calaveras Fault (CF) (red lines), towns along the SAF (black squares, PF = Parkfield, CA BW = Bitterwater, CA, SJB = San Juan Bautista), and regional rain gages (black diamonds, PN = Pinnacles National Monument, KC = King City, PV = Priest Valley). The large black outline shows the extent of UAVSAR line 14003, which coincides with the extent of our landslide mapping area, yellow shaded area represents extent of Fig. 1B. Other UAVSAR lines in Table 1.1 are oriented perpendicular to and partially overlap with the shown line 14003 extent. Inset shows location in California. (B) Unwrapped interferogram (line 14003, collected May 11, 2010 and 12 July 2011, 427 days elapsed between collections) with black outlines indicating mapped active landslides; the SAF is shown in red with arrows indicating right-lateral motion. Negative velocities indicate movement opposite the line-of-sight (LOS) direction and phase has been converted to m/yr. Arrow indicates radar LOS pointing from aircraft to ground. Black boxes show locations of Figs. 1.2 and 1.6.

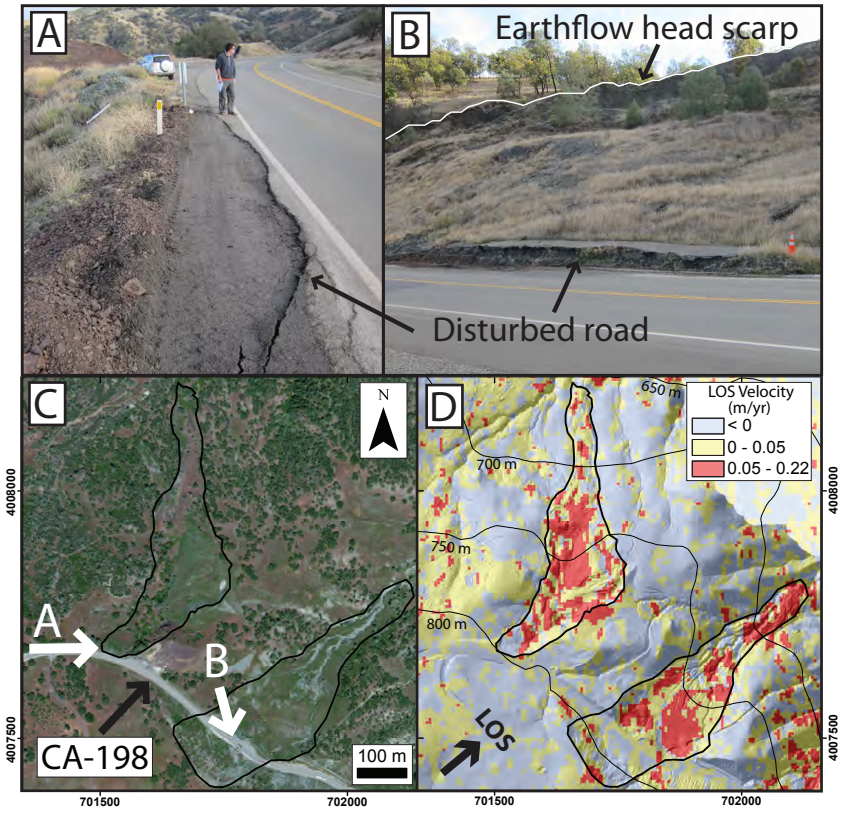

Figure 1.2: (A) and (B) Examples of deformed and fractured roads due to two separate earthflows crossing California State Highway 198. Ongoing highway maintenance confirms these earthflows are currently active. Note person and orange traffic cone for scale in (A) and (B), respectively. (C) Bing Maps aerial photograph showing extent of earthflows (black outlines) photographed in (A) and (B); white arrows denote location and orientation of photographs. (D) Unwrapped interferogram (line 14003, collected November 16, 2010 – July 12, 2011, 238 days elapsed between collections) showing movement of earthflows superimposed over high resolution airborne laser swath mapping shaded relief map (obtained from OpenTopography; http://www.opentopography.org); black arrow indicates aircraft line-of-sight (LOS) pointing from aircraft to ground, and contours show elevation in meters above sea level. The San Andreas Fault is ~850 m to the southwest from the earthflows shown. Borders on (C) and (D) show UTM coordinates, and the images are of the same aerial extent.

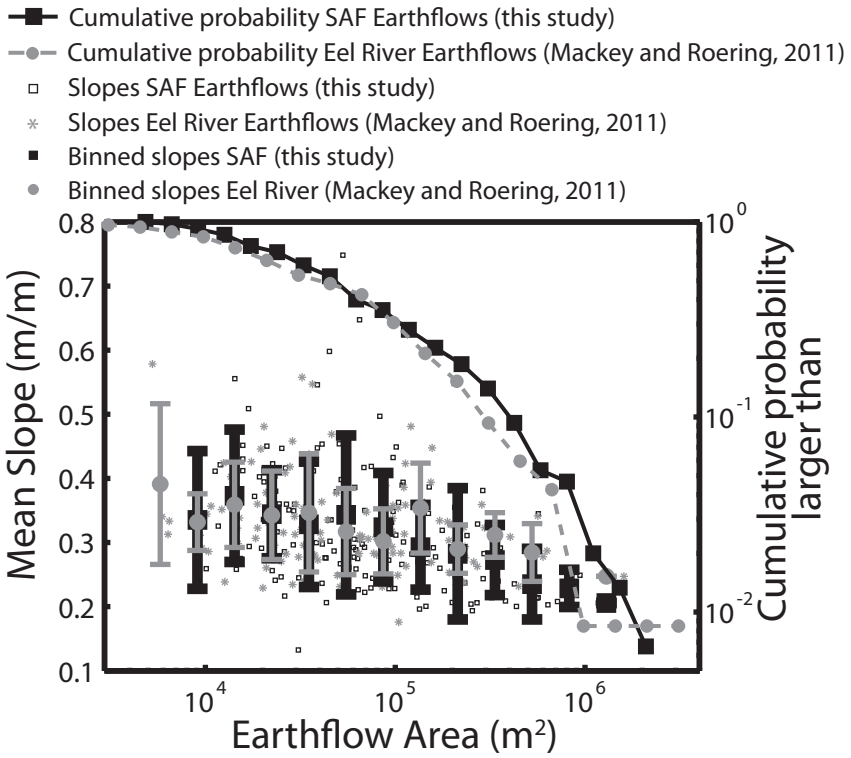

Figure 1.3. Mean slope versus earthflow area and cumulative probability of earthflow area for landsides examined in this study and in Mackey and Roering (2011). Small data points show individual earthflow slopes, large points are earthflows binned into logarithmically spaced slope intervals (with 1σ error bars), and lines show cumulative probability distribution. Both the earthflows in this study and in Mackey and Roering (2011) show lognormal probability distributions of earthflow area. SAF—San Andreas fault.

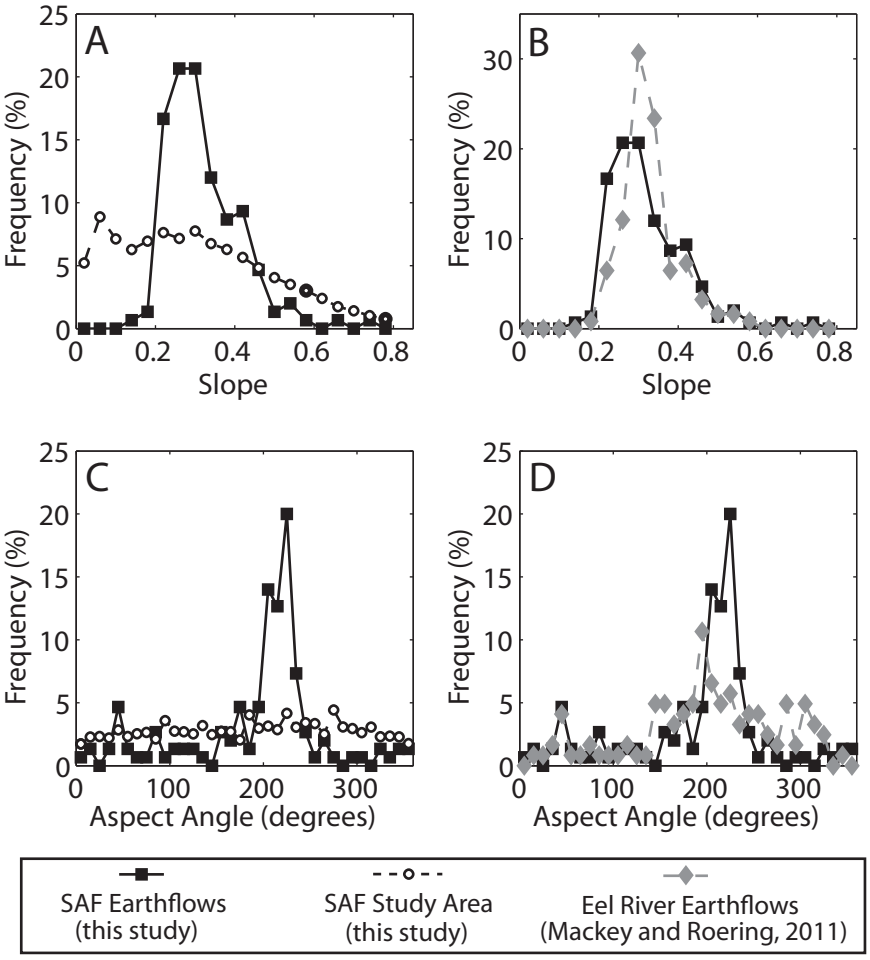

Figure 1.4: (A) Histogram of mean slopes of active earthflows (calculated as mean value of all slope pixels over the entire earthflow extent) compared with histogram of slopes across the entire study area. (B) Histogram of mean slopes for active earthflows in this paper ("SAF Earthflows") compared with those reported by Mackey and Roering (2011) ("Eel River Earthflows"). The Eel River Earthflows have a slightly higher mean slope and narrower distribution (0.33 +/- 0.1, mean +/- 1 sigma standard deviation) than the SAF Earthflows (0.32 +/- 0.1), although the populations are statistically indistinguishable (p = 0.62 in a two-sample t-test at 5% confidence level). (C) Histogram of average aspect for individual earthflows and the study area as a whole; ~65% of earthflows have aspects between 170-250° despite these hillslope aspects encompassing only ~25% of the study area. (D) Histograms of aspects of the earthflows examined in this study compared with those from Mackey and Roering (2011). For (A) and (B) slope data is binned in 0.04 m/m bins, for (C) and (D) aspect data is binned in 10 degrees bins with due north equal to 0 degrees. Both slope and aspect data calculated from the 10 m resolution National Elevation Dataset Digital Elevation Model.

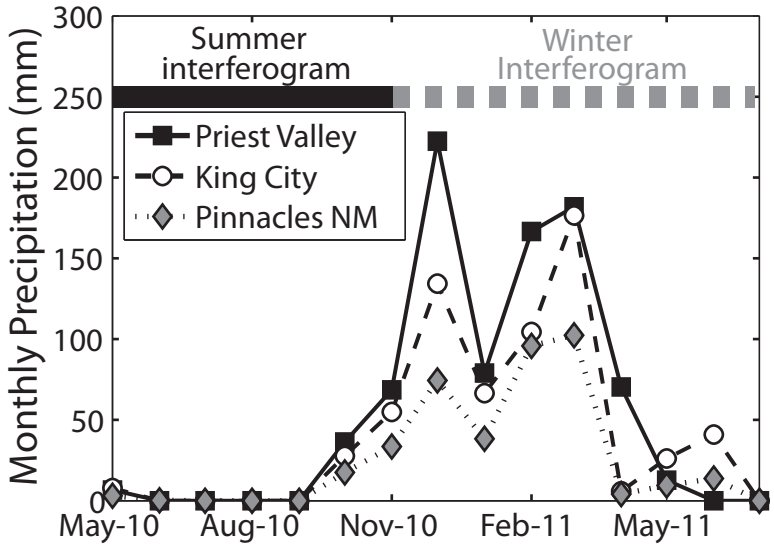

Figure 1.5: Monthly precipitation totals from rain gages near the study area for May 2010 – July 2011. Solid black and dashed gray line mark the time period covered by the summer and winter interferogram respectively. Note the absence of precipitation occurring over much of the summer interferogram interval, and the increased precipitation over the winter interferogram interval. See Fig. 1.1 for rain gage locations.

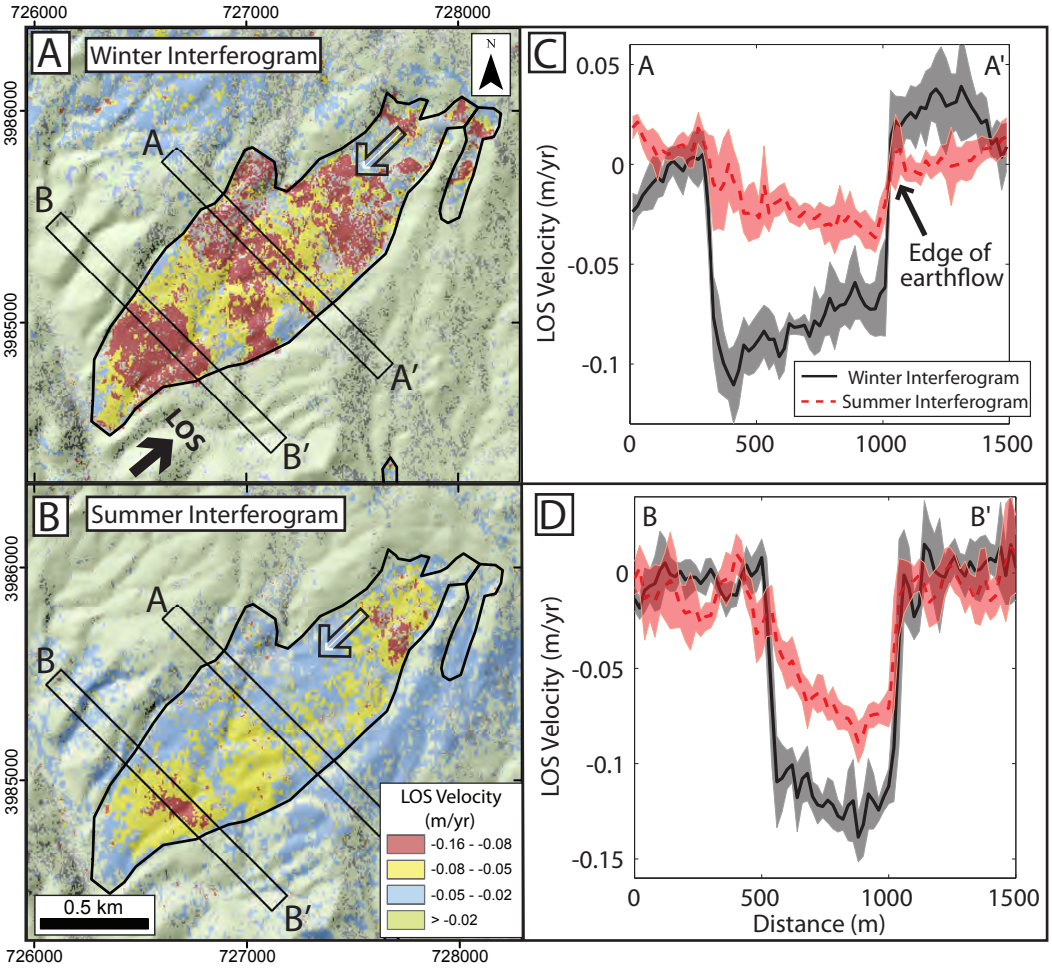

Figure 1.6: Line-of-sight (LOS) velocity measurements for an example earthflow for the (A) winter interferogram and (B) summer interferogram. See Fig. 1.1B for location. LOS direction (denoted by black arrow) points from aircraft to ground resulting in negative velocity for motion opposite direction of the LOS. Hollow arrow denotes landslide flow direction. A-A' and B-B' boxes in (A) and (B) show areas over which LOS velocity was averaged (over 5 m wide bins placed perpendicular to transect direction) to create velocity profiles. Comparison between (C) A-A' (D) and B-B' velocity transects show increased velocity for the winter interferogram (black line) for both transects; shaded areas show 1 sigma standard deviation in velocity. Borders show UTM coordinates in (A) and (B); speckled appearance of interferograms is due to exclusion of pixels with interferometric correlation less than 0.3.

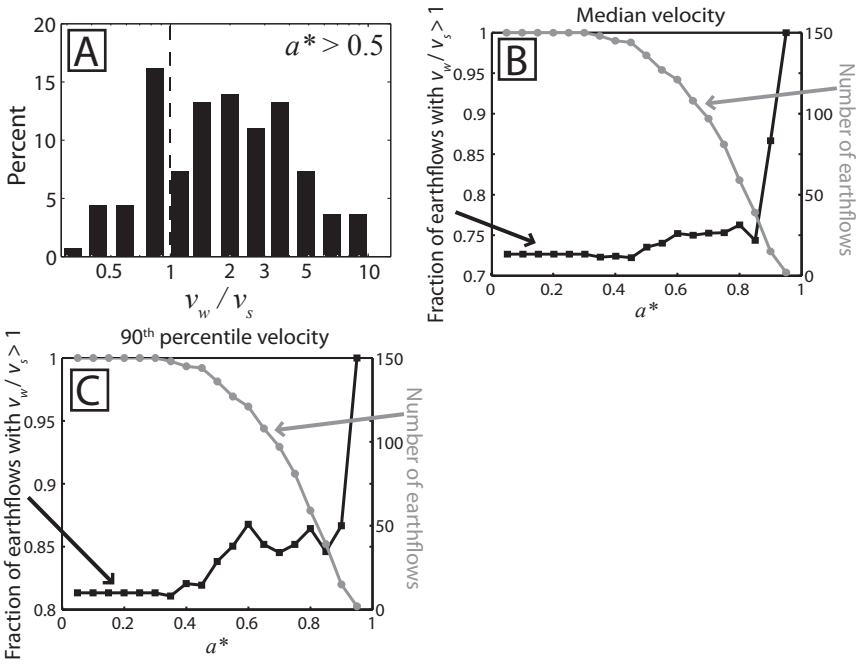

Figure 1.7: (A) Histogram of v_w / v_s for $a^* > 0.5$ for all earthflows, where vw and vs are the median line-of-sight (LOS) velocity of a given earthflow in the winter and summer interferograms, respectively, and a^* is the fraction of a given earthflow area with interferometric correlation values greater than 0.3. (B) Fraction of landslides showing higher median LOS velocities in the winter interferogram (i.e., $v_w / v_s > 1$) versus a* (black line). Gray line shows total number of earthflows for given a^* values. (C) Same as (B), but for 90th percentile LOS velocities.

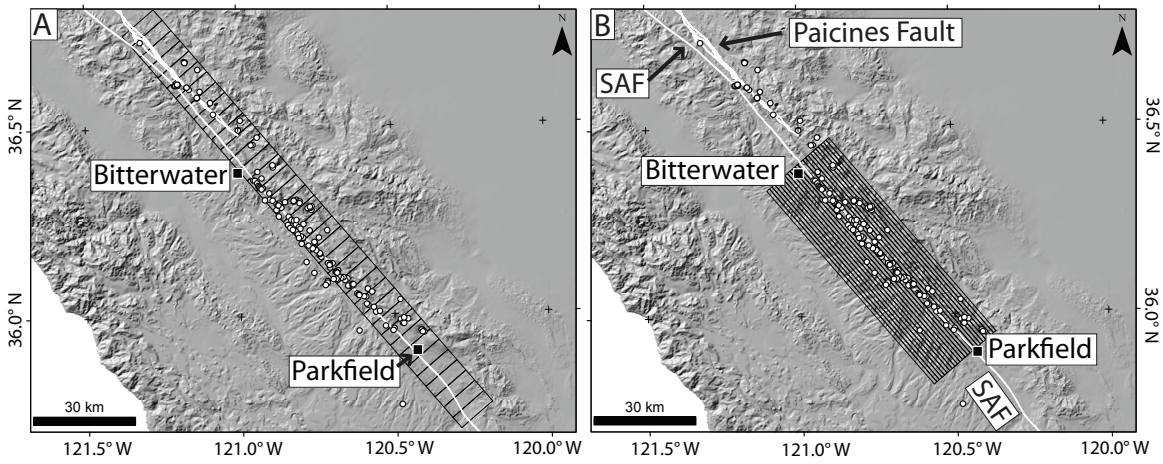

Figure 1.8: (A) Location of San Andreas Fault (SAF) perpendicular swaths (4 km by 12 km). (B) Location of SAF parallel swaths (1 km by 75 km). In both images white circles show location of active earthflows and white lines indicate location of SAF and Calaveras/Paicines fault system. Borders show latitude and longitude in decimal degrees.

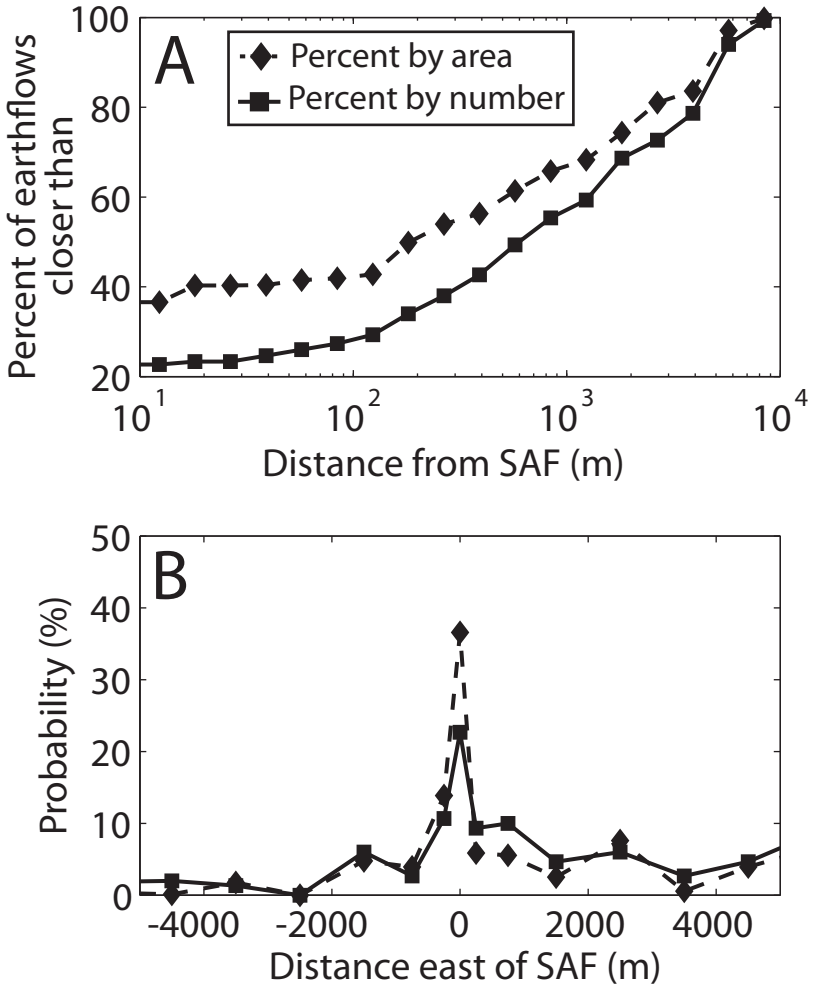

Figure 1.9: (A) Cumulative distribution of earthflows as a function of distance from the San Andreas Fault (SAF). (B) Probability of occurrence of active earthflows on either side of the fault. Note slightly higher probability of earthflow occurrence east of the SAF, possibly corresponding to greater fault damage (see text for details). For both figures, solid line shows distribution by number of landslides and dashed line is based on total landslide area. Distances are measured using the minimum distance between the earthflow and SAF.

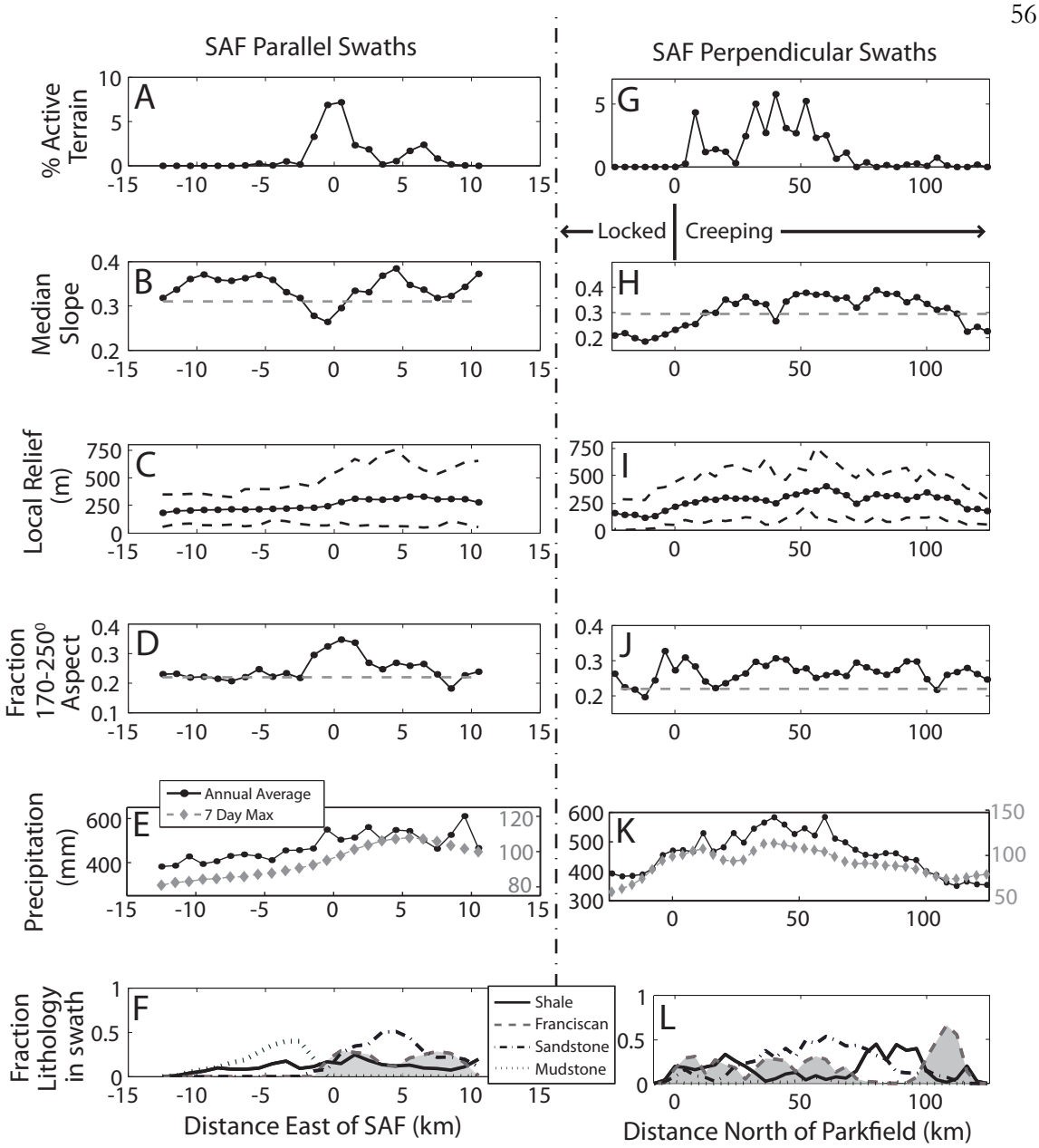

Figure 1.10: Summary statistics on earthflow activity and topography. (A,G) Percent of swath area covered by active earthflows. (B,H) Mean local topographic slope for each swath (black line) and median slope of all active earthflows (gray dashed line). Mean slope in each swath was calculated ignoring points with slopes less than 4 degrees to reduce the effect of non-earthflow terrain (e.g. terraces) which occupied large portions of some swaths. (C,I) Average, minimum, and maximum local relief within each swath calculated with a 1 km radius moving window. (D,J) Fraction of swath area occupied by topography with hillslope aspect between 170-250° (black line). Aspect range corresponds to the peak of observed active earthflow aspects (see Fig. 1.4C). Gray dashed line is expected fraction for evenly distributed hillslope directions. (E,K) Annual precipitation over the study period (May 2010 – July 2011) as estimated by PRISM data (black line and circles, left y-axis) and two-year recurrence interval predicted maximum seven-day rainfall intensity as estimated by NOAA (gray line and diamonds, right y-axis) (Percia, 2011). (F,L) Fraction of lithology present in each swath for the four major lithologies classified, Franciscan is shaded gray for ease in identification. (A-F) are for SAF parallel swaths and (G-L) are for SAF perpendicular swaths, each point represents a value for an individual swath.

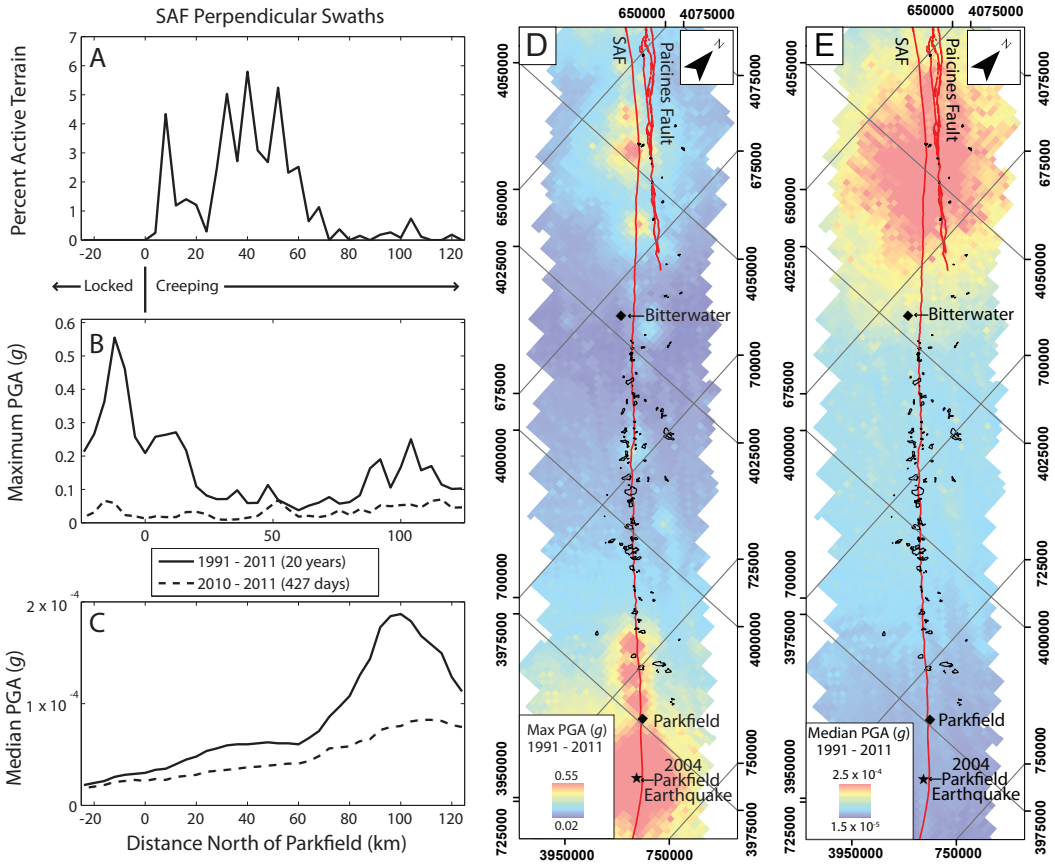

Figure 1.11: Association of ground motion predictions and earthflow activity. (A) Fraction of terrain composed of active earthflows for each San Andreas Fault (SAF) perpendicular swath segment (same as Fig. 10G). Maximum (B) and median (C) peak ground acceleration (PGA) estimated in each swath for all earthquakes during the 20-year period from 1991 – 2011 (solid line) and for earthquakes corresponding to the time period of UAVSAR measurements (May 2010 – July 2011, dashed line). (D) Spatial distribution of estimated maximum and (E) median PGA for the 20-year (1991 – 2011 period). Black outlines show mapped landslide locations, UTM coordinates are indicated on figure borders, note difference in color bar scale between (D) and (E).

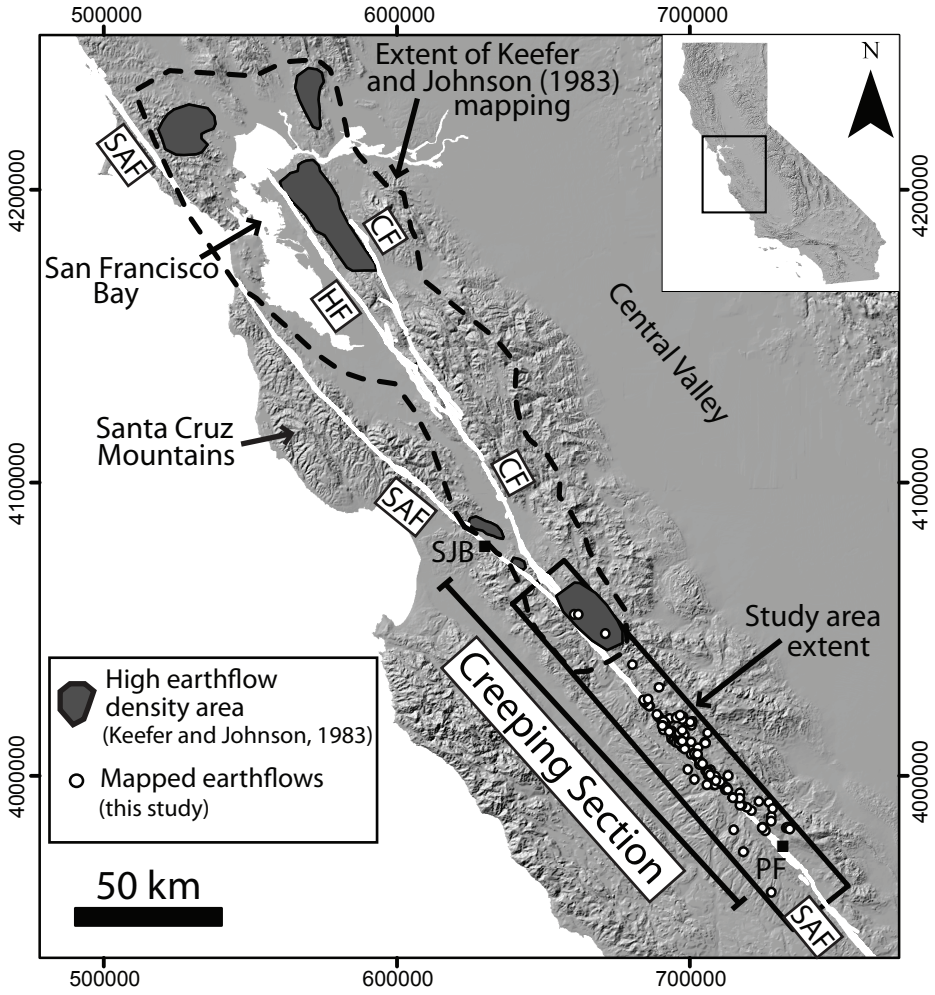

Figure 1.12: Map of the San Andreas Fault (SAF), Calaveras Fault (CF), and Hayward Fault (HF) showing the location of areas of high earthflow density mapped by Keefer and Johnson (1983) as digitized from their Fig. 1.1. White dots are earthflows mapped in this study. Town abbreviations are same as Fig. 1.1; inset shows location in California; borders show UTM coordinates in meters.

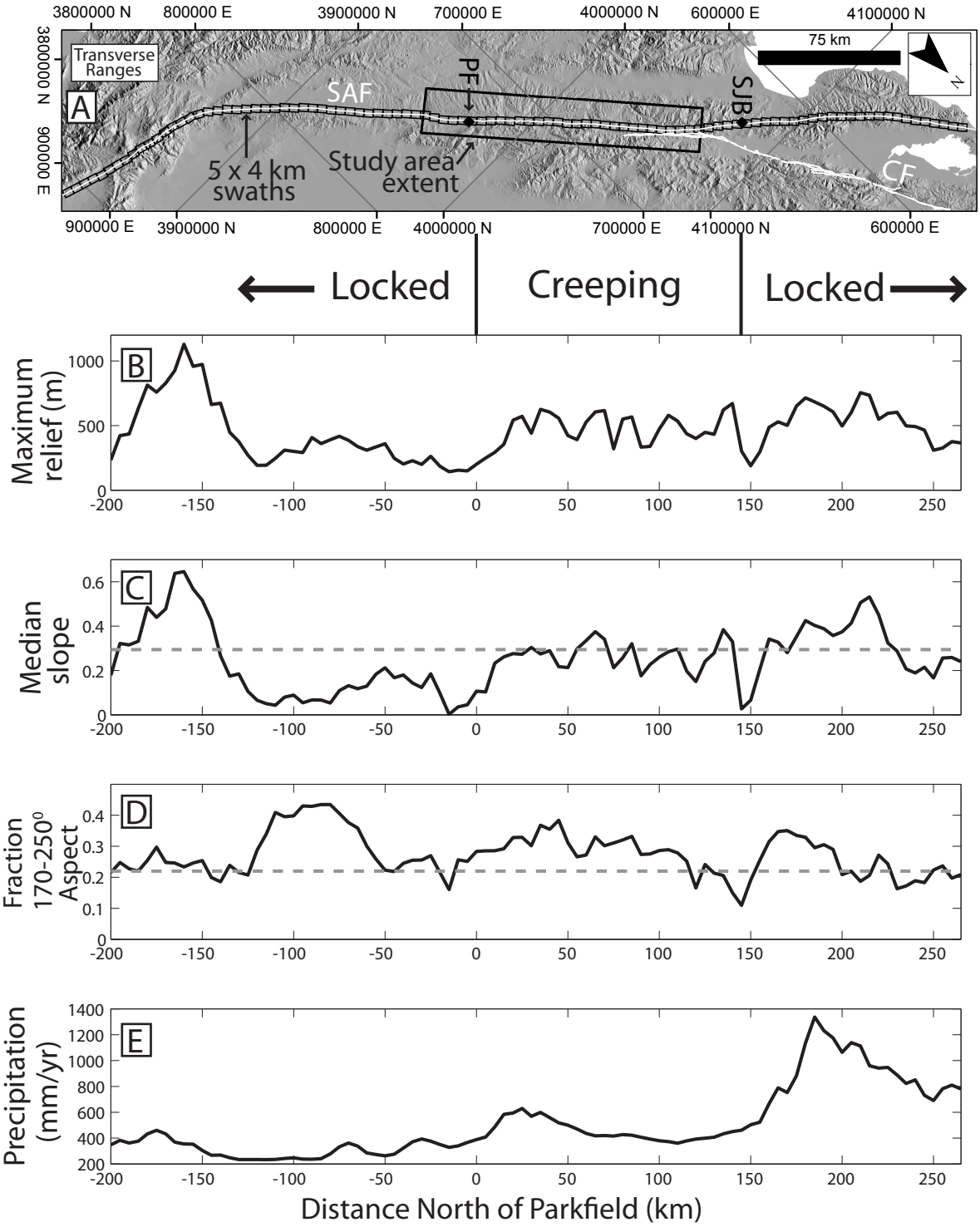

Figure 1.13: (A) Map of the San Andreas Fault (SAF) from the Transverse Ranges (southern extent) to the San Francisco Peninsula (northern extent) showing 4 km (cross-fault) by 5 km (along-fault) SAF centered swaths. Borders are UTM coordinates, abbreviations are same as Fig. 1.1. Also shown are swath-wide statistics of maximum relief (B), median hillslope gradient (C), fraction of area with southwest facing hillslopes (D), and 1971-2000 mean annual precipitation as estimated by PRISM data for ~0.8 x 0.8 km grid cells (E). Gray dashed lines in (C) and (D) are median slope of all active earthflows and expected fraction of aspects for evenly distributed hillslope directions, respectively.

C h a p t e r 2

INFLUENCE OF BED PATCHINESS, SLOPE, GRAIN HIDING, AND FORM DRAG ON GRAVEL MOBILIZATION IN VERY STEEP STREAMS

Joel S. Scheingross[1], Eric W. Winchell[2,3,4], Michael P. Lamb[1], William E. Dietrich[2]

[1] Division of Geological and Planetary Sciences, California Institute of Technology, Pasadena, CA, 91125, USA
[2] Department of Earth and Planetary Science, University of California, Berkeley, California, USA
[3] Now at Department of Geological Sciences, University of Colorado, Boulder, Colorado, USA
[4] Now at Institute of Arctic and Alpine Research, University of Colorado, Boulder, Colorado, USA

* Adapted from Scheingross, Joel S., et al. "Influence of bed patchiness, slope, grain hiding, and form drag on gravel mobilization in very steep streams," *Journal of Geophysical Research – Earth Surface*, V. 118, p. 982-1001 (2013)
DOI: 10.1002/jgrf.20067

2.1 Abstract

Steep streams are a major portion of channel networks and provide a link to transport sediment from hillslopes to lower gradient rivers. Despite their importance, key unknowns remain, perhaps foremost of which is evaluating, in steep streams, empirical laws for fluvial sediment transport developed for low-gradient rivers. To address this knowledge gap, we painted sediment in situ over three years to monitor incipient sediment motion and sediment patch development in five small (drainage areas of 0.04-2 km^2) and steep (slopes of 5 – 37%) tributaries of Elder Creek, California, USA. We found that channel beds organized into size-sorted sediment patches which displayed active fluvial transport of gravel annually, consistent year-to-year patch median-grain sizes, partial transport of bed material, and significantly higher values of critical Shields stress for incipient sediment motion compared to that observed for lower gradient rivers. The high critical Shields stresses (up to ≈ 0.5 for the median grain size) agree within a factor of ~3 to theoretical predictions, which accounts for slope-dependent hydraulics, grain hiding, and sediment patches. For grains of approximately the same size as the roughness length scale, slope-dependent hydraulics and bed patchiness are the dominant controls on critical Shields stress values, while grain hiding is important for grains larger or smaller than the roughness length scale. Form drag exists in our monitored tributaries, but has a smaller influence than the above effects. Our field observations show fluvial processes contribute to sediment mobilization in steep channels which are often considered to be dominated by debris flows.

2.2 Introduction

Sediment transport dynamics and rates in steep streams are important for routing sediment from hillslopes to river networks (Benda et al., 2005; Cui and Parker, 2005; Grant et al., 1990; Montgomery and Buffington, 1997; Wiele et al., 2007), aquatic habitat quality (Buffington et al., 2004; Lisle, 1989; Montgomery, 2004), and landscape evolution modeling (Dietrich et al., 2003; Tucker and Hancock, 2010). Nonetheless, the role of fluvial processes in conveying sediment through steep channels has received little study relative to lower gradient channels ($S < 1\%$, where S is channel bed slope), and may differ in important ways (Comiti and Mao, 2012). For example, in steep streams workers have emphasized the effects of grain hiding, form drag, slope-dependent incipient motion criterion, partial transport, and bed-sediment size patchiness on sediment transport (e.g., Church and Hassan, 2002; Lamb et al., 2008b; Mao et al., 2008; Recking, 2009; Yager et al., 2012a, b). In addition, recent work has shown that fluvial transport in steep streams can account for a large portion of the total sediment flux (e.g., Gomi and Sidle, 2003; Mao and Lenzi, 2007; Yager et al., 2012b), yet others have argued that periodic debris flows are primarily responsible for transporting sediment in streams with slopes greater than about 10% (e.g., Stock and Dietrich, 2003; Stock and Dietrich, 2006). Uncertainty about the dominant processes in steep channels remains, in part, due to a paucity of field data.

Accurate predictions of sediment transport in steep streams require knowledge of the conditions for incipient sediment motion, which is often calculated using a critical Shields stress (τ_{*c}) (Shields, 1936):

$$\tau_{*c} = \frac{\tau_c}{(\rho_s - \rho) gD}, \qquad (2.1)$$

where τ_c is the bed shear stress at incipient motion, ρ_s is the density of sediment, ρ is the density of water, g is acceleration due to gravity, and D is particle diameter. In low-gradient gravel-bed rivers, a constant value of $\tau_{*c} \approx 0.045$ has been shown to accurately predict the conditions for sediment motion (e.g., Buffington and Montgomery, 1997). In steep streams (e.g., $S > 5\%$), however, a constant value of τ_{*c} may not be appropriate. For example, some theoretical models for incipient sediment motion predict τ_{*c} decreases with slope due to the increased component of gravity in the downstream direction (e.g., Wiberg and Smith, 1987). Yet, flume data at slopes up to 47% show critical Shields stresses increase with channel gradient (e.g., Ashida and Bayazi, 1973; Bathurst et al., 1984; Mizuyama, 1977; Prancevic et al., 2011). Field data on incipient motion are limited for streams with $S > 5\%$, but also show an increase in critical Shields stress with increasing slope up to $S = 14\%$ (e.g., Lenzi et al., 2006; Mao and Lenzi, 2007; Mao et al., 2008; Mueller et al., 2005). Recent models show that the critical Shields stress may increase with channel slope due to changes in local flow velocity and turbulent fluctuations as the flow depth to grain size ratio decreases (Lamb et al., 2008b; Recking, 2009). Others suggest increased form drag due to the presence of immobile morphologic structures results in larger τ_{*c} with increasing channel slope (e.g., Buffington and Montgomery, 1999; Ferguson, 2012; Nitsche et al., 2011; Yager et al., 2012b).

Predicting incipient motion and bedload transport in steep channels is further complicated by the organization of the channel bed into distinct sediment patches (e.g., Dietrich et al., 2006; Paola and Seal, 1995; Yager et al., 2012a). Patches are sediment size-sorted areas on the bed which likely form through feedbacks between bed topography, shear stress distribution, and sediment transport (Nelson et al., 2009; Venditti et al., 2010). For example, Yager et al. (2012) showed that standard models for bedload transport developed in low-gradient streams over-predict transport rates by an order of magnitude in steep streams (S = 9.8 - 17%) because the models do not account for patches of immobile grains. Since the critical Shields stress is sensitive to the ratio of grain size to the local bed-roughness (Wiberg and Smith, 1987), the presence of patches has led workers to argue that patches with different grain-size distributions within the same river reach are mobilized at different bed shear stresses (e.g., Paola and Seal, 1995). The mobilization of relatively finer patches at lower bed shear stresses leads to reach-wide partial transport of sediment (i.e., a portion of the grain-size distribution present on the channel bed is absent in the bedload) (Paola and Seal, 1995; Yager et al., 2012a). While some have argued that grains within a single patch are all mobilized at the same critical shear stress (Paola and Seal, 1995), field data from steep streams suggests individual patches experience partial transport, with a preference for mobilizing finer grains (Yager et al., 2012a). At the individual particle scale, grain mobilization is a function of both the grain weight and grain size relative to roughness on the bed. Relatively coarse grains weigh more than fine grains, but also protrude further from the bed, and are thus subject to increased drag and lower friction angles (e.g., Egiazaroff, 1965; Einstein, 1950; Kirchner et al., 1990; Wiberg and Smith, 1987). These competing

effects, termed grain hiding, likely influence the mobilization of distinct grain sizes from individual patches.

In steep streams, accurate incipient-motion predictions likely require quantification of the extent of bed patchiness, grain hiding, form drag, and slope-dependent hydraulics. There is a general paucity of data on critical Shields stress for channels with $S > 5\%$, and no study has attempted to quantify the influence of patchiness, grain hiding, form drag, and slope-dependent hydraulics together in a field setting. This lack of data has led many modelers to treat steep channels with the same semi-empirical expressions (e.g., $\tau_{*c} \approx 0.045$) developed for lower gradient gravel-bed rivers (Lamb et al., 2008a; Sklar and Dietrich, 2004; Tsai et al., 2012; Tucker and Hancock, 2010; Whipple, 2004).

Here we present results from monitoring sediment mobilization via painting sediment patches and tracking the movement of individual grains in five steep (S = 5 - 37%) tributary reaches of Elder Creek, California, USA. We use our monitoring data to calculate critical Shields stresses and to quantify the effects of bed patchiness, grain hiding, form drag, and slope-dependent hydraulics via comparison to theory that allows isolation of these variables. In this paper we first introduce the study area and describe the study reaches. Second we present methods on monitoring hydraulics and sediment transport, including surveying channel geometry, field measurements of flow hydraulics, modeling bed shear stress with a non-uniform flow algorithm, and documenting grain mobilization via repeat surveys of marked tracer particles and patches. Third we discuss results from monitoring, including measured flow discharges and velocities, grain mobilization from patches, and travel distances of marked particles. Fourth we present

analysis of our data to calculate form drag and critical Shields stresses, and examine controls on incipient motion. Finally, we discuss the implications of our analysis for predicting grain entrainment and sediment transport in steep streams.

2.3 Study area and monitored tributaries

Elder Creek is a small (drainage area of 16.8 km^2) tributary of the South Fork Eel River located in northern California, USA (Fig. 2.1). The stream hosts a U.S. Geological Survey hydrologic benchmark station near its mouth with continuous discharge records from 1967 to 2013. The local lithology consists of interbedded arkosic sandstone and argillite of the Coastal Franciscan Belt (Jayko et al., 1989). The area has a Mediterranean climate with annual average precipitation of approximately ~2 m/yr, the vast majority of which falls as rain between the months of December and March (Mast and Chow, 2000). Elder Creek watershed is located entirely within the University of California's Angelo Coast Range Reserve, and has been free of grazing, logging, mining, and other disturbances since 1959 (the basin had only limited logging during the late nineteenth and early twentieth centuries) (Mast and Chow, 2000). While there are no records of modern debris flows within the catchment, debris flows have been active in the area in the Holocene (Scheingross et al., 2008), and many tributaries are incised into debris flow fans near their junction with the main stem of Elder Creek. Cosmogenic dating of modern stream sediment yields basin average erosion rates for Elder Creek of 0.16 – 0.18 mm/yr (Fuller et al., 2009).

We monitored five tributaries of Elder Creek over three water years from September 2007 to July 2010. In order to examine effects of slope and roughness on sediment motion we chose reaches spanning a range of channel gradients from 5 to 37% and median particle diameters of 57 to 155 mm. These reaches range in drainage area from 0.04 to 2 km^2, bankfull depths from 0.13 to 0.3 m, and bankfull widths from 1.1 to 4.1 m (Figs. 2.1 and 2.2, Table 2.1). Study reaches 2 and 4 are located in channels near the apex of debris flow fans which are deposited over a strath terrace of Elder Creek; the other reaches (1, 3, and 5) are located in channelized valleys. For each tributary, we selected short, straight reaches (~20-50 meters in length) for monitoring. All monitored reaches were mantled with coarse sediment, including boulders. There is no exposure of bedrock in the channel beds within any of the study reaches, and bedrock channel beds are rarely exposed in the Elder Creek tributaries in general. Sediment on the surface of monitored reaches is organized into distinct size-sorted patches. The steepest channels examined here (reaches 1 and 2, slopes of 37% and 18%, respectively) have a cascading morphology (in the sense of Montgomery and Buffington, 1997) and include isolated areas of soil development and leaf litter accumulation within channels (Figs. 2.2a, 2.2b); lower gradient channels have more pronounced step-pool morphology, but also include short cascading reaches (Figs. 2.2c, 2.2d, 2.2e).

2.4 Methods

Calculating critical Shields stresses for gravel entrainment in steep streams requires characterization of channel geometry, flow hydraulics, bed roughness, and

sediment transport. In this section we first describe our methods of surveying channel geometry and grain size distributions. Next we discuss our methods for measuring flow hydraulics and calibrating a flow algorithm to estimate bed shear stress. Finally we describe our methods for documenting sediment transport.

2.4.1 Channel geometry

We surveyed channel geometry with high-resolution ground-based light detection and ranging (LiDAR) in reaches 2 and 4; in the remaining three reaches we surveyed longitudinal profiles and cross-sections with a stadia rod and hand level. Points along longitudinal profiles were surveyed at high densities to capture breaks in slope due to steps, pools, and other structures. Despite large changes in local slope along a longitudinal profile, channel cross-sectional shape remained fairly constant over several meters (Fig. 2.2), therefore we spaced cross-section surveys approximately every two meters in reaches 1 and 3, and every four meters in reach 5.

2.4.2 Flow hydraulics

We measured stream discharge and reach average velocity for six flow events in reaches 2 and 4 (Table 2.2) using the salt dilution method whereby salt is injected into a stream as a tracer, and discharge is estimated assuming conservation of the tracer mass (Elder et al., 1990; Hudson and Fraser, 2005). This method is advantageous compared to the traditional slug-injection method as it yields the same results for injection of both dry salt and salt dissolved into solution. For each measurement we injected salt at a distance of 7 to 10 channel widths upstream of a conductivity meter. This length scale is near the low end of observed mixing lengths in mountain streams (Day, 1977b), and was chosen

to avoid large pools and backwater areas where water could stagnate and compromise the reliability of the measurement (Elder et al., 1990; Moore, 2003). A single conductivity probe was placed at the center of the channel and we manually recorded stream conductivity ensuring a minimum of 25 measurements to accurately characterize the passing salt wave (Day, 1977a). Conductivity was converted to salt concentration using a laboratory-measured calibration coefficient in stream water. We additionally calculated reach-averaged stream velocity based on the travel time from salt injection to the center of mass of the passing salt wave (i.e., the 'centroid velocity,' (Calkins and Dunne, 1970)).

For one discharge measurement (reach 5, 17 Feb 2009) we recorded the time of peak conductivity following salt injection, but did not make sufficient manual conductivity measurements to accurately characterize the shape of the passing salt wave. For this reach only, we calculated reach-averaged velocity using the time from salt injection to peak conductivity (i.e., the 'peak velocity' of Calkins and Dunne (1970)), and estimated discharge in the reach as $Q = Uwh$, where Q is water discharge, U is reach-averaged flow velocity, and w and h are reach-averaged width and flow depth, respectively, measured in the field.

In addition to measurements of flow hydraulics, we instrumented each study reach with a pressure transducer measuring atmospheric and total (atmospheric plus water) pressure at 15 minute intervals and a crest stage gage (placed adjacent to the pressure transducer and built to US Geological Survey standards (Holmes et al., 2001)) to measure peak water stage. These instruments allowed estimation of flow hydraulics for periods when we were unable to make manual measurements.

2.4.3 Modeling bed shear stress

In low-gradient streams, bed shear stress is often estimated assuming steady, uniform flow (i.e., $\tau = \rho g R S$, where τ is bed shear stress and R is the hydraulic radius); however, these assumptions may be invalid in the steep streams examined here which have flow cascading over steps and chutes. Instead, we used a non-uniform flow algorithm, HEC-RAS (Hydrologic Engineering Center River Analysis System, available at *http://www.hec.usace.army.mil/software/hec-ras/*), to estimate bed shear stress. HEC-RAS has been used successfully by others in channels with $S > 1\%$ (e.g., Church and Hassan, 2002; Thompson and Croke, 2008), and is convenient to use as it can model transcritical flow. HEC-RAS should be used with caution for $S > 10\%$ (reaches 1 and 2) where the gradually varied flow and hydrostatic assumptions used in the model may be invalid (US Army Corps of Engineers, 2010, pg. 2-20 to 2-21); however, available codes for rapidly varying, non-hydrostatic flows do not exist, to our knowledge. Here we describe the procedures for calibration of our flow algorithm with manually measured flow depths, velocities, and discharges.

Channel geometry for HEC-RAS was taken from our field surveys where each survey point in the long profile was used as a node (i.e., cross-section) within the model (Fig. 2.3). In reaches 1, 3, and 5 we did not survey a cross-section at each node within the longitudinal profile, and instead used the surveyed cross-section associated with the nearest node as the input to HEC-RAS based on our observation that variations in cross-section geometry was small over the scale of ~2-4 m compared to changes in river-bed elevation. This resulted in a high density of nodes within HEC-RAS sufficient to capture steps and other breaks in slope which affect flow hydraulics (Fig. 2.3, Table 2.3). For all

modeling, we set the upstream and downstream boundary conditions to critical depth based on the observations of steps and overspilling flow (e.g., Rouse, 1936). We then iterated with changing the flow resistance (i.e., Manning's n) to minimize the misfit between our manually measured flow depths and HEC-RAS predicted flow depths (Fig. 2.3), with all other parameters set to their default values (e.g., expansion and contraction coefficients set to 0.3 and 0.1, respectively).

We estimated the critical shear stress for sediment transport from patches assuming sediment was mobilized at the peak flow prior to sediment recovery. HEC-RAS parameter settings were the same as described above (i.e., critical upstream and downstream boundary conditions, and all other parameters set to default values). We iterated with changing both discharge and Manning's n in HEC-RAS until modeled flow depths matched (within 5%) flow depths measured with stage recorders and the predicted Manning's n matched the Darcy-Weisbach friction factor, f, predicted by *Ferguson* (2007) (where f and Manning's n can be related by definition by $n = \left[R^{2/3} S^{1/2} \right] / \left[u_* (8/f)^{1/2} \right]$, and u_* is the reach-averaged shear velocity defined as $u_* = (\tau / \rho)^{0.5}$). For all cases but patch 1a in reach 1, local stress was estimated from the cross section nearest the patch of interest. For patch 1a in reach 1 (the steepest reach, S = 37%), the flow was cascading between two cross-sections with locally changing channel gradient. Due to the complex flow for this case, we report the shear stress for both bounding cross-sections as a measure of possible variability.

2.4.4 Monitoring sediment transport

Within each reach we selected individual sediment size-sorted patches to monitor for grain mobilization, and marked patches (via spray painting) in place. Patches were typically ~0.5 by 0.5 m in areal extent, and we attempted to select patches with apparently mobile sediment, avoiding areas of the bed with lichen development or strongly interlocked grains. For reaches 1 - 4 we selected patches within the channel thalweg in order to minimize the influence of cross-channel variations in flow due to bars, wall drag, and other morphologic structures. Furthermore, we avoided pools or other areas subject to plunging flow and secondary currents. Perennial flow in reach 5 made it impossible to paint patches in situ within the thalweg; instead we painted emerged patches as close to the thalweg as possible at the end of summer when flow depth was lowest.

To compare transport of mobile gravel in active patches to reach-wide transport we additionally marked (via spray painting) an average of ten individual cobbles and boulders per reach, spanning a range of intermediate grain diameters (D = 90 to 450 mm). Repeat photographs of cobble and boulder position were used to determine mobilization of these larger grains.

We monitored sediment motion over three field seasons. Mobilized grains from painted patches served as particle tracers, and were recovered when found during and after storm events allowing measurements of the particle distance traveled and diameters of mobilized particles. During the 2008/2009 winter we made field visits to document sediment motion before, after, and during every storm. In the other two seasons of monitoring our results came from field measurements made at the end of the rainy season (Table 2.4).

We measured the grain-size distribution of painted patches using photographs. This allowed us to measure particle sizes without disturbing the position of grains on the bed. We employed a grid-by-number approach and set grid spacing equal to the maximum grain size present within the painted patch, which gives results similar to bulk-volume measurements (Bunte and Abt, 2001). Given the small areal extent of the patch (~0.25 m^2) and large grains (up to 150 mm) the total number of particles per count averaged ~25 grains. We measured the short axis of particles and multiplied the axis length by a factor of 1.07 to account for the fact that the true median axis is not always exposed in the photographic image (Bunte and Abt, 2001). Grain-size distributions for photographic pebble counts were comparable with field measurements of particle intermediate axes made using the grid-by-number method for select patches (Fig. 2.4). We additionally measured reach-averaged grain-size distribution spanning the full channel reach (including steps and immobile grains within the bed) using grid by number sampling of 100-200 grains per reach (Table 2.1).

Recovery of painted tracer particles from patches was limited by burial of grains, potential loss downstream where tributaries join Elder Creek, wearing away of paint, and the fact that painting in situ did not allow marking the underside of grains. We counted the painted grain-number density from photographs taken immediately after spray painting (i.e., before transport), and measured the patch area absent of painted grains from photographs taken the following summer after transport had ceased to estimate the number of transported grains (Fig. 2.5). We compared this estimate with the total number of recovered grains (Table 2.4) to calculate percent recovery from a patch for a given water year. For cases where aggradation occurred within a patch this method

underestimates the true recovery rate, thus recovery percents reported here are minimum estimates. Recovery rates varied from approximately 2 to 85%; low recovery rates were generally associated with fine patches that experienced significant mobility (and hence were more prone to burial and loss downstream).

2.5. Field monitoring results

In this section we report field results on flow hydraulics and sediment transport. Sediment transport results are reported in two sub-sections including painted-patch grain-size evolution and particle-travel distance. The flow hydraulic and sediment-transport data presented here are used to calculate critical Shields stress for grain entrainment in section 5.

2.5.1 Flow hydraulics

Flow in all study reaches responded to winter storms (Fig. 2.6). Two of the five tributaries had ephemeral flow (reaches 1 and 2, which experienced flow lasting hours to days following storms, but no sustained winter base flow), two showed intermittent flow (reaches 3 and 4, which experienced winter base flow for the majority of the rainy season), and one had perennial flow (reach 5). For the ephemeral and intermittent streams, flow events were generally longer and had larger peak-stage heights at the end of the winter season rather than the beginning. This is likely due to flow events early in the winter season raising the groundwater and (for the intermittent streams) creating winter base flow.

Peak discharges during the study period were relatively modest (the largest flood occurred in the 2007/2008 winter with a recurrence interval of 1.8 years on Elder Creek). Measured peak discharges ranged from 0.03 m^3/s for reach 2 to 0.19 m^3/s for reach 4 (Table 2.2). Measured peak reach-averaged velocity was 0.25 and 0.32 m/s and reach-averaged flow depth was 8.5 and 21 cm for reaches 2 and 4, respectively. These flow depths are of similar magnitude to the measured reach averaged median grain size (D_{50}, Table 2.1), and both mobile and immobile particles were often emergent from the flow at peak discharge (Fig. 2.2b).

We evaluated the performance of our HEC-RAS modeling by comparing the modeled water surface elevation to observed water surface elevations (Fig. 2.3) and by comparing the ratio of U / u_* to f predicted by Ferguson (2007):

$$\frac{U}{u_*} = \left(\frac{8}{f}\right)^{1/2} = \frac{a_1 a_2 (R / D_{84})}{[a_1^2 + a_2^2 (R / D_{84})^{(5/3)}]^{(1/2)}}, \qquad (2.2)$$

where a_1 = 6.5, a_2 = 2.5 as suggested by Ferguson (2007), and D_{84} is the grain size for which 84% of the reach-wide bed is finer. We found reasonable agreement between U / u_* and R/D_{84} (Fig. 2.7), suggesting that HEC-RAS accurately captures flow hydraulics and that f increases with decreased flow depth to roughness ratios for the streams in which we measured discharge. HEC-RAS modeled values of reach-averaged hydraulic radius, velocity, and bed shear stress ranged from 0.05 to 0.34 m, 0.2 to 1.1 m/s, and 105 to 406 Pa, respectively (Table 2.5).

2.5.2 Sediment mobilization and preservation of patches

Despite modest discharges during the study period, eight of the nine painted patches experienced grain mobilization annually. Field visits before and after storm events showed that sediment movement occurred during large discharge events in the middle to the end of the rainy season when stage heights were high. Intensive monitoring in winter 2008/2009 showed that transport from the patch in reach 1 was limited to a single storm event, two storm events produced sediment transport from the patch in reach 4, three storm events produced transport from patches in reach 2, and reach 3 experienced transport from patches in multiple events (reach 5 was not visited during storms due to inaccessibility).

Repeat pebble counts of painted patches show that patch median grain size (D_{50}) remained fairly constant (generally within a factor of three) over the study period for all cases (Fig. 2.8). However, when coarsening or fining did occur, these trends were often reflected in multiple patches across a reach, suggesting a reach-wide change in grain size.

Despite mobilization of gravel in patches, a large fraction of the bed was observed to be stationary over the study period both within painted patches and in the reaches as a whole. For patches with regular grain mobilization, the largest grains available in a patch were rarely moved (Fig. 2.9), thus providing evidence that the patches experienced partial transport. For example, 75% of transport events from individual patches failed to move grains larger than half the diameter of the maximum grain size present within the patch (Fig. 2.9). Of the fifty individually painted cobbles and boulders, only six cobbles moved. These were generally among the smaller grains (D < 150 mm) and were not interlocked. Transport distances for these painted cobbles and boulders were short (0.2 – 1 m). The lack of movement of large cobbles and boulders suggests that the tributaries underwent

reach-wide partial transport of sediment. Reach-wide partial transport was additionally documented in reach 2 where a small dam designed to trap sediment deployed in the 2008/2009 winter collected 4.3 kg of sediment and showed the maximum grain size moved through the reach (70 mm) was less than the reach-averaged median grain size (97 mm).

2.5.3 Particle travel distance

Particle travel distance is a function of both grain weight and the grain size relative to the bed (as smaller particles are more likely to become trapped behind larger particles (e.g., Einstein, 1950)). In a compilation of worldwide streams, Church and Hassan (1992) found an inverse relationship between particle size and distance traveled, and other more recent studies (e.g., Ferguson and Wathen, 1998; Hodge et al., 2011; Lenzi, 2004; Wilcock, 1997) have found similar trends. An inverse trend between particle size and distance transported is expected if grain weight is the dominant control on particle travel distance; however, preferential trapping of smaller particles within a bed composed of larger grains can cause deviations from this trend (e.g., Kirchner et al., 1990). *Church and Hassan* (1992) noted that distance transported may depend strongly on grain weight for particles with $D/D_{50} > \sim 2$, whereas particles with $D/D_{50} < \sim 2$ have a higher likelihood of being trapped within the bed of coarser grains and therefore their distance traveled may depend less on grain weight.

Data on transport distance for all recovered grains (i.e., all patches with mobile sediment) in this study show a slight inverse relationship between travel distance and grain size, and general agreement with the shape of the Church and Hassan (1992)

relationship, but a systematic offset to lower values of the normalized travel distance (Fig. 2.10). Data in Fig. 2.10 suggest smaller particles were transported slightly farther than larger particles in our studied reaches. Note that Church and Hassan (1992) normalized grain size by D_{50} of the bed subsurface, and that we normalize by D_{50} of the bed surface. This difference in normalization may explain the systematic offset between the data presented here and the Church and Hassan (1992) relationship because the surface of the reaches examined in this study were in most cases armored. Despite increased probability of trapping small grains for $D/D_{50} < 2$, we still observed an overall inverse relationship between grain size and particle transport distance. The increased travel distance of small particles allows for replacement of gravel within patches by similar sized grains which may be sourced from distances several meters upstream.

2.6 Analysis

In this section we present an analysis of our sediment transport data in order to estimate critical Shields stress for incipient motion, and compare our calculated Shields stress values to theoretical models. We then use flow hydraulic data to estimate form drag, and attempt to quantify individually the effects of form drag, slope-dependent hydraulics, bed patchiness, and grain hiding on critical Shields stress.

2.6.1 Critical Shields stress

Determining the exact timing of incipient motion for a given particle is difficult. Since no universal metric is used to define the onset of incipient motion (Buffington and Montgomery, 1997), we calculated critical Shields stresses using two different

approaches to avoid biases associated with a single technique. First, we used a flow competence approach and assumed the largest transported grain moved at the peak observed bed shear stress (τ_{max}) (Andrews, 1983). With this assumption equation (2.1) can be rewritten as

$$\tau_{*c} = \frac{\tau_{\max}}{(\rho_s - \rho) g D_{\max}} \quad , \tag{2.3}$$

where D_{max} is the largest grain observed to move from a given patch for a given storm event (or integration of multiple storms). This approach is frequently used in field studies of motion in streams with moderate to steep slopes (e.g., Church and Hassan, 2002; Lenzi et al., 2006; Mao et al., 2008; Thompson and Croke, 2008).

Second, we estimated τ_{*c} by assuming all transported grains deposited within one meter of the patch from which they originated were at incipient motion during the flood peak. For this method we calculated the critical Shields stress as

$$\tau_{*c} = \frac{\tau_{\max}}{(\rho_s - \rho) g D_{1meter}} , \tag{2.4}$$

where D_{1meter} is the mass weighted geometric mean grain diameter of all particles (always > 5 grains) recovered within one meter downstream of the patch from which they originated. We refer to the second approach as the "one-meter method." The one-meter method is similar to the particle displacement approach which is often used in steep streams (e.g. Lenzi et al., 2006; Mao et al., 2008); however, we were unable to measure sub-grain-diameter movement (as required for the particle displacement approach) since grains must move out of the painted patch in order to observe definitive movement. Note

that even though we had low recovery rates of grains transported from patches, estimates of D_{max} and D_{1meter} are likely accurate as large grains (i.e., D_{max}) are easier to see, less likely to be buried, and travel shorter distances than fine grains (Fig. 2.10). Recovery rates of grains deposited near the patch (i.e., D_{1meter}) should be high as these grains come from a small area which was thoroughly searched. For both the flow competence and one-meter methods we estimated τ_{max} locally using the modeled bed shear stress given by HEC-RAS (section 2.4.3, Table 2.4), which reflects shear stress spent on both mobile and immobile elements (i.e., the total shear stress).

Neither of the above approaches provides a perfect measure of the conditions for incipient motion. The flow competence approach assumes the largest grain recovered was mobilized at the highest calculated bed shear stress (and therefore that smaller grains are mobilized at lower shear stresses than larger grains, a condition that generally exists for gravel-bed streams (Parker, 2008)), and is only valid for cases where the largest grains in the patch remain stationary (i.e., partial transport of the patch, which was met in this study). *Wilcock* (1992) notes that flow competence estimates are subject to large errors as they are based on an extreme value of the transport grain-size distribution. Similarly, since the flow competence approach uses only a single grain to estimate critical Shields stress, the conditions for mobilization may largely be a function of local pocket geometry, protrusion, interaction with surrounding grains (e.g., locked in place or free to move), and other local conditions at the grain scale (e.g., Kirchner et al., 1990).

The one-meter method uses the geometric mean grain diameter of all particles recovered, thus averaging over grain-scale heterogeneity inherent with the flow competence method. However, the one-meter approach assumes that grains at incipient

motion are transported shorter distances than grains at high transport stages (e.g., Wiberg and Smith, 1985). While this is consistent with our data in general (Fig. 2.10), in some cases, the stopping location of a grain may be a function of the transported grain size relative to the local roughness on the bed (e.g., Dietrich et al., 2006) or a function of the transported grain size itself (e.g., Church and Hassan, 1992), which may introduce error in this method.

Our inferred critical Shields stress values for particles that moved are similar for both the flow competence and one-meter methods, and vary over two orders of magnitude from ~0.02 to 2. The majority of τ_{*c} estimates have values greater than those typically assumed for gravel-bedded rivers (i.e. $\tau_{*c} = 0.045$). Large variations in critical Shields stresses may result from slope-dependent hydraulic effects (e.g., Lamb et al., 2008b; Mueller et al., 2005; Recking, 2009), grain hiding, (Egiazaroff, 1965; Einstein, 1950; Wiberg and Smith, 1987), form drag on non-mobile structures (Yager et al., 2012b; Yager et al., 2007), and the presence of sediment patches (Yager et al., 2012a), all of which exist in the steep streams examined here. These are each evaluated in section 2.6.4 using a force-balance model.

2.6.2 Comparison to critical Shields stress models

We compared our field-estimated critical Shields stresses to the theoretical relationships proposed by Wiberg and Smith (1987) and Lamb et al. (2008b) (which gives similar results to Recking (2009)), as well as the empirical relationships proposed by Mueller et al. (2005) and Ferguson (2012). Wiberg and Smith (1987) proposed a force balance model which predicts grain motion for coarse grains primarily as a function

of the grain size relative to the local roughness (i.e. D/k_s, where D is the grain size of interest, and k_s is the local channel roughness for large particle Reynolds numbers). This model predicts that τ_{*c} decreases with increasing slope due to the additional component of gravity in the downstream direction. Lamb et al. (2008b) modified the Wiberg and Smith (1987) model to include slope-dependent hydraulic effects and fractional form drag, resulting in a prediction of increasing τ_{*c} with slope. For this section we set fractional form drag to zero in the Lamb et al. (2008b) model (the influence of form drag is examined in section 2.6.4). Mueller et al. (2005) predict a positive linear relationship between τ_{*c} (for the median particle size) and slope based on a fit to field data for slopes up to S = 0.05. Ferguson (2012) attributes the heightened τ_{*c} with increasing slope entirely to form drag.

We evaluated the ability of each model to predict our field data by performing a two-sample Kolmogorov-Smirnov test of the log-transformed field-estimated and model-predicted critical Shields stress data. The Kolmogorov-Smirnov test assesses the null hypothesis that two populations of values belong to the same distribution. In our case, rejection of the null hypothesis indicates a statistical difference between the field-estimated versus model-predicted critical Shields stress distributions, which we interpret to mean the model in question does a poor job of predicting critical Shields stress. The Kolmogorov-Smirnov test is advantageous to other goodness of fit measures (e.g., r^2 or residual sum of squares) as it examines the full cumulative distribution function and is thus less sensitive to a single outlier, and it is designed for small sample sizes (Zar, 1999).

The models described above differ widely in their ability to match our calculated critical Shields stresses (Fig. 2.11). The Wiberg and Smith (1987) model tends to underpredict critical Shields stresses, which is likely a result of the steep slopes examined here for which the model predicts decreased Shields stress due to the increased component of gravity in the downstream direction (Fig. 2.11a). Both the Mueller et al. (2005) and Ferguson (2012) models predict critical Shields stress for the median grain size only, and thus do not match well our data of grains both smaller and larger than the median size (Fig. 2.11b, c). The distribution of critical Shields stresses predicted by the Wiberg and Smith (1987), Mueller et al. (2005), and Ferguson (2012) models are statistically different from the distribution of our field-estimated values by the Kolmogorov-Smirnov test (for all three models $p < 0.001$).

The Lamb et al. (2008b) relationship is the only model for which we cannot reject the null hypothesis of the Kolmogorov-Smirnov test, and the predicted critical Shields stresses are generally within a factor of three of the field data (Fig. 2.13d). The factor of three in scatter is observed in other studies as well, including controlled flume experiments, and can arise from the stochastic nature of turbulent flow and sediment transport alone (e.g., Buffington and Montgomery, 1997; Kirchner et al., 1990; Mizuyama, 1977). The data consistency with the Lamb et al. (2008b) model suggests that slope-dependent hydraulic effects, local channel roughness, and grain hiding affect incipient sediment-motion.

2.6.3 Form drag

In steep streams the presence of large immobile grains and particle clusters leads to a reduced portion of the total shear stress available to act on the mobile sediment (e.g., Brayshaw et al., 1983; Buffington and Montgomery, 1999; Millar, 1999; Wiberg and Smith, 1991; Yager et al., 2012b; Yager et al., 2007). We accounted for this reduced shear stress on mobile grains by calculating a "fractional form drag," τ_{fd} / τ_T, where τ_{fd} is the bed shear stress spent on immobile morphologic structures and τ_T is the total bed shear stress. We calculated fractional form drag following *Yager et al.* (2012) as

$$\frac{\tau_{fd}}{\tau_T} = 1 - \frac{\tau_m}{\tau_T} = 1 - \frac{0.5\rho C_m U^2}{\tau_T} \quad , \qquad (2.5)$$

where τ_m is the shear stress on the mobile grains and C_m is the drag coefficient for mobile sediment. We used results from the HEC-RAS modeling to solve for the reach-averaged τ_T (section 2.4.3, Table 2.5). Drag coefficients for mobile sediment are not well known, thus we estimated C_m with three different methods to check for consistency.

The first two methods use hydraulic data reported by Marcus et al. (1992) for a steep mountain stream. Following Yager et al. (2012), we assumed $\tau_T = \tau_m$ in the data of Marcus et al. (1992) based on the observation of minimal boulders, steps, and other structures, and calculated C_m from fifteen separate flow measurements using a normal-flow approximation for τ_T so that

$$C_m = \frac{2\tau_T}{\rho U^2} = 2\left(\frac{u_*}{U}\right)^2 = \frac{2gRS}{U^2} \quad . \qquad (2.6)$$

Note, the channel studied by Marcus et al. (1992) likely has some form drag on immobile structures, and our estimates of C_m from this data should be considered maximum values.

These C_m estimates vary as a function of R/D_{84}, although the data are scattered. This scatter caused Yager et al. (2012) to adopt a constant value of C_m,

$$C_m = 0.44\,, \qquad (2.7)$$

which is an average of the mobile drag coefficients calculated from the *Marcus et al.* (1992) data. We used both the mean C_m value, and also fit a power law to the data (hereafter referred to as the "power-law C_m" method),

$$C_m = 0.57(R / D_{84-mobile})^{-0.96}\,, \qquad (2.8)$$

with $r^2 = 0.42$, and where $D_{84\text{-}mobile}$ is the reach-averaged grain size for which 84% of mobile sediment is finer. Equation (2.8) allowed calculations of a flow-depth dependent mobile drag coefficient for sediment transport events in this study where reach-averaged R was obtained from HEC-RAS, and $D_{84\text{-}mobile}$ was calculated from our reach-averaged pebble counts ignoring all grains larger than the maximum observed mobile particle for a given reach (based on painted particle tracer data) (Table 2.1).

In addition to the two techniques described above, we also calculated C_m using the variable power equation (VPE) of *Ferguson* (2007) (hereafter referred to as the "VPE C_m" method) following methods similar to those proposed by Rickenmann and Recking (2011) for flow resistance partitioning. We set $D_{84\text{-}mobile}$ as the roughness length scale, solved for the Darcy-Weisbach friction factor, f, and estimated C_m directly by substituting equation (2.2) into (2.6). This last method is independent of the Marcus et al. (1992) measurements, is based on a large compilation of flow resistance data, and has been shown to accurately predict flow resistance in steep streams (Rickenmann and Recking,

2011), although its application to form drag rather than flow resistance has not been tested directly.

In our monitored tributaries τ_{fd} / τ_T ranged from 0.14 to 0.90, 0.12 to 0.95, and 0.71 to 0.92 with mean values of 0.65, 0.74, and 0.81 for C_m estimated with the power-law, mean, and VPE methods, respectively (Fig. 2.12, Table 2.5). Note equation (2.7) (i.e., mean C_m) produced two outliers with $\tau_{fd} / \tau_T < 0$ which were ignored as negative fractional form drag cannot exist. The results are similar across the three different methods, with all methods predicting large values of form drag and overlapping interquartile ranges (Fig. 2.12).

We compared our calculated fractional form drag in the Elder Creek tributaries to other streams using data from Buffington and Montgomery (1999) and Yager et al. (2012). We calculated τ_{fd} / τ_T from data reported by Buffington and Montgomery (1999) using the difference between the observed median grain sizes and the median grain sizes expected for a channel with no form drag. τ_T was calculated assuming uniform flow (i.e., $\tau_T = \rho g h S$, where h is the reach-averaged flow depth and was used in place of hydraulic radius, which was not reported), τ_{fd} was calculated using the observed grain-size distribution on the bed, $\tau_{fd} = \tau_{*c}(\rho_s - \rho) g D_{50}$ (which assumes that the median grain size is set by a representative bed shear stress), and τ_{*c} was set to 0.03 as suggested by Buffington and Montgomery (1999). To calculate fractional form drag from Yager et al. (2012) we digitized data reporting total shear stress (τ_T) and shear stress on mobile sediment ($\tau_T - \tau_{fd}$) (their figure A1d for variable C_m), and calculated a discharge-dependent range of fractional form drag.

The range of τ_{fd} / τ_T from approximately 0.1 to 0.9 in Elder Creek tributaries is comparable to (although larger than) the fractional form drag we calculated from the data of Yager et al. (2012) ($0.53 < \tau_{fd} / \tau_T < 0.80$) for a stream of 9.8% gradient, and to data from Buffington and Montgomery (1999) ($0.27 < \tau_{fd} / \tau_T < 0.95$) on lower gradient streams with $S = 0.2$ - 2.7% (Fig. 2.12). While the lower limit of the τ_{fd} / τ_T range is smaller in the Elder Creek tributaries, we note the 25th percentile values of τ_{fd} / τ_T are greater than 0.65 for all three methods, similar to the range of values reported by Yager et al. (2012). Larger values of fractional form drag in the Elder Creek tributaries and the Yager et al. (2012) data may be expected due to the presence of immobile steps and boulders as opposed to the plane bed and pool-riffle sequences analyzed by Buffington and Montgomery (1999). Our range of calculated form drag is also comparable to that required for the Lamb et al. (2008b) critical Shields stress model to best match their field data compilation (τ_{fd} / τ_T approximately 40 to 80%, in their Fig. 2.10).

2.6.4 Relative influence form drag, channel slope, patches, and grain hiding on critical Shields stress

In this section we use our field data and the models of Wiberg and Smith (1987) and Lamb et al. (2008b) to investigate the influence of form drag, slope, bed patchiness, and grain hiding on critical Shields stress values. While there exist a number of theoretical and empirical models to predict critical Shields stress (discussed above), we use the Wiberg and Smith (1987) and Lamb et al. (2008b) models because they provide a framework to isolate the effects of form drag, channel slope, grain hiding, and bed patchiness independently.

2.6.4.1 Influence of form drag

Our field-estimated critical Shields stresses use HEC-RAS-modeled total bed shear stress, and thus include any form drag present within the channel. To asses the form drag influence, we compared field-estimated critical Shields stresses to model predictions which account for form drag by setting τ_{fd} / τ_T in the Lamb et al. (2008b) model to values calculated using the mean (i.e., equation 2.6), power law (i.e., equation 2.7), and VPE C_m methods (section 2.6.3). We also set τ_{fd} / τ_T to a constant value of $\tau_{fd} / \tau_T = 0.5$ which best matches the field and flume data collection of Lamb et al. (2008b), as well as $\tau_{fd} / \tau_T = 0$ for the sake of comparison. For all four form drag parameterizations, as well as the case of no form drag, we cannot reject the null hypothesis of the Kolmogorov-Smirnov test at the 5% significance level (p values of 0.07, 0.12, 0.19, 0.30, and 0.93 for the mean C_m, power law C_m, $\tau_{fd} / \tau_T = 0$, VPE C_m, and $\tau_{fd} / \tau_T = 0.5$ form drag parameterizations, respectively). This result implies that it may be possible to explain the field-estimated critical Shields stress values with or without the inclusion of form drag, and thus, the effect of form drag may be small compared to other factors which influence critical Shields stress (i.e., grain hiding, bed patchiness, and slope-dependent hydraulics discussed below). Setting fractional form drag to a constant value of $\tau_{fd} / \tau_T = 0.5$ visually appears to match the field data well (Fig. 2.13a), and we use this value for the remainder of the model calculations; however, using other form drag parameterizations does not change the main points of this paper.

2.6.4.2 Influence of hydraulics at steep slopes

Changes in the flow velocity structure, turbulent fluctuations, and grain emergence at low flow depth to bed-roughness ratios leads to increased τ_{*c} for steep slopes (Lamb et al., 2008b; Recking, 2009). To isolate these slope-dependent effects on critical Shields stress we compared our results to model predictions of Wiberg and Smith (1987) which do not include these effects. Following the methodology of Lamb et al. (2008b) we added a fractional form drag term (τ_{fd} / τ_T = 0.5) to the Wiberg and Smith (1987) model so that differences between the Lamb et al. (2008b) and Wiberg and Smith (1987) models reflect only the inclusion of slope-dependent flow hydraulics and grain emergence in the former. The Wiberg and Smith (1987) model tends to under-predict the field-estimated critical Shields stress values, and is statistically distinct from the distribution of field data (p = 0.0002 in a two sample Kolmogorov-Smirnov test, Fig. 2.13b). This implies that incipient sediment motion is influenced by slope-dependent hydraulics.

2.6.4.3 Influence of patches and local roughness

The agreement between calculated and modeled critical Shields stresses in Figure 2.13a was achieved in part because of the field identification of individual, size-sorted sediment patches used to define the local roughness scale of the bed (i.e., k_s). Because steep streams include both relatively mobile fine gravel and less mobile cobbles and boulders (e.g., Yager et al., 2012a, b), using reach-averaged median grain size ($D_{50\text{-}reach}$) as the roughness length scale (i.e., $k_s = D_{50\text{-}reach}$), as opposed to local median-grain size of the patch ($D_{50\text{-}patch}$) as the roughness length scale (i.e., $k_s = D_{50\text{-}patch}$), can lead to predictions of no sediment motion due to artificially inflated critical Shields stresses. To illustrate this point we compared Lamb et al. (2008b) model predictions of critical

Shields stresses to our data using patch- versus reach-averaged median grain size as the bed roughness length scale, with $\tau_{fd} / \tau_T = 0.5$. Setting $k_s = D_{50\text{-}reach}$ tends to over-predict critical Shields stress and results in statistically distinct distributions of field and model data ($p < 10^{-5}$, two sample Kolmogorov-Smirnov test, Fig. 2.13c), while using $k_s = D_{50\text{-}patch}$ does not ($p = 0.93$, two sample Kolmogorov-Smirnov test, Fig. 2.13a). These results imply that initial sediment motion in steep channels is influenced by local roughness controlled by bed surface patchiness.

2.6.4.4 Influence of grain hiding

We compared our calculated τ_{*c} values to those predicted by the *Lamb et al.* (2008b) model with $D/k_s = 1$ (i.e., ignoring grain hiding), versus D/k_s set equal to the value measured in the field. For both cases we set $\tau_{fd} / \tau_T = 0.5$, and used a two sample Kolmogorov-Smirnov test to evaluate model performance. A model without grain hiding can lead to both over and under-predictions of τ_{*c} depending on whether D/k_s is less or greater than unity, respectively. This effect is illustrated in Fig. 2.13d where model predictions with $D/k_s = 1$ are approximately evenly distributed above and below the 1:1 line. The distribution of critical Shields stresses predicted with $D/k_s = 1$ are statistically distinct at the 5% significance level from the field-estimated Shields stresses (where D/k_s is allowed to vary, $p = 0.037$), implying that including grain hiding within patches influences initial motion in our dataset.

We also examined the influence of relative grain size using a hiding function (e.g., Parker, 2008),

$$\frac{\tau_c}{\tau_{ks}} = \left(\frac{D}{k_s}\right)^{1-\gamma}, \qquad (2.9)$$

where τ_c is the critical shear stress for the grain size of interest, τ_{ks} is the critical shear stress for $D = k_s$, and γ is a non-dimensional constant that describes the relative importance of hiding effects on grain mobilization. Following the terminology of Parker (2008), we refer to the case when $\gamma = 0$ as "size independence" (the critical shear stress to mobilize grains is linearly proportional to grain diameter, hence there are no hiding effects), and when $\gamma = 1$ as "equal threshold" (hiding effects dominate causing all grains to move at the same critical shear stress).

We estimated γ using our field data to find a best fit to equation (2.9). We used HEC-RAS modeling to estimate τ_c (τ_{max} in Table 2.4), and calculated τ_{ks} using the Lamb et al. (2008b) model (with $\tau_{fd} / \tau_T = 0.5$). We found $\gamma = 0.51$ based on a linear best fit to our log-transformed incipient motion data (Fig. 2.14). The data are scattered ($r^2 = 0.26$), but our γ value of 0.51 is statistically distinct from equal threshold of motion (i.e., $\gamma = 1$) based on a *t*-test ($p = 0.002$). The best-fit γ value is lower than other values reported in high gradient streams by Mao et al. (2008) (0.79 and 0.64) and Yager et al. (2012) (γ = 0.62), and is also lower than data compiled by Parker (2008) which shows a mean value of $\gamma = 0.79 \pm 0.16$ (mean ± standard deviation) on modest sloping gravel-bed streams (S = 1-1.5%). This low γ value indicates a reduced influence of hiding effects in steep streams and suggests that small grains are relatively easier to transport than large grains, ultimately leading to the preference of mobilization of distinct size classes during a given flow event. A preference to transport smaller grains (i.e., $D/k_s < 1$) is supported by our observations of particle transport distances (Fig. 2.10) and partial transport (Fig. 2.9), and

leads to increased τ_{*c} values compared to assuming the median grain size will be mobilized (i.e., $D/k_s = 1$).

2.6.4.5 Summary of dominant effects on initial motion

We examined the net effect of form drag, slope-dependent hydraulics, bed patchiness, and grain hiding by calculating the ratio of the field-estimated ($\tau_{*c\text{-}field}$) to model-predicted ($\tau_{*c\text{-}model}$) critical Shields stress (Fig. 2.15). Effects which increase critical Shields stress result in $\tau_{*c\text{-}field} / \tau_{*c\text{-}model} > 1$, while effects which decrease critical Shields stress result in $\tau_{*c\text{-}field} / \tau_{*c\text{-}model} < 1$. We took the median $\tau_{*c\text{-}field} / \tau_{*c\text{-}model}$ value as a proxy for the general degree to which a specific effect increases or decreases critical Shields stress according to the model. Slope-dependent hydraulics and form drag generally led to increased critical Shields stress compared to that which is expected without these effects (median $\tau_{*c\text{-}field} / \tau_{*c\text{-}model}$ of 2.9 and 1.8, respectively). Size-sorted patches caused reduction of critical Shields stress by a factor of 2.3 (median $\tau_{*c\text{-}field} / \tau_{*c\text{-}model}$ of 0.44) compared to that which is expected without patches. For our field data, grain hiding did not cause a substantial change in the median critical Shields stress compared to that which is expected without grain hiding, because the effect is only significant at the tails of the distribution (i.e. $D/k_s \neq 1$). However, grain hiding is statistically significant by both the Kolmogorov-Smirnov (Fig. 2.13d) and *t*-test (Fig. 2.14) when examining the entire data set.

2.7. Discussion

2.7.1 Controls on incipient motion, patch evolution, and partial transport

We found that accounting for the effects of slope-dependent hydraulics, grain hiding, and local variation in grain size and bed roughness due to sediment-size sorted patches yielded critical Shields stress predictions that matched our field data within a factor of ~3. Accounting for slope-dependent hydraulics and local roughness variation due to patches appeared to have the strongest controls on predicting incipient motion for our field data for grains with $D/k_s \approx 1$, although, these effects have opposite influences on critical Shields stress (Fig. 2.15).

The influence of slope-dependent hydraulics generally resulted in increased critical Shields stress as shown by our field data to model comparison (Figs. 2.13 and 2.15) as well as other field data (e.g., Mao et al., 2008; Mueller et al., 2005) and theory (e.g., Ferguson, 2012; Lamb et al., 2008b; Recking, 2009). This heightened τ_{*c} may help explain why sediment-transport equations tend to over-predict bedload flux by greater than an order of magnitude in steep streams (Yager et al., 2012b).

The presence of size-sorted patches generally led to decreased critical Shields stresses compared to those expected without patches in the streams examined here. This is likely due to the fact that local sediment sorting allows for patches of finer material and reduces the influence of grain hiding (e.g., Paola and Seal, 1995), suggesting that sediment transport is sensitive to local variations in bed roughness (which can induce complex feedbacks between bed topography and shear stress distribution (Nelson et al., 2009; Venditti et al., 2010)). Using reach-averaged roughness rather than local roughness can result in erroneous predictions of no sediment transport for cases when sediment transport does occur, thus impacting sediment routing and habitat availability predictions (Fig. 2.13c). While there have been several studies attempting to quantify slope-

dependent hydraulic effects (e.g., Lamb et al., 2008b; Nikora et al., 2001; Recking, 2009) and grain hiding (e.g., Egiazaroff, 1965; Einstein, 1950; Kirchner et al., 1990; Wiberg and Smith, 1987), no such quantification exists for predicting sediment-patch locations in mountain streams, although progress has been made for low gradient channels (Venditti et al., 2010). Grain hiding within patches can both increase or decrease critical Shields stress depending on whether D/k_s is less than or greater than unity, respectively (Fig. 2.14).

Form drag on immobile elements likely exists in the Elder Creek tributaries examined here, and has been shown to influence flow hydraulics and sediment transport in other rivers (e.g., Buffington and Montgomery, 1999; Ferguson, 2007; Rickenmann and Recking, 2011; Yager et al., 2012b); however, correction for form drag on immobile elements did not appear to greatly improve model predictions of critical Shields stress to our field data, which may indicate that form drag has a smaller influence on incipient motion than the other effects examined.

Accounting for local roughness length scales, slope-dependent hydraulics, and grain hiding, allows predictions for specific areas of the bed (i.e., specific patches) and grain-size distributions (i.e., specific grain sizes within a patch) which will be active as a function of bed shear stress during modest discharge events. In steep streams with distinct patches of different size sediment, and where grain hiding is important (i.e. $\gamma < 1$), such calculations result in predictions of both reach-wide partial transport of sediment and partial transport within individual patches. Reach-wide partial transport is common in moderate gradient and steep gravel-bed streams (Church and Hassan, 2002; Gomi and Sidle, 2003; Haschenburger and Wilcock, 2003; Hassan and Church, 2001; Mao and

Lenzi, 2007; Thompson and Croke, 2008; Yager et al., 2012a), and was observed in the tributaries examined here (Fig. 2.9). Partial transport within patches has been documented by *Yager et al.* (2012a) in two high gradient streams (S = 5% and 9.8%), and is also observed for patches in this study. Both reach-wide and patch-scale partial transport of sediment during moderate discharge events in steep streams may be a result of grain hiding and the presence of distinct size-sorted patches across the bed.

In addition to influencing grain entrainment, patches likely also play a role in grain deposition. We observed near constant median grain sizes of patches over the monitoring period, suggesting mobilized grains were replaced by sediment of similar sizes (Fig. 2.8). This process of grain replacement with unchanging patch grain-size distribution and areal extent has been observed previously in streams up to S = 9.8% (Yager et al., 2012a) and other lower gradient gravel-bed streams (Dietrich et al., 2006; Yuill et al., 2010), but has not been documented in channels with slopes up to 37% examined here. Such observations lend support to arguments for patch evolution via feedbacks between bed topography, bed shear stress, and sediment transport (Nelson et al., 2009; Venditti et al., 2010).

During very large floods the coupling between local roughness, patch evolution, and sediment transport is likely disrupted via reorganization of the channel bed and resetting of the local roughness length scale. Studies in the Erlenbach River, Switzerland (S = 9.8%), for example, showed partial transport under modest flow conditions, and bed reorganization, boulder mobilization, and the destruction of step-pool morphology in extreme events (discharges with 25-50 year recurrence intervals) (Turowski et al., 2009; Yager et al., 2012a). This also has been documented in other moderate to high gradient

rivers where mobilization of grains greater than the median-grain size only occurs during floods of recurrence intervals greater than 5 to 10 years (Haschenburger and Wilcock, 2003; Mao and Lenzi, 2007; Thompson and Croke, 2008). We expect to find bed reorganization and mobilization of all grains in very large floods in the tributaries examined here, although it is possible large grains are only moved in debris flow events and subsequent fluvial action may undermine these grains and abrade them in place.

2.7.2 Influence of fluvial processes in steep streams on landscape evolution

Data on incipient motion and patch development in high gradient streams are rare, and this is the first attempt, to our knowledge, to document field-based critical Shields values for streams with $S > 14\%$. While it is often assumed that steep streams are dominated by debris flow processes (e.g., Stock and Dietrich, 2003; Stock and Dietrich, 2006), we found that fluvial processes active at moderate gradient gravel-bedded streams ($S \approx$ 1-5%) occurred in the steep streams examined here ($S > 5\%$); although often only a select fraction of the bed was mobilized as the reaches experienced partial transport of sediment. These results show fluvial processes play a key role in transporting gravel downstream during storms in very steep channels (at least up to 37% slope), with implications for sediment routing models and habitat assessment for aquatic organisms (which often have distinct relationships with the local substrate (e.g., Lisle, 1989)).

While our results show fluvial sediment transport occurs, it is difficult to assess the relative importance of fluvial versus debris flow processes over landscape evolution timescales in our study area. Almost all of the tributaries joining Elder Creek are incised into debris flow fans, which often have boulders larger than one meter in diameter. These

entrenched channels with imbricated cobbles suggest that fluvial processes entrain and transport material from debris flow deposits (and gravel entering the river between debris flow events) to lower gradient streams within the Elder Creek watershed. Fluvial and debris flow processes likely occur over different time scales in the tributaries monitored here, with fluvial mobilization of gravel on an annual basis, and intermittent debris flow activity occurring over centuries to millennia (Scheingross et al., 2008).

2.8. Conclusions

We monitored mobilization of sediment in five small (drainage areas of 0.04 to 2 km^2) and steep (S = 5 – 37%) tributaries of Elder Creek, CA. Our results show smaller grains tended to travel further distances than larger grains and sediment patches tended to maintain near constant median grain sizes temporally. There was partial transport of sediment both reach-wide and within individual patches, indicating that large portions of the bed (usually composed of large grains) are immobile during modest flow conditions. Flow resistance was similar to that predicted by *Ferguson* [2007] where the friction factor increased with increasing relative roughness. Using three different methods to calculate form drag on immobile elements, we found that form drag on immobile structures accounted for approximately 80% of the total bed stress, with the remaining 20% of the total bed stress available for sediment transport. Field-estimated values of the Shields stress at incipient motion range from 0.02 to 2 and agree with theoretical predictions within a factor of ~3 when slope-dependent changes in flow hydraulics, sediment-size sorted patches, and grain hiding effects were taken into account. We saw

no improvement of model predictions when including the effect of form drag, suggesting form drag influences critical Shields stress less than the other effects examined. Slope-dependent hydraulics and the presence of patches had the strongest (although opposite) influence on incipient motion, resulting in increased and decreased τ_{*c}, respectively. For grains smaller or larger than roughness length scale, grain hiding influenced incipient motion. Larger grains tended to move at higher shear stresses leading to partial transport both within patches and reach-wide.

Our results suggest that accounting for the effects of local variation in roughness due to patches, slope-dependent hydraulics, and grain hiding allows for prediction of both specific patches that will be active, and for the approximate grain size distribution mobilized from patches as a function of bed shear stress. Such predictions offer an improvement over traditional methods (i.e., assuming $\tau_{*c} \approx 0.045$ and that all grains are mobilized at the same time), and should be useful for sedimentation engineering, stream restoration efforts, and predictions of aquatic habitat availability. In very steep channels, often considered to be dominated by debris flows, our results show that fluvial sediment transport occurs even for modest flows with implications for sediment routing and landscape evolution.

2.9 Notation:

C_m – drag coefficient for mobile sediment [dimensionless].
D – grain size [L].
D_{16}, D_{50}, D_{84} – grain size for which 16, 50, and 84%, respectively, of the grain size distribution is finer [L].
$D_{50\text{-}patch}$ – grain size for which 50% of the grain size distribution of a patch is finer [L].
$D_{50\text{-}reach}$ – grain size for which 50% of the grain size distribution reach-wide is finer [L].
$D_{84\text{-}mobile}$ – grain size for which 84% of the mobile sediment reach-wide is finer [L].
D_{1meter} – mass weighted geometric mean grain diameter of particles transported < 1 m from a patch [L].

D_{max} – maximum grain size moved from a patch [L].
f – Darcy-Weisbach friction factor [dimensionless].
g – acceleration due to gravity [L T^{-2}].
h – reach-averaged flow depth [L].
k_s – roughness length scale [L].
L – tracer particle travel distance [L].
L_{D50} – Expected travel distance for a grain with the median diameter grain size based on a power law fit to L versus D [L].
R – reach-averaged hydraulic radius [L].
S – channel gradient [dimensionless].
U – reach-averaged flow velocity [L T^{-1}].
u_* – bed shear velocity [L T^{-1}].
γ – hiding function constant [dimensionless].
ρ – fluid density [M L^{-3}].
ρ_s – sediment density [M L^{-3}].
τ – bed shear stress [M L^{-2} T^{-2}].
τ_{max} – bed shear stress at peak stage height [M L^{-2} T^{-2}].
τ_c – critical bed shear stress [M L^{-2} T^{-2}].
τ_{fd} – bed shear stress borne on immobile morphologic structures [M L^{-2} T^{-2}].
τ_{ks} – critical bed shear stress for the median grain size [M L^{-2} T^{-2}].
τ_m – shear stress borne on the mobile sediment [M L^{-2} T^{-2}].
τ_T – total bed shear stress [M L^{-2} T^{-2}].
τ_{*c} – critical bed Shields stress [dimensionless].
$\tau_{*c\text{-}field}$ – field-estimated values of critical bed Shields stress [dimensionless].
$\tau_{*c\text{-}model}$ - model-predicted values of critical bed Shields stress [dimensionless].

2.10 Acknowledgements:

Support for this work came from the National Center for Earth-Surface Dynamics, NASA BioMars Grant to WED, the Charles H. Ramsden Endowed Fund to JSS, and NSF EAR-0922199 grant to MPL. JSS was partially supported by an NSF Graduate Research Fellowship. We thank Toby Minear for assistance with terrestrial LiDAR scanning. Airborne laser swath mapping data were provided by the National Center for Airborne Laser Mapping. Jonathan Perkins, Peter Nelson, Kathleen Swanson, Jasper Oshun, Eric Kleinsasser, Alessandro Uccelli, Sam Peach, Colin Phillips, Evan Scheingross, Matt Stuckey, and Clark Winchell assisted with field work. We thank Peter Steel for facilitating land access and logistical support at the University of California's Angelo Coast Range Reserve. This manuscript greatly benefited from constructive reviews by Dieter Rickenmann, André Zimmermann, and an anonymous reviewer, as well as editing by Alexander Densmore and John Pitlick.

2.11 References:

Andrews, E. D. (1983), Entrainment of gravel from naturally sorted riverbed material, *Geological Society of America Bulletin*, *94*(10), 1225-1231.

Ashida, K., and M. Bayazi (1973), Initiation of motion and roughness of flows in steep channels, *International Association of Hydraulic Research Proceedings 15th Congress, Istanbul, Turkey*, *1*, 475-484.

Bathurst, J. C., H. H. Cao, and W. H. Graf (1984), Hydraulics and sediment transport in a steep flume. Data from the EPFL study, *Rep. 64*, Institute of Hydrology, Wallingford, Oxon, England.

Benda, L., M. A. Hassan, M. Church, and C. L. May (2005), Geomorphology of steepland headwaters: The transition from hillslopes to channels, *Journal of the American Water Resources Association*, *41*(4), 835-851.

Brayshaw, A. C., L. E. Frostick, and I. Reid (1983), The hydrodynamics of particle clusters and sediment entrainment in coarse alluvial channels, *Sedimentology*, *30*(1), 137-143, doi:10.1111/j.1365-3091.1983.tb00656.x.

Buffington, J. M., and D. R. Montgomery (1997), A systematic analysis of eight decades of incipient motion studies, with special reference to gravel-bedded rivers, *Water Resources Research*, *33*(8), 1993-2029, doi:10.1029/96WR03190.

Buffington, J. M., and D. R. Montgomery (1999), Effects of hydraulic roughness on surface textures of gravel-bed rivers, *Water Resources Research*, *35*(11), 3507-3521, doi:10.1029/1999WR900138.

Buffington, J. M., D. R. Montgomery, and H. M. Greenberg (2004), Basin-scale availability of salmonid spawning gravel as influenced by channel type and hydraulic roughness in mountain catchments, *Canadian Journal of Fisheries and Aquatic Sciences*, *61*(11), 2085-2096, doi:10.1139/f04-141.

Bunte, K., and S. R. Abt (2001), Sampling surface and subsurface particle-size distributions in wadable gravel- and cobble-bed streams for analyses in sediment transport, hydraulics, and streambed monitoring, *Rep. RMRS-GTR-74*, United States Department of Agriculture, Rocky Mountain Research Station, Fort Collins, CO.

Calkins, D., and T. Dunne (1970), A salt tracing method for measuring channel velocities in small mountain streams, *Journal of Hydrology*, *11*, 379-392.

Church, M., and M. A. Hassan (1992), Size and distance of travel of unconstrained clasts on a streambed, *Water Resources Research*, *28*(1), 299-303, doi:10.1029/91WR02523.

Church, M., and M. A. Hassan (2002), Mobility of bed material in Harris Creek, *Water Resources Research*, *38*(11), doi:10.1029/2001wr000753.

Comiti, F., and L. Mao (2012), Recent advances in the dynamics of steep channels, in *Gravel-bed rivers: Processes, tools, environments*, edited by M. Church, P. M. Biron and A. G. Roy, Wiley-Blackwell, Chichester.

Cui, Y. T., and G. Parker (2005), Numerical model of sediment pulses and sediment-supply disturbances in mountain rivers, *Journal of Hydraulic Engineering-Asce*, *131*(8), 646-656, doi:10.1061/(asce)0733-9429(2005)131:8(646).

Day, T. J. (1977a), Field procedures and evaluation of a slug dilution gauging method in mountain streams, *Journal of Hydrology New Zealand*, *16*(2), 113-133.

Day, T. J. (1977b), Observed mixing lengths in mountain streams, *Journal of Hydrology*, *35*(1-2), doi:10.1016/0022-1694(77)90081-6.

Dietrich, W. E., D. G. Bellugi, L. S. Sklar, J. D. Stock, A. M. Heimsath, and J. J. Roering (2003), Geomorphic transport laws for predicting landscape from and dynamics, in *Prediction in geomorphology*, edited by P. R. Wilcock and R. Iverson, American Geophysical Union, Washington DC.

Dietrich, W. E., P. A. Nelson, E. Yager, J. G. Venditti, M. P. Lamb, and L. Collins (2006), Sediment patches, sediment supply, and channel morphology, in *River, coastal and estuarine morphodynamics, RCEM 2005*, edited by G. Parker and M. H. Garcia, pp. 79-90, Taylor and Francis/Balkema, The Netherlands.

Egiazaroff, I. V. (1965), Calculation of non-uniform sediment concentrations, *Journal of Hydraulic Engineering*, *91*(4), 225-248.

Einstein, H. A. (1950), The bedload function for sediment transport in open channel flows, *Rep. Technical Bulletin no. 1026*, US Department of Agriculture, Washington DC.

Elder, K., R. Kattelmann, and R. Ferguson (1990), Refinements in dilution gauging for mountain streams, in *Hydrology in mountainous regions, I - hydrological measurements; the water cycle*, Proceedings of two Lausanne Symposia, IAHS Publication no. 193.

Ferguson, R. (2007), Flow resistance equations for gravel- and boulder-bed streams, *Water Resources Research*, *43*(5), doi:10.1029/2006wr005422.

Ferguson, R. I. (2012), River channel slope, flow resistance, and gravel entrainment thresholds, *Water Resources Research*, *48*, doi:10.1029/2011wr010850.

Ferguson, R. I., and S. J. Wathen (1998), Tracer-pebble movement along a concave river profile: Virtual velocity in relation to grain size and shear stress, *Water Resources Research*, *34*(8), 2031-2038, doi:10.1029/98WR01283.

Fuller, T. K., L. A. Perg, J. K. Willenbring, and K. Lepper (2009), Field evidence for climate-driven changes in sediment supply leading to strath terrace formation, *Geology*, *37*(5), 467-470, doi:10.1130/g25487a.1.

Gomi, T., and R. C. Sidle (2003), Bed load transport in managed steep-gradient headwater streams of southeastern Alaska, *Water Resources Research*, *39*(12), doi:10.1029/2003wr002440.

Grant, G. E., F. J. Swanson, and M. G. Wolman (1990), Pattern and origin of stepped-bed morphology in high-gradient streams, western Cascades, Oregon, *Geological Society of America Bulletin*, *102*(3), 340-352, doi:10.1130/0016-7606(1990)102<0340:paoosb>2.3.co;2.

Haschenburger, J. K., and P. R. Wilcock (2003), Partial transport in a natural gravel bed channel, *Water Resources Research*, *39*(1), doi:10.1029/2002wr001532.

Hassan, M. A., and M. Church (2001), Sensitivity of bed load transport in Harris Creek: Seasonal and spatial variation over a cobble-gravel bar, *Water Resources Research*, *37*(3), 813-825, doi:10.1029/2000WR900346.

Hodge, R. A., T. B. Hoey, and L. S. Sklar (2011), Bed load transport in bedrock rivers: The role of sediment cover in grain entrainment, translation, and deposition, *Journal of Geophysical Research-Earth Surface*, *116*, doi:10.1029/2011jf002032.

Holmes, R. R., Jr., P. J. Terrio, M. A. Harris, and P. C. Mills (2001), Introduction to field methods for hydrologic and environmental studies, US Geological Survey Open-file report 01-50, Urbana, Illinois.

Hudson, R., and J. Fraser (2005), Introduction to salt dilution gauging for streamflow measurement part IV: The mass balance (or dry injection) method, *Streamline Watershed Management Bulletin*, *9*(1), 6-12.

Jayko, A. S., M. C. Blake, R. J. McLaughlin, H. N. Ohlin, S. D. Ellen, and H. M. Kelsey (1989), Reconnaissance geologic map of the Covelo 30- by 60- minute quadrangle, northern California, *Rep. Miscenellenous Field Studies Map MF-2001*, scale 1:100,000, United States Geological Survey, Washington, DC.

Kirchner, J. W., W. E. Dietrich, F. Iseya, and H. Ikeda (1990), The variability of critical shear-stress, friction angle, and grain protrusion in water-worked sediments, *Sedimentology*, *37*(4), 647-672.

Lamb, M. P., W. E. Dietrich, and J. G. Venditti (2008a), Is the critical shields stress for incipient sediment motion dependent on channel-bed slope?, *Journal of Geophysical Research-Earth Surface*, *113*(F2), doi:10.1029/2007jf000831.

Lamb, M. P., W. E. Dietrich, and L. S. Sklar (2008b), A model for fluvial bedrock incision by impacting suspended and bed load sediment, *Journal of Geophysical Research-Earth Surface*, *113*(F3), doi:10.1029/2007jf000915.

Lenzi, M. A. (2004), Displacement and transport of marked pebbles, cobbles and boulders during floods in a steep mountain stream, *Hydrological Processes*, *18*(10), 1899-1914, doi:10.1002/hyp.1456.

Lenzi, M. A., L. Mao, and F. Comiti (2006), When does bedload transport begin in steep boulder-bed streams?, *Hydrological Processes*, *20*(16), 3517-3533, doi:10.1002/hyp.6168.

Lisle, T. E. (1989), Sediment transport and resulting deposition in spawning gravels, north coastal California, *Water Resources Research*, *25*(6), 1303-1319, doi:10.1029/WR025i006p01303.

Mao, L., and M. A. Lenzi (2007), Sediment mobility and bedload transport conditions in an alpine stream, *Hydrological Processes*, *21*(14), 1882-1891, doi:10.1002/hyp.6372.

Mao, L., G. P. Uyttendaele, A. Iroume, and M. A. Lenzi (2008), Field based analysis of sediment entrainment in two high gradient streams located in alpine and andine environments, *Geomorphology*, *93*(3-4), 368-383, doi:10.1016/j.geomorph.2007.03.008.

Marcus, W. A., K. Roberts, L. Harvey, and G. Tackman (1992), An evaluation of methods for estimating Mannings-n in small mountain streams, *Mountain Research and Development*, *12*(3), 227-239.

Mast, M. A., and D. W. Chow (2000), Environmental characteristics and water-quality of hydrologic benchmark network stations in the Western United States, *Rep. 1173-D*, United States Geological Survey, Washington, DC.

Meyer-Peter, E., and R. Muller (1948), Formulas for bed-load transport, *Proc. of the 2nd Congress of the Internaional Association for Hydraulic Structures Research*, Stockholm, 39-64.

Millar, R. G. (1999), Grain and form resistance in gravel-bed rivers, *Journal of Hydraulic Research*, *37*(3), 303-312.

Mizuyama, T. (1977), Bedload transport in steep channels, Ph.D. dissertation thesis, Kyoto University, Kyoto, Japan.

Montgomery, D. R. (2004), Geology, geomorphology, and the restoration ecology of salmon, *GSA Today*, *14*(11), 4-12.

Montgomery, D. R., and J. M. Buffington (1997), Channel-reach morphology in mountain drainage basins, *Geological Society of America Bulletin*, *109*(5), 596-611.

Moore, R. D. (2003), Introduction to salt dilution gauging for streamflow measurement: Part 1, *Streamline Watershed Management Bulletin*, *7*(4), 20-23.

Mueller, E. R., J. Pitlick, and J. M. Nelson (2005), Variation in the reference shields stress for bed load transport in gravel-bed streams and rivers, *Water Resources Research*, *41*(4), doi:10.1029/2004WR003692.

Nelson, P. A., W. E. Dietrich, and J. G. Venditti (2010), Bed topography and the development of forced bed surface patches, *Journal of Geophysical Research-Earth Surface*, *115*, doi:10.1029/2010jf001747.

Nelson, P. A., J. G. Venditti, W. E. Dietrich, J. W. Kirchner, H. Ikeda, F. Iseya, and L. S. Sklar (2009), Response of bed surface patchiness to reductions in sediment supply, *Journal of Geophysical Research-Earth Surface*, *114*, doi:10.1029/2008jf001144.

Nikora, V., D. Goring, I. McEwan, and G. Griffiths (2001), Spatially averaged open-channel flow over rough bed, *Journal of Hydraulic Engineering-Asce*, *127*(2), doi:10.1061/(asce)0733-9429(2001)127:2(123).

Nitsche, M., D. Rickenmann, J. M. Turowski, A. Badoux, and J. W. Kirchner (2011), Evaluation of bedload transport predictions using flow resistance equations to account for macro-roughness in steep mountain streams, *Water Resources Research*, *47*, doi:10.1029/2011wr010645.

Paola, C., and R. Seal (1995), Grain-size patchiness as a cause of selective deposition and downstream fining, *Water Resources Research*, *31*(5), 1395-1407, doi:10.1029/94WR02975.

Parker, G. (2008), Transport of gravel and sediment mixtures, in *Sedimentation engineering processes, measurements, modeling, and practice*, edited by M. H. Garcia, American Society of Civil Engineers.

Prancevic, J. P., M. P. Lamb, and B. M. Fuller (2011), Assessing the slope dependency of the critical shields stress in very steep streams using laboratory flume experiments, abstract EP21C-0708, paper presented at 2011 Fall Meeting, AGU, San Francisco, Calif. 5-9 Dec.

Recking, A. (2009), Theoretical development on the effects of changing flow hydraulics on incipient bed load motion, *Water Resources Research*, *45*, doi:10.1029/2008wr006826.

Rickenmann, D., and A. Recking (2011), Evaluation of flow resistance in gravel-bed rivers through a large field data set, *Water Resources Research*, *47*, doi:10.1029/2010wr009793.

Rouse, H. (1936), Discharge characteristics of the free overfall, *Civil Engineering*, *6*(4), 257-260.

Scheingross, J. S., J. K. Willenbring, and W. E. Dietrich (2008), Erosion rates and debris flow history reconstruction: A comparsion of carbon and cosmogenic nuclide dating techniques, *Eos Trans. AGU, 89(53), Fall Meet. Suppl., Abstract H51D-0852*.

Shields, A. (1936), Anwendung der aehnlichkeitsmechanik und der turbulenzforschung auf die geschiebebewegung, *Mitt. Preuss. Versuchsanst. Wasserbau Schiffbau*, *26*(26).

Sklar, L. S., and W. E. Dietrich (2004), A mechanistic model for river incision into bedrock by saltating bed load, *Water Resources Research*, *40*(6), doi:10.1029/2003wr002496.

Stock, J., and W. E. Dietrich (2003), Valley incision by debris flows: Evidence of a topographic signature, *Water Resources Research*, *39*(4), doi:10.1029/2001wr001057.

Stock, J. D., and W. E. Dietrich (2006), Erosion of steepland valleys by debris flows, *Geological Society of America Bulletin*, *118*(9-10), 1125-1148, doi:10.1130/b25902.1.

Thompson, C., and J. Croke (2008), Channel flow competence and sediment transport in upland streams in southeast Australia, *Earth Surface Processes and Landforms*, *33*(3), 329-352, doi:10.1002/esp.1558.

Tsai, V. C., B. Minchew, M. P. Lamb, and J.-P. Ampuero (2012), A physical model for seismic noise generation from sediment transport in rivers, *Geophysical Research Letters*, *39*, doi:10.1029/2011gl050255.

Tucker, G. E., and G. R. Hancock (2010), Modelling landscape evolution, *Earth Surface Processes and Landforms*, *35*(1), 28-50, doi:10.1002/esp.1952.

Turowski, J. M., E. M. Yager, A. Badoux, D. Rickenmann, and P. Molnar (2009), The impact of exceptional events on erosion, bedload transport and channel stability in a step-pool channel, *Earth Surface Processes and Landforms*, *34*(12), 1661-1673, doi:10.1002/esp.1855.

Whipple, K. X. (2004), Bedrock rivers and the geomorphology of active orogens, *Annual Review of Earth and Planetary Sciences*, *32*, 151-185, doi:10.1146/annurev.earth.32.101802.120356.

Wiberg, P. L., and J. D. Smith (1985), A theoretical-model for saltating grains in water, *Journal of Geophysical Research-Oceans*, *90*(NC4), 7341-7354, doi:10.1029/JC090iC04p0734.

Wiberg, P. L., and J. D. Smith (1987), Calculations of the critical shear-stress for motion of uniform and heterogeneous sediments, *Water Resources Research*, *23*(8), 1471-1480, doi:10.1029/WR023i008p01471.

Wiberg, P. L., and J. D. Smith (1991), Velocity distribution and bed roughness in high-gradient streams, *Water Resources Research*, *27*(5), 825-838, doi:10.1029/90wr02770.

Wiele, S. M., P. R. Wilcock, and P. E. Grams (2007), Reach-averaged sediment routing model of a canyon river, *Water Resources Research*, *43*(2), doi:10.1029/2005wr004824.

Wilcock, P. R. (1992), Flow competence - a criticism of a classic concept, *Earth Surface Processes and Landforms*, *17*(3), 289-298, doi:10.1002/esp.3290170307.

Wilcock, P. R. (1997), Entrainment, displacement and transport of tracer gravels, *Earth Surface Processes and Landforms*, *22*(12), 1125-1138,

Yager, E. M., J. W. Kirchner, and W. E. Dietrich (2007), Calculating bed load transport in steep boulder bed channels, *Water Resources Research*, *43*(7), doi:10.1029/2006wr005432.

Yager, E. M., W. E. Dietrich, J. W. Kirchner, and B. W. McArdell (2012a), Prediction of sediment transport in step-pool channels, *Water Resources Research*, *48*, doi:10.1029/2011wr010829.

Yager, E. M., W. E. Dietrich, J. W. Kirchner, and B. W. McArdell (2012b), Patch dynamics and stability in steep, rough streams, *Journal of Geophysical Research-Earth Surface*, *117*, doi:10.1029/2011jf002253.

Yuill, B., M. Nichols, and E. Yager (2010), Coarse bed material patch evolution in low-order, ephemeral channels, *Catena*, *81*(2), 126-136, doi:10.1016/j.catena.2010.02.002.

Zar, J. H. (1999), *Biostatistical analysis*, 4th ed., Prentice Hall, Upper Saddle River, New Jersey.

Table 2.1: Reach-averaged hydraulic geometry and basic characteristics of monitored reaches[a]

Reach	Drainage area (km^2)	Local slope (%)	Bankfull depth (m)	Bankfull width (m)	D_{16} (mm)	D_{50} (mm)	D_{84} (mm)	$D_{84\text{-}mobile}$ (mm)
1	0.04	37	0.13	1.1	10	57	133	45
2	0.12	18	0.15	1.5	21	97	279	145
3	0.55	7[b]	0.15	3.5	15	101	286	143
4	0.84	9	0.3	4.1	23	155	446	197
5 (Misery Creek)	2	5	0.28	3.5	11	72	201	90

[a] D_{16}, D_{50}, and D_{84}, are the 16th, median, and 84th percentile grain sizes, respectively, for reach-averaged pebble counts (including steps and immobile grains). $D_{84\text{-}mobile}$ is the 84th percentile grain size for reach-averaged pebble counts of mobile sediment.

[b] This reach features a ~1 m alluvial step. The local slope below the step is 5% and the local slope above the step is 9%.

Table 2.2: Reach-averaged flow hydraulic measurements[a]

Reach	Date	Discharge (m^3/s)	U (m/s)	h (m)
2	17 Feb 2009	0.0006	0.033	0.03
2	23 Feb 2009	0.014	0.19	0.085
2	24 Feb 2009	0.03	0.25	0.09
2	3 March 2009	0.013	0.16	0.08
4	24 Feb 2009	0.19	0.32	0.21
4	3 March 2009	0.14	0.19	-

[a] U and h are measured reach-averaged flow velocity and flow depth, respectively. Measurements made on 24 February 2009 represent near bankfull discharge.

Table 2.3: Spacing of HEC-RAS channel geometry

Reach	Modeled reach length (m)	Number of longitudinal profile nodes	Number of unique surveyed cross-sections	Average node spacing (m)
1	16.4	30	8	0.55
2	16.6	39	39	0.43
3	16.1	18	9	0.89
4	34.3	20	20	1.72
5 (Misery Creek)	19.8	16	7	1.24

Table 2.4: Transport data for patches in specific sediment transport events[a]

Reach	Patch	Storm	D_{1meter} (mm)	D_{max} (mm)	Number of grains recovered	Number of grains < 1 m from patch	k_s (mm)	τ_{max} (Pa)
1	1a	Winter 2007/2008	37	54	127	49	15.9	178
1	1a	24-Feb-09	7	10	28	27	12.5	329
1	1a	Winter 2009/2010	21	30	15	15	11.5	194
2	2a	Winter 2007/2008	38	112	100	15	50.2	124
2	2a	24-Feb-09	18	19	11	11	30.4	95
2	2a	Winter 2009/2010	-	20	10	0	38.3	106
2	2b	Winter 2007/2008	61	90	90	7	36.7	203
2	2b	25-Dec-08	21	25	19	19	50.3	108
2	2b	24-Feb-09	89	115	125	44	50.3	172
2	2b	Winter 2009/2010	-	110	58	5	52.4	185
3	3a	Winter 2007/2008	-	76	114	3	25.1	104
3	3a	14-Nov-08	14	20	27	27	33.6	12
3	3a	25-Dec-08	19	30	116	79	33.6	19
3	3a	24-Feb-09	57	70	126	13	33.6	28
3	3a	Winter 2009/2010	-	52	51	0	25	52
3	3c	Winter 2007/2008	-	72	26	4	58.8	119
3	3c	25-Dec-08	16	20	8	8	62.7	30
3	3c	24-Feb-09	26	45	109	100	62.7	39
3	3c	Winter 2009/2010	-	48	60	1	40.2	65
4	4a	Winter 2007/2008	-	25	8	1	64.1	204
4	4a	24-Feb-09	11	90	79	57	85.6	176
4	4a	Winter 2009/2010	-	40	9	2	53.4	209
5	5a	Winter 2007/2008	-	48	10	0	38.6	93
5	5a	24-Feb-09	24	35	48	29	33.3	47
5	5a	Winter 2009/2010	-	32	3	0	34.5	82
5	5b	Winter 2007/2008	33	45	51	10	14.1	53
5	5b	24-Feb-09	22	30	71	11	13.5	21
5	5b	Winter 2009/2010	-	130	11	3	19.4	44

[a] D_{1meter} is the the mean grain size of the recovered tracer particles deposited within one meter downstream of the patch, where " - " indicates five or less grains were collected within one meter of the patch and one-meter estimates were not made. D_{max} is maximum grain size recovered from a given patch in a given storm event. k_s is the geometric mean grain size of the patch from where moved grains originated. τ_{max} is HEC-RAS calculated peak shear stress used in calculating critical Shields stress. Listing of individual storm dates (e.g. 24-Feb-09) indicates measurements were made for a specific storm event. Listing of a season (e.g. Winter 2007/2008) indicates measurements integrate multiple storm events over an entire season, with the peak observed discharge event assumed to have transported all the sediment.

Table 2.5: Reach-averaged flow hydraulic data for specific sediment transport events[a]

Reach	Storm	τ_T (Pa)	U (m/s)	R (m)	$R/D_{84\text{-mobile}}$	τ_{fd}/τ_T power-law Cm	τ_{fd}/τ_T mean Cm	τ_{fd}/τ_T VPE Cm
1	Winter 2007/2008	199	0.50	0.08	1.78	0.77	0.72	0.89
1	24-Feb-09	239	0.30	0.05	1.00	0.89	0.92	0.92
1	Winter 2009/2010	222	0.34	0.05	1.21	0.86	0.89	0.91
2	Winter 2007/2008	256	0.48	0.12	0.82	0.68	0.8	0.75
2	25-Dec-08	150	0.20	0.06	0.44	0.83	0.94	0.87
2	24-Feb-09	216	0.37	0.10	0.67	0.75	0.87	0.76
2	Winter 2009/2010	233	0.42	0.11	0.73	0.74	0.85	0.77
3	Winter 2007/2008	185	0.86	0.32	2.24	0.37	0.12	0.73
3	14-Nov-08	231	0.22	0.09	0.59	0.90	0.95	0.9
3	25-Dec-08	202	0.28	0.11	0.78	0.85	0.91	0.87
3	24-Feb-09	172	0.33	0.14	0.95	0.79	0.86	0.85
3	Winter 2009/2010	164	0.51	0.20	1.39	0.63	0.65	0.79
4	Winter 2007/2008	388	0.72	0.26	1.33	0.70	0.71	0.84
4	24-Feb-09	406	0.53	0.20	1.01	0.79	0.85	0.85
4	Winter 2009/2010	388	0.75	0.27	1.37	0.68	0.68	0.83
5	Winter 2007/2008	107	1.05	0.34	3.83	0.14	-1.27	0.71
5	24-Feb-09	108	0.48	0.20	2.22	0.71	0.53	0.89
5	Winter 2009/2010	105	0.91	0.30	3.35	0.25	-0.74	0.74

[a] τ_T, U, and R are reach-averaged bed shear stress, flow velocity, and hydraulic radius calculated with HEC-RAS. $D_{84\text{-mobile}}$ is the 84th percentile reach-averaged mobile grain size, and τ_{fd}/τ_T is fractional form drag for the power-law, mean, and VPE C_m methods (section 2.6.1). Listing of individual storm dates (e.g. 24-Feb-09) indicates measurements were made for a specific storm event. Listing of a season (e.g. Winter 2007/2008) indicates measurements integrate multiple storm events over an entire season, with the peak observed discharge event assumed to have transported all the sediment.

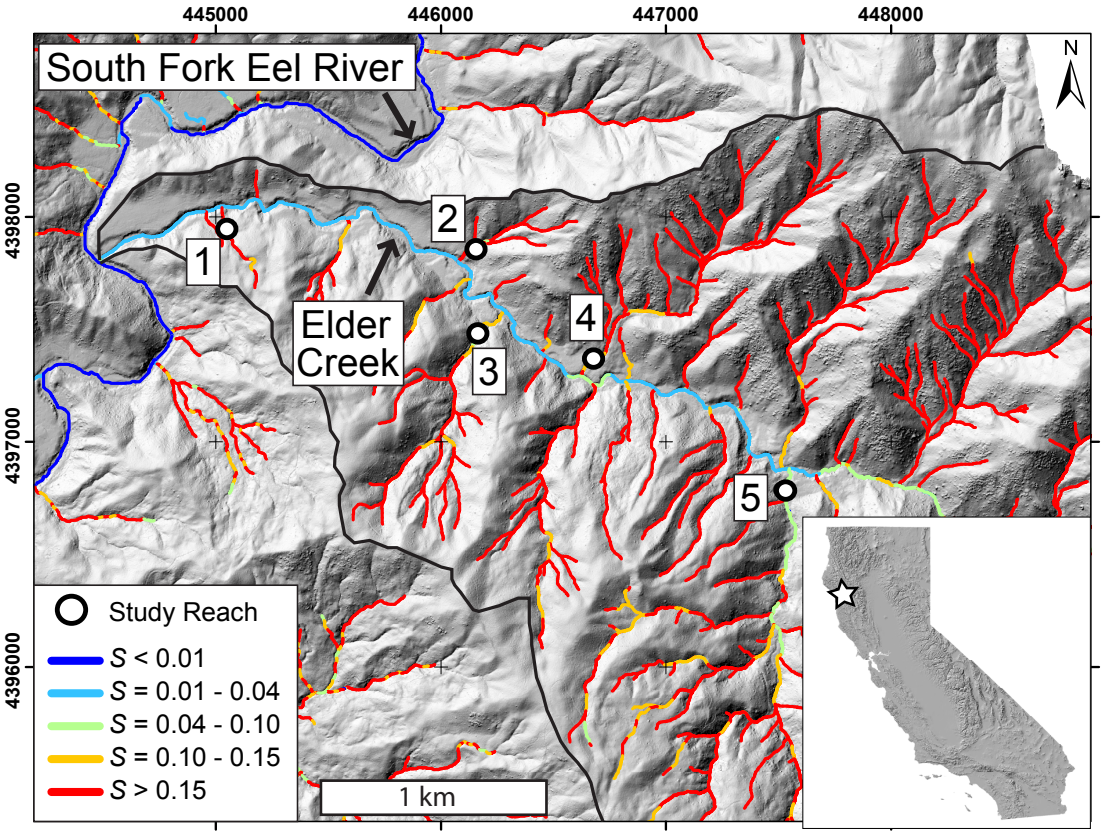

Figure 2.1: Airborne laser swath mapping (1 m^2 resolution) derived shaded relief map showing the Elder Creek watershed and the location of the five tributary reaches we studied (white circles with numbered boxes). The stream network is color coded by channel slope (S) calculated over channel lengths with 10 m change in elevation; note the vast majority of the channel network exists at slopes greater than 15%. UTM coordinates are displayed along figure borders. Inset shows outline of California with star indicating approximate location of the study site.

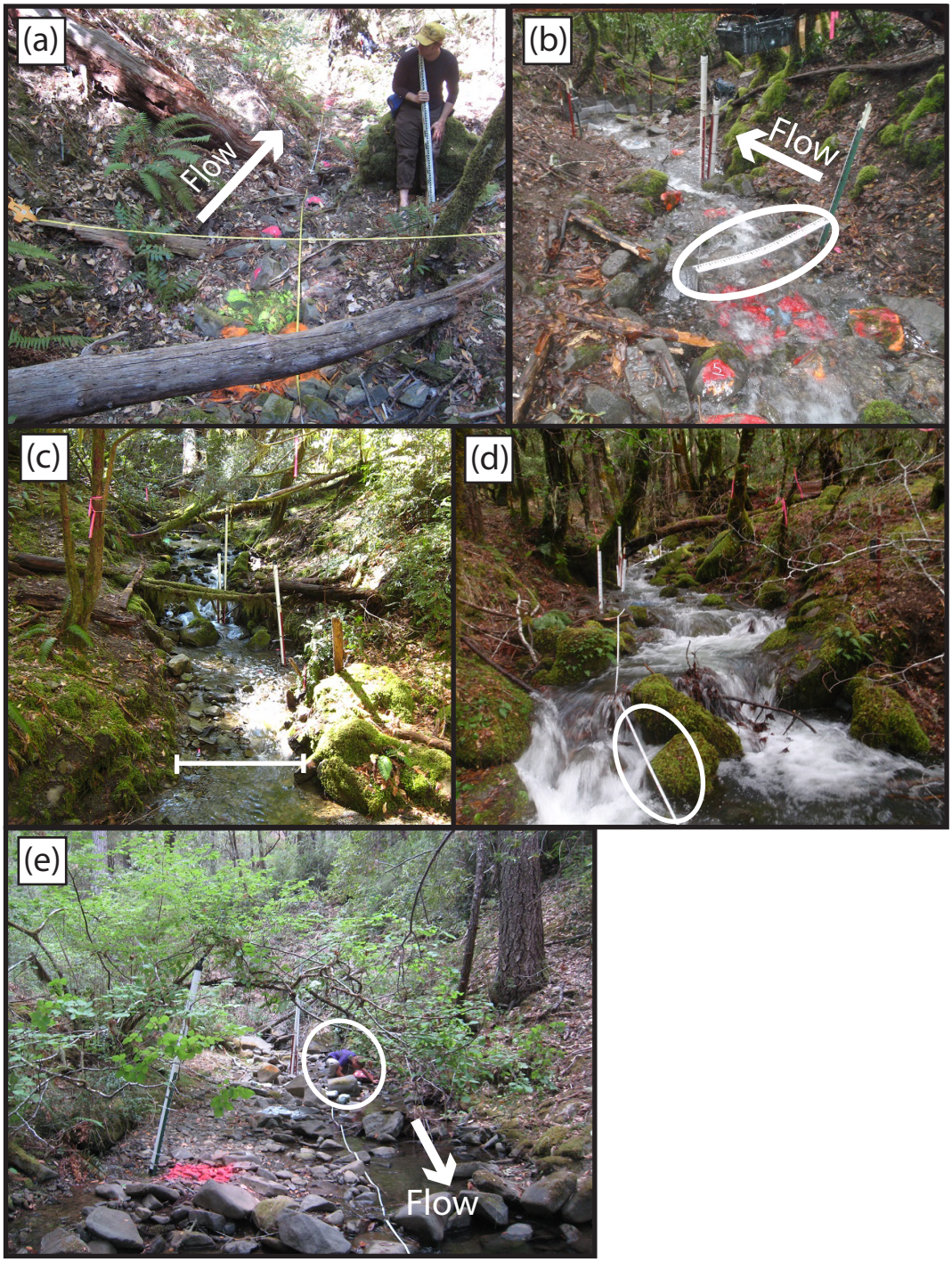

Figure 2.2: Field photographs of study reaches. (a) Reach 1; (b) reach 2, circled staff gage is 1 meter long; (c) reach 3, channel width indicated by white line in foreground is ~2 meters; (d) reach 4, note circled 1.2 cm wide white measuring tape stretched parallel to stream for scale; and (e) reach 5 (Misery Creek), note person (circled, crouching) for scale. Photos (b) and (d) show near bank full conditions. Vertical, white PVC pipes house pressure transducers and crest stage gages measuring water depth.

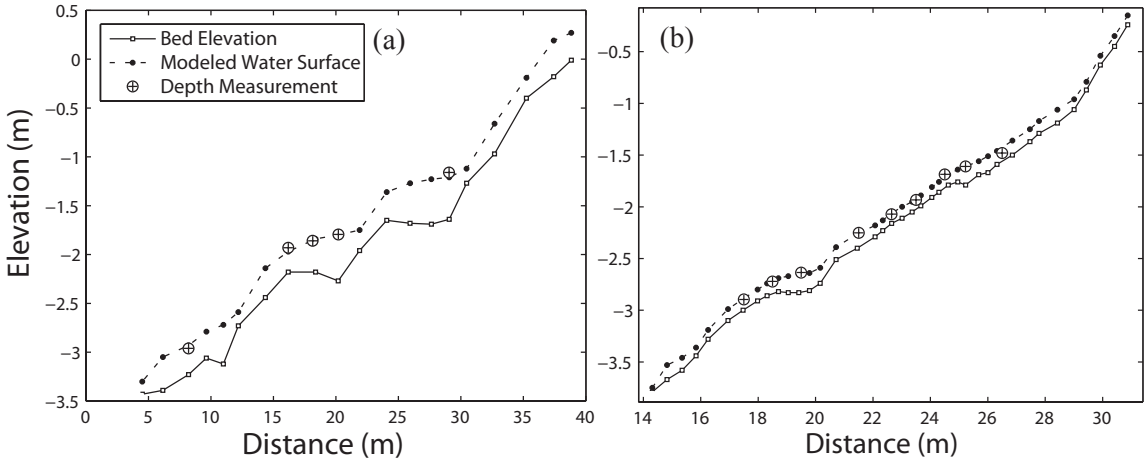

Figure 2.3: Comparison of modeled water surface to flow depth measurements. HEC-RAS modeling for the (a) 3 March 2009 event in reach 2, and (b) the 24 February 2009 event in reach 4. See Table 2.2 for manual flow measurements in each event.

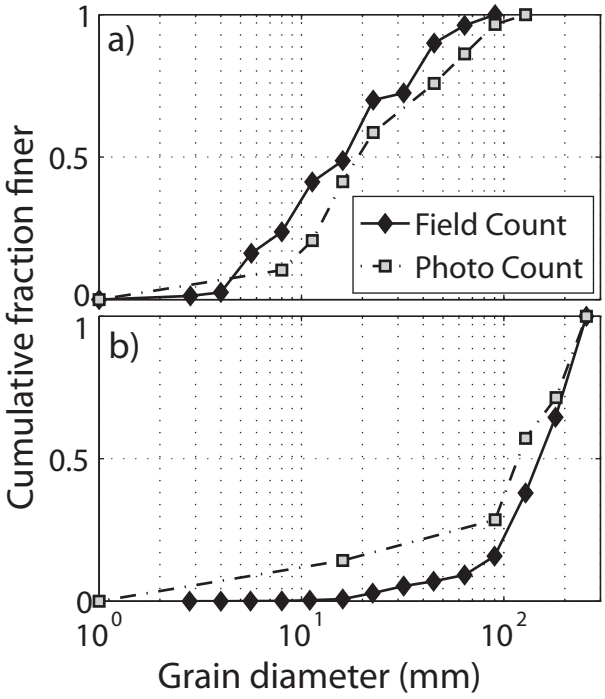

Figure 2.4: Comparison of field and photo-based grid-by-number pebble counts for reach 5, patch 5b (a) and reach 4, patch 4a (b). Median grain sizes generally agree within less than a factor of two, and there is no systematic bias toward over or under predicting grain size distributions with the photograph-based method. Differences in manual and photograph counts should be expected as the exact grains counted in each method were not the same, and the use of a grid-by-number method over a small area limits the total number of grains counted.

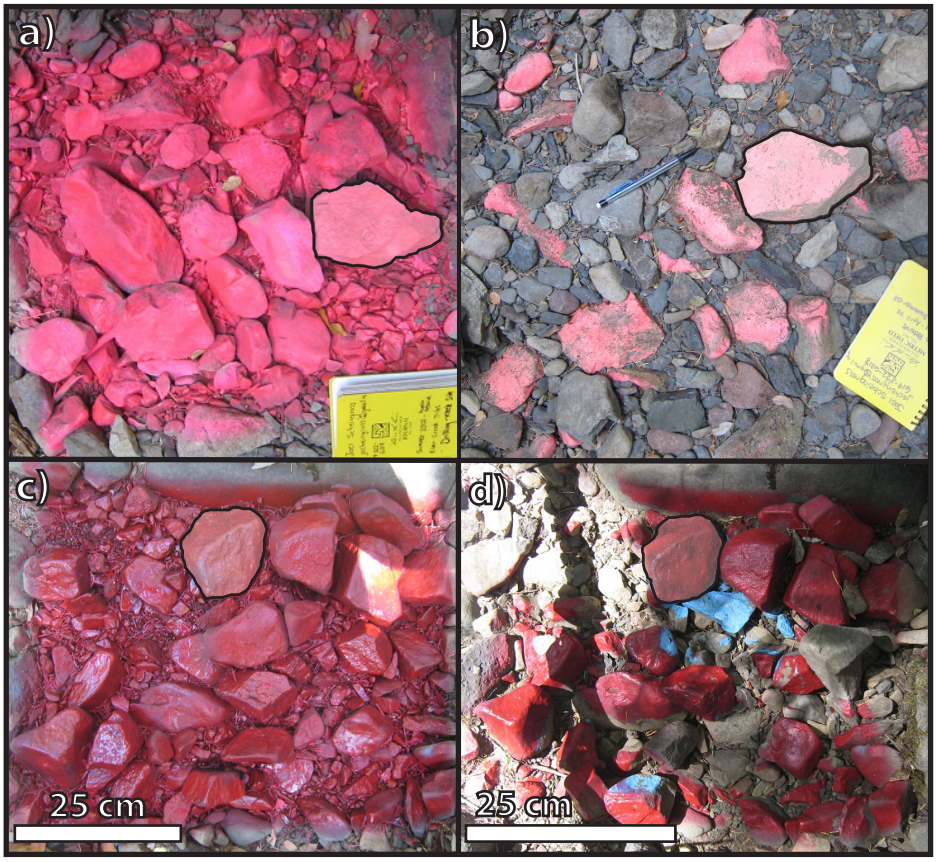

Figure 2.5: (a) Patch 3a (reach 3) immediately after spray painting in summer 2007 and (b) summer 2008 after one year of fluvial transport. (c) Patch 2b (reach 2) in summer 2008 and (d) summer 2009. Blue grains in (d) were painted in summer 2007, buried in winter 2007/2008 (when the patch was painted red), and then re-exposed in winter 2008/2009. Flow is left to right in all images. Yellow notebooks in (a) and (b) are ~18 cm in length, white scale bars are ~25 cm in length in (c) and (d). Black outlined and highlighted grains show a single unmoved grain to help visually orient between photos.

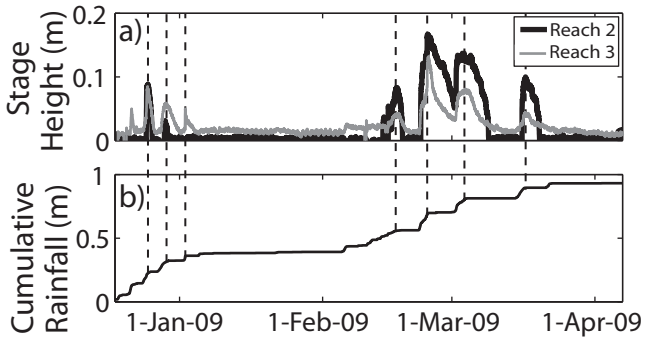

Figure 2.6: (a) Hydrographs of water stage height for reaches 2 and 3 during winter 2008/2009. (b) Cumulative rainfall for the same time period as in (a) from a weather station < 2 km from the Elder Creek watershed. Dashed vertical lines are for reference.

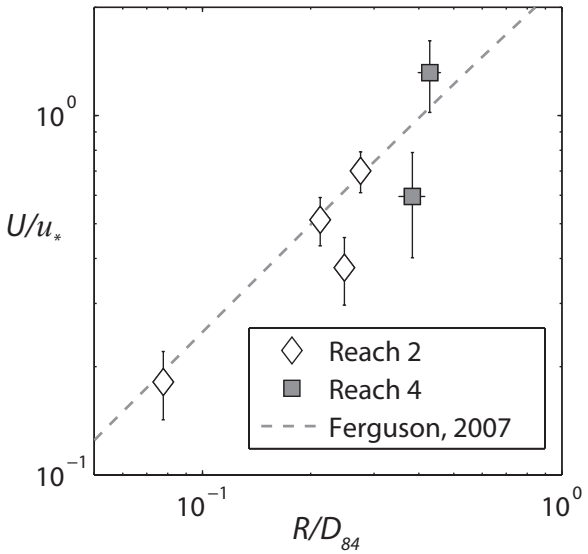

Figure 2.7: Comparison of the HEC-RAS iterated values of U/u_* to those predicted by Ferguson [2007] (eq. 2.2) as a function of R/D_{84}. U, u_*, and R are the reach-averaged flow velocity, shear velocity, and hydraulic radius, respectively, as predicted by HEC-RAS. D_{84} is the grain size for which 84% of the bed is finer (i.e., the reach-averaged D_{84}). Horizontal and vertical error bars show standard error of the mean, error is smaller than the symbol where no error bars are shown.

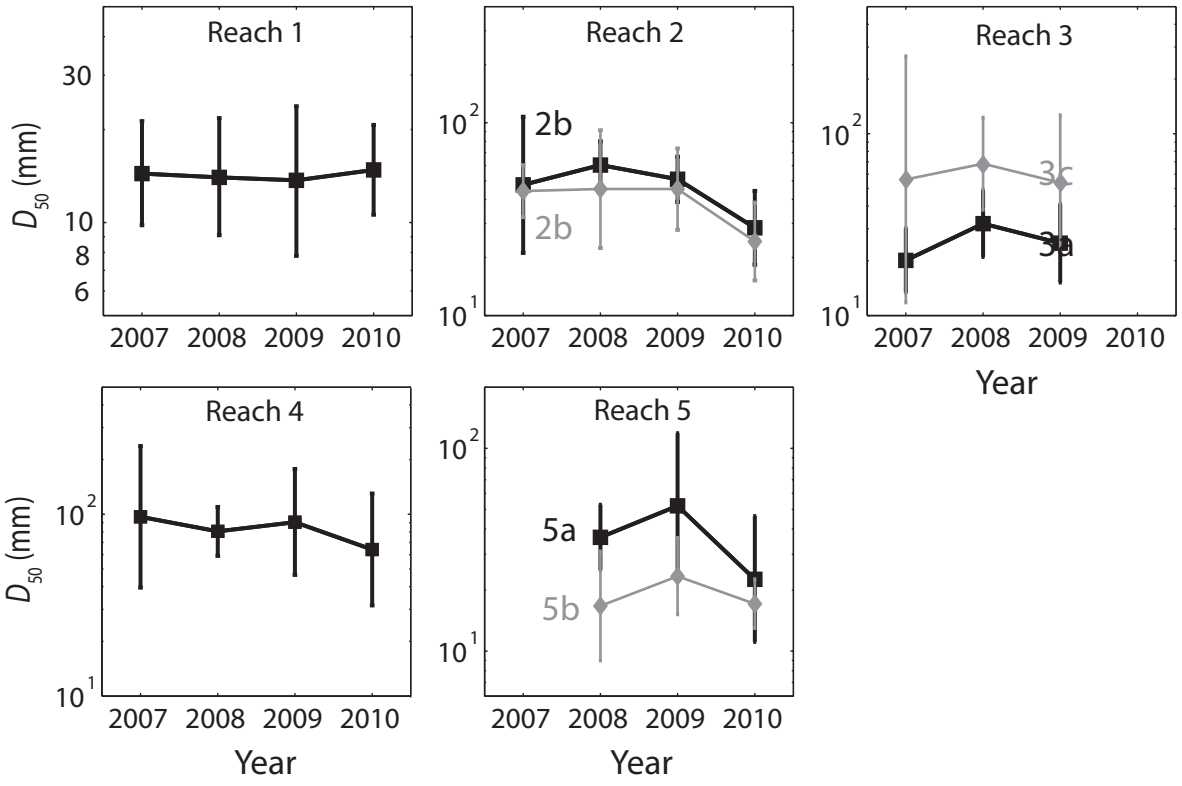

Figure 2.8: Median grain size (D_{50}) and 95% confidence intervals [Bunte and Abt, 2001] for individual patches examined in this study. Each plot represents a different studied reach, and each line series within a plot is a unique patch for the given reach (noted by patch label where appropriate, i.e., "2b" is patch 2b from Table 3).

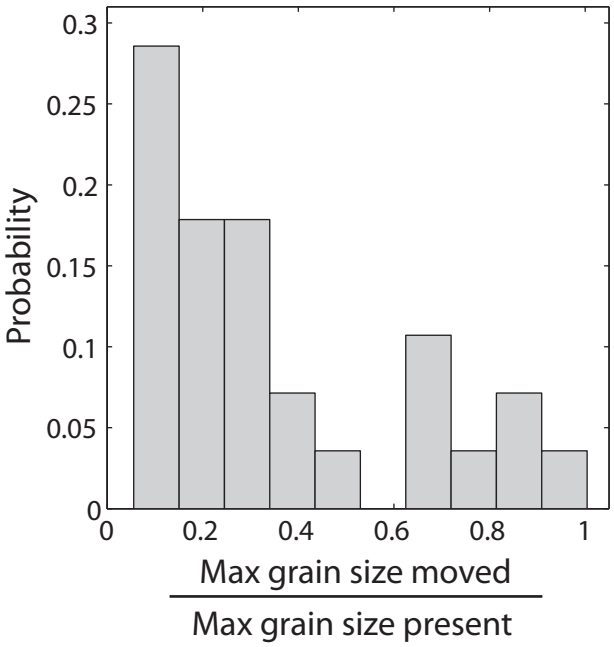

Figure 2.9: Probability distribution of the maximum grain size moved from a patch for a given storm event relative to the maximum grain size available in the patch for movement. This data integrates all observed transport events for each individual patch over the three year study period.

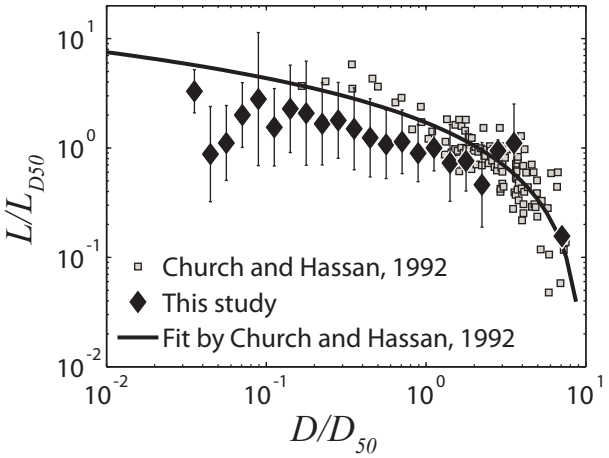

Figure 2.10: Binned relative grain size moved versus relative distance traveled for tracer pebbles in this study (black diamonds) and other studies (gray squares). Error bars are 1 geometric standard deviation of binned data. Solid black line is prediction from Church and Hassan [1992]. L is the travel distance of a single particle, L_{D50} is the expected travel distance of the median grain size based on a power law fit to the data, D is the grain size of the moved particle, and D_{50} is median grain size of the surface (this study) or subsurface (Church and Hassan [1992]).

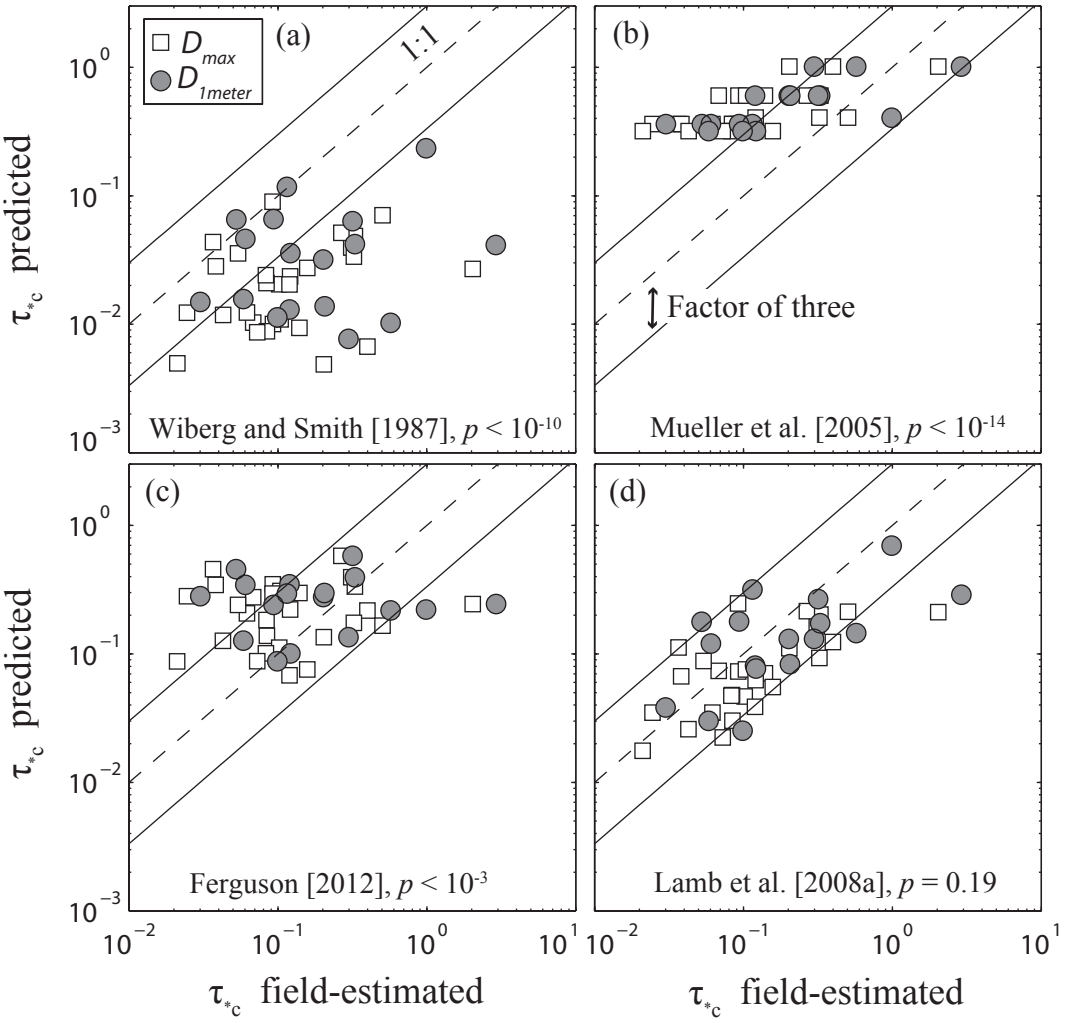

Figure 2.11: Comparison of theoretical and empirical predictions to calculated critical Shields stresses (τ_{*c}). Theories examined include (a) Wiberg and Smith [1987], (b) Mueller et al. [2005], (c) Ferguson [2012] and (d) Lamb et al. [2008a]. In all plots dashed line is 1:1 line and solid lines show factor of three deviation from 1:1 line. Open squares and gray circles are Shields stresses calculated using the flow competence (D_{max}) and one-meter (D_{1meter}) methods, respectively. For Ferguson [2012] predictions, all constants were set to recommended values in Ferguson [2012], D_{84} was set to $D_{84\text{-}mobile}$, D_{50} was set to the D_{50} of the local patch in question, and the HEC-RAS calculated reach-averaged hydraulic radius was used in place of flow depth. For both the Wiberg and Smith [1987] and Lamb et al. [2008a] predictions fractional form drag was set equal to 0. Results of the two sample Kolmogorov–Smirnov test comparing field-estimated vs. model-predicted Shields stress distributions are displayed for each plot, $p < 0.05$ indicates distributions are statistically different at the 5% significance level.

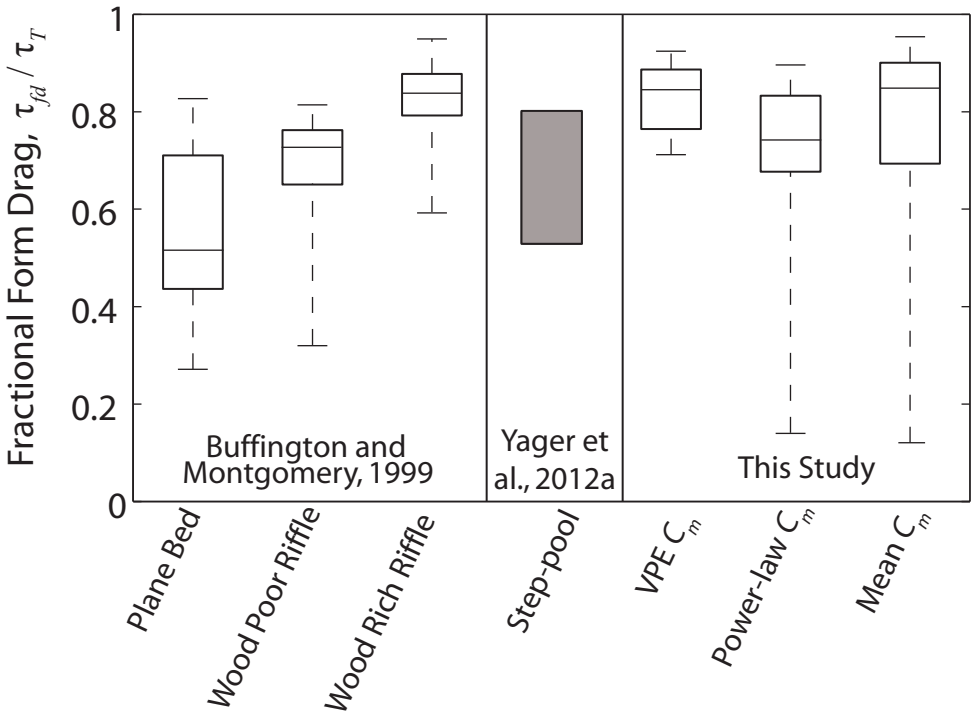

Figure 2.12: Box and whisker plots of fractional form drag (τ_{fd} / τ_T) from different morphology channels in Buffington and Montgomery [1999] and from this study; solid gray box shows range of form drag calculated from Yager et al. [2012a]. For this study, we report fractional form drag ranges using the VPE, power law, and mean C_m methods (see text for details). Boxes bound the data between the 25th to 75th percentile values, the line within the box is the data median, and whiskers show data extent.

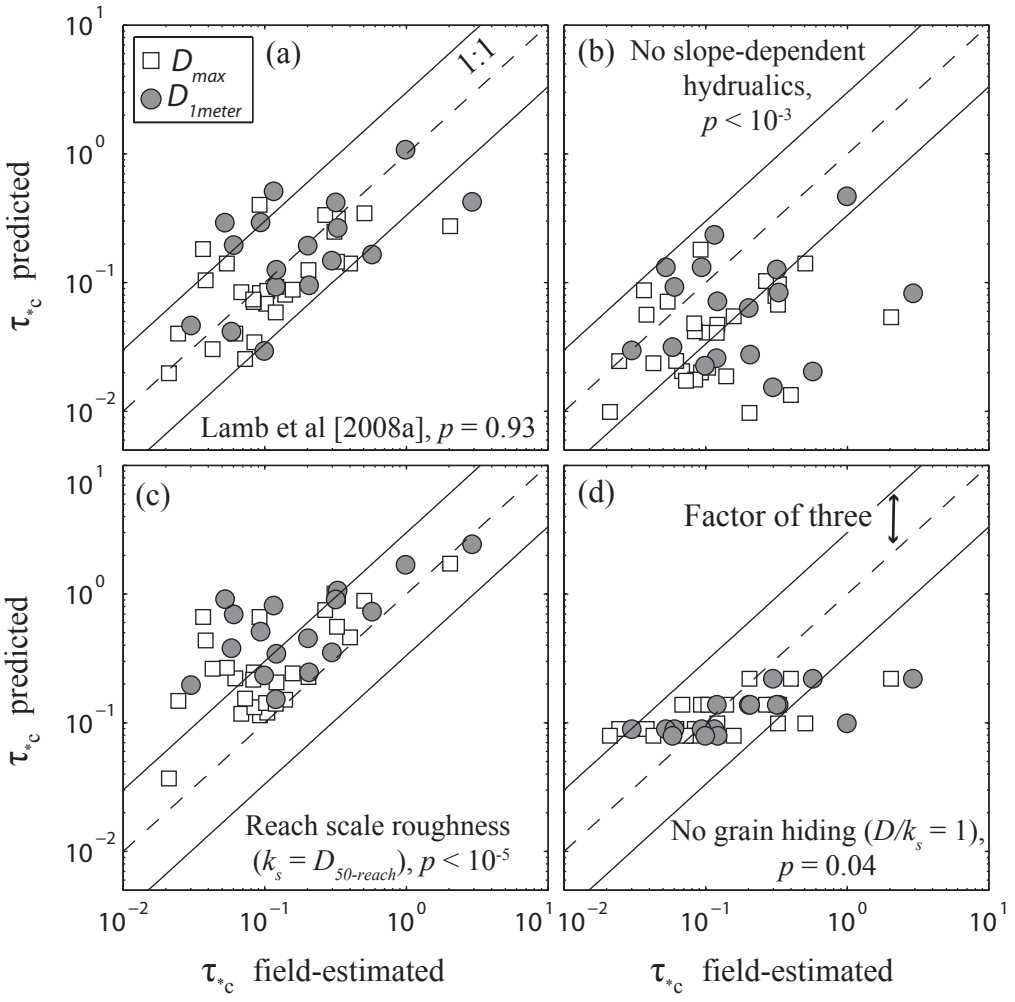

Figure 2.13: Comparison of modeled to calculated critical Shields stress (τ_{*_c}) examining the effects of slope-dependent hydraulics, bed patchiness, and grain hiding. (a) Lamb et al. [2008a] predictions which include the effects of slope-dependent hydraulics, form drag, grain hiding, and patches. (b) Form drag modified Wiberg and Smith [1987] model which includes form drag, patches, and grain hiding effects, but does not include slope-dependent hydraulics. (c) Lamb et al. [2008a] model predictions (where the reach-averaged D50 was used as the roughness length scale rather than the patch D_{50}) which includes form drag, slope-dependent hydraulics, and grain hiding effects, but does not include the effect of bed patchiness. (d) Lamb et al. [2008a] model predictions (with $D/k_s = 1$) which includes form drag, patches, and slope-dependent hydraulics effects, but does not include grain hiding effects. For all predictions fractional form drag was set to 0.5, in plots (a, b, and d) the patch D_{50} was used as the roughness length scale, ks. In all plots dashed line is 1:1 line and solid lines show factor of three deviation from 1:1 line, open squares and gray circles are Shields stress calculated using the flow competence (D_{max}) and one-meter (D_{1meter}) methods, respectively. Results of the two sample Kolmogorov–Smirnov test comparing field-estimated vs. model-predicted Shields stress distributions are displayed for each plot, $p < 0.05$ indicates distributions are statistically different at the 5% significance level.

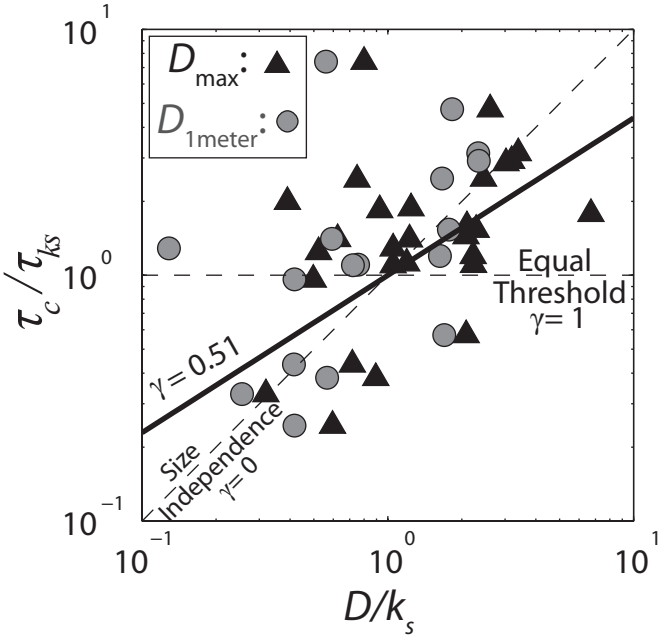

Figure 2.14: Calculated critical shear stress (τ_c) normalized by shear stress for $D = D_{50} = k_s$ of the patch surface (τ_{ks}) versus sediment size (D) normalized by the roughness length k_s for both flow competence and one-meter data. Here D is D_{max} for flow competence data and D_{1meter} for the one-meter method, and k_s is the mass weighted geometric mean grain diameter of the surface of the patch from which the grain originated. The solid line is a best fit to all the data ($\tau_c/\tau_{ks} = (D/k_s)^{1\text{-}0.49}$), $r^2 = 0.10$. Also labeled are lines of equal threshold and size independence.

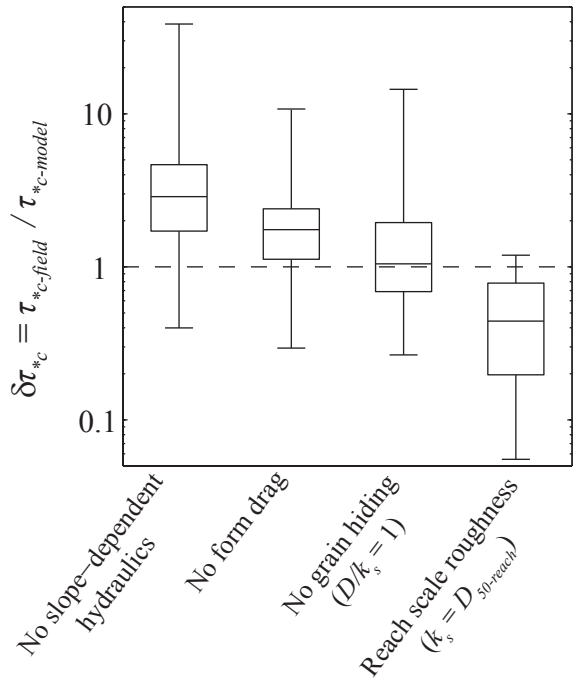

Figure 2.15: Box and whisker plots of the ratio ($\delta\tau_{*c}$) of field ($\tau_{*c\text{-}field}$) to model ($\tau_{*c\text{-}model}$) calculated critical Shields stress (τ_{*c}). Boxes bound the data between the 25th to 75th percentile values, the line within the box is the data median, and whiskers show data extent. For all model predictions, fractional form drag was set to 0.5 and the patch median grain size was used as the roughness length scale, unless otherwise specified. Model predictions used include the Wiberg and Smith [1987] theory ('no slope-dependent hydraulics'), Lamb et al. [2008a] theory with fractional form drag set to zero ('no form drag'), Lamb et al. [2008a] theory with $D/k_s = 1$ ('no grain hiding'), and Lamb et al. [2008a] theory where the reach-averaged D_{50} was used as the roughness length scale rather than the patch D_{50} ('reach scale roughness').

C h a p t e r 3

EXPERIMENTAL EVIDENCE FOR FLUVIAL BEDROCK INCISION BY SUSPENDED AND BEDLOAD SEDIMENT

Joel S. Scheingross[1], Fanny Brun[1,2], Daniel Y. Lo[1], Khadijah Omerdin[1], Michael P. Lamb[1]

[1] Division of Geological and Planetary Sciences, California Institute of Technology, Pasadena, CA, 91125, USA
[2] Geosciences Department, Ecole Normale Supérieure, 24 rue Lhomond, 75005 Paris, France

* Adapted from Scheingross, Joel S., et al. "Experimental evidence for fluvial bedrock incision by suspended and bedload sediment," *Geology*, V. 42, no. 6, p. 523-526 (2014) DOI: 10.1130/G35432.1

3.1 Abstract

Fluvial bedrock incision sets the pace of landscape evolution and can be dominated by abrasion from impacting particles. Existing bedrock incision models diverge on the ability of sediment to erode within the suspension regime, leading to competing predictions of lowland river erosion rates, knickpoint formation and evolution, and the transient response of orogens to external forcing. We present controlled abrasion mill experiments designed to test fluvial incision models in the bed-load and suspension regimes by varying sediment size while holding fixed hydraulics, sediment load, and substrate strength. Measurable erosion occurred within the suspension regime, and erosion rates agree with a mechanistic incision theory for erosion by mixed suspended and bed-load sediment. Our experimental results indicate suspension-regime erosion can dominate channel incision during large floods and in steep channels, with significant implications for the pace of landscape evolution.

3.2 Introduction

River incision into bedrock controls the flux of sediment to basins, links hillslopes to channels, and dictates the rate at which landscapes evolve (e.g., Whipple et al., 2013). Bedrock incision theory allows predictions of fluvial response to external perturbations, and the most commonly used models assume erosion is proportional to stream power or bed shear stress (e.g., Howard and Kerby, 1983). Such models have been widely used in landscape evolution modeling (e.g., Tucker and Slingerland, 1994), as well as in studies examining feedbacks between climate, tectonics, and topography (e.g., Willett, 1999).

However, stream-power models do not explicitly capture the physical processes of river erosion (i.e., the coupling of fluid flow, sediment transport, and channel erosion), limiting their predictive ability.

An alternative approach is to more directly account for processes eroding rock. The saltation-abrasion model (Sklar and Dietrich, 2004) predicts river-bed abrasion from single-sized sediment transported in bed load over a planar bed, and several of its basic tenets have been confirmed in laboratory and field settings (e.g., Sklar and Dietrich, 2001; Johnson and Whipple, 2010). This has led the model, and other similar models (e.g., Turowski et al., 2007), to be widely adopted in predicting reach-scale erosion (e.g., Cook et al., 2012), river-profile evolution (e.g., Crosby et al., 2007), and landscape evolution (e.g., Egholm et al., 2013). The saltation-abrasion model differs from the stream-power model in important and sometimes counter-intuitive ways. For example, the saltation-abrasion model predicts decreased erosion rates for heightened bed shear stresses, leading to slower transient river network response to base level change (Crosby et al., 2007; Gasparini et al., 2007), the preservation of relief in tectonically inactive mountain ranges over much longer time scales than with stream-power modeling (Egholm et al., 2013), and the formation of landforms which do not arise in stream-power modeling such as permanent fluvial hanging valleys (Crosby et al., 2007) and static knickpoints that can grow infinite in height (Sklar and Dietrich, 2008). Additionally, in sand- and silt-bedded rivers and deltas where the majority of bed sediment is transported in suspension during floods, the saltation-abrasion model predicts zero erosion, counter to stream-power predictions and field observations of fluvial incision into consolidated sediment (Nittrouer et al., 2011; Shaw et al., 2013).

Differences between the saltation-abrasion and stream-power models arise, in part, because the saltation-abrasion model assumes an infinite hop length for particles transported within the suspension regime, such that particles are assumed not to impact the bed and erosion rates are predicted to be zero (Sklar and Dietrich, 2004; 2006). The transition from the bed-load regime to the suspension regime is often defined as the point in which bed shear velocity, u_* (a fluid turbulence proxy), surpasses particle terminal settling velocity, w_s (Bagnold, 1966; McLean, 1992), such that turbulence strongly influences particle trajectories. In the suspension regime, some particles are advected high into the water column by turbulence (i.e., the suspended load); however, the largest concentration of particles is still near the bed (Rouse, 1937) where particles impact the bed via rolling, sliding, and saltation (i.e., bed load), and there is active exchange of particles between the bed-load layer and suspended load above (e.g., McLean, 1992; Garcia and Parker, 1993). To account for erosion due to particle-bed impacts within the suspension regime, Lamb et al. (2008) (hereafter referred to as the total-load model) recast the saltation-abrasion model in terms of near-bed sediment concentration rather than particle hop lengths. The saltation-abrasion and total-load models produce similar results for erosion within the bed-load regime, but within the suspension regime the total-load model predicts nonzero erosion rates that increase with increasing fluid bed stress, leading to contrasting predictions for landscape evolution, especially during large floods and in steep channels where bed sediment is suspended.

Laboratory experiments offer a means to test the validity of existing bedrock-erosion theories under controlled conditions that are otherwise difficult to achieve in natural rivers. Previous experimental work suggests that channel-bed erosion in the

suspension regime is possible (Sklar and Dietrich, 2001; Cornell, 2007; Chatanantavet et al., 2010), but experiments have not been conducted that allow full testing of existing models within the suspension regime. Herein we present results from controlled abrasion mill experiments and find significant rates of erosion within the suspension regime, in agreement with the total-load erosion model, and with important implications for landscape evolution.

3.3 Experimental setup

In natural river channels, erosion rates are likely influenced by multiple sediment sizes in transport, complex bed topography, and jointed rock that may promote plucking (e.g., Hancock et al., 1998). Our goal is not to reproduce this complexity, but rather to test the competing predictions of the saltation-abrasion and total-load erosion models under the simplest possible scenarios and in accordance with inherent assumptions in the models, including single-sized sediment, and a planar river bed of massive, unjointed rock. Testing existing models under these simplified conditions is important because such baseline tests have yet to be performed, and the existing theories are widely applied to natural landscapes and used in landscape evolution simulations despite these assumptions (e.g., Cook et al., 2012; Egholm et al., 2013).

To explore bedrock erosion rates over a wide range of transport conditions, we conducted experiments in abrasion mills (Fig. 3.1) identical to those used by Sklar and Dietrich (2001) in their study of erosion rates in the bed-load regime. In abrasion mills, suspension of sediment can be achieved by increasing the flow speed (i.e., increasing u_*), decreasing the sediment size (i.e., decreasing w_s), or both. Increasing flow speed to

suspend gravel in the abrasion mills is problematic, however, because higher flow speeds require larger diameter mills to eliminate co-varying changes in secondary flow circulation. Thus, we chose to conduct experiments varying sediment diameter ($0.46 < D < 44$ mm; Table S3.1) to achieve flow conditions spanning both the suspension and bed-load regimes ($0.15 < u_* / w_s < 2.9$), while holding propeller speed (1000 rpm, $u_* \approx 0.15$ m/s; Sklar and Dietrich, 2004) and total sediment load (70 g) constant to match previous experiments (Sklar and Dietrich, 2001). Note that under the imposed conditions of constant sediment load and flow speed, finer sediment will necessarily produce smaller erosion rates, regardless of whether transport is in the suspension regime or not, because of smaller particle mass and fall velocity. Erosion rates should also approach zero with decreasing grain size as impacts become viscously damped for particle Stokes numbers (St, a non-dimensional number which weights the kinetic energy of particle impacts to the fluid viscosity) below ~10–100 (Joseph et al., 2001).

To achieve measurable erosion rates, we used low-tensile strength ($\sigma_T = 0.32$ MPa) polyurethane foam as a highly erodible bedrock simulant rather than natural rock. Tests show foam follows the same erosion-rate scaling relationship with tensile strength as observed by Sklar and Dietrich (2001) for rock and concrete (Supplementary Material, Fig. S3.1), allowing our results to be properly scaled to natural rock.

For each experiment, we secured a 38-mm-thick foam disc to the base of the abrasion mill, loaded the mill with siliciclastic, well sorted, sub-angular to sub-rounded sediment, and filled the mill to a depth of 49 cm with water. A propeller induced flow and sediment transport, and experiments were run long enough for measurable wear of the foam disc by either volume loss (using a submillimeter-precision laser scanner) or

mass loss (using a 0.1-g precise scale), depending on total volume eroded. For grain diameters $D \leq 2.4$ mm we collected flow samples at three elevations above the bed (1, 3, and 10 cm) to quantify the suspended sediment concentration profile (Fig. 3.1; Supplementary Material).

3.4 Sediment transport

Using a transparent mill, we observed that grains with $D \geq 7$ mm ($u_*/w_s \leq 0.44$) were transported exclusively in bed load, moving via rolling, sliding, and saltating along the bed, grains with $D \leq 1.2$ mm ($u_*/w_s \geq 1.3$) moved in both bed and suspended load, and grains ~2.0–2.4 mm diameter ($0.61\ u_*/w_s \leq 1.0$) were intermediate between exclusive bed load and intermittent suspension (Fig. S3.2; Movies S3.1–S3.4). In the radial direction, sediment concentrated in an annulus around the center of the mill due to secondary circulation (Sklar and Dietrich, 2001; 2004); however, secondary circulation was typically less than ~10% of the mean azimuthal flow velocity and did not appear to strongly influence erosion rates (Supplementary Material).

Measurements of sediment concentration, c, for $D < 2$ mm had vertical profiles (Fig. 3.2) comparable to those predicted by classic theory (Rouse, 1937),

$$c = c_b \left[\frac{(1/z) - (1/H)}{(1/H_b) - (1/H)} \right]^{\frac{w_s}{\beta \kappa u_*}}, \quad (3.1)$$

where z is height above the bed, H is flow depth, c_b and H_b are near-bed sediment concentration and bed-load layer thickness calculated following Lamb et al. (2008), β is a dimensionless constant weighting the diffusivities of sediment relative to fluid momentum, and $\kappa = 0.41$ is von Karman's constant. Despite the different flow hydraulics

in abrasion mills versus the unidirectional, steady, turbulent boundary layer assumed in the derivation of Equation 3.1, the Rouse model shows reasonable agreement with our measurements for $\beta = 2$ (Fig. 3.2), a value similar to that found in unidirectional flows (e.g., $\beta = 0.5–3$; Graf and Cellino, 2002).

3.5 Bedrock erosion

Measurable erosion of synthetic bedrock occurred in all experiments, including those within the suspension regime. Under fixed total sediment load, erosion rates decreased with decreasing grain size from ~10^2 cm^3/hr for the largest grains that were transported in the bed-load regime ($D = 40$ mm, $u_*/w_s = 0.15$) to ~10^{-2} cm^3/hr for the smallest grains that were transported in the suspension regime ($D = 0.46$ mm, $u_*/w_s = 2.9$) (Fig. 3.3A; Table S3.1). The observed erosion rate versus grain size relationship for the bed-load regime matches that observed by Sklar and Dietrich (2001) or grains eroding limestone, except we observed higher erosion rates due to the use of a lower tensile strength substrate. To directly compare our results to those of Sklar and Dietrich (2001) we scaled volumetric foam erosion rates ($E_{v\text{-}f}$) to equivalent values for erosion of limestone ($E_{v\text{-}ls}$) using the tensile-strength scaling relationship proposed by Sklar and Dietrich (2001) and confirmed here (Fig. S3.1B), i.e.,

$$E_{v-ls} = E_{v-f}\left(\frac{\sigma_{T-ls}}{\sigma_{T-f}}\right)^{-2}, \quad (3.2)$$

where $\sigma_{T\text{-}f}$ and $\sigma_{T\text{-}ls}$ are the tensile strengths of foam (0.32 MPa) and limestone (9.8 MPa), respectively. The scaled foam data collapse to nearly the same values as those found by

Sklar and Dietrich (2001), and extend the combined data set to smaller sediment sizes with higher u_*/w_s (Fig. 3.3A).

The saltation-abrasion model (Sklar and Dietrich, 2004) predicts zero erosion for $D < \sim 2$ mm due to the onset of suspension, which does not match our data (Fig. 3.3B). The total-load model (Lamb et al., 2008), on the other hand, over-predicts erosion rates within the suspension regime when viscous dampening of impacts is neglected. The best model fit to the data is the total-load abrasion model where impacts are viscously damped for $St < 75$, this value is within the range of partial dampening found in particle-wall collision studies (e.g., Joseph et al., 2001).

3.6 Discussion and implications

Our experimental results provide direct evidence for fluvial incision in the suspension regime, show viscous dampening reduces erosion rates for low-energy impacts, and support the use of the total-load model for predicting erosion in both the bed-load and suspension regimes. Our observations show that suspension-regime erosion occurs because particles are transported both in a bed-load layer with high sediment concentrations near the bed, and in a more dilute suspended-load layer above (e.g., Fig. 3.2; Fig. S3.2), with active interchange of particles between the two layers and active particle-bed impacts. Erosion rates in our experiments decreased across the bed-load to suspension regime primarily because we decreased grain size while holding sediment load and flow speed constant, and, under these conditions, smaller particles have lower kinetic energy upon impact, regardless of the transport mode. The total-load model predicts that suspension-regime erosion rates would be of similar magnitude to bed-load-

regime rates if experiments were instead conducted by varying u_* while holding grain size constant (Fig. 3.4), and would outpace bed-load regime rates by several orders of magnitude if sediment load increases with u_* (Supplementary Material; Fig. S3.3). Although more difficult experimentally, these alternate scenarios are likely in natural rivers during floods, suggesting that erosion by sediment in the suspension regime may be more important in natural rivers than demonstrated in our experiments.

In natural rivers, the relative efficiency of erosion within the suspension regime depends strongly on the ability of a flood to suspend bed sediment. Bankfull floods in gravel-bed rivers rarely suspend bed material (Parker et al., 2007), such that, for typical mass flux ratios of bed to suspended load, erosion from gravel and cobbles moving exclusively in bed load likely outpace suspension-regime erosion from sand and silt which have smaller impact velocities and in which impacts may be viscously damped.

Suspension-regime erosion will dominate fluvial abrasion when bed sediment is suspended however, which regularly occurs in sand-bedded rivers, in coarse-grained rivers during large floods, and in steep channels and knickzones. For example, the total-load model successfully predicts erosion of consolidated mud in the Wax Lake Delta where the majority of grain sizes present on the bed are transported in the suspension regime during bankfull flows (Shaw et al., 2013). These conditions are common in other lowland distributary rivers (e.g., Nittrouer et al., 2011), where the dominance of suspension-regime transport would cause the saltation-abrasion model to erroneously predict zero erosion. Suspension of bed material can also occur during large-magnitude storms in coarse-bedded mountain rivers. For example, typhoon-induced floods in the Da'an River, Taiwan, resulted in ~20 m of vertical incision over a four year period (Cook

et al., 2012). We calculate that grains up to 1 m in diameter were within the suspension regime in the narrowest portion of the gorge where erosion was rapid (Supplementary Material), which is far larger than the median grain diameter of the bed material (15 cm; Cook et al., 2012), suggesting that the bulk of erosion occurred within the suspension regime.

In landscape evolution modeling, suspension-regime erosion causes erosion rates to increase on steep channel slopes, similar to stream-power models (Supplementary Material; Fig. S3.3), and may prevent formation of over-steepened, non-eroding reaches that develop in simulations that use the saltation-abrasion model (e.g., Wobus et al., 2006; Crosby et al., 2007; Sklar and Dietrich, 2008). Suspension-regime erosion additionally allows steep river reaches to propagate more rapidly through a landscape resulting in faster transmission of changes in base-level than observed with saltation-abrasion models (Crosby et al., 2007; Gasparini et al., 2007), and this in turn may influence the predictions of morphology and lifespan of mountain ranges. For example, recent predictions using the saltation-abrasion model attribute the long-term preservation of relief in tectonically inactive mountain ranges to landslide-modulated sediment supply to river networks (Egholm et al., 2013). However, including suspension-regime erosion in modeling should yield higher erosion rates which, will more rapidly reduce relief both on steep slopes and under high rates of sediment supply if bed sediment is suspended (e.g., Fig. S3.3).

3.7 Acknowledgements

We thank Leonard Sklar for enlightening discussions and donation of an abrasion mill, and Chris Borstad for conversations on fracture mechanics. Brandon McElroy kindly measured our fine sediment sizes, and Brian Fuller built the abrasion mills. Discussion with Roman DiBiase, reviews from Phairot Chatanatavet, Nicole Gasparini, Leslie

Hasbargen, Leonard Sklar, and an anonymous reviewer, and editorial comments from James Spotila greatly improved this manuscript. Support came from a National Science Foundation (NSF) Graduate Research Fellowship to Scheingross, NSF grant EAR-1147381 grant to Lamb, and a California Institute of Technology Summer Undergraduate Research Fellowship to Lo.

3.8 References

Bagnold, R.A., 1966, An approach to the sediment transport problem for general physics: Washington, D.C., U.S. Geological Survey Professional Paper 422-I.

Chatanantavet, P., Whipple, K.X., and Adams, M.A., 2010, Experimental study of bedrock incision processes by both suspended load and bedload abrasions: American Geophysical Union Fall Meeting, San Francisco, California, Abstract EP22A–04.

Cook, K.L., Turowski, J.M., and Hovius, N., 2012, A demonstration of the importance of bedload transport for fluvial bedrock erosion and knickpoint propagation: Earth Surface Processes and Landforms, v. 38, p. 683–695, doi:10.1002/esp.3313.

Cornell, K.M., 2007, Suspended Sediment Erosion in Laboratory Flume Experiments [Masters Thesis]: Cambridge, Massachusetts, Massachusetts Institute of Technology, 50 p.

Crosby, B.T., Whipple, K.X., Gasparini, N.M., and Wobus, C.W., 2007, Formation of fluvial hanging valleys: Theory and simulation: Journal of Geophysical Research–Earth Surface, v. 112, no. F3, doi:10.1029/2006jf000566.

Egholm, D., Knudsen, M., and Sandiford, M., 2013, Lifespan of mountain ranges scaled by feedbacks between landsliding and erosion by rivers: Nature, v. 498, p. 475–478, doi:10.1038/nature12218.

Garcia, M., and Parker, G., 1993, Experiments on the entrainment of sediment into suspension by a dense bottom current: Journal of Geophysical Research–Oceans, v. 98, no. C3, p. 4793–4807, doi:10.1029/92JC02404.

Gasparini, N.M., Whipple, K.X., and Bras, R.L., 2007, Predictions of steady state and transient landscape morphology using sediment-flux-dependent river incision models: Journal of Geophysical Research–Earth Surface, v. 112, no. F3, doi:10.1029/2006JF000567.

Graf, W.H., and Cellino, M., 2002, Suspension flows in open channels; experimental study: Journal of Hydraulic Research, v. 40, p. 435–447, doi:10.1080/00221680209499886.

Hancock, G.S., Anderson, R.S., and Whipple, K.X, 1998, Beyond power: Bedrock river incision process and form, in Tinkler, K., and Wohl, E.E., eds., Rivers Over Rock: Fluvial Processes in Bedrock Channels: Washington, D.C., American Geophysical Union, Geophysical Monograph 107, p. 35–60.

Howard, A.D., and Kerby, G., 1983, Channel changes in badlands: Geological Society of America Bulletin, v. 94, no. 6, p. 739–752, doi:10.1130/0016-7606(1983)94<739:CCIB>2.0.CO;2.

Johnson, J.P.L., and Whipple, K.X, 2010, Evaluating the controls of shear stress, sediment supply, alluvial cover, and channel morphology on experimental bedrock incision rate: Journal of Geophysical Research–Earth Surface, v. 115, doi:10.1029/2009JF001335.

Joseph, G.G., Zenit, R., Hunt, M.L., and Rosenwinkel, A.M., 2001, Particle-wall collisions in a viscous fluid: Journal of Fluid Mechanics, v. 433, p. 329–346, doi:10.1017/S0022112001003470.

Lamb, M.P., Dietrich, W.E., and Sklar, L.S., 2008, A model for fluvial bedrock incision by impacting suspended and bed load sediment: Journal of Geophysical Research–Earth Surface, v. 113, no. F3, doi:10.1029/2007JF000915.

McLean, S.R., 1992, On the calculation of suspended-load for noncohesive sediments: Journal of Geophysical Research–Oceans, v. 97, no. C4, p. 5759–5770, doi:10.1029/91JC02933.

Nittrouer, J.A., Mohrig, D., Allison, M.A., and Peyret, A.-P.B., 2011, The lowermost Mississippi River: A mixed bedrock-alluvial channel: Sedimentology, v. 58, p. 1914–1934, doi:10.1111/j.1365-3091.2011.01245.x.

Parker, G., Wilcock, P.R., Paola, C., Dietrich, W.E., and Pitlick, J., 2007, Physical basis for quasi-universal relations describing bankfull hydraulic geometry of single-thread gravel bed rivers: Journal of Geophysical Research–Earth Surface, v. 112, no. F4, doi:10.1029/2006JF000549.

Rouse, H.R., 1937, Modern conceptions of the mechanics of turbulence: Transactions of the American Society of Civil Engineers, v. 102, p. 463–543.

Shaw, J.B., Mohrig, D., and Whitman, S.K., 2013, The morphology and evolution of channels on the Wax Lake Delta, Louisiana, USA: Journal of Geophysical Research–Earth Surface, v. 118, p. 1562–1584, doi:10.1002/jgrf.20123.

Sklar, L.S., and Dietrich, W.E., 2001, Sediment and rock strength controls on river incision into bedrock: Geology, v. 29, p. 1087–1090, doi:10.1130/0091-7613(2001)029<1087:SARSCO>2.0.CO;2.

Sklar, L.S., and Dietrich, W.E., 2004, A mechanistic model for river incision into bedrock by saltating bed load: Water Resources Research, v. 40, doi:10.1029/2003WR002496.

Sklar, L.S., and Dietrich, W.E., 2006, The role of sediment in controlling steady-state bedrock channel slope: Implications of the saltation-abrasion incision model: Geomorphology, v. 82, p. 58–83, doi:10.1016/j.geomorph.2005.08.019.

Sklar, L.S., and Dietrich, W.E., 2008, Implications of the saltation-abrasion bedrock incision model for steady-state river longitudinal profile relief and concavity: Earth Surface Processes and Landforms, v. 33, p. 1129–1151, doi:10.1002/esp.1689.

Tucker, G.E., and Slingerland, R.L., 1994, Erosional dynamics, flexural isostasy, and long-lived escarpments: A numerical modeling study: Journal of Geophysical Research. Solid Earth, v. 99, no. B6, p. 12229–12243, doi:10.1029/94JB00320.

Turowski, J.M., Lague, D., and Hovius, N., 2007, Cover effect in bedrock abrasion: A new derivation and its implications for the modeling of bedrock channel morphology: Journal of Geophysical Research–Earth Surface, v. 112, no. F4, doi:10.1029/2006JF000697.

Whipple, K.X., DiBiase, R.A., and Crosby, B.T., 2013, Bedrock Rivers, in Shroder, J.,Jr., and Wohl, E., eds.,Treatise on Geomorphology, Volume 9: San Diego, California, Academic Press, doi:10.1016/B978-0-12-374739-6.00254-2.

Willett, S.D., 1999, Orogeny and orography: The effects of erosion on the structure of mountain belts: Journal of Geophysical Research–Solid Earth, v. 104, no. B12, p. 28957–28981, doi:10.1029/1999JB900248.

Wobus, C.W., Crosby, B.T., and Whipple, K.X., 2006, Hanging valleys in fluvial systems: Controls on occurrence and implications for landscape evolution: Journal of Geophysical Research–Earth Surface, v. 111, no. F2, doi:10.1029/2005JF000406.

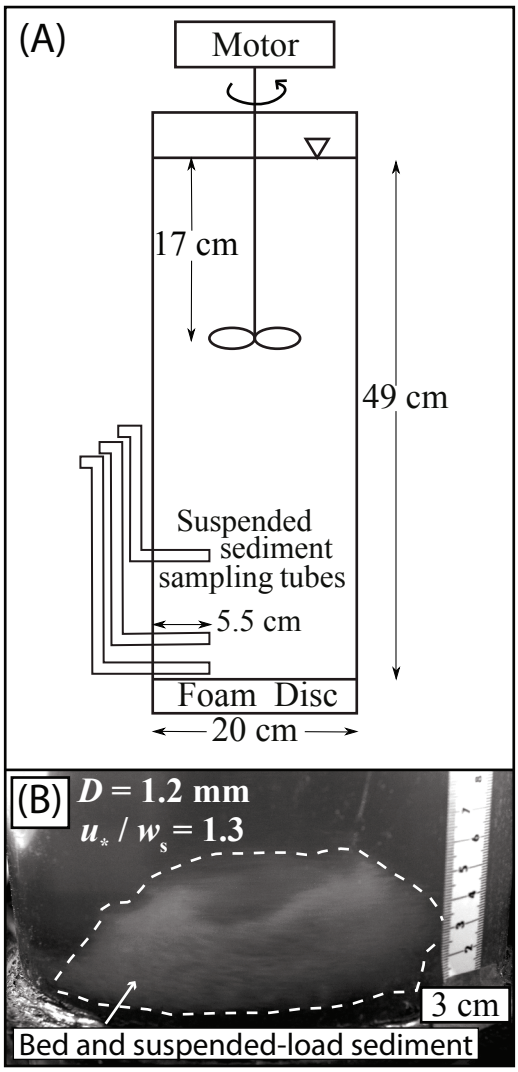

Figure 3.1. Schematic diagram of abrasion mill and sediment concentration measurement system (modified from Sklar and Dietrich, 2001). B: Contrast-enhanced, side-view photograph of suspension-regime transport within an abrasion mill.

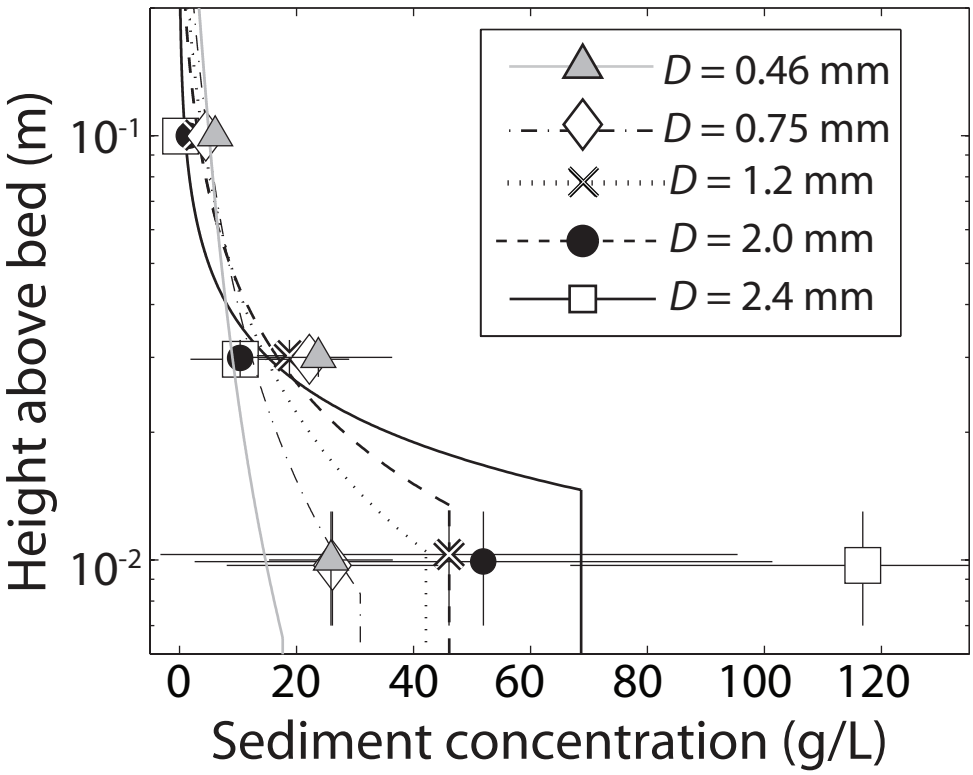

Figure 3.2. Rouse sediment concentration profiles (dashed and solid lines) for different grain sizes with $\beta = 2$ (β is a dimensionless constant weighting the diffusivities of sediment relative to fluid momentum), for a total sediment load of 70 g. Symbols correspond to the mean of the sediment concentration measurements (n = 3); x- and y-error bars represent the geometric standard deviation of the measurements and the radius of the sampling tubing (3 mm), respectively.

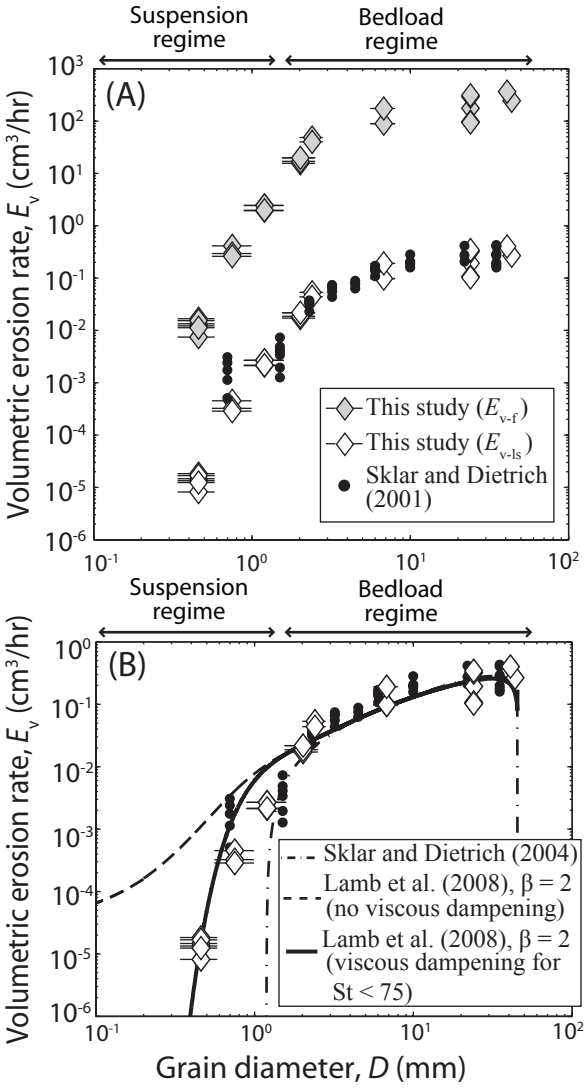

Figure 3.3. A: Volumetric erosion rate, E_v, versus grain size, D, in this study and from previous experiments eroding limestone. We show both measured foam erosion rates ($E_{v\text{-}f}$) and limestone-equivalent rates ($E_{v\text{-}ls}$; Eq. 2.2). Error bars correspond to the limits of unimodal grain size distributions as reported in Table A1.1. B: Same as panel A with lines showing theoretical predictions of the saltation-abrasion model (Sklar and Dietrich, 2004), and the total-load model (Lamb et al., 2008) with and without viscous dampening. The cover term was neglected due to low sediment loading, and non-dimensional constant k_v was set to 3×10^5 to account for the fact that particle tensile strength was greater than substrate tensile strength (see Sklar and Dietrich [2004] for details).

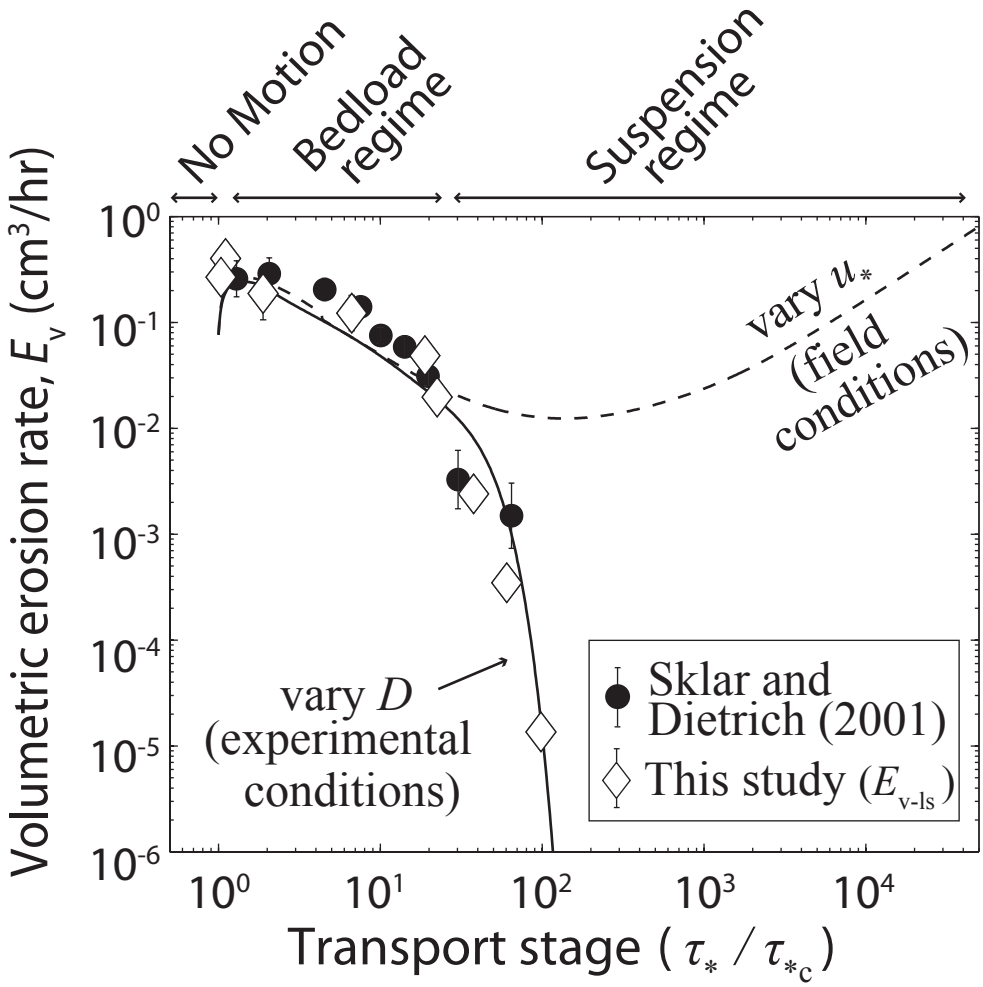

Figure 3.4. Volumetric erosion rate, E_v, versus transport stage, τ_*/τ_{*_c}, for abrasion mill experiments. Lines show theoretical predictions of the total-load model (Lamb et al., 2008) for transport stage varied by changing grain size (D, solid line), as was done in the abrasion mill experiments, and by changing shear velocity (u_*) with constant flow depth (dashed line). Symbols show mean and 1 sigma standard deviation of erosion rates for abrasion mill experiments, with foam erosion rates converted to limestone-equivalent rates ($E_{v\text{-}ls}$) using Eq. 3.2. Models include viscous dampening of impacts for particle Stokes number < 75, $\beta = 2$, $k_v = 3 \times 10^5$, and neglect cover.

Supplementary material for Chapter 3

S3.1 Scaling foam-to-rock erosion

The erosion rate of natural rock and concrete has been shown to depend primarily on the substrate tensile strength, σ_T (Sklar and Dietrich, 2001). To test this scaling relationship for polyurethane foam, we designed a set of abrasion mill experiments eroding foam of different tensile strengths ($0.3 < \sigma_T < 17$ MPa, Table S3.2) and densities (0.06 to 0.96 g/cm^3) while holding all other variables constant, including sediment load (150 g) and grain size (D = 6 mm). These experiments are identical to erosion-rate versus tensile-strength experiments presented in Sklar and Dietrich (2001), except here we use a foam substrate rather than rock or concrete. Results show foam erosion rates by mass loss, E_m, varied inversely with tensile strength from ~10^1 to 10^{-2} g/hr, and were slightly lower than E_m measurements from Sklar and Dietrich (2001) for material of similar tensile strength (Fig. S3.1A). Accounting for the low density of foam compared to rock results in a reasonable match between foam and rock erosion, where volumetric erosion rates, E_v, scale with σ_T^{-2} (Fig. S3.1B). This agreement suggests that foam acts as a suitable rock analog.

Note that Sklar and Dietrich (2004) further proposed that erosion rate depends on the material Young's modulus, Y, and a (material specific) non-dimension constant, k_v. Unlike natural rock which has little variation in Y and k_v, the Young's modulus of foam used in this study varied from 3.9 to 330 MPa. This implies that to achieve the observed relationship between foam tensile strength and erosion rate, either k_v must vary in proportion to Y (which goes against the theoretical expectation of constant k_v (Engle, 1978)), or that Young's modulus may have little influence on erosion rate, as has recently

been suggested (Beyeler et al., 2009). In either case, the agreement in erosion rate versus tensile-strength relationship for foam, natural rock, and concrete allows results obtained between the three substrates to be directly compared.

S3.2 Sediment concentration measurements

We sampled suspended and bedload sediment within abrasion mills using 6.4 mm diameter siphons inserted through the abrasion mill walls, a sampling velocity (~0.65 ± 0.1 m/s) similar to the mean flow velocity (Winterstein and Stefan, 1983), and sample volumes that did not exceed 1.75 L (~12% of the abrasion mill water volume). Sediment concentration was measured by weighing and drying the samples, and weighing the sediment.

A3.3 Secondary circulation

We used high speed video (240 frames per second) looking up through the bottom of a clear abrasion mill with foam removed to track particle motion and quantify secondary flow circulation. We manually tracked individual particle trajectories for distances of one to four full rotations about the mill, and averaged trajectories over seven frames to calculate the ratio of azimuthal to radial distance traveled. For five grains of 6.8 mm diameter, we found median values of azimuthal to radial distance traveled ranged from ~7 – 17. Particle trajectories for grains smaller than 6 mm could not be measured

due to high particle velocities and small particle size which exceeded the speed and resolution of our high speed camera.

Sklar and Dietrich (2001; 2004) attributed suspension-regime erosion in abrasion mill experiments to secondary circulation, which they argued induced bedload transport in a way not representative of natural rivers. However, our observations are consistent with previous workers who showed that high concentrations of particles and active particle-bed interactions are expected near the bed (i.e., in a bedload layer) even within the suspension regime (e.g., Rouse, 1937; McLean, 1992). Furthermore, although secondary circulation is an important component of flow in the abrasion mills, several observations suggest it did not dominate particle trajectories or strongly influence bedrock erosion rates. First, secondary circulation in natural rivers with flow around bends as well as in straight channels is of similar magnitude (~10% of the mean azimuthal flow velocity (Dietrich and Smith, 1983; Nikora and Roy, 2012)) to our abrasion mill observations (Fig. S3.2; Movies S3.1–4). Second, the agreement between sediment-concentration measurements and Rouse-profile predictions (Fig. 2) suggest the abrasion mills reasonably replicate natural river fluid flow and sediment transport. Third, we observed fluting and grooves on the eroded foam surfaces parallel to the azimuthal flow direction, suggesting radial sediment transport due to secondary circulation did not exert a detectable influence on erosion.

S3.4 Role of slope, flow depth, sediment size, and sediment load

Suspension of sediment during fluvial transport can be achieved either by decreasing particle size (i.e., lowering settling velocity, w_s), or increasing fluid shear

stress (i.e., increasing shear velocity, u_*). In the experiments presented here, we decreased grain size while holding shear velocity and sediment load constant to achieve suspension. While tractable experimentally, this is not an ideal representation of natural bedrock rivers where the transition from bedload to suspension regime transport occurs primarily due to increases in shear velocity associated with flood events, which additionally tend to increase sediment supply (e.g., Leopold et al., 1964). Here we explore how changes in grain size, shear velocity, and sediment supply influence erosion rates in both the bedload and suspension regimes.

We ran the total-load and saltation-abrasion models under variable transport stage, $\tau_*/\ \tau_{*c}$, where τ_* is the non-dimensional Shields stress defined as

$$\tau_* = \frac{\tau}{\left(\rho_s - \rho_f\right) gD} \ , \qquad \text{(S3.1)}$$

τ is bed shear stress, g is acceleration due to gravity, ρ_s = 2650 kg/m^3 and ρ_f = 1000 kg/m^3 are the sediment and fluid densities, respectively, and τ_{*c} = 0.03 is the critical Shields stress for sediment motion. We assumed steady, uniform flow such that

$$\tau = \rho_f u_*^2 = \rho_f ghS \ , \qquad \text{(S3.2)}$$

where h and S are the channel flow depth and slope, respectively. Under these assumptions, increases in $\tau_*/\ \tau_{*c}$ arise from increasing h or S, or decreasing D. The total-load model is dependent upon h and S individually, whereas the saltation-abrasion model is dependent upon shear velocity (i.e., the product hS). We varied transport stage to cover conditions from incipient motion to well within the suspension regime ($10^0 < \tau_*/\ \tau_{*c} < 10^4$). Values of $\tau_*/\ \tau_{*c}$ do not correspond to identical values of $u_*/\ w_s$ across different

model runs; however, the transition from bedload to suspension regime transport generally occurs when $\tau_*/\ \tau_{*c}$ exceeds ~20-40. We ran two separate scenarios, first for a constant sediment load, q_s, and second, letting $q_s = 0.5q_{sc}$, where $q_{sc} = 5.7(RgD^3)^{1/2}(\tau_* - \tau_{*c})^{3/2}$ is the sediment transport capacity calculated using the empirical fit of Fernandez Lueque and van Beek (1976), and $R = (\rho_s - \rho_f)/\rho_f$ is the submerged specific density of sediment. For all cases we used base conditions representative of the South Fork Eel River, California, USA (D = 60 mm, h = 0.95 m, S = 0.0053, q_s = 8.9 x 10^{-4} m^2/s), which has been used as a reference site for the saltation-abrasion and total-load models previously (Sklar and Dietrich, 2004; 2006; 2008; Lamb et al., 2008). Models were run by varying one of either grain size, channel slope, or flow depth while holding the remaining two variables constant.

Under constant sediment load, parameterizations of the total-load and saltation-abrasion models generally agree within the bed load regime ($\tau_*/\ \tau_{*c}$ < ~20), but diverge within the suspension-regime (Fig. S3.3A). The saltation-abrasion model predicts that erosion rates tend towards zero as the threshold for suspension is approached regardless of how changes in transport capacity are achieved (thin gray lines in Fig. S3.3A), in contrast to total-load model predictions (black lines in Fig. S3.3A). When transport stage varies with grain size (as was the case for the abrasion mill experiments presented here), the total-load model predicts erosion rates decrease with increasing $\tau_*/\ \tau_{*c}$ due to reduced kinetic energy of fine grain impacts, asymptotically approaching zero erosion near the threshold for viscous dampening (dashed black line in Fig. S3.3). For transport stage varying with flow depth (black dashed-dotted line), or varying with slope (solid black line), both of which are likely in field situations but which we were unable to test

experimentally, the total-load model predicts non-zero erosion rates. Increases in transport stage reduce near-bed sediment concentration due to faster particle advection and the lofting of a portion of the sediment load above the bedload layer as particles enter suspension. These effects decrease the number of particle impacts, and in turn, erosion rates. For the case of varying slope, decreases in near-bed sediment concentration are offset by increases in impact velocity for $\tau_* / \tau_{*c} > \sim 100$, such that suspension-regime erosion rates match and can exceed bed load-regime erosion rates (see Lamb et al. (2008) for further discussion).

Bedrock erosion in mountain channels occurs during floods large enough to mobilize bed-sediment, and increases in flood-magnitude generally yield increases in sediment supply (e.g., Leopold et al., 1964). Repeating the above analysis for sediment supply proportional to transport capacity (Fig. S3.3B) gives markedly different total-load model predictions to those made under constant sediment supply (Fig. S3.3A), as setting $q_s = 0.5 q_{sc}$ maximizes erosion rates for a given grain size and shear velocity (Sklar and Dietrich, 2004). When transport stage is varied by reducing grain size, erosion rates decrease with transport stage well before the threshold for suspension in the saltation-abrasion model is reached (thin gray dashed line in Fig. S3.3B), because increased sediment supply does not offset the effect of reduced kinetic energy of impact for fine grains. When transport stage is varied by changing shear velocity, total-load erosion rates increase monotonically with τ_* / τ_{*c} (solid and dashed-dotted black lines in Fig. S3.3B), and suspension-regime erosion rates can exceed bedload regime erosion rates by multiple orders of magnitude. Thus, for large-magnitude floods in bedrock rivers, we expect suspension-regime erosion to contribute significantly to, and in cases dominate,

the total fluvial abrasion signal, as likely occurred during typhoon-induced storms in the Da'an River, Taiwan (Cook et al, 2012). Additionally, in the suspension regime, bedrock erosion can occur even if the sediment supply exceeds the bedload transport capacity, because the excess sediment, which otherwise would form a static cover and protect the bed, can be transported as suspended load.

Saltation-abrasion and total-load erosion rate predictions can also be compared to those predicted using a stream power model (e.g., Howard and Kerby, 1983),

$$E = K\tau^{\gamma} \quad , \qquad \text{(S3.3)}$$

where we set K = 0.41 mm / (year Pa) and γ = 1 to match the observed long-term erosion rates in the South Fork Eel River (Sklar and Dietrich, 2006). Unlike the saltation-abrasion and total-load models, stream power predicts monotonically increasing erosion rate with transport stage, independent of sediment supply, slope, flow depth, or grain size (thick gray dashed line in Fig. S3.3). When sediment supply is proportional to sediment transport capacity, the ratio of suspension-regime to bedload-regime erosion rates predicted by the total-load model roughly matches that predicted by stream-power for $2 < \tau_*/\tau_{*c} < \sim 200$ (Fig. S3.3B).

S3.5. Da'an River suspension calculations

We calculated u_*/w_s in the Da'an River, Taiwan for all reaches in which Cook et al. (2012) report data (their Table III) for a characteristic typhoon-induced flood

discharge of 1300 m^3/s. We solved for shear velocity by combining Equations S3.1 and S3.2 using reported values of non-dimesnional Shields stress and the medium grain diameter (D = 15 cm) (Cook et al., 2012). We estimated terminal settling velocity for a range of particle sizes using the Dietrich (1982) empirical formula with values appropriate for natural particles (Corey Shape Factor = 0.8; Powers Roundness = 3.5), and defined the maximum grain size expected to be in the suspension regime, D_{susp}, as the largest grain for which $u_*/w_s \geq 1$ (Table S3.3). Note that Cook et al. (2012) removed the constraint suppressing suspension-regime erosion in their implementation of the saltation-abrasion model such that they calculated non-zero erosion rates in reaches within the suspension regime. Viscous dampening of particle impacts is not expected to influence abrasion rates for floods which produced measurable erosion in the Da'an River due to the presence of coarse bed-material and large particle Stokes numbers.

S3.6 References

Beyeler, J.D., Sklar, L.S., Litwin, K., Johnson, J.P., Collins, G.C., and K.X. Whipple, 2009, The dependence of bedrock erodibility on rock material properties: Is tensile strength enough?: American Geophysical Union Fall Meeting, Abstract EP21C-0616, San Francisco, CA.

Cook, K. L., Turowski, J. M., and Hovius, N., 2012, A demonstration of the importance of bedload transport for fluvial bedrock erosion and knickpoint propagation: Earth Surface Processes and Landforms, v. 38, no. 7, p. 683-695, doi:doi: 10.1002/esp.3313.

Dietrich, W. E., 1982, Settling velocity of natural particles: Water Resources Research, v. 18, no. 6, p. 1615-1626, doi:10.1029/WR018i006p01615.

Dietrich, W. E., and Smith, J. D., 1983, Influence of the point-bar on flow through curved channels: Water Resources Research, v. 19, no. 5, p. 1173-1192, doi:10.1029/WR019i005p01173.

Engle, P., 1978, Impact wear of materials: New York, Elsevier Science.

Fernandez-Luque, R., and R. van Beek, 1976, Erosion and transport of bedload sediment: Journal of Hydrualic Research, v. 14, p. 127-144, doi:10.1080/00221687609499677.

Howard, A. D., and Kerby, G., 1983, Channel changes in badlands: Geological Society of America Bulletin, v. 94, no. 6, p. 739-752.

Lamb, M. P., Dietrich, W. E., and Sklar, L. S., 2008, A model for fluvial bedrock incision by impacting suspended and bed load sediment: Journal of Geophysical Research-Earth Surface, v. 113, no. F3, doi:10.1029/2007jf000915.

Leopold, L. B., Wolman, M. G., and Miller, J. P., 1964, Fluvial processes in geomorphology, San Francisco, W.H. Freeman and Company.

McLean, S. R., 1992, On the calculation of suspended-load for noncohesive sediments: Journal of Geophysical Research-Oceans, v. 97, no. C4, p. 5759-5770, doi:10.1029/91jc02933.

Nikora, V., and Roy, A. G., 2012, Secondary flows in rivers: Theoretical framework, recent advances, and current challenges, *in* Church, M., Biron, P. M., and Roy, A. G., eds., Gravel-bed rivers: Processes, tools, environments, John Wiley & Sons, West Sussex, United Kingdom, p. 3-22.

Rouse, H. R., 1937, Modern conceptions of the mechanics of turbulence: Trans. Am. Soc. Civ. Eng., v. 102, no. 1, p. 463-543,

Sklar, L. S., and Dietrich, W. E., 2001, Sediment and rock strength controls on river incision into bedrock: Geology, v. 29, no. 12, p. 1087-1090, doi:10.1130/0091-7613(2001)029<1087:sarsco>2.0.co;2.

-, 2004, A mechanistic model for river incision into bedrock by saltating bed load: Water Resources Research, v. 40, no. 6, doi:10.1029/2003wr002496.

-, 2006, The role of sediment in controlling steady-state bedrock channel slope: Implications of the saltation-abrasion incision model: Geomorphology, v. 82, no. 1-2, p. 58-83, doi:10.1016/j.geomorph.2005.08.019.

-, 2008, Implications of the saltation-abrasion bedrock incision model for steady-state river longitudinal profile relief and concavity: Earth Surface Processes and Landforms, v. 33, no. 7, p. 1129-1151, doi:10.1002/esp.1689.

Winterstein, T., and Stefan, H., 1983, Suspended sediment sampling in flowing water: Laboratory study of the effects of nozzle orientation withdrawal rate and particle size: Saint Anthony Falls Laboratory, External Memorandum M-168, University of Minnesota, 97 p.

S3.7 Movie captions

Movie S3.1. Side view of suspension-regime transport for D = 1.2 mm sand (u_*/w_s = 1.3) taken with a high speed camera (240 frame per second, total elapsed time is ~3.25 seconds).

Movie S3.2. View looking up through clear abrasion mill with D = 1.2 mm sand in suspension-regime transport (u_*/w_s = 1.3) taken with a high speed camera (240 frame per second, total elapsed time is ~3.25 seconds). The abrasion mill is 20 cm in diameter.

Movie S3.3. Side view of bedload regime transport for D = 6.8 mm gravel (u_*/w_s = 0.44) taken with a high speed camera (240 frame per second, total elapsed time is ~3.25 seconds).

Movie S3.4. View looking up through clear abrasion mill of bedload regime transport for D = 6.8 mm gravel (u_*/w_s = 0.44) taken with a high speed camera (240 frame per second, total elapsed time is ~3.25 seconds). The abrasion mill is 20 cm in diameter. Note radial particle velocity due to secondary circulation exists, but is substantially smaller than azimuthal particle velocity.

Table A1.1: Erosion rates for sediment of varying grain size under constant sediment load and shear stress*

Experiment ID	D_{16} (mm)	D (mm)	D_{84} (mm)	Volume Eroded (cm^3)	Measurement Technique†	Time Eroded (hr)	Volumetric Erosion Rate (cm^3/hr)	u_*/w_s §	% Viscously-Damped Impacts#	Corey Shape Factor	Powers Roundness
D-0.46-A	0.34	0.46	0.58	4.9	Scan	365.4	0.0134	2.9	99.7	0.5	2.5
D-0.46-B	0.34	0.46	0.58	6.1	Scan	365.4	0.0167	2.9	99.7	0.5	2.5
D-0.46-C	0.34	0.46	0.58	4.5	Scan	365.4	0.0122	2.9	99.7	0.5	2.5
D-0.46-D	0.34	0.46	0.58	6.6	Scan	430.0	0.0153	2.9	99.7	0.5	2.5
D-0.46-E	0.34	0.46	0.58	3.2	Scan	430.0	0.00746	2.9	99.7	0.5	2.5
D-0.46-F	0.34	0.46	0.58	4.9	Scan	430.0	0.0113	2.9	99.7	0.5	2.5
D-0.75-A	0.56	0.75	0.99	6.2	Scan	21.0	0.295	1.8	82.3	0.5	2.5
D-0.75-B	0.56	0.75	0.99	5.5	Scan	21.0	0.261	1.8	82.3	0.5	2.5
D-0.75-C	0.56	0.75	0.99	8.7	Scan	21.0	0.413	1.8	82.3	0.5	2.5
D-1.2-A	0.89	1.20	1.58	9.7	Scan	5.0	1.94	1.3	35.5	0.5	2.5
D-1.2-B	0.89	1.20	1.58	12.2	Scan	5.0	2.44	1.3	35.5	0.5	2.5
D-1.2-C	0.89	1.20	1.58	9.9	Scan	5.0	1.97	1.3	35.5	0.5	2.5
D-1.2-D	0.89	1.20	1.58	6.1	Scan	2.5	2.45	1.3	35.5	0.5	2.5
D-2.0-A	1.55	2.02	2.50	25.5	Scan	1.5	17.0	1.00	7.26	0.48	2.5
D-2.0-B	1.55	2.02	2.50	29.8	Scan	1.5	19.8	1.00	7.26	0.48	2.5
D-2.0-C	1.55	2.02	2.50	29.8	Scan	1.5	19.9	1.00	7.26	0.48	2.5
D-2.0-D	1.55	2.02	2.50	23.5	Scan	1.5	15.6	1.00	7.26	0.48	2.5
D-2.4-A	2.0	2.4	2.8	73.0	Scan	1.5	48.6	0.61	3.77	0.69	5
D-2.4-A	2.0	2.4	2.8	60.0	Scan	1.5	40.0	0.61	3.77	0.69	5
D-6.8-A	5.6	6.8	8.0	29.8	Scan	0.3	89.3	0.44	<0.1	0.57	3.5
D-6.8-A	5.6	6.8	8.0	29.8	Scan	0.3	89.3	0.44	<0.1	0.57	3.5
D-6.8-A	5.6	6.8	8.0	58.0	Scan	0.3	174	0.44	<0.1	0.57	3.5
D-24-A	22.0	24.0	26.0	292.2	Scale	1.0	292	0.25	<0.01	0.5	4.5
D-24-B	22.0	24.0	26.0	156.3	Scale	0.5	313	0.25	<0.01	0.5	4.5
D-24-C	22.0	24.0	26.0	73.4	Scale	0.4	176	0.25	<0.01	0.5	4.5
D-24-D	22.0	24.0	26.0	40.6	Scale	0.4	97.5	0.25	<0.01	0.5	4.5
D-24-E	22.0	24.0	26.0	39.1	Scale	0.4	93.8	0.25	<0.01	0.5	4.5
D-40-A	-	40.9	-	182.8	Scale	0.5	366	0.16	<0.01	0.65	5.5
D-40-B	-	43.7	-	121.9	Scale	0.5	244	0.15	<0.01	0.65	5.5

[*] For all experiments, sediment loading was 70 g, propeller was set to 1000 RPM, and the substrate was 0.064 g/cm^3 foam with 0.324 MPa tensile strength and 3.92 MPa Young's modulus. Grains 2.02 mm in diameter and smaller were measured via particle image analysis with a Microtrac DIA, and D_{16}, D, and D_{84} are the 16th percentile, median, and 84th percentile grain size of the sediment used for erosion. Grains 2.4 mm in diameter and larger were hand sieved and manually measured; for these grains, D_{16}, D, and D_{84} represent the lower limit, average, and upper limit of the particle distribution, respectively. A single grain was used where D_{16} and D_{84} are not reported.

[†] Scan refers to eroded volume measured with sub-mm precision laser scanning, and scale refers to mass eroded measured with 0.1-g precision dry-weighing before and after experiments. The two methods gave similar results when both were performed, for certain cases mass loss measurements were advantageous over volume loss measurements, and vice versa (for example, low-density foam with small erooded volumes leads to negligible mass loss such that scan measurements are more accurate).

[§] u_* is the fluid shear velocity. w_s is the terminal settling velocity calculated for particles of size D using measured values of Corey Shape Factor and Powers Roundess and the Dietrich (1982) empirical formula.

[#] Percent of viscously damped impacts was calculated for particles of size D assuming damping of impacts for Stokes numbers <75, and impact velocities based on particle fall height and Gaussian turbulent fluctuations as parametrized in Lamb et al (2008).

Table A1.2: Erosion rate for foam of varying tensile strength and Young's modulus*

Experiment ID	Tensile Strength (MPa)	Young's Modulus (MPa)	Density (g/cm^3)	Run Time (hr)	Mass Loss (g)	Volumetric Erosion Rate (cm^3/hr)
Tensile-1-A	0.32	3.92	0.064	1.0	5.6	87.4
Tensile-1-B	0.32	3.92	0.064	1.0	6.6	103
Tensile-1-C	0.32	3.92	0.064	1.0	4.3	67.1
Tensile-1-D	0.32	3.92	0.064	1.0	5.2	81.2
Tensile-1-E	0.32	3.92	0.064	1.0	4.3	67.1
Tensile-1-F	0.32	3.92	0.064	2.0	7.0	54.6
Tensile-1-G	0.32	3.92	0.064	2.0	10.0	78.0
Tensile-1-H	0.32	3.92	0.064	2.0	9.7	75.7
Tensile-1-I	0.32	3.92	0.064	0.7	21.0	447
Tensile-2	0.50	5.38	0.096	4.0	20.6	53.6
Tensile-3	1.79	25.58	0.240	18.0	11.1	2.57
Tensile-4	2.70	47.18	0.320	67.0	11.4	0.531
Tensile-5	5.38	104.80	0.481	71.4	16.6	0.484
Tensile-6	9.20	186.04	0.641	121.2	2.0	0.026
Tensile-7	13.17	265.79	0.769	121.2	2.0	0.021
Tensile-8	16.62	329.56	0.961	168.0	4.0	0.025

* For all experiments, sediment loading was 150 g of 5.6-6.3 mm sieved grains, and propeller was set to 1000 RPM. Mass loss measurements were made by weighing discs before and after the experiment with a 0.1-g precision scale. Eroded discs are commercially available closed cell polyurethane foam (http://precisionboard.com). Tensile strength and Young's modulus are measured by the manufacturer using standard procedures (American Society for Testing and Materials standard D-1623).

Table A1.3: Da'an River suspension calculations[*]

Reach	Shields Stress	Bed Shear Stress (Pa)	D_{susp}[†] (cm)	Transport Stage[§]
Pre-uplift/upstream of uplift	0.091	221	0.98	2.0
Pond in 1999	0.016	38.8	0.19	0.36
Upstream of hinge	0.081	197	0.86	1.8
Downstream of hinge	0.18	437	2.2	4.0
Scarp/knickpoint in 2001	1.02	2480	15	23
Pond in 2004	0.047	114	0.50	1.0
Narrow knickpoint	50.6	123000	110	1100
Knickzone	0.4	971	6.1	8.9
Gorge downstream of knickzone in 2010	0.11	267	1.2	2.4

[*] Shields stress data and reach naming convention as reported by Cook et al. (2012). All calculations based on a water discharge of 1300 m^3/s.

[†] D_{susp} is the largest grain size capable of being within the suspension regime for the reported bed shear stress.

[§] Transport stage calculated assuming a critical Shields Stress of 0.045 (Cook et al., 2012).

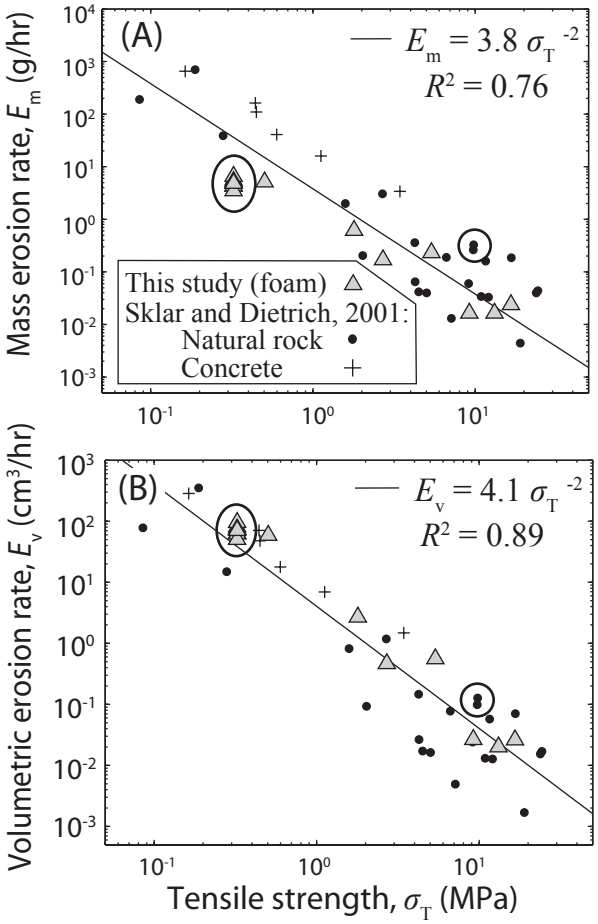

Figure A1.1. (A) Mass erosion rate (E_m) and (B) volumetric erosion rate (E_v) for foam, rock, and concrete versus tensile strength (σ_T). Solid lines in (A) and (B) show power-law best fit to the data, subject to the theoretical expectation that erosion is inversely proportional to the squre of tensile strength (Sklar and Dietrich, 2004). The similar scaling between erosion rate and tensile strength for variable-density foam and natural rock suggests that foam is a suitable rock analog. Circled triangles and dots correspond to the foam (σ_T= 0.32 MPa) and limestone (σ_T = 9.8 MPa) used in erosion-rate versus grain-size experiments (Figs. 3.3 and 3.4; Table A1.1). Mass erosion rates from Sklar and Dietrich (2001) were converted to volumetric erosion rates using densities provided by L. Sklar (personal communication, 2014).

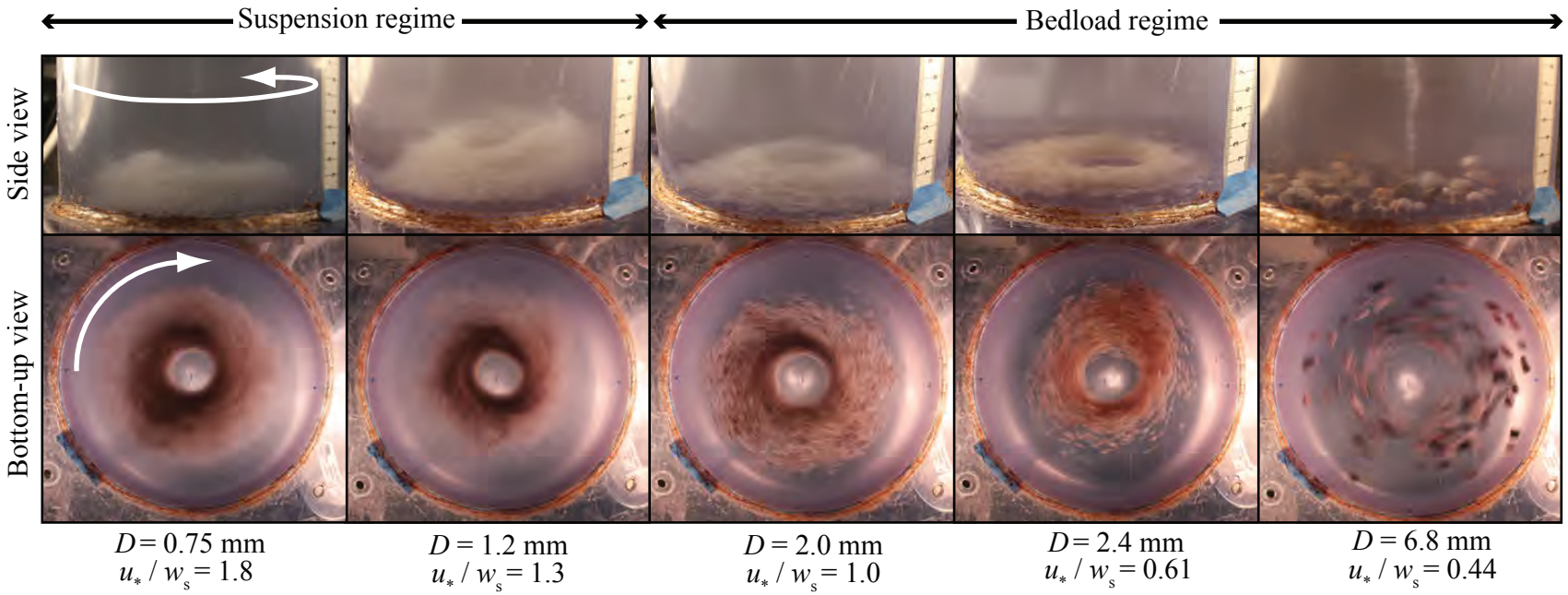

Figure A1.2. Side view and bottom-up view photographs showing sediment transport for five different grain sizes in abrasion mill experiments. White arrows indicate flow direction. For both cases, an unerodible clear bed was used for easier visualization. For bottom-up view photographs, note the orientation of particle streaks (due to slow shutter speed) indicate transport dominantly in the azimuthal flow direction. The sediment free area at the center of the mill is the location where the propeller-induced vortex impinges on the bed. In side view photos, ruler on right shows units of cm; in bottom view photographs, the abrasion mill is 20 cm in diameter for scale. Grains of 2.0 and 2.4 mm diameter were intermediate between exclusively bed load and full suspension, moving via long hop lengths, but with hop height rarely exceeding the predicted maximum bedload layer height of ~1.5 cm using the Sklar and Dietrich (2004) empirical relationship.

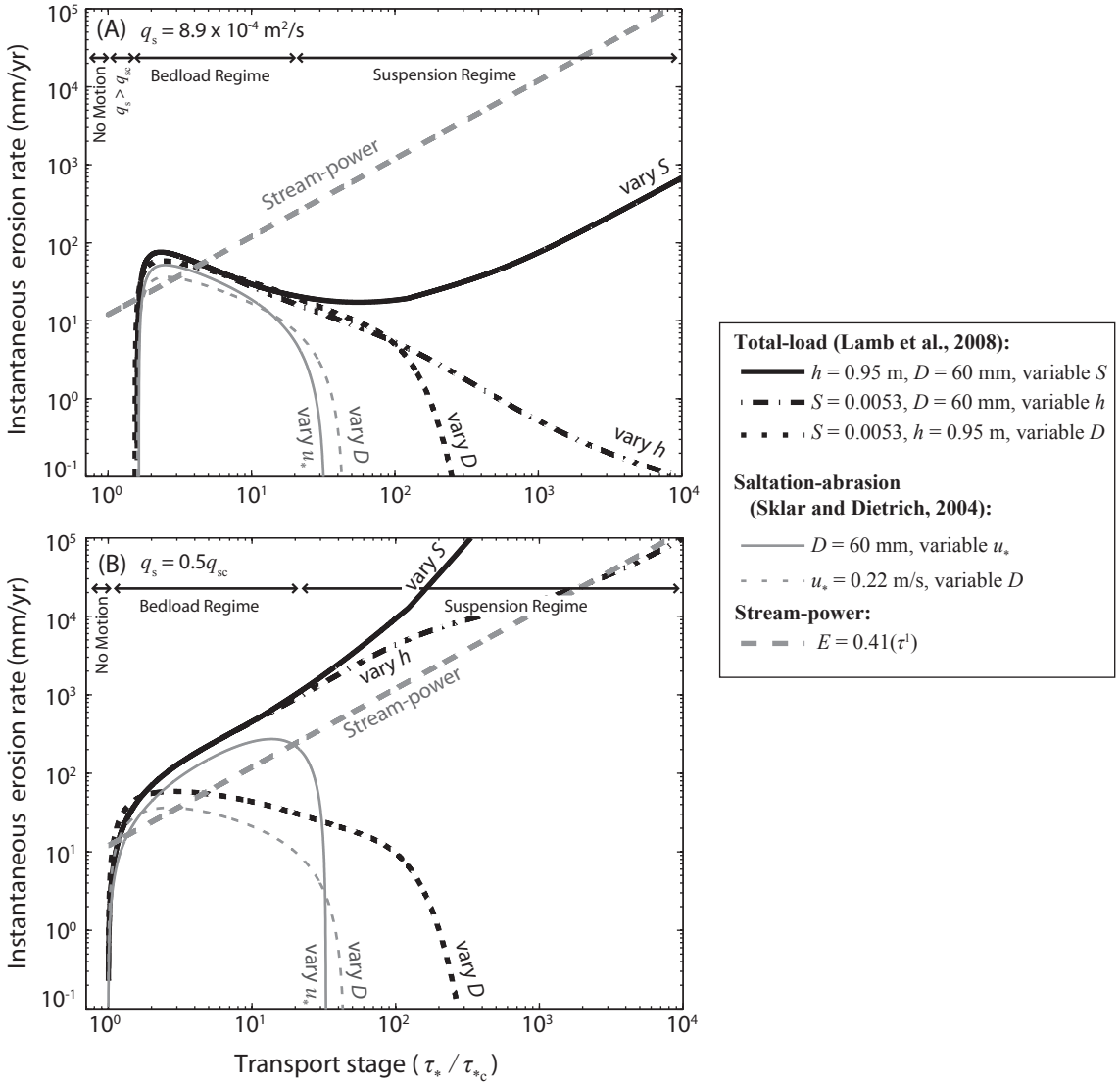

Figure A1.3. Erosion rate predicted with saltation-abrasion, total-load, and stream-power models under variable transport stage (τ_*/ τ_{*c}) for conditions representative of the South Fork Eel River, California. Transport stage was varied by changing one of either grain size (D), flow depth (h), or slope (S), while (A) holding sediment supply (q_s) constant or (B) setting sediment supply to half of the transport capacity (q_{sc}). Note the saltation-abrasion model is dependent upon shear velocity, u_* (i.e., the product hS), rather than h or S individually. Following Sklar and Dietrich (2004) we set base values of D, h, S, and q_s to 60 cm, 0.95 m, 0.0053, and 8.9 x 10^{-4} m^2/s, respectively. For all models rock tensile strength was 7 MPa, Young's modulus was 5 x 10^4 MPa, non-dimensional constant k_v was 10^6, and impacts with particle Stokes numbers < 75 were viscously damped. τ is bed shear stress.

C h a p t e r 4

SEDIMENT TRANSPORT THROUGH SELF-ADJUSTING, BEDROCK-WALLED WATERFALL PLUNGE POOLS

Joel S. Scheingross and Michael P. Lamb

Division of Geological and Planetary Sciences, California Institute of Technology, Pasadena, CA, 91125, USA

* Adapted from Scheingross and Lamb, "Sediment transport through self-adjusting, bedrock-walled waterfall plunge pools," currently under review, *Journal of Geophysical Research – Earth Surface*.

4.1 Abstract

Many waterfalls have deep plunge pools that are often partially or fully filled with sediment. Sediment fill may control plunge-pool bedrock erosion rates, partially determine habitat availability for aquatic organisms, and affect sediment routing and debris-flow initiation. Currently, there exists no mechanistic model to describe sediment transport through waterfall plunge pools. Here, we develop an analytical model to predict waterfall plunge-pool sediment-transport capacity by combining existing jet theory with sediment-transport mechanics. Our model allows calculation of plunge-pool sediment-transport capacity from field-measureable variables, and predicts plunge-pool sediment-transport capacity increases with increasing water discharge, waterfall drop height, and water velocity, and decreases with increasing plunge-pool depth, radius, and sediment grain size. Applying the model allows estimation of plunge-pool alluvial depth, and predicts that plunge pools self-adjust their depth in response to changes in imposed sediment supply. To test our theoretical predictions, we performed laboratory experiments measuring plunge-pool sediment-transport capacity under varying waterfall and plunge-pool geometries, flow hydraulics, and sediment size. These experiments support our conceptual model whereby plunge-pools self-adjust their alluvial depth to reach equilibrium with the imposed sediment supply; however, our theory has variable success in matching the observed depths. The model can be used to predict periods of sediment fill and evacuation in bedrock-walled plunge pools in response to variable water discharge and sediment supply.

4.2. Introduction

Landscape evolution in mountain areas is often set by waterfall processes, where waterfalls can retreat at rapid rates and dominate sediment production (Crosby and Whipple, 2006; Hayakawa et al., 2008; Mackey et al., 2014; DiBiase et al., 2015). Many waterfalls display deep, bedrock plunge pools at their base (e.g., Fig. 4.1). When present, such pools have been argued to focus bedrock erosion through undercutting of the waterfall face (e.g., Gilbert, 1890, 1907; Holland and Pickup, 1976; Young, 1985; Haviv et al., 2010) and vertical incision at the plunge-pool floor (Howard et al., 1994; Lamb et al., 2007), although additional waterfall-erosion mechanisms exist including toppling of bedrock columns (e.g., Young, 1985; Weissel and Seidl, 1997; Lamb and Dietrich, 2009).

Waterfall plunge pools can fill with sediment and evacuate to bedrock over annual timescales (Fig. 4.1A-D). When empty of sediment, plunge pools provide critical habitat for a wide range of aquatic organisms (Hawkins et al., 1993). Low water velocities within plunge pools may provide refuge for aquatic organisms during periods of high flow (e.g., Rempel et al., 1999). During warm periods, thermal stratification of deep pools provides cool water, allowing fish to escape lethal temperatures reached in shallower water (e.g., Matthews et al., 1994; Nielsen et al., 1994; Matthews and Berg, 1997; Torgersen et al., 1999). As water flow within river networks become disconnected during droughts, individual plunge pools provide isolated refugia for invertebrates and fish (Boulton, 2003; Lake, 2003; Magoulick and Kobza, 2003), and have been highlighted as areas of high priority for protection from disturbance and sedimentation (Bond et al., 2008). These ecological benefits are diminished when plunge pools partially or completely fill with sediment. In addition, plunge-pools completely filled with

sediment in steep mountain catchments pose a natural hazard, as the availability of a thick, alluvial deposit below a waterfall jet provides ideal conditions for mobilization of debris flows via the 'firehose effect' (e.g., Griffiths et al., 2004; Larsen et al., 2006; Godt and Coe, 2007). As such, developing plunge-pool sediment-transport capacity theory can aid land managers in predicting habitat availability and in natural hazards assessments

While there has been recent progress on predicting sediment transport in steep streams (e.g., Yager et al., 2007; Recking, 2009; Nitsche et al., 2011), including those with small vertical steps (Zimmermann et al., 2010; Yager et al., 2012), such models cannot be applied to waterfall plunge pools, where the impinging waterfall jet and deep plunge pool create significantly different hydraulics than those assumed in existing river sediment-transport models (e.g., Meyer-Peter and Mueller, 1948; Parker et al., 1982). Over long timescales, plunge-pool sediment –transport capacity is a key unknown needed to make more realistic waterfall retreat models (Lamb et al., 2007; Lamb et al., 2015), and the lack of a specific theory has led to the application of river-erosion models to waterfall plunge-pool systems which may be inappropriate (e.g., Seidl et al., 1994; Chatanantavet and Parker, 2006; Berlin and Anderson, 2007; Crosby et al., 2007; Loget and Van Den Driessche, 2009).

Most existing work on sediment transport through plunge pools has focused on soil-mantled landscapes where plunge pools form beneath small alluvial headcuts, and below man-made dams and sills. For example, Mason and Arumugam (1985) compiled laboratory and larger-scale prototype data from engineered overfalls and spillways to develop an empirical formula predicting maximum plunge-pool alluvial-scour depth for clear-water discharge. Field studies (Lenzi and Comiti, 2003; Lenzi et

al., 2003) and laboratory experiments (Lenzi et al., 2002; Gaudio and Marion, 2003; Marion et al., 2004; Tregnaghi et al., 2011) have led to empirical relations to predict geometry and time-evolution of scour holes formed beneath sills and check-dams. Similarly, Pagliara and colleagues have conducted extensive laboratory experiments evaluating the influence of jet impact angle, jet air entrainment, tailwater depth, grain size, clear-water discharge, and more on the dimensions and evolution of plunge-pools formed into loose sediment (e.g., Pagliara et al., 2008a; Pagliara and Palermo, 2008; Pagliara et al., 2010; Pagliara et al., 2012b). While the above studies focused on developing empirical relations, Stein et al. (1993) employ an approach which has been widely adopted (e.g., Bormann and Julien, 1991; Stein and Julien, 1993; Alonso et al., 2002; Hanson et al., 2002; Stein and LaTray, 2002) to predict the maximum scour depth of plunge pools below channel headcuts based on the threshold of grain motion.

Applying the existing work to bedrock plunge pools in mountain streams is difficult for two main reasons. First, existing work has focused on alluvial plunge pools carved into loose sediment where the plunge-pool geometry evolves over similar timescales to that of changes in flow hydraulics (e.g., Stein and Julien, 1993; Gaudio and Marion, 2003; Pagliara et al., 2008b; Tregnaghi et al., 2011) and sediment supply (e.g., Marion et al., 2006; Wells et al., 2010; Pagliara et al., 2011, 2012a). This is in contrast to bedrock-bound plunge pools carved into massive, crystalline rock and dominated by erosion from particle impacts (e.g. Fig. 4.1). For these plunge pools, the bedrock geometry likely evolves over order $10^2 – 10^5$ yr timescales, such that the flow hydraulics and geometry of bedrock walls are decoupled over the timescale of individual floods. Sediment fill, however, can be deposited on top of the bedrock floor, allowing alluvial

pool-depth to vary in response to changing hydraulics and sediment supply over individual flood timescales (e.g., Fig. 4.1).

Second, for plunge pools below channel headcuts and dams, there is often negligible sediment supply from upstream, thereby enhancing the ability of the waterfall jet to scour sediment from the plunge pool compared to a natural channel transporting sediment. Despite many studies on plunge-pool hydraulics (e.g., Ervine et al., 1997; Robinson et al., 2000; Bennett and Alonso, 2005; Pasternack et al., 2007) and sediment transport under clear-water flow (Mason and Arumugam, 1985; Bennett et al., 2000; Lenzi et al., 2002; Pagliara et al., 2006), there exist a limited number of experiments addressing the influence of upstream sediment supply on resulting plunge-pool morphology (Marion et al., 2006; Wells et al., 2010; Pagliara et al., 2011, 2012a). There experiments show that plunge pools tend to shallow their alluvial depth in response to increasing sediment supply; however, no theory has been developed to date to predict equilibrium scour depth as a function of sediment supply. These rare studies illustrate the need to include sediment supply into mechanistic theory of plunge-pool sediment transport.

In this paper we focus specifically on sediment-transport mechanics at deep waterfall plunge pools which have bedrock-sidewalls and sediment deposited over bedrock floors (e.g., Fig. 4.1). We first propose a conceptual model where plunge-pool sediment-transport capacity is modulated by dynamic adjustment of pool alluvial-depth. Second we develop a physically-based model to predict the sediment-transport capacity and alluvial depth of bedrock-bound waterfall plunge pools. Third we describe controlled laboratory experiments designed to test the bedrock plunge-pool sediment-

transport model and we further explore model predictions and limitations. Fourth, we apply the model at field scale. Finally, we discuss the implication of these results in the context of bedrock plunge-pool sediment transport over short timescales and bedrock erosion over longer timescales.

4.3. Hypothesis and motivation

Similar to alluvial rivers which self-adjust their slope, width, and depth in response to changes in sediment supply (e.g., Mackin, 1948; Lane, 1955), we envision bedrock-bound waterfall plunge pools are dynamic systems that self-adjust their alluvial depth to maintain an equilibrium between plunge-pool sediment-transport capacity (Q_{sc_pool}, units of [L^3/T], see Notation section at end of document) and the imposed sediment supply from upstream (Fig. 4.2). For example, a bedrock plunge-pool that reaches an equilibrium, steady-state alluvial depth for a given sediment supply and water discharge is expected to deposit sediment and aggrade to a new equilibrium alluvial depth following an increase in sediment supply or decrease in water discharge. Conversely, following a decrease in sediment supply or increase in water discharge, pools are expected to scour and deepen until either a new equilibrium alluvial depth is reached or the bedrock plunge-pool floor is exposed. Changes in plunge-pool alluvial depth influence Q_{sc_pool} in at least two distinct ways. First, decreasing alluvial pool-depth results in a reduction in shear stress at the pool floor, as the waterfall jet must diffuse through a deeper water column before impinging upon the bed, thus decreasing the ability of the jet to entrain sediment (e.g., Albertson et al., 1950; Rajaratnam, 1976; Stein et al., 1993). Changes in alluvial pool-depth likely also influence lift forces within the pool, although

this effect has yet to be studied in detail (Fiorotto and Rinaldo, 1992; Pasternack et al., 2007). Second, as alluvial pool-depth increases, sediment must be suspended higher in the water column in order to be transported out and over the plunge pool-lip and into the river reach downstream. Under this framework, plunge pools formed from clear-water overspill such as those below dams and sills (e.g., Mason and Arumugam, 1985; Gaudio et al., 2000; Bollaert and Schleiss, 2003), should have deeper alluvial depths than natural plunge pools, all else held constant, due to the presence of upstream sediment supply in natural systems (e.g., Marion et al., 2006; Wells et al., 2010; Pagliara et al., 2011, 2012a).

To explore the potential validity of this hypothesis for natural waterfalls we conducted field surveys of 75 waterfall plunge-pool systems to estimate the degree of sediment filling in nature. The vast majority of the bedrock-bound plunge pools we surveyed had alluvial plunge-pool floors, and in many cases were completely filled with sediment to the level of the downstream plunge-pool lip (Table S4.1, Fig. 4.1, see Section 4.7.2 for field-survey details). Observations of sediment deposited over bedrock plunge-pool floors as well as cycles of sediment fill and evacuation suggest that plunge-pools dynamically adjust their alluvial depth in response to changes in water discharge and sediment supply. Quantitative predictions of sediment fill and evacuation from natural plunge pools therefore require theory to predict waterfall plunge-pool sediment-transport capacity, which we develop below.

4.4. Theory

We seek to develop theory to predict the sediment-transport capacity of waterfall plunge pools that have fixed bedrock walls and fluctuating levels of alluvial fill.

The ideal theory should work over short timescales (i.e., individual flood events) during which fluid hydrodynamics and sediment transport are coupled to allow for predictions of evolving plunge-pool alluvial depth, but should also be computationally tractable to use over geomorphic timescales where plunge-pool bedrock geometry evolves due to abrasion from impacting particles (e.g., Lamb et al., 2007). This approach is akin to a geomorphic transport law (sensu Dietrich et al., 2003), and should allow for coupling with existing sediment-transport and bedrock-erosion models such that waterfall plunge-pool sediment transport and erosion processes can be included in larger-scale river long-profile and landscape evolution models. Self-adjustment of bedrock plunge-pool alluvial depth in response to changes in sediment supply and flow hydraulics allows sediment transport-capacity models to predict equilibrium alluvial plunge-pool depth via iteratively solving for the depth at which the plunge-pool sediment-transport capacity is equal to the imposed sediment supply from upstream.

Natural plunge pool exhibit complex velocity patterns where the impinging waterfall jet spreads within the pool before impacting the bed and circulates (e.g., Robinson et al., 2000; Bennett and Alonso, 2005; Pasternack et al., 2007). Determining such flow fields requires running computationally-intensive 3D numerical simulations (e.g., Xu et al., 2002) which goes against our goal of developing theory which can be applied over geomorphically-relevant timescales. Instead, we make simplifying assumptions for the plunge-pool geometry and flow field which allow us to develop an analytical solution. Our model is simplified to cylindrical, bedrock plunge-pools, and allows for the deposition or scour of a planar alluvial fill deposited over a bedrock plunge-pool floor (e.g., Figs. 4.1F, 4.2). Following advances in river sediment-transport

capacity, we develop a 1-D (radially-averaged) sediment-transport capacity for bedrock plunge pools under assumptions of a channel-spanning pool, and a circular waterfall jet which impacts the center of the plunge-pool floor. We hypothesize that sediment transport is most sensitive to vertically-directed flow, as it is this flow which suspends grains above the plunge-pool lip, allowing transport out of the pool. To this end, we simplify water flow within the plunge pool by assuming the pool can be divided into two separate, cylindrical regions, a "jet-descending region" where the waterfall jet flows downwards to the plunge-pool floor and entrains sediment, and a "jet return-flow region" where upward-directed flow carries sediment to the water surface and out of the pool (Fig. 4.2). We neglect radial advection of sediment between the two regions, and instead drive radial transport by turbulent diffusion.

Throughout the theory development we describe plunge-pool hydraulics and sediment transport within a radial coordinate system with an origin at the point of jet impact on the plunge-pool floor where the vertical (z) and radial (r) coordinates are positive in the upward and outward direction, respectively (Fig. 4.2).

4.4.1: Plunge-pool bed shear stress

In our theory, the impinging waterfall jet provides shear stress to entrain and suspend sediment within the jet-descending region. Existing river and jet hydrodynamic theory show that water flow accelerates towards the brink of the waterfall due to the loss of hydrostatic pressure (Rouse, 1936, 1937b; Hager, 1983), and, once past the brink, the waterfall jet is commonly modeled as accelerating during freefall through the air (e.g., Stein et al., 1993; Ervine et al., 1997). The jet decelerates after impacting the water surface of the plunge pool, but this deceleration is not immediate. The jet first

travels a finite length below the water surface before the friction from the surrounding water is felt at the jet centerline, and the velocity of the jet centerline only begins to decrease for depths beyond this length. We adopt terminology from the jet hydraulics literature (e.g., Albertson et al., 1950; Rajaratnam, 1976), where the zone in which the jet centerline maintains constant velocity is referred to as the Zone of Flow Establishment (ZOFE), and the zone where the jet velocity decreases with distance is known as the Zone of Established Flow (ZOEF) (Fig. 4.2).

We calculate plunge-pool bed shear stress, τ_{pool}, where the waterfall jet impinges on the alluvial plunge-pool floor following the framework of Stein et al. (1993) which is commonly used to model soil headcuts (e.g., Stein and Julien, 1993; Alonso et al., 2002; Hanson et al., 2002; Flores-Cervantes et al., 2006). Within the jet-descending region, τ_{pool} is calculated as

$$\tau_{pool} = \rho C_{f\_pool} u_{impact}^2 , \qquad (4.1)$$

where C_{f_pool} is an empirical friction factor and ρ is fluid density, and u_{impact} is the waterfall jet velocity at impact with the plunge-pool floor. u_{impact} depends on whether the jet is within the ZOEF or ZOFE, such that calculating u_{impact} first requires an estimate of the length scale of the ZOFE, λ, which is commonly represented as (e.g., Stein et al., 1993)

$$\lambda = 2C_d^2 r_{jet} \sin\beta . \qquad (4.2)$$

Here C_d is a diffusion constant empirically found to be ~2.6 for plunge pools (Beltaos and Rajaratnam, 1973; Beltaos, 1976), r_{jet} is the radius of the waterfall jet, and β is the angle of jet impact with respect to the plunge-pool water surface. We calculate β

from the water velocity at the waterfall upstream lip, u_{brink}, and the waterfall drop height, H_{drop}, i.e.,

$$\beta = \tan^{-1}\left(\frac{\sqrt{2gH_{drop}}}{u_{brink}}\right) . \qquad (4.3)$$

Stein et al. (1993) does not offer a method to calculate the jet radius. We assume a circular jet and apply conservation of mass (i.e., $Q_w = u_{jet} A_{jet}$, where Q_w is water discharge and u_{jet} and A_{jet} are the jet water velocity and cross-sectional area at impact with the plunge-pool water surface, respectively) to solve for r_{jet} as

$$r_{jet} = \left(\frac{A_{jet}}{\pi}\right)^{1/2} = \left(\frac{Q_w}{\pi u_{jet}}\right)^{1/2} . \qquad (4.4)$$

The velocity of the waterfall jet at impact with the plunge-pool water surface is calculated assuming conservation of energy and neglecting jet break-up or slowing due to air drag and wind, i.e.,

$$u_{jet} = \sqrt{u_{brink}^2 + 2gH_{drop}} . \qquad (4.5)$$

The jet-centerline velocity within the plunge pool is constant with depth in the ZOFE (i.e., for $z > z_\lambda$, where z_λ is the elevation at the boundary between the ZOFE and ZOEF) and decreases with depth within the ZOEF (i.e., for $z < z_\lambda$). Jet impact velocity on the pool floor can be calculated following well-established theory as (e.g., Albertson et al., 1950; Stein et al., 1993),

$$u_{impact} = u_{jet} \text{ for } z_{sed} > z_\lambda , \qquad (4.6a)$$

$$u_{impact} = u_{jet}\sqrt{\frac{\lambda}{z_{water} - z_{sed}}} \text{ for } z_{sed} < z_\lambda , \qquad (4.6b)$$

where z_{water} and z_{sed} are the elevations of the plunge-pool water surface and plunge-pool floor, respectively. Note that if no sediment is deposited on the pool floor, $z_{sed} = z_{BR}$, where z_{BR} is the elevation of the plunge-pool bedrock floor.

Combining Eqs (1) – (6) allows calculation of plunge-pool shear stress from upstream flow conditions (u_{brink} and Q_w), waterfall plunge pool geometry (z_{sed} and H), tailwater elevation (z_{water}) and constants (C_{f_pool} and C_d), i.e.,

$$\tau_{pool} = \rho C_{f\_pool}(u_{brink}^2 + 2gH_{drop}) \text{ for } z_{sed} > z_\lambda \ , \qquad (4.7a)$$

$$\tau_{pool} = \rho C_{f\_pool}(u_{brink}^2 + 2gH_{drop})\left[2C_d^2 \frac{Q_w^{1/2}}{\left(\pi\sqrt{u_{brink}^2 + 2gH_{drop}}\right)^{1/2}(z_{water} - z_{sed})} \sin(\tan^{-1}[\sqrt{2gH_{drop}} / u_{brink}])\right]^{1/2}$$
$$\text{for } z_{sed} < z_\lambda < 1 \ , \qquad (4.7b)$$

Calculating τ_{pool} requires an estimate of the flow velocity at the waterfall brink. The loss of hydrostatic pressure at the waterfall lip causes flow to accelerate towards the brink, such that u_{brink} can be solved for straight 1-D escarpments following established theory (Rouse, 1936, 1937b; Hager, 1983) as

$$u_{brink} = u_n\left(\frac{0.4 + \mathrm{Fr_n^2}}{\mathrm{Fr_n^2}}\right) \text{ for } \mathrm{Fr_n} > 1 \ , \qquad (4.8a)$$

$$u_{brink} = u_n\left(\frac{1.4}{\mathrm{Fr_n^{2/3}}}\right) \text{for } \mathrm{Fr_n} < 1 \quad , \qquad (4.8b)$$

For horseshoe-shaped waterfalls where flow converges laterally, Eq. (4.8) can be replaced with the theory of Lapotre and Lamb (2015). $\mathrm{Fr_n}$ and u_n in Eq. (4.8) are the Froude number and flow velocity under the assumption of normal flow, which is expected to occur upstream of the waterfall. $\mathrm{Fr_n}$ is the ratio of water velocity relative to the shallow water wave speed and is defined as

$$Fr_n = \frac{u_n}{\sqrt{gh_n}} \quad , \tag{4.9}$$

where h_n is the normal flow depth upstream and g is gravitational acceleration (Fig. 4.2). Due to the normal flow assumption (i.e., $\tau_{river} = \rho g h_n S = \rho C_{f\_river} u_n^2$, where τ_{river} and C_{f_river} are the river-bed shear stress and friction-factor, respectively), Fr_n can also be represented by the ratio of channel slope, S, and C_{f_river}, i.e.,

$$Fr_n = \sqrt{\frac{S}{C_{f\_river}}} \quad . \tag{4.10}$$

Finally, we estimate the tailwater depth ($z_{water} - z_{lip}$, where z_{lip} is the elevation of the downstream plunge-pool lip, Fig. 4.2) by assuming conservation of mass for water flow (i.e., $Q_w = u_{lip} W [z_{water} - z_{lip}]$, where W is reach-averaged channel width) and a Froude number of 1 at the downstream plunge-pool lip such that

$$\sqrt{g(z_{water} - z_{lip})} = u_{lip} = \frac{Q_w}{W(z_{water} - z_{lip})} . \tag{4.11}$$

Equation (4.11) can be rearranged to solve for z_{water} directly, and, when combined with measurements of the elevation of the plunge-pool alluvial or bedrock floor, can be used to determine the plunge-pool alluvial depth ($z_{water} - z_{sed}$).

Combining Eqs. (4.7) - (4.11) and again assuming conservation of mass for water flow ($Q_w = u_n W h_n$) allows τ_{pool} to be calculated from five field-measureable variables (z_{sed}, H_{drop}, Q_w, S, W) and five key constants (C_d, C_{f_pool}, C_{f_river}, g, ρ).

Many empirical relations exist to estimate C_{f_river} (e.g., Garcia, 2008), and relationships are often based on ratios of channel roughness or grain size (D) to flow depth, e.g.,

$$C_{f\_river} = [8.1(h_n / D)^{(1/6)}]^{-2} \quad . \qquad (4.12)$$

Parker (1991) compiled data for sand and gravel-bedded streams showing a range in C_{f_river} from ~ $10^{-3} - 10^{-1}$. In comparison to river friction factors, less work has been done to estimate the plunge-pool friction factor. Stein et al. (1993) estimate C_{f_pool} with a Blasius flow assumption, $C_{f\_pool} = 0.0275\left(\mathrm{Re}_{jet}\right)^{-0.25}$, where Re_{jet} is the waterfall jet Reynolds number. In natural plunge pools during conditions of sediment transport the waterfall jet should be fully turbulent ($\mathrm{Re}_{jet} >> 10^2$) such that C_{f_pool} should be independent of Re_{jet}, and we set $C_{f\_pool} = 10^{-3}$ here. This value falls within the range of river friction factors from the Parker (2008) compilation, and also within the range predicted by modifying Eq. (4.12) for plunge pools (i.e., $C_{f\_pool} = [8.1([z_{water} - z_{sed}] / D)^{(1/6)}]^{-2}$, which yields estimates of $10^{-4} < C_{f\_pool} < 10^{-2}$ for common values of plunge-pool alluvial depths and grain sizes).

4.4.2: Jet spreading and return flow

Within the ZOEF, the waterfall jet diffuses into the surrounding water, resulting in a reduction in velocity and an increase in planform area (e.g., Albertson et al., 1950; Rajaratnam, 1976). Decades of experimental work has shown that within the ZOEF turbulent jets decrease in velocity and increase in width as they extend further from the point of impingement with the water surface, and are characterized by self-similar velocity profiles (e.g., Abramovich and Schindel, 1963; Bradbury, 1965; Giger et al., 1991; Rowland et al., 2009). The radial spreading of the jet within the ZOEF is typically described by the length of its half-width, $b(z)$, which represents the radial distance at which the jet velocity has dropped to one half of the centerline velocity. Within the ZOEF ($z < z_\lambda$) we assume the half-width increases with increasing depth following existing

theoretical expectations and experimental observations (e.g., Abramovich and Schindel, 1963; Giger et al., 1991), such that

$$b(z) \approx 0.1(z_{water} - z - \gamma) \text{ for } z < z_\lambda , \qquad (4.13a)$$

where γ is a virtual origin which we assume is equal to 0. The half-width is less sensitive to depth within the ZOFE ($z_{sed} > z_\lambda$) (e.g., Albertson et al., 1950), such that we assume a constant half-width within this zone based on the half-width at $z = \lambda$, i.e.,

$$b(z) \approx 0.1(z_{water} - z_\lambda - \gamma) \text{ for } z > z_\lambda , \qquad (4.13b)$$

where we again assume $\gamma = 0$. For jets that impact the plunge-pool water surface at near vertical angles, Eq. (4.13b) reduces to $b(z) \approx 1.4 r_{jet}$.

At radial distances of $r > 2b(z)$ the jet velocity approaches that of the surrounding fluid, and we define the extent of the jet-descending region to be a vertically-oriented cylinder of radius $\delta = 2b(z=z_{sed})$ centered on the point of jet impingement on the plunge-pool floor (Fig. 4.2).

We define the jet return-flow region at radial distances $\delta < r < r_{pool}$, where r_{pool} is the plunge-pool radius. We assume water flows upwards in this region to return to the surface, thus providing a net upward directed current which can aid in the suspension and transport of sediment out of the plunge pool (Fig. 4.2). We estimate the averaged-upward velocity within the jet return-flow region, w_{up}, from conservation of mass, i.e.,

$$w_{up} = \frac{Q_w}{(A_{pool} - A_{jet})} , \qquad (4.14)$$

where $A_{pool} = \pi r_{pool}^2$ is the plunge pool cross-sectional area. Equation (4.14) represents a plunge-pool-averaged estimation, assuming w_{up} is constant with z and r. Note that Eq. (4.14) uses the jet radius at impact with the water surface rather than a radius based on

the size of the jet-descending flow region, this is because plunge-pool sediment-transport capacity is sensitive to conditions at the downstream plunge-pool lip. As such, we use an upward flow velocity that is most appropriate near the top of the plunge-pool, this should improve predictions of plunge-pool sediment transport capacity, but may create unrealistic predictions of return-flow velocity near the plunge-pool floor.

4.4.3: Plunge-pool sediment concentration

We track sediment concentration along the boundaries of the jet return-flow region of the plunge pool by solving an equation of conservation of mass for sediment concentration assuming radially-uniform flow where sediment is mixed due to turbulent diffusion from the waterfall jet and vertical advection from a balance between the upward-directed return flow and particle gravitational settling. This approach predicts sediment concentration decays non-linearly with distance above the plunge-pool floor and away from the sediment source zone, and is similar to classic descriptions of vertical sediment concentration in low-gradient rivers (e.g., Rouse, 1937a) and more recent attempts to describe lateral variation in sediment concentration across floodplains (e.g., Pizzuto, 1987).

We assume particles are in suspension and follow the fluid such that, for steady flow within a cylindrical plunge-pool, the equation of conservation of sediment concentration, c, can be written as

$$\frac{1}{r}\frac{\partial}{\partial r}(ru_r c)+\frac{1}{r}\frac{\partial}{\partial \theta}(u_\theta c)+\frac{\partial}{\partial z}([w_{up}-w_s]c)=0 \ . \qquad (4.15)$$

Here θ is an azimuthal coordinate, u_r and u_θ, represent flow velocities in the radial and azimuthal directions, respectively, and w_s is particle gravitational settling velocity

(positive in the downward direction) which we calculate following Ferguson and Church (2004)),

$$w_s = \frac{RgD^2}{a_1 \nu + \sqrt{0.75 a_2 RgD^3}} \quad , \qquad (4.16)$$

where $R = (\rho_s - \rho)/\rho$ is the submerged sediment density with ρ_s as the sediment density, v is the kinematic fluid viscosity, and $a_1 = 20$ and $a_2 = 1.1$ are empirical constants. Equation (4.16) assumes a dilute flow; for cases of high sediment concentration grain-grain interactions may alter w_s predictions (Richardson and Zaki, 1954), but such effects are not considered here. We define the net particle settling velocity as $w_{net} = w_s - w_{up}$ which represents a balance between the upward return-flow and particle gravitational settling velocity.

Decomposing velocities and sediment concentration into temporal averages (denoted by overbars) and fluctuating components (denoted by prime marks), (i.e., $u_r(r,t) = \overline{u_r(r)} + u_r(r,t)'$, $w_{up}(t) = \overline{w_{up}} + w_{up}(t)'$, and $c(r,z,t) = \overline{c(r,z)} + c(r,z,t)'$ where t is time (i.e., Reynolds decomposition)), neglecting the mean radial velocity based on our assumption of purely vertical flow (i.e., $\overline{u_r(r)} = 0$), and assuming radially-symmetric flow allow Eq. (4.15) to reduce to

$$\frac{1}{r}\frac{\partial}{\partial r}(r\overline{u_r'c'}) + \frac{\partial}{\partial z}(\overline{w_{up}'c'}) - w_{net}\frac{\partial \bar{c}}{\partial z} = 0 \quad , \qquad (4.17)$$

Equation (4.17) states that variation in sediment concentration throughout the plunge-pool is set by a balance between turbulent diffusion and particle settling, and neglecting radial advection in Eq. (4.17) is partially supported by a recent study showing turbulent kinetic energy is a better predictor of scour in alluvial plunge-pools compared

to bed shear stress (Ghaneeizad et al., 2015). Solving Eq. (4.17) throughout the plunge-pool requires applying boundary conditions that are difficult to determine. As plunge-pool sediment transport capacity is sensitive to sediment concentrations at the downstream plunge-pool lip, we solve for sediment concentration only along boundaries at the bottom of the pool and along the walls to avoid applying poorly-defined boundary conditions. We assume there exists a thin layer of well-mixed along the plunge-pool alluvial floor of thickness h_b, sediment similar in concept to a bedload layer, and define sediment concentration along boundaries at the pool wall ($r = r_{pool}$ and $h_b < z < z_{water}$) and floor within the jet return-flow region (i.e., $\delta < r < r_{pool}$ and $z = h_b$)

There is no radial flux of sediment through the plunge-pool walls, such that at $r = r_{pool}$ Eq. (4.17) reduces to

$$\frac{\partial}{\partial z}\left(\overline{w_{up}^{'}c^{'}(r_{pool},z)}\right) - w_{net}\frac{\partial\overline{c(r_{pool},z)}}{\partial z} = 0\,. \qquad (4.18)$$

This reduction is technically only valid at $z < z_{lip}$ as radial fluxes at $z_{lip} < z < z_{water}$ are responsible for transporting sediment out of the pool; however, for pools that are deep relative to the tailwater depth, Eq. (4.18) should approximately hold over all elevations. Equation (4.18) represents a balance between net particle settling and turbulent diffusion similar to classic descriptions of sediment suspension for shear flows (e.g., Rouse, 1937a). Following such practices, we represent the mixing of sediment against its concentration gradient with a kinematic eddy viscosity, v_e, making the additional assumption of constant v_e throughout the plunge pool,

$$\overline{w_{up}^{'}c^{'}(r_{pool},z)} = -v_e\frac{\partial\overline{c(r_{pool},z)}}{\partial z}\,, \qquad (4.19)$$

Substituting Eq. (4.19) into (18) and integrating under the condition of zero net vertical sediment flux at the water surface yields

$$\frac{d\overline{c(r_{pool},z)}}{dz} = -\frac{w_{net}}{v_e}\overline{c(r_{pool},z)} = -\frac{\overline{c(r_{pool},z)}}{L_d} \quad . \qquad (4.20)$$

The quantity v_e / w_{net} has represents a length scale (L_d) over which turbulence mixes sediment, similar in concept to a diffusion length scale. Large values of L_d indicate that turbulence is effective in mixing sediment throughout the pool and should contribute to higher sediment concentrations at areas away from the point of jet impingement on the bed; low values of L_d indicate particle settling dominates over turbulence, leading to enhanced sediment concentration near the point of jet impingement on the bed.

We solve for $c(r_{pool}, z)$ by integrating Eq. (4.20) and applying the boundary condition of a known reference sediment concentration at the top of the well-mixed layer, $c\ (r = r_{pool}, z = h_b) = c_0$,. Assuming L_d is not a function of z, this integration yields

$$\overline{c(r_{pool},z)} = c_0 \exp\left(-\frac{(z-h_b)}{L_d}\right). \qquad (4.21)$$

We take a similar approach to solve for sediment concentration at the top of the well-mixed layer within the jet return-flow region (i.e., $\delta < r < r_{pool}$ and $z = h_b$). Following our conceptualization of sediment mobilization within the jet-descending region, there is no entrainment of sediment within the jet return-flow region such that Eq. (4.17) reduces to

$$\frac{1}{r}\frac{\partial}{\partial r}\left(r\overline{u_r' c'(r,h_b)}\right) - w_{net}\frac{\partial\overline{c(r,h_b)}}{\partial z} = 0 \quad . \qquad (4.22)$$

We again represent the mixing of sediment radially against its concentration gradient with a kinematic eddy diffusivity which is assumed to be the same as in Eq. (4.19), i.e.,

$$\overline{u_r' c'(r, h_b)} = -v_e \frac{\partial \overline{c(r, h_b)}}{\partial r} \quad . \tag{4.23}$$

Substituting Eq. (4.23) into (22), and, for simplicity, assuming that v_e is not a function of r, yields

$$\frac{\partial^2 \overline{c(r, h_b)}}{\partial r^2} + \frac{1}{r} \frac{\partial \overline{c(r, h_b)}}{\partial r} + \frac{w_{net}}{v_e} \frac{d\overline{c(r, h_b)}}{dz} = 0 \quad . \tag{4.24}$$

Equation (4.24) is a second-order linear partial differential equation which we solve using separation of variables and by applying boundary conditions of no sediment flux at the plunge-pool walls, known sediment concentration, c_b, at the boundary between the jet-descending and return-flow regions, and that sediment concentration along the floor and walls must match at ($r = r_{pool}$, $z = h_b$), i.e.,

$$\frac{\partial \overline{c(r_{pool}, h_b)}}{\partial r} = 0 \quad , \tag{4.25a}$$

$$\overline{c(\delta, h_b)} = c_b \quad , \tag{4.25b}$$

$$\overline{c(r_{pool}, h_b)} = c_0 \exp\left(-\frac{(z - h_b)}{L_d} \right) = c_0 \quad , \tag{4.25c}$$

Solving Eq. (4.24) with the boundary conditions specified in Eq. (4.25) yields

$$\overline{c(r, h_b)} = c_b \left(\frac{I_0(r / L_d) + \dfrac{I_1(r_{pool} / L_d)}{K_1(r_{pool} / L_d)} K_o(r / L_d)}{I_0(\delta / L_d) + \dfrac{I_1(r_{pool} / L_d)}{K_1(r_{pool} / L_d)} K_0(\delta / L_d)} \right), \tag{4.26}$$

where the c_0 term has canceled out. I_0, K_0, I_1, and K_1 in Eq. (4.26) are the modified Bessel functions of the first and second kind of order 0 and 1, respectively, and appear in Eq. (4.26) due to the cylindrical geometry imposed. Formulating the same problem in a rectangular geometry would yield a solution with cross-stream exponential decay of sediment concentration, analogous to Pizzuto (1987), and may be more appropriate for waterfalls with wide, curtain-like jets. Note that Eq. (4.26) is derived specifically for the jet return-flow region and should hold $r > \delta$. For $r < \delta$ we set $\overline{c(r,h_b)} = c_b$ under the assumption that turbulence allows for well-mixed sediment concentration with respect to r within the jet-descending region.

Finally, combining Eq. (4.25c) and (26) to solve for c_0 yields our final equation to predicted sediment concentration along the plunge-pool wall,

$$\overline{c(r_{pool},z)} = c_b \exp\left(-\frac{(z-h_b)}{L_d}\right)\left(\frac{I_0(r/L_d)+\frac{I_1(r_{pool}/L_d)}{K_1(r_{pool}/L_d)}K_o(r/L_d)}{I_0(\delta/L_d)+\frac{I_1(r_{pool}/L_d)}{K_1(r_{pool}/L_d)}K_0(\delta/L_d)}\right), \qquad (4.27)$$

The exponential decay term in Eq. (4.27) describes the decrease in sediment concentration with distance above the bed, similar to the standard Rouse profile commonly used to predict sediment concentration in low-gradient rivers (Rouse, 1937a). This term differs from the Rouse profile in that it accounts for upward transport of particles via both turbulent diffusion and advection from the waterfall jet return flow, whereas the Rouse profile only includes turbulent diffusion as it was derived for rivers under steady uniform flow which do not experience net upward advection of sediment. The second term in brackets in Eq. (4.27) predicts a non-linear radial decay of sediment concentration with distance away from the sediment source zone.

Note that when $L_d < 0$ (which can occur if $w_{net} < 0$, i.e., upward advective velocity is greater than particle gravitational settling) we set $\overline{c(r_{pool}, z)} = c_b$ as the modified Bessel functions yield imaginary solutions for negative quantities. Finally, when $z < h_b$ (i.e., for pool depths shallower than the bedload layer) we remove the exponential term from Eq. (4.27) and set $\overline{c(r, h_b)} = c_b$ to avoid an exponential increase in sediment concentration with depth.

To apply Eq. (4.27) we must additionally specify means to calculate v_e, h_b, and c_b. Following the approach of Prandtl (1925), we assume v_e scales with turbulent fluctuations on the plunge-pool floor, which we represent with the plunge pool-shear velocity, u_{*pool}, as is commonly observed in open-channel flows (e.g., Nezu and Nakagawa, 1993), and a mixing length scale over which the impinging jet diffuses into the pool, for which we use λ, i.e.,

$$v_e = k_1(\tau_{pool} / \rho)^{1/2} \lambda = k_1 u_{*pool} \lambda . \qquad (4.28)$$

Here, k_1 is a coefficient which we set equal to 1. Similar Prandtl-style approaches have been previously applied to turbulent jets (e.g., Albertson et al., 1950; Abramovich and Schindel, 1963; Bradbury, 1965). These studies typically use a turbulent mixing length scale related to the jet half-width as they are primarily interested in describing the lateral spread of the jet within the ZOEF, whereas we seek a simple approximation of v_e that characterizes both radial and vertical turbulence throughout the plunge pool. Using a mixing length scale related to jet half-width instead of λ affects the absolute magnitude, but not the trends, of plunge-pool sediment-transport capacity predictions presented below.

We assume the height of the well-mixed zone of sediment near the bed extends to the peak saltation height of bedload particles, and estimate h_b with the empirical formula from the Sklar and Dietrich (2004) data compilation for non-cohesive particles with large particle Reynolds numbers, i.e., $h_b = 1.44D(\tau_{*pool} / \tau_{*c} - 1)^{0.5}$. τ_{*c} is the non-dimensional critical Shields stress for incipient grain motion which is observed to be approximately constant (i.e., $\tau_{*c} = 0.045$) for gravel-sized particles and larger (Buffington and Montgomery, 1997), τ_{*c} varies for smaller particle sizes but can be approximated based on the empirical fit of Brownlie (1981). τ_{*pool} is the non-dimensional Shields stress at the base of the plunge pool and is defined as

$$\tau_{*\mathrm{pool}} = \frac{\tau_{pool}}{(\rho_s - \rho)gD} \quad . \quad (4.29)$$

Following standard entrainment theory (e.g., van Rijn, 1984), we assume that for plunge-pools with alluvial-floors the near-bed sediment concentration is equal to the sediment entrainment rate, which scales with plunge-pool transport stage (τ_{*pool} / τ_{*c}), i.e.,

$$c_b = k_2 \left(\frac{\tau_{*\mathrm{pool}}}{\tau_{*\mathrm{c}}} - 1 \right)^{1.5} \quad . \quad (4.30)$$

For cases where $\tau_{*pool} < \tau_{*c}$, there is no sediment entrainment and we set $c_b = 0$. For very high transport stages c_b can grow to unreasonable values; we limit c_b to a maximum value 0.2 as $c_b > 0.2$ is often associated with debris flows where grain-grain interactions play an increasingly important role and the fluid/sediment mixture demonstrates different rheology than assumed in our theory for dilute sediment in water (Takahashi, 2014). k_2 in Eq. (4.30) is an empirical parameter which varies in existing literature. Van Rijn (1984) suggests k_2 is a function of grain size, and ranges from ~10^{-4}

$< k_2 < \sim 10^{-2}$ for reasonable sediment sizes. Re-arranging standard bedload transport models (e.g., Fernandez Luque and van Beek, 1976), to yield estimates of near-bed sediment concentration rather than bedload flux allows estimations of k_2 ranging from $\sim 10^{-3} < k_2 < \sim 10^{-1}$ depending on flow conditions. We set $k_2 = 0.02$ based on our experimental data (Section 4.6) and note it is within the range of reasonable values predicted from the literature.

Figure 4.3 shows profiles of sediment concentration along the bed and walls normalized near-bed concentration for an example waterfall plunge pool. Note that $\overline{c(r, h_b)} / c_b$ is predicted to be constant and equal to 1 for $r < \delta$; this area represents well-mixed sediment within the jet-descending region. Similarly, $\overline{c(r_{pool}, z)} / c_b$ is constant for $z < h_b$ where we assume sediment is well-mixed in a thin layer near the plunge-pool floor. The combination of decay of sediment concentration with increasing radial and vertical distance from the point of jet impingement results in the plunge-pool lip having the lowest sediment concentration.

4.4.4: Plunge-pool sediment-transport capacity and equilibrium alluvial depth

For alluvial-floored pools, we define plunge-pool sediment-transport capacity (Q_{sc_pool}) as the flux of sediment transported from the plunge pool to the river reach immediately downstream, and calculate Q_{sc_pool} as the product of water discharge (Q_w) and the average sediment concentration at the downstream plunge-pool lip, i.e.,

$$Q_{sc\_pool} = Q_w \int_{z=z_{lip}}^{z=z_{water}} \overline{c(r_{pool}, z)} dz \quad . \qquad (4.31)$$

For plunge pools that have large alluvial depths relative to tailwater thickness, Eq. (4.31) can be approximated by

$$Q_{sc\_pool} = Q_w \overline{c(r_{pool}, z_{lip})} \ . \qquad (4.32)$$

Combining, existing plunge-pool bed shear stress theory, standard flow hydraulics upstream of the waterfall, jet spreading and return flow, and our model for plunge-pool sediment concentration allows for an analytical expression of Q_{sc_pool} based on 7 field-measureable variables (Q_w, r_{pool}, z_{sed}, D, H_{drop}, S, and W) and 9 key constants (C_{f_river}, C_{f_pool}, C_d, k_1, k_2, γ, ρ, ρ_s, and g) from Eqs. (4.7) – (4.11), (4.13), (4.14), (4.16), and (4.27) - (4.31). Note that due to the exponential and modified Bessel function terms in Eq. (4.27), Q_{sc_pool} only goes to zero in the limit when z or r go to infinity, or when $c_b = 0$. Following standard practice for bedload transport threshold of motion, we set $Q_{sc\_pool} = 0$ when sediment flux falls below a dimensionless reference level ($Q_{sc\_pool} = 0$ for $Q_{*s\_pool} < 2 \times 10^{-5}$, where $Q_{*s\_pool} = Q_{sc\_pool} / (2r_{pool}RgD^3)^{1/2}$ is the dimensionless sediment flux) (e.g., Parker and Klingeman, 1982; Parker et al., 1982). Finally, while we have formulated the above model to predict sediment-transport capacity, the model can also be used to predict equilibrium plunge-pool alluvial depth under an imposed sediment flux from upstream by iteratively solving for the depth at which the plunge-pool sediment-transport capacity is equal to the imposed sediment supply. In this case, if the predicted equilibrium alluvial-depth is deeper than the plunge-pool bedrock floor, the pool is predicted to be free of sediment cover.

4.4.5: Non-dimensionalization

Inspection of Eqs. (4.27), (4.30), and (4.32) shows that $\overline{c(r_{pool}, z_{lip})}$ can be predicted from four non-dimensional variables,

$$\overline{c(r_{pool}, z_{lip})} = \frac{Q_{sc\_pool}}{Q_w} = f\left(\frac{\tau_{*pool}}{\tau_{*c}}, \frac{(z_{lip} - h_b)}{L_d}, \frac{r_{pool}}{L_d}, \frac{\delta}{L_d}\right) . \qquad (4.33)$$

Here, Q_{sc_pool}/Q_w is the ratio of plunge-pool sediment-transport capacity to water discharge and is equal to sediment concentration at the pool lip (Eq. 32). $\tau_{*pool}/\ \tau_{*c}$ is the plunge-pool transport stage, and is a function of six independent variables (Q_w, W, S, H_{drop}, z_{sed}, and D) and five key constants (C_{f_pool}, C_{f_river}, C_d, R, and g) . Entrainment of sediment from the plunge-pool floor only occurs when $\tau_{*pool}/\ \tau_{*c} > 1$; however, note that unlike standard low-gradient river bedload transport models (e.g., Meyer-Peter and Mueller, 1948), $\tau_{*pool}/\ \tau_{*c} > 1$ is a necessary but insufficient condition for $Q_{sc\_pool} > 0$. This is because sediment transport out of the waterfall plunge pool requires both entrainment of particles from the plunge-pool floor and suspension of particles up and over the plunge-pool lip.

Suspension of sediment out of the plunge pool is governed by the remaining three non-dimensional terms in Eq. (4.33), which all compare a length related to the plunge pool or jet geometry relative to the sediment diffusion length L_d. The term $(z_{lip} - h_b) / L_d$ governs the vertical distribution of sediment concentration in our model, such that when L_d is large relative to $(z_{lip} - h_b)$ sediment is efficiently mixed in the vertical direction, resulting in higher sediment concentrations at the top of the plunge pool, and larger sediment transport capacities. Both r_{pool}/L_d and δ /L_d characterize the lateral distribution of sediment concentration, but work in opposite ways. Large values of r_{pool} relative to L_d indicate the plunge pool is wide compared to the turbulent mixing length scale, resulting in lower sediment concentrations at the pool walls and smaller Q_{sc_pool}. In contrast, large values of δ relative to L_d indicate that the size of the sediment source zone from which the jet entrains is the dominant length scale influencing lateral sediment concentration, resulting in increased sediment concentration and Q_{sc_pool}. $(z_{lip} - h_b)/L_d$, r_{pool}/L_d, and δ /L_d

are all functions of seven independent variables (Q_w, W, S, H_{drop}, z_{sed}, r_{pool}, and D) and 8 key constants (C_{f_river}, C_{f_pool}, C_d, k_1, γ, ρ, ρ_s, and g).

4.5. Experimental methods

4.5.1 Experiment design and scaling

We designed laboratory flume experiments in order to test the quantitative predictions of our plunge-pool sediment-transport capacity model. We systematically and independently varied waterfall drop height, water discharge, grain size, and plunge pool radius in order to observe their effect on plunge-pool sediment-transport capacity and depth. We attempted to achieve dynamic similarity with natural waterfalls by keeping flow supercritical and in the fully turbulent regime (e.g., Paola et al., 2009). Reynolds numbers for our experiments varied between ~4000 – 5000 at upstream waterfall brink, and Reynolds particle numbers ranged from ~1000 - 4000 depending on flow discharge and grain size. Froude numbers at the waterfall brink ranged from ~1.5 – 2, similar to mountain rivers which typically have super-critical flow during floods.

Over 10 experimental sets, we made a total of 52 measurements of waterfall plunge-pool sediment-transport capacity, each with a unique combination of dimensional variables (Table S4.2). Ideally, we would design experiments to vary a single parameter in non-dimensional space; however, the self-adjustment of plunge-pool alluvial depth in response to changing sediment supply made this logistically challenging as all our non-dimensional parameters (i.e., Eq. 33) are functions of alluvial pool-depth. Instead, we designed our experiments so that the range of dimensionless variables explored overlapped in non-dimensional space with our measurements from natural waterfalls

(Fig. 4.4, Table S4.1, see Section 4.7.2 for field-survey details). Although our experimental waterfalls are smaller than natural waterfalls, the overlap in non-dimensional space should allow the dynamics in the experiments to be comparable to those in natural waterfalls (e.g., Lamb et al., 2015).

4.5.2: Experiment setup and methods

Our experimental set up (Fig. 4.5) consisted of a 9.6 cm wide and 2.06 m long upstream flume with a fixed rough bed of 2.4 mm sub-rounded quartz grains. The upstream flume was raised and cantilevered over a downstream flume (24 cm wide by 80 cm long) forming a waterfall where a fully-ventilated jet cascaded off the upstream flume and into a plunge pool positioned within the downstream flume below. Water and sediment spilled out from the plunge pool into the surrounding downstream flume and eventually into a tailbox from which a pump drew water to supply upstream. We designed our experiments to explore plunge-pool dynamics without complications from the downstream river sediment-transport capacity (e.g., the formation of bars or ridges at the downstream plunge-pool lip (e.g., Pagliara et al., 2008b)), thus sediment transported out of the plunge pool was immediately evacuated from the system. A pipe flow meter (with accuracy ± 1.5%) measured water discharge and measurements were confirmed by weighing the mass of water discharge collected in a bucket over 10-30 second increments. A rotating auger fed sediment from a hopper into the system immediately upstream of the waterfall brink allowing sediment flux into the plunge pool to be controlled independently from upstream river sediment-transport capacity (Fig. 4.5). We calibrated the auger feed rate by placing a mesh-bottomed bucket in the waterfall jet and weighing the mass of de-watered sediment collected over 60 second increments.

Unlike previous experiments evaluating plunge-pool scour in alluvial beds where jet hydraulics set the extent of the plunge-pool width and depth (e.g., Stein and Julien, 1993; Gaudio and Marion, 2003; Lenzi and Comiti, 2003; Pagliara et al., 2006; Wells et al., 2010), we used clear, cylindrical PVC tubes ranging from ~10 – 20 cm diameter as artificial plunge pools (Fig. 4.5b) to simulate the dynamics of bedrock-walled plunge-pools with fluctuating alluvial sediment fill (e.g., Figs. 4.1 and 4.2). Pipes were sufficiently deep so that the alluvial plunge-pool floor was free to self-adjust without hitting the pipe bottom. These smooth-walled tubes were placed within the downstream flume, and aligned so that the waterfall jet impacted the center of the tube. The angle of jet impact on the plunge-pool surface was dictated by the water discharge and waterfall drop height but was typically at angles of ~80 degrees, and we back-tilted the PVC tubes by ~10 degrees to force impingement perpendicular to the plunge pool walls. Pipe back-tilting allowed the jet to impinge directly on the plunge-pool alluvial floor, but also caused the downstream lip of the plunge pool to be raised to slightly higher elevations than the upstream lip. For plunge pools with diameters greater than ~15 cm, the ~2 cm difference in elevation between the upstream and downstream plunge-pool lip caused preferential water flow out the upstream end of the plunge pool; we mitigated this effect by affixing 10 degree wedges to the top of the PVC tubes creating plunge-pool tops perpendicular to gravity. We observed no preferential water flow out the upstream plunge-pool lip for 10.2 cm diameter pipes due to the smaller elevation difference between the upstream and downstream plunge-pool lip, and thus did not affix a wedge onto these plunge pools. Comparisons of plunge-pool depth and sediment flux for 10.2 cm diameter plunge pools with and without a wedge showed differences on the same

scale as the error associated with topographic bed roughness and variability in sediment feed rate.

We inferred plunge-pool sediment-transport capacity by feeding sediment at a known rate from upstream, and allowing the pool to reach a stable, steady-state depth such that the sediment flux into the pool equaled the sediment flux out. The imposed sediment flux from upstream was thus equal to the sediment-transport capacity of the plunge pool for the given experimental conditions at steady state. We designed experiments to exploit our conceptual model prediction of a dynamic relationship between plunge-pool depth and sediment-transport capacity whereby a pool self-adjusts its depth in order to pass the imposed sediment load. We measured plunge-pool sediment-transport capacity for several experimental sets. In each set, we forced self-adjustment of plunge-pool alluvial depth via changing the imposed sediment supply, while holding all other independent parameters constants.

Each experimental set began with a plunge pool filled with single-grain-size sediment and water. Imposing clear-water discharge caused the pool to scour to steady-state alluvial depth where the jet still entrained sediment, but was no longer able to suspend sediment out of the pool. After recording this depth, a small step-wise increase in sediment from upstream was imposed forcing aggradation of the pool to a new steady-state alluvial depth. This process was repeated with subsequent increases in sediment flux until the plunge pool either filled to its lip with sediment or the maximum sediment flux of the feeder was reached. For each steady-state depth, we measured the maximum, minimum, and average depths across the plunge-pool alluvial floor based on cm scale topographic variability; we use the difference between the maximum and minimum

depths as a representation of measurement error. At the end of the experimental set, we returned to clear-water discharge to confirm the pool alluvial depth returned to the original clear-water value observed at the set start. Each experimental set thus yielded multiple measurements of plunge-pool sediment-transport capacity as the pool self-adjusted its depth in response to the imposed sediment supply (Table S4.2). Steady-state alluvial depths following changes in imposed sediment flux were typically reached in < 1 minute, and we waited until pool depths were constant over a period of ~5-10 minutes (~10-15 minutes total wait time) before changing the imposed sediment flux. Assuming the entire sediment supply contributes to pool aggradation, the wait time expected to reach a steady-state alluvial depth (Δt_{wait}) can be calculated as $\Delta t_{wait} = \Delta z_{sed} A_{pool} / Q_s$, and our wait times varied from ~1.5 to 300 times Δt_{wait}, with an average of ~30 Δt_{wait}. Plunge-pool sediment beds typically had cm scale topographic variability across their surface as the impinging jet created a small scour hole at its point of impact. For each steady-state alluvial-bed configuration, we measured the maximum, minimum, and average plunge-pool depths with a ruler. We measured depth while the experiment was running (i.e., the dynamic depth (sensu, Pagliara et al., 2006)) to prevent sediment suspended in the water column from settling onto the bed which would result in artificially shallow depths.

We explored measuring sediment-transport capacity using narrow (7.8 cm diameter) pipes, but these experiments were subject to a host of problems. For these narrow pipes the waterfall jet diameter began to approach that of the pipe, and it was difficult to keep the jet centered within the pool and impinging on the plunge-pool alluvial floor. Small (order mm) shifts in the pipe location caused the jet to impinge on the pipe sidewalls rather than the alluvial-pool floor, and this resulted in changes in the

equilibrium alluvial pool-depth of the same order as achieved by varying sediment supply, thus complicating the analysis of these results. Furthermore, for many of these experiments the large waterfall jet to plunge-pool radius ratio allowed the jet to spread to $\delta > r_{pool}$ such that the entire plunge-pool floor was within the jet-descending region, violating our model assumption of distinct jet-descending and return-flow regions. Our model performed poorly when attempting to predict sediment-transport capacity for these narrow pipes, and we do not report the results from narrow pipe experiments here as they probe conditions for which our model was not designed to handle.

4.6. Experimental and theoretical results

In this section we first describe sediment transport observations from our flume experiments. We then present model predictions and experimental measurements of plunge-pool sediment-transport capacity under changing sediment supply, pool depth, water discharge, waterfall drop height, grain size, pool radius, and Froude number. Finally we compare our experimental results to existing plunge-pool scour depth formulae, evaluate the overall model performance, and discuss model limitations.

4.6.1: Sediment transport observations

For a typical experimental set, plunge pools initially completely filled with sediment rapidly scoured to deeper alluvial depths after turning on clear-water discharge. The rate of plunge-pool scour decreased as pools progressively deepened and approached their steady-state alluvial depth. At steady-state depth under clear-water discharge, sediment was mobilized from the bed, but not suspended high enough to be transported over the plunge-pool walls.

Following the onset of an imposed sediment flux from upstream, plunge-pool sediment transport continued to occur primarily via suspension of grains. The impinging jet created a small scour hole in the sediment bed where grains were initially entrained. Scour holes were characterized by steep walls which acted as ramps, and mobilized grains would roll or saltate a short distance up this ramp before becoming suspended in the return flow of the jet (Fig. 4.5b, Movie S1). Suspended grains were typically concentrated on the downstream side of the waterfall jet, but were observed throughout the plunge pool. Grains were suspended in a mixture of water and air (with air likely entrained by the impinging jet) and were brought to the top of the water column within this mixture before being transported out of the plunge pool as water spilled up and over the pool walls. Both the rate of entrainment of sediment and the vigor with which the water, air, and sediment mixture boiled over the plunge-pool walls appeared to fluctuate over timescales of order 1 s, likely reflecting turbulence within the pool.

As plunge pools aggraded to shallow alluvial depths, the concentration of sediment in the water column and vigor with which grains were suspended visually increased and an active layer of sediment transport developed near the plunge-pool floor. This active layer visually appeared to be ~5 grain diameters thick and was defined by a zone of highly concentrated grains below a more dilute layer above (although it was difficult to precisely and consistently define this boundary). Grains in the active layer were those which had moved through the jet-created scour hole and appeared to be in a state of incipient suspension (grains were partially suspended off the plunge-pool floor, and actively moving ~1-2 grain diameters up and down in the vertical direction). When pools aggraded sufficiently close to the plunge-pool lip (depths less than ~5 cm in our

experiments), the sediment bed appeared fluidized, and the pool rapidly aggraded the short remaining distance to the top of the pool lip, after which grains were transported out of the pool as bedload.

4.6.2: Influence of sediment supply and pool depth

In all our experiments, we observed plunge pools aggraded in response to step-wise increases in imposed sediment supply with all other parameters held constant (Fig. 4.6, Table S4.2). The magnitude of pool aggradation was typically greatest when switching from clear-water discharge to a small sediment supply, with subsequent increases in sediment supply resulting in continued aggradation, but at a magnitude that was often on the same order as the topographic roughness of the plunge-pool floor. An exception to this was for pools which aggraded to shallow enough alluvial depths to allow fluidization of the bed, and in turn rapid aggradation of the plunge pool (e.g., filled squares in Figs. 4.6C and D). For all experiments, plunge-pool equilibrium depth under clear-water flow was the same at the start and end of the experiment set within measurement error. We interpret observations of plunge-pool aggradation following an increase in sediment supply to be in agreement with our conceptual model of self-adjustment of alluvial plunge-pool depth to maintain equilibrium between sediment supply and transport capacity.

Our plunge-pool sediment-transport capacity model shows variability in its goodness of fit to the experimental data when setting the constant $k_2 = 0.02$ (solid lines in Fig. 4.6). In all cases, the model predicts sediment-transport capacity increases with decreasing plunge-pool depth in agreement with our experimental observations where pools aggraded their alluvial depth in response to increased sediment supply. The

relationship between plunge-pool alluvial depth and sediment-transport capacity is controlled by two main factors in our model. First, deeper alluvial-depths require sediment to be entrained higher in the water column in order to be transported out of the plunge pool, resulting in reduced sediment concentration at the plunge-pool lip, and, in turn, reduced values of Q_{sc_pool}. Second, within the ZOEF, τ_{pool} decreases with increasing pool depth, which in turn reduces both the entrainment of sediment from the pool floor (lower c_b) and the efficiency of turbulent mixing (lower L_d). This second influence disappears when $z_{sed} > z_\lambda$ and τ_{pool} is independent of alluvial-depth (Eq. 7), resulting in a different relationship between sediment supply and equilibrium-alluvial plunge-pool depth (this transition is marked by red stars in Fig. 4.6).

4.6.3: Influence of water discharge, waterfall drop height, and grain size

We explored the influence of changing waterfall drop height, water discharge, grain size, and pool radius on plunge-pool sediment-transport capacity by varying one of these parameters while holding all other variables constant. For the same imposed sediment load, plunge pools with greater water discharges in our experiments always had deeper alluvial floors than those with smaller discharges (Fig. 4.6A). Similarly, greater waterfall drop heights (Fig. 4.6B), and finer grain sizes always led to deeper alluvial pool-depth (Fig. 4.6C), all else held constant. Because plunge-pool alluvial depth tracks directly with plunge-pool sediment-transport capacity in our experiments, deeper alluvial pool-depths at the same imposed sediment supply imply higher sediment transport capacities such that we interpret our experimental observations as evidence that plunge-pool sediment-transport capacity increases with increasing waterfall drop height, increasing water discharge, and decreasing grain size.

While the exact value of theoretical predictions show variable success in predicting sediment-transport capacity (19 of 40 theoretical predictions agree with experimental observations within measurement error in Figs. 4.6A-C), the theory does capture the experimental observations which show that increasing water discharge, increasing waterfall drop height, and decreasing grain size all result in increased sediment-transport capacity (Fig. 4.6).

Increases in water discharge and waterfall drop height both increase the total energy that is delivered to the plunge pool; however changes in water discharge and drop height have distinct effects within our theoretical framework. Increases in water discharge lead to non-linear increases in Q_{sc_pool} in our model for three distinct reasons. First, because Q_{sc_pool} is calculated as the product of sediment concentration at the plunge-pool lip and water discharge (Eq. 31), increasing Q_w results in a direct increase in Q_{sc_pool} even for cases of constant sediment concentration. Second, w_{up} increases with water discharge due to both increased water flux and larger waterfall jet radii (which force the return flow through a smaller annulus) (Eq. 14), allow partially offsetting of gravitational particle settling, and in turn increased sediment concentration at the plunge-pool lip. Third, τ_{pool} increases with water discharge, which acts to increase both sediment entrainment (c_b) and turbulent mixing (L_d).

Unlike increasing water discharge which leads to wider waterfall jets and larger w_{up} values, increase in H_{drop} cause waterfall jets to narrow and w_{up} to decrease (Eqs. 4, 5, and 14). Despite this effect, plunge-pool sediment-transport capacity still increases with waterfall drop height in our model framework primarily due to the associated increase in waterfall jet velocity with H_{drop} (Eq. 5). Higher jet velocity acts to increase τ_{pool}, leading

to enhanced sediment entrainment and increased efficiency of turbulent mixing, as discussed above.

Increases in grain size decrease plunge-pool sediment-transport capacity in our model due to the decrease in transport stage and increase in particle settling velocity associated with larger grains. Note that, because τ_{pool} is independent of grain size, the decrease in transport stage with grain size (due to the normalization by D in calculating Shields stress) acts to lower c_b, but does not influence the kinematic eddy viscosity. However, the increased settling velocity for large particles does result in lowering L_d, ultimately leading to reduced sediment concentrations throughout the plunge pool.

4.6.4: Influence of plunge-pool radius

The influence of plunge-pool radius on sediment-transport capacity is not as straightforward in our experiments compared to changing Q_w, H_{drop}, and D. For experiments with D = 7 mm grains, plunge pools with r_{pool} = 7.7 cm were completed filled with sediment even for clear-water discharge, while narrow (r_{pool} = 5.1 cm) pools showed steady-state alluvial depths which decreased with increasing sediment supply. This trend is in agreement with our theory where decreasing plunge-pool radius leads to higher sediment-transport capacity and deeper equilibrium pool-depth (Fig. 4.6D). However, when using finer sediment (D = 2.4 mm), plunge pools of different radii had approximately the same depth (within measurement error) for identical forcing (with the exception of at the largest sediment fluxes when small differences in pool depth emerged), in contrast to our model predictions that sediment-transport capacity should increase with decreasing r_{pool} (Fig. 4.6E).

Increases in plunge-pool radius result in a reduction of Q_{sc_pool} in our model for two main reasons. First, increasing radius causes a decrease in sediment concentration at the plunge-pool lip as there is a longer length scale over which sediment must be transported (e.g., Fig. 4.3). Second, for a constant water discharge and jet diameter, increases in plunge-pool radius reduce w_{up} thereby enhancing the influence of particle gravitational settling (lowering L_d) and reducing sediment concentrations in the plunge pool.

The discrepancy in properly accounting for variations in plunge pool radius on sediment-transport capacity in coarse versus fine grain sediment may indicate a grain-size control on the size of the sediment source zone which is not accounted for in the model framework. If this is correct, performing replicate experiments with wider plunge pools and fine grain sizes would be expected to show similar behavior to that observed for coarse grain sizes (i.e., a decrease in sediment-transport capacity with increasing pool radius). Similarly, replicate experiments with narrower plunge pools and coarse grain sizes may be expected to show no variation in sediment-transport capacity with pool radius. However, performing experiments with $r_{pool} < 5.2$ cm is difficult as the plunge-pool diameter approaches that of waterfall jet, significantly complicating the interpretation of results as discussed above.

4.5.5: Influence of Froude number

Although not explored experimentally, our model predicts plunge-pool sediment-transport capacity is independent of Fr_n for subcritical flows ($Fr_n < 1$). This is because flow acceleration towards the waterfall brink results in a constant value of u_{brink} (Rouse, 1936, 1937b; Hager, 1983) for $Fr_n < 1$. For supercritical flows ($Fr_n > 1$),

increasing Fr_n gives increasing u_{brink} which raise τ_{pool} values (Eq. 7), ultimately leading to increases in Q_{sc_pool}; however, this effect is small compared to the influence of changing water discharge, waterfall drop height, grain size, pool depth, and pool radius examined above. Note that Fr may also play an additional role for 2-D waterfalls with lateral flow convergence (Lapotre and Lamb, 2015).

4.6.6: Comparison to previous models and overall model performance

There exist no previously published models capable of predicting waterfall plunge-pool sediment-transport capacity subject to sediment supply from upstream; however, there are multiple theories which predict maximum alluvial-plunge-pool depth under clear-water flow. We compared our experimental measurements of maximum clear-water alluvial-plunge-pool depth (Table S4.2) to predicted theoretical alluvial depths using a variety of existing models.

Theoretical model often assume clear-water pool-depth is set by the threshold of motion for sediment (e.g., Stein et al., 1993). To compare to such models, we calculated expected clear-water depths by solving for the alluvial pool-depth where $\tau_{*pool} < \tau_{*c}$ using Eq. (4.7) and setting $\tau_{*c} = 0.045$. This method causes over-prediction of observed steady-state depths by a factor of ~1.5 to 4 (Fig. 4.7A), suggesting that grain motion alone is not sufficient to explain sediment transport from deep, cylindrical pools. Our clear-water experiments showed sediment was mobilized from the alluvial-pool floor, but not suspended high enough to clear the plunge-pool lip, suggested that steady-state pool depths are set by the ability of the waterfall jet to suspend sediment out of the pool rather than be the ability to mobilize grains.

We also compared our clear-water results with prediction of steady-state alluvial-depth from the empirical models of Pagliara et al. (2006) and Mason and Arumugan (1985). These models produced mixed results with the Pagliara et al. (2006) model tending to over-predict experimental clear-water depths by up to a factor of ~2 (Fig. 4.7C), while the Mason and Arumugan (1985) model under-predicts our experimental alluvial depths up to a factor of ~2.5 (Fig. 4.7B). Part of this mis-match between experimental observations and model predictions may arise from the fact that these models are designed to predict scour depth of alluvial-pools with self-formed walls in contrast to our experiments with fixed, cylindrical walls. To partially mitigate this effect, we used the 2D Pagliara et al. (2006) model which more closely fits our conceptualization of bedrock-bound cylindrical pools than the 3D model which also exists (Pagliara et al., 2008a). Mis-match between experimental observation and Mason and Arumugan [1985] model predictions may also come from calibration of their model using a database which included scour of cohesive soils in contrast to the loose alluvium in our experiments.

Our model tends to over-predict equilibrium-alluvial clear water plunge-pool depth by up to a factor ~2 (Fig. 4.7D). This may occur in part due to the decay of sediment concentration in our model such that $\overline{c(r_{pool}, z_{lip})}$ is always positive for $\tau_{*pool}/\ \tau_{*c} > 1$. Steady-state clear-water pool depths are typically defined in our model for $\tau_{*pool}/\ \tau_{*c} > 1$ but where sediment transport falls below the reference Q_{*s_pool} value (e.g., $Q_{sc\_pool} = 0$ for $Q_{*s\_pool} < 2 \times 10^{-5}$, Section 4.4.4). Using a larger value of Q_{*s_pool} would shift points closer to the 1:1 line in Figure 4.7D; however, achieving agreement with theory predictions within a factor of ~1.5 requires unreasonably high Q_{*s_pool} values.

Models based on the threshold of motion (e.g., Stein et al., 1993) as well as the empirical models of Pagliara et al. (2006) and Mason and Arumugan (1985) are not designed to account for sediment supply, and predict a constant depth independent of sediment supply (as demonstrated by the shifting of points leftwards in Figs. 4.7A - C). The theory developed here accounts for the influence of upstream sediment supply, and shifts predictions of steady-state plunge-pool alluvial depth under variable sediment supply such that 37 of our 40 measurements match our theoretical predictions within a factor of ~1.5 with 19 of 40 measurements matching theoretical predictions within measurement error ($R^2 = 0.8$ when comparing to the 1:1 line in Fig. 4.7D). The ability to predict steady-state pool-alluvial depth subject to an imposed sediment flux allows examination of plunge-pool evolution in natural streams which cannot be adequately explored with existing clear-water only theory.

Predictions of plunge-pool sediment-transport capacity have increased variability compared to steady-state alluvial-depth predictions due to the non-linear relationship between Q_{sc_pool} and alluvial depth (Fig. 4.6). As such, our order cm scale measurement error in pool depth results in approximately order of magnitude variability in predictions of sediment-transport capacity. Accounting for this range in measurement error, 31 of our 40 measurements from our sediment supply experiments match our theory-predicted Q_{sc_pool} within a factor 1.5 (and 37 of 40 measurements match within a factor of ~2.5) (Fig. 4.6). For clear-water experiments at steady-state depths where $Q_{sc\_pool} = 0$ by definition, our model predicts $Q_{sc\_pool} > 0$, but is highly non-linear in this region (Fig. 4.6). While our predictions of sediment-transport capacity have higher error than steady-state pool depth, we note large errors are common in predictions of sediment-transport

capacity, for example using standard sediment-transport capacity equations in steep mountain streams often leads to order of magnitude or larger error (e.g., Recking, 2010; Nitsche et al., 2011; Yager et al., 2012).

4.6.7: Discussion of limitations of model predictions

Our plunge-pool sediment-transport capacity model has variable success in matching the experimentally-observed values of plunge pool steady-state alluvial depth. This could occur due to incorrect parameterizations of constants within our model (e.g., k_2, C_{f_pool}, ν_e, etc.), or due to the lack of inclusion of important physical processes within our model framework. We explored the effect of changing the sediment entrainment coefficient k_2, the mixing length-scale and coefficient k_1 (which determine the eddy viscosity ν_e), and the plunge-pool friction factor C_{f_pool}. Increases in k_2, C_{f_pool}, and ν_e all lead to predictions of higher sediment-transport capacity or deeper equilibrium alluvial pool-depth, all else held constant. While changing these coefficient values can lead to better predictions for a single experimental set, they cause predictions for other experimental sets to worsen and do not collapse the data overall. This suggests that discrepancies between the model predictions and experimental observations likely come from physical processes present within plunge-pools which are not incorporated within our model.

Our experimental sediment transport observations (Section 4.6.1) highlight many physical processes that are not included in our theory development. For example, for shallow alluvial pool-depths ($z_{sed} < \sim 5$ cm) we observed a change in process where stress from the impinging jet went into fluidization of the bed, reducing the stress available to entrain grains, and likely changing the effective fluid density and viscosity in that region

(e.g., Coussot, 1997). This process promotes shallower pools, and its lack of inclusion within our model framework is evident by model-predictions of deeper alluvial pool-depths than experimentally observed cases where the bed fluidized (Exp 9 and Exp 10 in Figs. 4.6C and 4.6D). Similarly, we observed grain-grain interactions within the near-bed active layer and at times between grains suspended in the water column in our experiments (Movie S1). These grain-grain interactions are not accounted for in our model, but could yield lower settling velocities via hindered settling (e.g., Richardson and Zaki, 1954; Kneller and Branney, 1995; Tomkins et al., 2005). We also note that for very shallow pools there is likely a process change from transport via suspension of grains to bedload transport. Our model assumes transport occurs by suspension everywhere except in the bedload layer within the jet-descending region, such that if bedload transport dominates for shallow pools, pools may be deeper than predicted by our theory.

Our experimental plunge pools demonstrated complex hydraulics where eddies of various scales developed causing the flow to overturn, sediment transport occurred in pulses, and sediment was concentrated on the downstream pool wall (Fig. 4.5B, Movie S1). These observations call into question our parameterization of radially uniform flow, a constant eddy viscosity in the vertical and radial directions, and assumption of constant w_{up} within the jet return-flow regions. While these assumption are necessary to achieve an analytical solution, eddy viscosities are typically parametrized to vary with distance for shear flows (e.g., Rouse, 1937a), and the upward return flow is likely highly variable as shown by velocity measurements below overfalls (e.g., Robinson et al., 2000; Bennett and Alonso, 2005). Including radially-variable and radially non-uniform eddy viscosity

and jet return flow may help to improve for changing plunge-pool radius where our model performs poorly (e.g., Figs. 4.6D and E).

Our experiments had a small degree of aeration within the waterfall jet, and the impinging jet further entrained air into the plunge-pool (e.g., Fig. 4.5B, Movie S1). Air entrainment in steps and waterfalls is common (e.g., Valle and Pasternack, 2006); however, the relationship between plunge-pool depth and aeration is complicated. Experiments have shown jet aeration typically leads to a reduction in plunge-pool alluvial depth (e.g., Canepa and Hager, 2003; Xu et al., 2004; Pagliara et al., 2006), although aeration has also been suggested to more efficiently allowing plucking of bedrock blocks which could increase pool bedrock depths (Bollaert, 2002; Bollaert and Schleiss, 2003). Within our experiments, air entrainment could have competing effects where the formation of void space could lower the fluid density making it more difficult to entrain grains (e.g., Eq. 29), while the collapse of air bubbles and pockets could provide lift forces to aid in grain entrainment and suspension (e.g., Pasternack et al., 2007). Including air entrainment within our model framework may lead to improved sediment-transport predictions, although, we also note the effects of air entrainment may be partially subsumed into the constant k_2 which is partially-tuned to match experimental data.

The extent to which these effects (i.e., bed fluidization, grain-grain interactions, complex flow hydraulics, and aeration) influence sediment transport may also depend on the particle grain size. For example, large-grains with high settling velocities may be more sensitive to small changes in flow-hydraulics and aeration than smaller grains. This may be a possible explanation for our experimental observations of sediment-transport independent of plunge-pool radius for D = 2.4 mm grains compared to decreasing

sediment-transport capacity with increasing plunge-pool radius observed for D = 7 mm grains (Figs. 4.6D and E).

These limitations highlight topics for future research that could be addressed to improve model predictions. Despite these limitations, we are encouraged that our plunge-pool sediment-transport model captures the dynamics of self-adjusting alluvial pool-depths, and also agrees with our experimental observations that plunge-pool sediment-transport capacity increases in response to increasing water discharge, increasing waterfall drop height, and decreasing grain size. Our model thus provides a starting point to predict how changes in waterfall geometry and flow hydraulics may influence plunge-pool sediment transport.

4.7. Application to natural waterfalls

In this section we first use a reference field site to explore the influence of the key non-dimensional variables governing sediment-transport capacity. Second, we use measurements from our field survey of waterfall plunge-pools to compare the observed alluvial depths to model predictions for cases of clear water discharge and with sediment supply.

4.7.1 Influence of non-dimensional variables on plunge-pool sediment-transport capacity

Here we explore the model predictions at field scale by independently varying the non-dimensional variables defined in Eq. (4.33) using values from Lower Switzer Falls (Table S4.1) as a reference site. Lower Switzer Falls, located on Arroyo Seco in the San Gabriel Mountains, CA, is a 5 m tall waterfall which empties into a ~9 m diameter bedrock-bound plunge pool. The plunge pool has been observed to go through multiple

sediment fill and evacuation cycles between 2009 and 2015, suggesting that sediment is actively transported through the pool, and we set the plunge-pool alluvial depth constant at 2 m for all calculations here. Sediment deposited on the plunge-pool floor during our field visits has been predominately sand and fine gravel, although the pool has a downstream bar of imbricated, rounded cobbles ranging in diameter from ~ 10 cm – 1 m. We set D = 0.1 m in all our calculations for Lower Switzer Falls, this approximates a balance between the fine grains we observe deposited in the plunge pool and the cobbles deposited downstream, and is in line with the median grain size we measure downstream on Arroyo Seco ranging from ~0.02 – 0.2 m. Arroyo Seco water discharge has been monitored by the U.S. Geological Survey since 1910 (gauge 11098000), and we estimate water flux at Lower Switzer Falls (~11 km upstream from the gage) assuming a linear scaling of discharge with drainage area.

We calculated Q_{sc_pool}/Q_w as a function of $\tau_{*pool}/\ \tau_{*c}$, $(z_{lip}–h_b)/L_d$, r_{pool}/L_d, and $\delta\ /L_d$ following Eq. (4.33). In each calculation, we set base values of non-dimensional variables based on their Lower Switzer Falls value, and then varied a single parameter individually while holding the others 3 parameters constant to explore model predictions. Increases in transport stage increase Q_{sc_pool}/Q_w proportionally to the quantity $(\tau_{*pool}/\ \tau_{*c}\text{-}1)^{1/2}$ from Eq. (4.30) up until the point at which c_b = 0.2 and is set constant (Fig. 4.8A). Similarly, increases in $(z_{lip}–h_b)/L_d$ result in an exponential decrease in Q_{sc_pool}/Q_w from the exponential term in Eq. (4.27) (Fig. 4.8B). The influence of changing r_{pool}/L_d, and $\delta\ /L_d$ is slightly more complicated as these quantities appear in multiple locations in the modified Bessel functions in Eq. (4.27). For cases when $r_{pool}/L_d\ > \delta\ /L_d$, Q_{sc_pool}/Q_w decreases non-inearly with increasing r_{pool}/L_d and increases non-linearly with increasing $\delta\ /L_d$, reflecting

the influence of changing plunge pool radius and sediment source zone size, respectively (Figs. 4.8C and D). Cases when $r_{pool}/L_d < \delta /L_d$ correspond to plunge pool radii smaller than the jet-descending region, and for these cases we set $c(r,z) = c_0(z)$ to so that there is no radial variation in Q_{sc_pool}/Q_w.

4.7.2. Waterfall field surveys

Our field survey focused on waterfalls within the San Gabriel Mountains, California, but also included waterfalls in the Sierra Nevada Mountains, California, and on the island of Kauai, Hawaii. These three field localities cover a range of sediment supply regimes where sediment supply is high in the San Gabriel Mountains due to high erosion rates (~0.1 – 1 mm/yr (DiBiase et al., 2010)) and the occurrence of wildfires which led to enhanced sediment supply during the period when many of our field observations were made (2009 – 2011) (Lamb et al., 2011). In contrast, sediment supply is variable across the waterfalls we surveyed in Kauai, HI, due to a strong rainfall gradient which modulates the rate of shallow landsliding (Ferrier et al., 2013). All surveyed waterfalls had clearly defined bedrock steps and ranged in drop height from 1 – 120 m, in plunge-pool bedrock radius from 0.5 – 40 m, and had upstream drainage areas ranging from < 1 – 94 km^2 (Table S4.1). We surveyed pools during periods of low flow as waterfalls are often inaccessible and hazardous to survey during large flood events. Many plunge pools were filled or partially-filled with sediment during our field campaign, with alluvial depths ranging from 0 m (i.e., completely-filled with sediment) to 5 m. We estimated plunge-pool alluvial depth using a variety of methods (see Supplement and Table S4.1). Grain size estimates were estimated visually in the field or via a random-walk pebble count. Channel slope upstream of the waterfall was taken

from digital elevation models ranging in resolution from 1m-LiDAR (most of the San Gabriel Mountain locations) to 10m-National Elevation Dataset data. We estimated water discharge using 2-year recurrence interval discharge values taken from US Geological Survey stream gages located either within the same catchment as our field surveyed waterfall, or within an adjacent catchment. We assumed a linear scaling between discharge and drainage area to convert discharge values taken at stream gage locations to waterfall locations which were often at smaller drainage areas.

4.7.3. Importance of upstream sediment supply on plunge-pool alluvial depth

Our field surveys allow comparison of plunge-pool alluvial depth field measurements to the expected clear-water alluvial depth using existing empirical formulations (e.g., Pagliara et al., 2006) as well as the theory developed here. Our surveyed plunge pools are ~3-300 times shallower than predicted for clear-water overspill during a 2-year recurrence interval flood when using the empirical formula of Pagliara *et al.* (2006) (Fig. 4.9A). The Pagliara *et al.* (2006) empiricism assumes both clear-water discharge and self-formed alluvial pool walls, such that it is difficult to determine whether or not the discrepancy between prediction and field measurements is due to differences in pool geometry or the influence of imposed sediment supply from upstream. Comparing field measurements of alluvial pool-depth to the predicted clear-water depth using the theory developed can address this discrepancy as our model is developed for cylindrical, bedrock bound plunge pools similar to those we surveyed in the field. As with the Pagliara *et al.* (2006) predictions, surveyed pools are shallower than predicted under clear-water flow using our theory (Fig. 4.9B), suggesting that natural plunge pools are likely adjusted to a characteristic, non-zero sediment flux from

upstream. The few plunge pools with field depths deeper than predicted for clear water tended to be characterized by relatively coarse sediment within the pool, which we interpret may have been deposited in a larger flood event than the two-year recurrence interval flood used in our calculations.

The difference between the observed pool depths and those predicted by clear-water theory in Fig. 4.9B can be explained as a result of upstream sediment supply. We used out model to calculate the expected sediment concentration for a two year recurrence interval flood discharge (Q_s/Q_w) that is necessary to fit the observed pool alluvial depths at steady state (Fig. 4.9). This analysis indicates that the observed pool depths can be explained by upstream sediment concentrations that range from less than a tenth of a percent to greater than ten percent by volume, and our field sediment concentration values partially overlap with the range of sediment concentrations ($c \approx 10^{-1} - 10^{-3}$) observed in experiments of plunge-pool develop into alluvial beds (Stein and Julien, 1994). Higher predicted sediment concentrations are associated with shallower pool depths in our field survey, suggesting that shallower pools are adjusted to higher sediment supply, in agreement with our conceptual model.

4.8. Implications for habitat, hazards, and bedrock erosion

We interpret our experimental observations of plunge pools filling in response to increases in sediment supply to support our conceptual model of self-adjustment of pool alluvial depth in response to changes in sediment supply from upstream. Waterfall plunge-pools typically have small volumes compared to total fluvial sediment flux over the course of a flood, so that storage of sediment in (or scour of sediment out of) pools

does not largely influence overall sediment budgets. During floods, sediment supply may be large relative to pool volumes, such that plunge pools are likely to fill or empty rapidly. As such, field-measurements of alluvial pool-depth are likely sensitive to recent flow conditions and sediment load.

The depth of sediment fill has implications for habitat availability and natural hazards, with deep, sediment-free pools providing habitat for aquatic organisms (e.g., Matthews et al., 1994; Lake, 2003; Magoulick and Kobza, 2003; Bond et al., 2008) and sediment-filled pools providing conditions to initiate debris flows (e.g., Griffiths et al., 2004; Larsen et al., 2006). The model developed here provides a first-order tool for land-managers to estimate sediment filling and evacuation of waterfall plunge pools in response to changes in river hydraulics or upstream sediment supply. For cases where the upstream sediment supply (Q_s) is known, our plunge-pool sediment-transport capacity model can be used to route sediment through plunge pools and track plunge-pool alluvial filling and evacuation, as sediment should be deposited in pools when $Q_{sc\_pool} < Q_s$, sediment should pass through pools when $Q_{sc\_pool} = Q_s$, and sediment should be scoured from pools when $Q_{sc\_pool} > Q_s$. For example, increases in upstream sediment supply from disturbances such as wildfire or land-use change may result in filling of plunge pools. Similarly, pools are likely to fill during periods of reduced water discharge, but may scour to bedrock during large floods.

Our plunge-pool sediment-transport capacity model can be coupled with physically-based bedrock erosion models (e.g., Sklar and Dietrich, 2004; Lamb et al., 2007) to predict waterfall plunge-pool bedrock abrasion over geomorphically relevant timescales. Over such timescales, cycles of sediment fill and evacuation from waterfall

plunge-pools should influence bedrock erosion as vertical incision requires exposure of the pool bedrock floor, while plunge-pool walls are free to erode even when the bed is covered. Plunge-pool sediment-transport capacity therefore may modulate relative vertical versus lateral erosion rates in waterfall plunge pools by dictating the deposition or scour of sediment from the plunge-pool floor. When $Q_{sc\_pool} > Q_s$, pools can scour to bedrock and vertically incise, whereas when $Q_{sc\_pool} < Q_s$ sediment deposits at the base of the pool, armoring the bed, and preventing vertical incision (but potentially still allowing for lateral erosion), analogous to the role sediment cover plays in controlling channel bedrock width (e.g., Sklar and Dietrich, 2004; Finnegan et al., 2007; Turowski et al., 2008).

4.9. Conclusions

We developed an analytical model to predict waterfall plunge-pool sediment-transport capacity based on seven field-measurable variables (water discharge, waterfall drop height, plunge-pool depth and radius, grain size, and upstream channel slope and width). Our model is developed for bedrock-bound pools with cylindrical geometry where alluvial pool-depth is free to fluctuate. We assume that plunge-pools self-adjust their alluvial depth to reach equilibrium with the imposed sediment supply from upstream, such that the model can be used to predict steady-state plunge-pool alluvial depth subject to a given sediment supply and water discharge. Laboratory experiments demonstrated self-adjustment of plunge-pool alluvial depth in response to changes in sediment supply, and both experiments and theory showed plunge-pool sediment-transport capacity increases with increasing water discharge and waterfall drop

height, and decreases with decreasing grain size. The theory, however, has variable success with matching experimental observations within measurement error, and this is likely due to complicated flow hydraulics, grain-grain interactions, and jet aeration which is not accounted for in the theory development but is observed experimentally. Field surveys of over 70 waterfall plunge pools show that pools tend to be filled with sediment to alluvial depths shallower than that predicted for 2-year recurrence interval clear-water discharge, suggesting that the upstream sediment supply plays an important role in plunge-pool morphodynamic evolution. The model presented here provides a framework to explore how sediment is routed through bedrock-bound waterfall plunge pools, and can be used to estimate periods of sediment fill or evacuation in assessment of habitat availability or for hazards mitigation, as well as in predictions of plunge-pool bedrock erosion.

4.10 Acknowledgements

We are grateful to Brian Fuller for assistance with laboratory experiments, and benefitted from conversations with Jeff Prancevic, Andy Thompson, Patrick Sanan, Mike Gurnis, and Jeremy Venditti. Roman DiBiase and Chris Brennen assisted with waterfall surveys, and, together with Kelin Whipple, kindly shared photographs and data from plunge pools in the San Gabriel Mountains. Greg Pasternack, two anonymous reviewers, and the Associate Editor provided constructive comments which improved the structure and presentation of this manuscript. We thank Mike Oxford and the US Forest Service for access to the San Dimas Experimental Forest. We acknowledge funding from the National Science Foundation via grant EAR-1147381 to M.P.L and a Graduate Research Fellowship to J.S.S, as well as funding from NASA grant 12PGG120107.

4.11 Notation

A_{jet}	waterfall jet area [L^2]
A_{pool}	plunge pool area [L^2]
C_d	waterfall jet diffusion coefficient [dimensionless]
C_{f_pool}	plunge pool friction factor [dimensionless]
C_{f_river}	river friction factor [dimensionless]
D	grain diameter [L]
Fr_n	normal Froude number upstream of the waterfall [dimensionless]
H_{drop}	waterfall drop height [L]
L_d	characteristic length scale over which turbulence mixes sediment [L]

Q_s	upstream sediment supply [L/T^3]
Q_{*s_pool}	dimensionless plunge pool sediment flux [dimensionless]
Q_{sc_pool}	plunge-pool sediment-transport capacity [L/T^3]
Q_w	water discharge [L/T^3]
R	submerged sediment density [dimensionless]
$\mathrm{Re}_{\mathrm{jet}}$	waterfall jet Reynolds number [dimensionless]
S	channel slope [dimensionless]
W	channel width [L]
b	jet half width [L]
c	sediment concentration [dimensionless]
$\bar{c}$	sediment concentration temporally averaged over turbulence [dimensionless]
c_b	reference near-bed sediment concentration in jet-descending region [dimensionless]
c_o	reference sediment concentration at ($r = r_{pool}$, $z = h_b$) [dimensionless]
g	gravitational acceleration [L/T^2]
h_b	thickness of the well-mixed layer along the plunge-pool floor [L]
h_n	normal flow depth upstream of the waterfall [L]
h_{pool}	plunge-pool depth [L]
k_1	coefficient in estimating kinematic eddy diffusivity [dimensionless]
k_2	constant in sediment entrainment formula [dimensionless]
r_{jet}	waterfall jet radius at point of impact with water surface [L]
r_{pool}	plunge pool radius [L]
t	time [T]
Δt_{wait}	expected wait time to reach steady-state alluvial pool-depth [T]
u_{*pool}	shear velocity at the plunge-pool bed [L/T]
u_{brink}	water velocity at the waterfall brink [L/T]
u_{impact}	jet velocity upon impact with the plunge-pool floor [L/T]
u_{jet}	jet velocity upon impact with the plunge-pool water surface [L/T]
u_{lip}	water velocity at the downstream plunge-pool lip [L/T]
u_n	normal water velocity upstream of the waterfall [L/T]
u_r	radial water velocity [L/T]
u'_r	turbulent fluctuations in radial water velocity [L/T]
u_θ	azimuthal water velocity [L/T]
w	vertical water velocity [L/T]
w_{net}	net particle settling velocity [L/T]
w_s	particle gravitational settling velocity [L/T]
w_{up}	vertical velocity of the jet return flow [L/T]
w'_{up}	turbulent fluctuations in vertical velocity of the jet return flow [L/T]
z	vertical coordinate [L]
z_{BR}	elevation of the plunge-pool bedrock floor [L]
z_{lip}	elevation of the downstream plunge-pool lip [L]
z_{sed}	elevation of the plunge-pool alluvial floor [L]
z_{water}	elevation of the plunge-pool water surface [L]
z_λ	elevation of the boundary between the ZOEF and ZOFE [L]
β	angle of waterfall jet impact [rad]

γ	virtual origin in estimation of jet half-width [L]
δ	radial distance which sets boundary between descending-flow and je return-flow regions, equal to twice the jet half-width measured at the pool alluvial floor [L]
θ	azimuthal coordinate [L]
λ	length of ZOFE [L]
ν_e	kinematic eddy diffusivity [L^2/T]
ρ	fluid density [M/L^3]
ρ_s	sediment density [M/L^3]
τ_{pool}	plunge-pool bed shear stress [$M\ L^{-1}\ T^{-2}$]
τ_{river}	river bed shear stress [$M\ L^{-1}\ T^{-2}$]
τ_{*c}	critical Shields stress for grain motion [dimensionless]
τ_{*pool}	plunge-pool bed Shields stress [dimensionless]

4.12 References

Abramovich, G., and Schindel, L., 1963, The theory of turbulent jets, Cambridge, MA, MIT Press, 671 p.:

Albertson, M. L., Dai, Y. B., Jensen, R. A., and Rouse, H., 1950, Diffusion of submerged jets: Transactions of the American Society of Civil Engineers, v. 115, p. 639-664.

Alonso, C. V., Bennett, S. J., and Stein, O. R., 2002, Predicting head cut erosion and migration in concentrated flows typical of upland areas: Water Resources Research, v. 38, no. 12.

Beltaos, S., 1976, Oblique impingement of plane turbulent jets: Journal of the Hydraulics Division-Asce, v. 102, no. 9, p. 1177-1192.

Beltaos, S., and Rajaratnam, N., 1973, Plane turbulent impinging jets: Journal of Hydraulic Research, v. 11, no. 1, p. 29-59.

Bennett, S. J., and Alonso, C. V., 2005, Kinematics of flow within headcut scour holes on hillslopes: Water Resources Research, v. 41, no. 9.

Bennett, S. J., Alonso, C. V., Prasad, S. N., and Romkens, M. J. M., 2000, Experiments on headcut growth and migration in concentrated flows typical of upland areas: Water Resources Research, v. 36, no. 7, p. 1911-1922.

Berlin, M. M., and Anderson, R. S., 2007, Modeling of knickpoint retreat on the Roan Plateau, western Colorado: Journal of Geophysical Research-Earth Surface, v. 112, no. F3.

Bollaert, E., 2002, The influence of plunge pool air entrainment on the presence of free air in rock joints, *in* Schleiss, A., and Bollaert, E., eds., Rock scour due to falling high-velocity jets: Lisse, the Netherlands, A.A. Balkema Publishers.

Bollaert, E., and Schleiss, A., 2003, Scour of rock due to the impact of plunging high velocity jets Part I: A state-of-the-art review: Journal of Hydraulic Research, v. 41, no. 5, p. 451-464.

Bond, N. R., Lake, P. S., and Arthington, A. H., 2008, The impacts of drought on freshwater ecosystems: an Australian perspective: Hydrobiologia, v. 600, p. 3-16.

Bormann, N. E., and Julien, P. Y., 1991, Scour Downstream of Grade-Control Structures: Journal of Hydraulic Engineering-Asce, v. 117, no. 5, p. 579-594.

Boulton, A. J., 2003, Parallels and contrasts in the effects of drought on stream macroinvertebrate assemblages: Freshwater Biology, v. 48, no. 7, p. 1173-1185.

Bradbury, L. J., 1965, Structure of a self-preserving turbulent plane jet: Journal of Fluid Mechanics, v. 23, p. 31-64.

Brownlie, W. R., 1981, Prediction of flow depth and sediment discharge in open channels: W.M. Keck Laboratory of Hydraulics and Water Resources.

Buffington, J. M., and Montgomery, D. R., 1997, A systematic analysis of eight decades of incipient motion studies, with special reference to gravel-bedded rivers: Water Resources Research, v. 33, no. 8, p. 1993-2029.

Canepa, S., and Hager, W. H., 2003, Effect of jet air content on plunge pool scour: Journal of Hydraulic Engineering-Asce, v. 129, no. 5, p. 358-365.

Chatanantavet, P., and Parker, G., 2006, Modeling the bedrock river evolution of western Kaua'i, Hawai'i, by a physically-based incision model based on abrasion, *in* Parker, G., and Garcia, M., eds., River, Coastal and Estuarine Morphodynamics 2005, Taylor and Francis Group.

Coussot, P., 1997, Mudflow rheology and dynamics, Rotterdam, Balkema, IAHR Monograph Series.

Crosby, B. T., and Whipple, K. X., 2006, Knickpoint initiation and distribution within fluvial networks: 236 waterfalls in the Waipaoa River, North Island, New Zealand: Geomorphology, v. 82, no. 1-2, p. 16-38.

Crosby, B. T., Whipple, K. X., Gasparini, N. M., and Wobus, C. W., 2007, Formation of fluvial hanging valleys: Theory and simulation: Journal of Geophysical Research-Earth Surface, v. 112, no. F3.

DiBiase, R. A., Whipple, K. X., Heimsath, A. M., and Ouimet, W. B., 2010, Landscape form and millennial erosion rates in the San Gabriel Mountains, CA: Earth and Planetary Science Letters, v. 289, no. 1-2, p. 134-144.

DiBiase, R. A., Whipple, K. X., Lamb, M. P., and Heimsath, A. M., 2015, The role of waterfalls and knickzones in controlling the style and pace of landscape adjustment in the western San Gabriel Mountains, California: Geological Society of America Bulletin, v. 127, no. 3-4, p. 539-559.

Dietrich, W. E., Bellugi, D., Heimsath, A. M., Roering, J. J., Sklar, L., and Stock, J. D., 2003, Geomorphic transport laws for predicting the form and evolution of landscapes, *in* Wilcock, P. R., and Iverson, R. M., eds., Geophysical Monograph Series, Volume 135, American Geophysical Union, p. 103-132.

Ervine, D. A., Falvey, H. T., and Withers, W., 1997, Pressure fluctuations on plunge pool floors: Journal of Hydraulic Research, v. 35, no. 2, p. 257-279.

Ferguson, R. I., and Church, M., 2004, A simple universal equation for grain settling velocity: Journal of Sedimentary Research, v. 74, no. 6, p. 933-937.

Fernandez Luque, R., and van Beek, R., 1976, Erosion and transport of bed-load sediment: Journal of Hydraulic Research, v. 14, p. 127-144.

Ferrier, K. L., Perron, J. T., Mukhopadhyay, S., Rosener, M., Stock, J. D., Huppert, K. L., and Slosberg, M., 2013, Covariation of climate and long-term erosion rates across a steep rainfall gradient on the Hawaiian island of Kaua'i: Geological Society of America Bulletin, v. 125, no. 7-8, p. 1146-1163.

Finnegan, N. J., Sklar, L. S., and Fuller, T. K., 2007, Interplay of sediment supply, river incision, and channel morphology revealed by the transient evolution of an experimental bedrock channel: Journal of Geophysical Research-Earth Surface, v. 112, no. F3.

Fiorotto, V., and Rinaldo, A., 1992, Fluctuating Uplift and Lining Design in Spillway Stilling Basins: Journal of Hydraulic Engineering-Asce, v. 118, no. 4, p. 578-596.

Flores-Cervantes, J. H., Istanbulluoglu, E., and Bras, R. L., 2006, Development of gullies on the landscape: A model of headcut retreat resulting from plunge pool erosion: Journal of Geophysical Research-Earth Surface, v. 111, no. F1.

Garcia, M. H., 2008, Sediment transport and morphodynamics, *in* Garcia, M. H., ed., Sedimentation Engineering: Processes, Measurements, Modeling, and Practice: Reston, Virginia, American Society of Civil Engineers.

Gaudio, R., and Marion, A., 2003, Time evolution of scouring downstream of bed sills: Journal of Hydraulic Research, v. 41, no. 3, p. 271-284.

Gaudio, R., Marion, A., and Bovolin, V., 2000, Morphological effects of bed sills in degrading rivers: Journal of Hydraulic Research, v. 38, no. 2, p. 89-96.

Ghaneeizad, S. M., Atkinson, J. F., and Bennett, S. J., 2015, Effect of flow confinement on the hydrodynamics of circular impinging jets: implications for erosion assessment: Environmental Fluid Mechanics, v. 15, no. 1, p. 1-25.

Giger, M., Dracos, T., and Jirka, G. H., 1991, Entrainment and mixing in plane turbulent jets in shallow-water: Journal of Hydraulic Research, v. 29, no. 5, p. 615-642.

Gilbert, G. K., 1890, The history of the Niagara River, extracted from the sixth annual report to the commissioners of the state reservation at Niagara, Albany, NY.

-, 1907, The rate of recession of Niagara Falls: US Geological Survey Bulletin, v. 306, p. 1-31.

Godt, J. W., and Coe, J. A., 2007, Alpine debris flows triggered by a 28 July 1999 thunderstorm in the central Front Range, Colorado: Geomorphology, v. 84, no. 1-2, p. 80-97.

Griffiths, P. G., Webb, R. H., and Melis, T. S., 2004, Frequency and initiation of debris flows in Grand Canyon, Arizona: Journal of Geophysical Research-Earth Surface, v. 109, no. F4.

Hager, W. H., 1983, Hydraulics of plane free overfall: Journal of Hydraulic Engineering-Asce, v. 109, no. 12, p. 1683-1697.
Hanson, G. J., Robinson, K. M., and Cook, K. R., 2002, Scour below an overfall: Part II. Prediction: Transactions of the ASAE, v. 45, no. 4, p. 957-964.
Haviv, I., Enzel, Y., Whipple, K. X., Zilberman, E., Matmon, A., Stone, J., and Fifield, K. L., 2010, Evolution of vertical knickpoints (waterfalls) with resistant caprock: Insights from numerical modeling: Journal of Geophysical Research-Earth Surface, v. 115.
Hawkins, C. P., Kershner, J. L., Bisson, P. A., Bryant, M. D., Decker, L. M., Gregory, S. V., McCullough, D. A., Overton, C. K., Reeves, G. H., Steedman, R. J., and Young, M. K., 1993, A hierarchical approach to classifying stream habitat features: Fisheries, v. 18, no. 6, p. 3-12.
Hayakawa, Y. S., Yokoyama, S., and Matsukura, Y., 2008, Erosion rates of waterfalls in post-volcanic fluvial systems around Aso volcano, southwestern Japan: Earth Surface Processes and Landforms, v. 33, no. 5, p. 801-812.
Holland, W. N., and Pickup, G., 1976, Flume study of knickpoint development in stratified sediment: Geological Society of America Bulletin, v. 87, no. 1, p. 76-82.
Howard, A. D., Dietrich, W. E., and Seidl, M. A., 1994, Modeling fluvial erosion on regional to continental scales: Journal of Geophysical Research-Solid Earth, v. 99, no. B7, p. 13971-13986.
Kneller, B. C., and Branney, M. J., 1995, Sustained High-Density Turbidity Currents and the Deposition of Thick Massive Sands: Sedimentology, v. 42, no. 4, p. 607-616.
Lake, P. S., 2003, Ecological effects of perturbation by drought in flowing waters: Freshwater Biology, v. 48, no. 7, p. 1161-1172.
Lamb, M. P., and Dietrich, W. E., 2009, The persistence of waterfalls in fractured rock: Geological Society of America Bulletin, v. 121, no. 7-8, p. 1123-1134.
Lamb, M. P., Finnegan, N. J., Scheingross, J. S., and Sklar, L. S., 2015, New insights into the mechanics of fluvial bedrock erosion through flume experiments and theory: Geomorphology, v. 244, p. 33-55.
Lamb, M. P., Howard, A. D., Dietrich, W. E., and Perron, J. T., 2007, Formation of amphitheater-headed valleys by waterfall erosion after large-scale slumping on Hawai'i: Geological Society of America Bulletin, v. 119, no. 7-8, p. 805-822.
Lamb, M. P., Scheingross, J. S., Amidon, W. H., Swanson, E., and Limaye, A., 2011, A model for fire-induced sediment yield by dry ravel in steep landscapes: Journal of Geophysical Research-Earth Surface, v. 116.
Lane, E. W., 1955, The importance of fluvial morphology in hydraulic engineering: Proceedings of the American Society of Civil Engineers, v. 81, no. 745.
Lapotre, M. G. A., and Lamb, M. P., 2015, Hydraulics of floods upstream of horseshoe canyons and waterfalls: Journal of Geophysical Research-Earth Surface, v. 120, no. 7.
Larsen, I. J., Pederson, J. L., and Schmidt, J. C., 2006, Geologic versus wildfire controls on hillslope processes and debris flow initiation in the Green River canyons of Dinosaur National Monument: Geomorphology, v. 81, no. 1-2, p. 114-127.
Lenzi, M. A., and Comiti, F., 2003, Local scouring and morphological adjustments in steep channels with check-dam sequences: Geomorphology, v. 55, no. 1-4, p. 97-109.
Lenzi, M. A., Marion, A., and Comiti, F., 2003, Local scouring at grade-control structures in alluvial mountain rivers: Water Resources Research, v. 39, no. 7.
Lenzi, M. A., Marion, A., Comiti, F., and Gaudio, R., 2002, Local scouring in low and high gradient streams at bed sills: Journal of Hydraulic Research, v. 40, no. 6, p. 731-739.
Loget, N., and Van Den Driessche, J., 2009, Wave train model for knickpoint migration: Geomorphology, v. 106, no. 3-4, p. 376-382.
Mackey, B. H., Scheingross, J. S., Lamb, M. P., and Farley, K. A., 2014, Knickpoint formation, rapid propagation, and landscape response following coastal cliff retreat at the last interglacial sea-level highstand: Kaua'i, Hawai'i: Geological Society of America Bulletin, v. 126, no. 7-8, p. 925-942.
Mackin, J. H., 1948, Concept of the graded river: Geological Society of America Bulletin, v. 59, no. 5, p. 463-511.
Magoulick, D. D., and Kobza, R. M., 2003, The role of refugia for fishes during drought: a review and synthesis: Freshwater Biology, v. 48, no. 7, p. 1186-1198.
Marion, A., Lenzi, M. A., and Comiti, F., 2004, Effect of sill spacing and sediment size grading on scouring at grade-control structures: Earth Surface Processes and Landforms, v. 29, no. 8, p. 983-993.

Marion, A., Tregnaghi, M., and Tait, S., 2006, Sediment supply and local scouring at bed sills in high-gradient streams: Water Resources Research, v. 42, no. 6.
Mason, P. J., and Arumugam, K., 1985, Free jet scour below dams and flip buckets: Journal of Hydraulic Engineering-Asce, v. 111, no. 2, p. 220-235.
Matthews, K. R., and Berg, N. H., 1997, Rainbow trout responses to water temperature and dissolved oxygen stress in two southern California stream pools: Journal of Fish Biology, v. 50, no. 1, p. 50-67.
Matthews, K. R., Berg, N. H., Azuma, D. L., and Lambert, T. R., 1994, Cool water formation and trout habitat use in a deep pool in the Sierra-Nevada, California: Transactions of the American Fisheries Society, v. 123, no. 4, p. 549-564.
Meyer-Peter, E., and Mueller, R., Formulas for bedload transport, *in* Proceedings Proceedings of the 2nd Congress, IAHR, Stockholm, 1948, p. 39-64.
Nezu, L., and Nakagawa, H., 1993, Turbulence in open channel flows, Rotterdam, Netherlands, IAHR Monographs, 281 p.:
Nielsen, J. L., Lisle, T. E., and Ozaki, V., 1994, Thermally stratified pools and their use by Steelhead in northern California Streams: Transactions of the American Fisheries Society, v. 123, no. 4, p. 613-626.
Nitsche, M., Rickenmann, D., Turowski, J. M., Badoux, A., and Kirchner, J. W., 2011, Evaluation of bedload transport predictions using flow resistance equations to account for macro-roughness in steep mountain streams: Water Resources Research, v. 47.
Pagliara, S., Amidei, M., and Hager, W. H., 2008a, Hydraulics of 3D plunge pool scour: Journal of Hydraulic Engineering-Asce, v. 134, no. 9, p. 1275-1284.
Pagliara, S., Hager, W. H., and Minor, H. E., 2006, Hydraulics of plane plunge pool scour: Journal of Hydraulic Engineering-Asce, v. 132, no. 5, p. 450-461.
Pagliara, S., Hager, W. H., and Unger, J., 2008b, Temporal Evolution of Plunge Pool Scour: Journal of Hydraulic Engineering-Asce, v. 134, no. 11, p. 1630-1638.
Pagliara, S., and Palermo, M., 2008, Plane plunge pool scour with protection structures: Journal of Hydro-Environment Research, v. 2, no. 3, p. 182-191.
Pagliara, S., Palermo, M., and Carnacina, I., 2011, Expanding pools morphology in live-bed conditions: Acta Geophysica, v. 59, no. 2, p. 296-316.
-, 2012a, Live-bed scour downstream of block ramps for low densimetric Froude numbers: International Journal of Sediment Research, v. 27, no. 3, p. 337-350.
Pagliara, S., Palermo, M., and Roy, D., 2012b, Stilling basin erosion due to vertical crossing jets: Journal of Hydraulic Research, v. 50, no. 3, p. 290-297.
Pagliara, S., Roy, D., and Palermo, M., 2010, 3D plunge pool scour with protection measures: Journal of Hydro-Environment Research, v. 4, no. 3, p. 225-233.
Paola, C., Straub, K., Mohrig, D., and Reinhardt, L., 2009, The "unreasonable effectiveness" of stratigraphic and geomorphic experiments: Earth-Science Reviews, v. 97, no. 1-4, p. 1-43.
Parker, G., 1991, Selective Sorting and Abrasion of River Gravel .2. Applications: Journal of Hydraulic Engineering-Asce, v. 117, no. 2, p. 150-171.
-, 2008, Transport of gravel and sediment mixtures, *in* Garcia, M. H., ed., Sedimentation Engineering: Processes, Measurements, Modeling, and Practice: Reston, Virginia, American Society of Civil Engineers.
Parker, G., and Klingeman, P. C., 1982, On why gravel bed streams are paved: Water Resources Research, v. 18, no. 5, p. 1409-1423.
Parker, G., Klingeman, P. C., and McLean, D. G., 1982, Bedload and size distribution in paved gravel-bed streams: Journal of the Hydraulics Division-Asce, v. 108, no. 4, p. 544-571.
Pasternack, G. B., Ellis, C. R., and Marr, J. D., 2007, Jet and hydraulic jump near-bed stresses below a horseshoe waterfall: Water Resources Research, v. 43, no. 7.
Pizzuto, J. E., 1987, Sediment diffusion during overbank flows: Sedimentology, v. 34, no. 2, p. 301-317.
Prandtl, L., 1925, A report on testing for built-up turbulence: Zeitschrift Fur Angewandte Mathematik Und Mechanik, v. 5, p. 136-139.
Rajaratnam, N., 1976, Turbulent Jets, Amsterdam, Elsevier, Developments in water science.
Recking, A., 2009, Theoretical development on the effects of changing flow hydraulics on incipient bed load motion: Water Resources Research, v. 45.

-, 2010, A comparison between flume and field bed load transport data and consequences for surface-based bed load transport prediction: Water Resources Research, v. 46.
Rempel, L. L., Richardson, J. S., and Healey, M. C., 1999, Flow refugia for benthic macroinvertebrates during flooding of a large river: Journal of the North American Benthological Society, v. 18, no. 1, p. 34-48.
Richardson, J., and Zaki, W., 1954, Sedimentation and fluidisation: Part I: Transactions of the Institution of Chemical Engineers, v. 32, p. 35-53.
Robinson, K. M., Cook, K. R., and Hanson, G. J., 2000, Velocity field measurements at an overfall: Transactions of the ASAE, v. 43, no. 3, p. 665-670.
Rouse, H. R., 1936, Discharge characteristics of the free overfall: Civil Engineering, v. 6, p. 257-260.
-, 1937a, Modern conceptions of the mechanics of turbulence: Trans. Am. Soc. Civ. Eng., v. 102, no. 1, p. 463-543.
-, 1937b, Pressure distribution and acceleration at the free overfall: Civil Engineering, v. 7, p. 518.
Rowland, J. C., Stacey, M. T., and Dietrich, W. E., 2009, Turbulent characteristics of a shallow wall-bounded plane jet: experimental implications for river mouth hydrodynamics: Journal of Fluid Mechanics, v. 627, p. 423-449.
Seidl, M. A., Dietrich, W. E., and Kirchner, J. W., 1994, Longitudinal profile development into bedrock - an analysis of Hawaiian channels: Journal of Geology, v. 102, no. 4, p. 457-474.
Sklar, L. S., and Dietrich, W. E., 2004, A mechanistic model for river incision into bedrock by saltating bed load: Water Resources Research, v. 40, no. 6.
Stein, O. R., Alonso, C. V., and Julien, P. Y., 1993, Mechanics of jet scour downstream of a headcut: Journal of Hydraulic Research, v. 31, no. 6, p. 723-738.
Stein, O. R., and Julien, P. Y., 1993, Criterion delineating the mode of headcut migration: Journal of Hydraulic Engineering-ASCE, v. 119, no. 1, p. 37-50.
-, 1994, Sediment concentration below free overfall Journal of Hydraulic Engineering-Asce, v. 120, no. 9, p. 1043-1059.
Stein, O. R., and LaTray, D. A., 2002, Experiments and modeling of head cut migration in stratified soils: Water Resources Research, v. 38, no. 12.
Takahashi, T., 2014, Debris flow: Mechanics, predictons, and countermeasures, The Netherlands, CRC Press.
Tomkins, M. R., Baldock, T. E., and Nielsen, P., 2005, Hindered settling of sand grains: Sedimentology, v. 52, no. 6, p. 1425-1432.
Torgersen, C. E., Price, D. M., Li, H. W., and McIntosh, B. A., 1999, Multiscale thermal refugia and stream habitat associations of chinook salmon in northeastern Oregon: Ecological Applications, v. 9, no. 1, p. 301-319.
Tregnaghi, M., Marion, A., Bottacin-Busolin, A., and Tait, S. J., 2011, Modelling time varying scouring at bed sills: Earth Surface Processes and Landforms, v. 36, no. 13, p. 1761-1769.
Turowski, J. M., Hovius, N., Hsieh, M.-L., Lague, D., and Chen, M.-C., 2008, Distribution of erosion across bedrock channels: Earth Surface Processes and Landforms, v. 33, no. 3, p. 353-363.
Valle, B. L., and Pasternack, G. B., 2006, Air concentrations of submerged and unsubmerged hydraulic jumps in a bedrock step-pool channel: Journal of Geophysical Research-Earth Surface, v. 111, no. F3.
van Rijn, L. C., 1984, Sediment transport, part II: Suspended load transport: Journal of Hydraulic Engineering, v. 110, p. 1613-1641.
Weissel, J. K., and Seidl, M. A., 1997, Influence of rock strength properties on escarpment retreat across passive continental margins: Geology, v. 25, no. 7, p. 631-634.
Wells, R. R., Bennett, S. J., and Alonso, C. V., 2010, Modulation of headcut soil erosion in rills due to upstream sediment loads: Water Resources Research, v. 46.
Xu, W. L., Deng, J., Qu, J. X., Liu, S. J., and Wang, W., 2004, Experimental investigation on influence of aeration on plane jet scour: Journal of Hydraulic Engineering-Asce, v. 130, no. 2, p. 160-164.
Xu, W. L., Liao, H. S., Yang, Y. Q., and Wu, C. G., 2002, Turbulent flow and energy dissipation in plunge pool of high arch dam: Journal of Hydraulic Research, v. 40, no. 4, p. 471-476.
Yager, E. M., Dietrich, W. E., Kirchner, J. W., and McArdell, B. W., 2012, Prediction of sediment transport in step-pool channels: Water Resources Research, v. 48.
Yager, E. M., Kirchner, J. W., and Dietrich, W. E., 2007, Calculating bed load transport in steep boulder bed channels: Water Resources Research, v. 43, no. 7.

Young, R., 1985, Waterfalls: Form and process: Zeitschrift fur Geomorphologie, no. Supplementband 55, p. 81-95.

Zimmermann, A., Church, M., and Hassan, M. A., 2010, Step-pool stability: Testing the jammed state hypothesis: Journal of Geophysical Research-Earth Surface, v. 115.

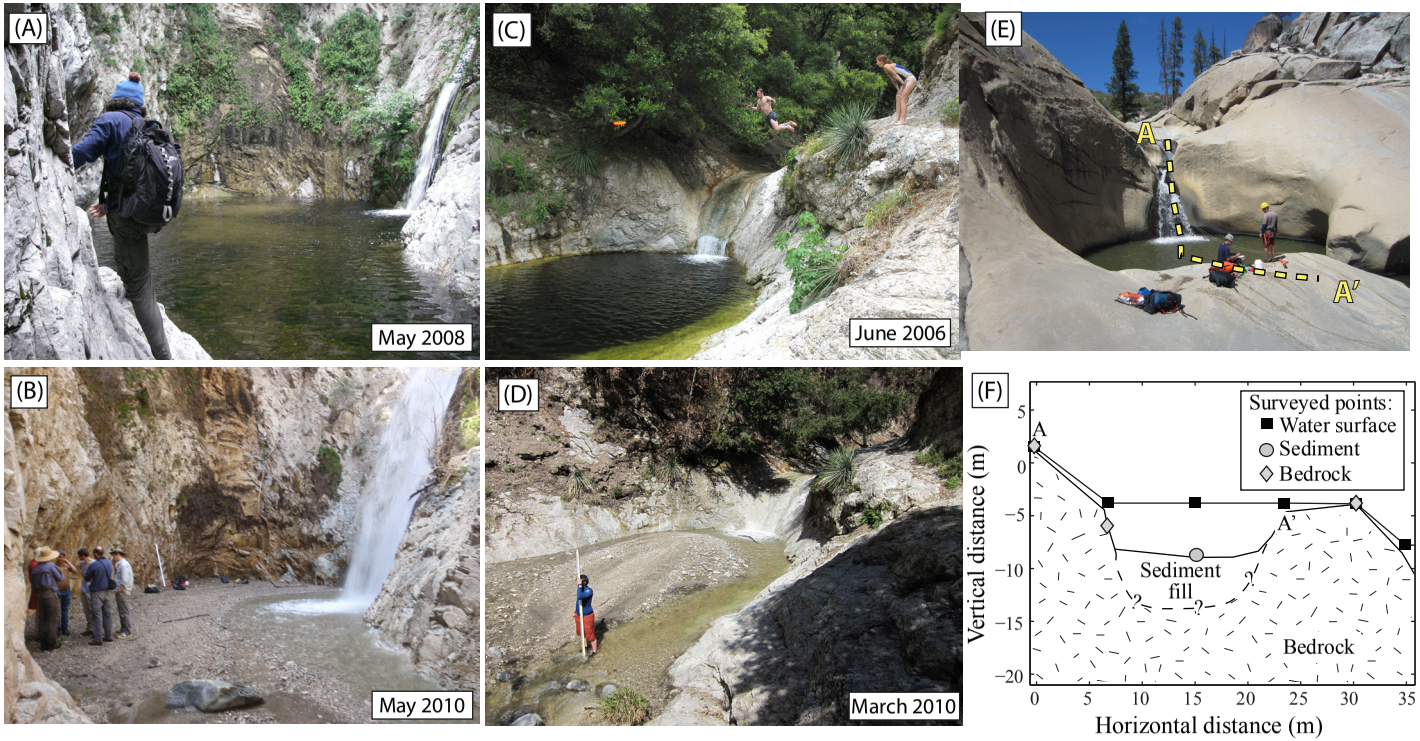

Figure 4.1: (A) - (D) Show examples of sediment filling and evacuation of waterfall plunge pools on Arroyo Seco, San Gabriel Mountains, California. (A) and (B) are of Upper Switzer Falls (USF, Table A2.1), (C) and (D) are of an un-named ~2.5 meter bedrock step (ASP4, Table S4.1). (E) Photo and (F) surveyed long-profile through a deep waterfall plunge-pool with cylindrical geometry on Dry Meadow Creek, California (STC3, Table S4.1).

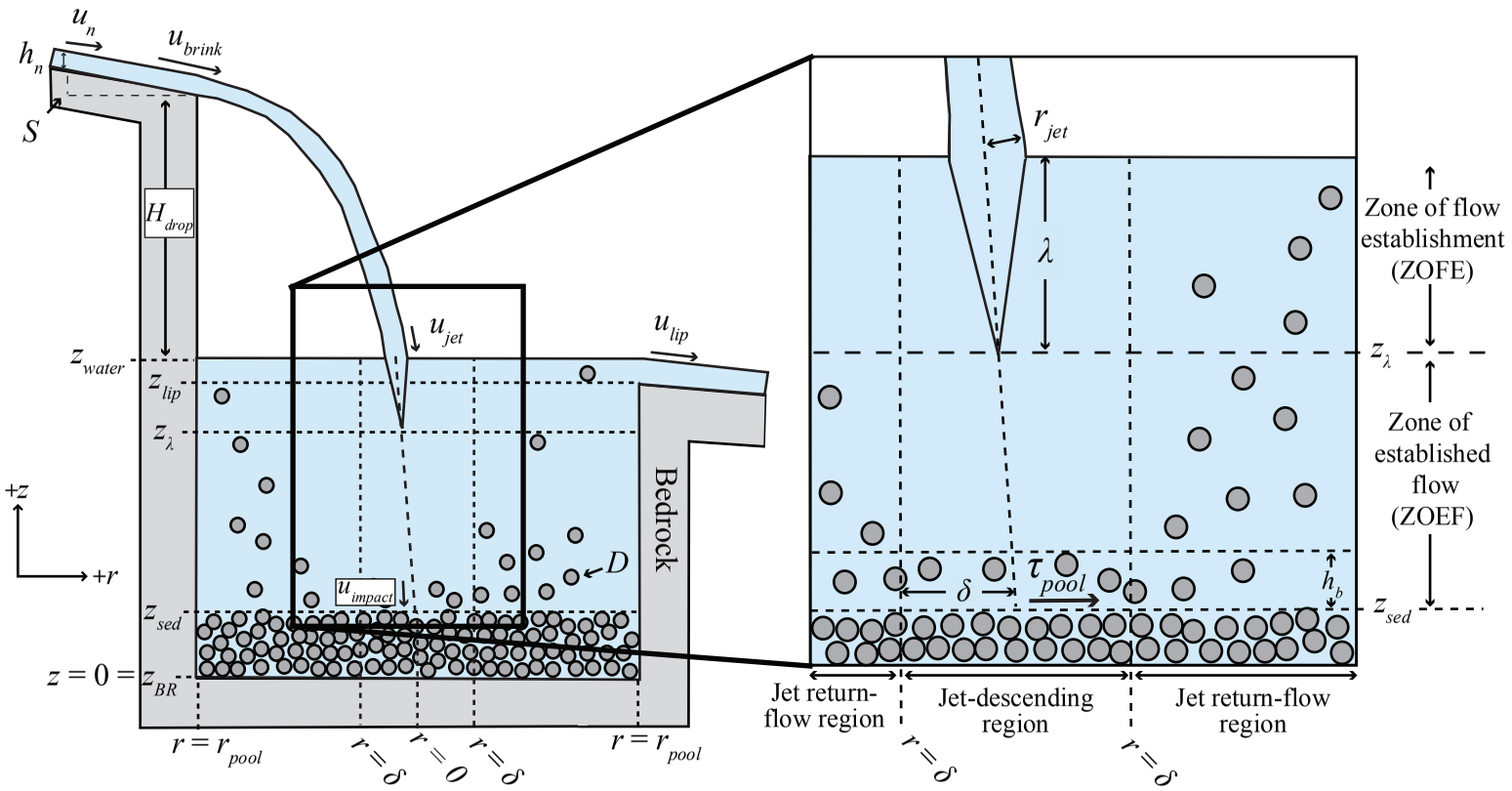

Figure 4.2: Schematic of waterfall plunge pool system with key variables labeled. Inset shows jet-descending and return-flow regions, as well as zones of flow establishment (ZOFE) and established flow (ZOEF).

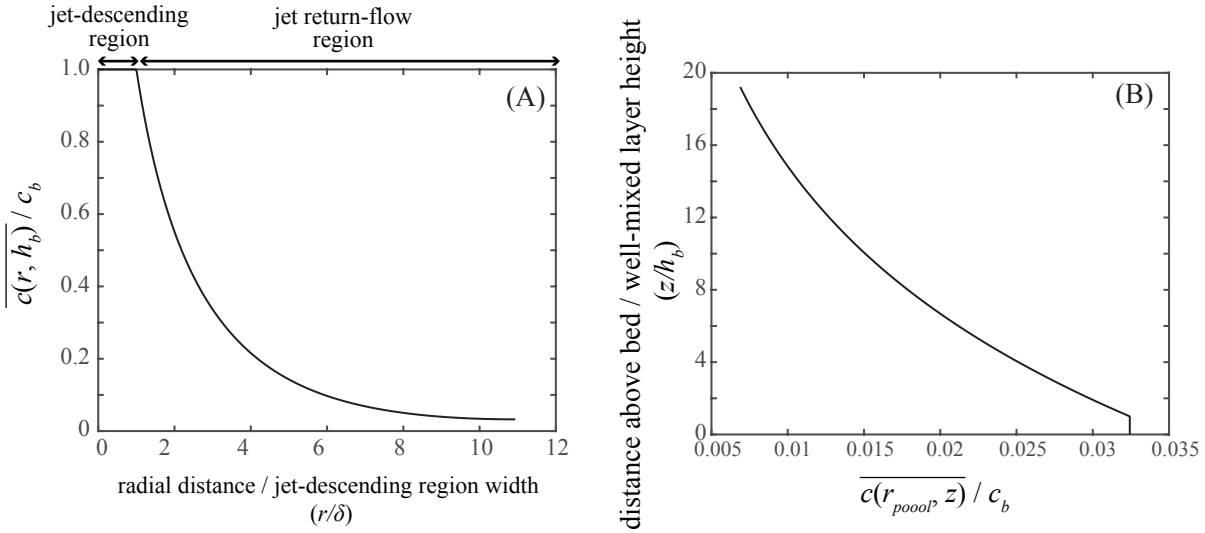

Figure 4.3: Profiles of radial (A) and vertical (B) sediment concentration normalized by near-bed concentration in the jet-descending region (c_b) along the plunge pool floor at $z = h_b$ and along the plunge-pool wall at r = rpool, respectively. For this calculation Q_w = 4.8 m^3/s, H = 5 m, D = 0.1 m, r_{pool} = 4.4 m, and Fr_n = 1.9.

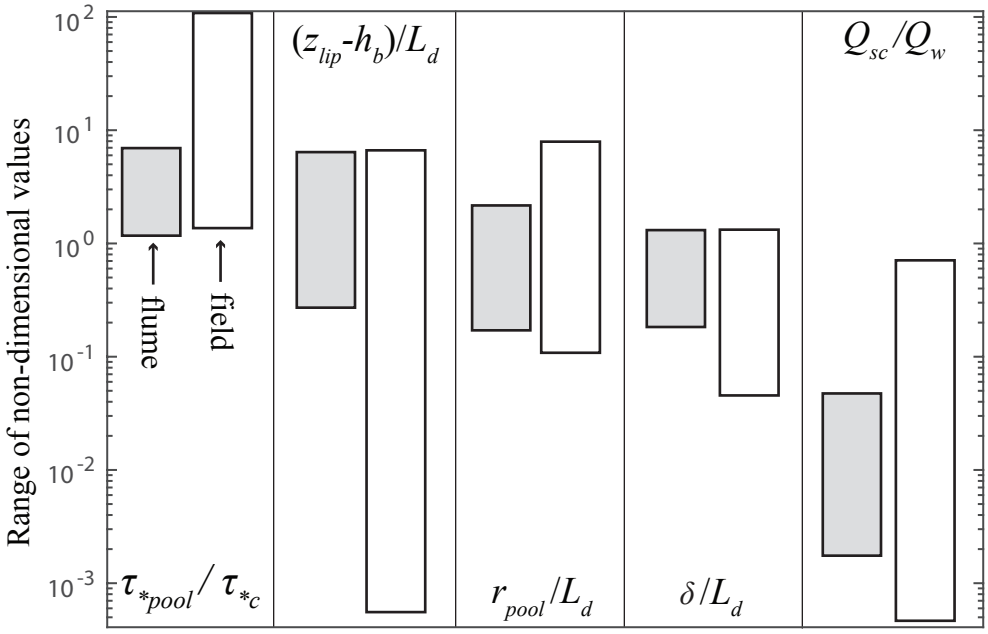

Figure 4.4: Comparison of range of non-dimensional variables influencing plunge-pool sediment-transport capacity from flume measurements (gray boxes, Table S4.2) versus field measurements (white boxes, Table S4.1). Note that field values of non-dimensional variables were calculated using the median grain diameter deposited within the plunge pool and we set $C_{f\_river} = 0.01$ as estimating the river friction factor requires detailed hydraulic measurements which are difficult to make near waterfalls which are often inaccessible during periods of high flow.

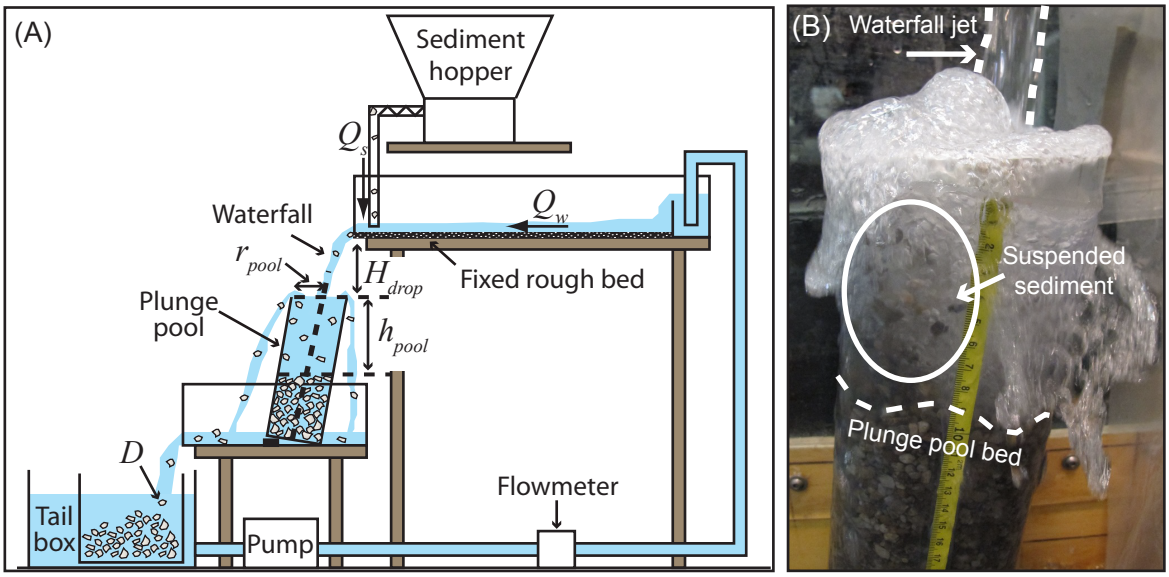

Figure 4.5: (A) Flume schematic with key variables labeled. (B) Example photo of sediment transport through a waterfall plunge pool during Experiment 12 (Table S2). Plunge pool is 10.2 cm in diameter and yellow tape is marked in cm increments for scale.

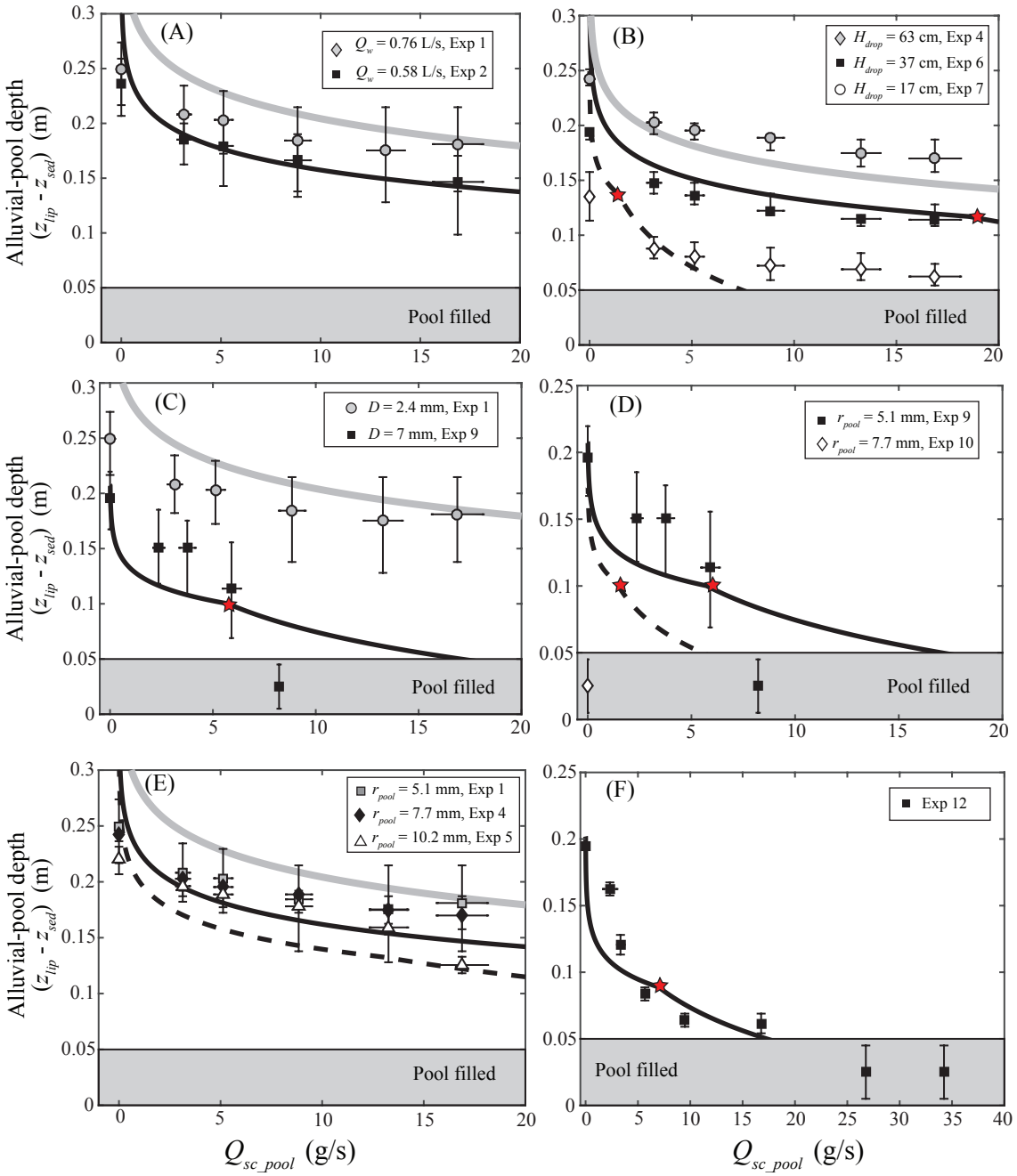

Figure 4.6: Plots of experimentally measured equilibrium plunge-pool depth versus imposed upstream sediment flux for experiments varying (A) water discharge (Q_w), (B) waterfall drop height (H), (C) grain size (D), (D) plunge pool radius (r_{pool}) with 7 mm diameter sediment, and (E) plunge pool radius with 2.4 mm diameter sediment, with all other variables held constant. (F) Shows Exp 12 with D = 5.6 mm sediment. See Table S4.2 for all experimental parameter values. Lines show theoretical predictions where theory and experimental data match in color (e.g., gray circles match gray lines, black squares match black lines, and white triangles match white lines). All data points are at steady state so that imposed sediment flux is equal to plunge-pool sediment-transport capacity (Q_{sc_pool}), vertical error bars reflect topographic variability across the plunge-pool floor and horizontal error bars show standard deviation of sediment flux measurements. Symbols show experimental measurements (Table S4.2) and lines show model predictions. Red stars indicate transition from ZOEF (above red star) to ZOFE (below red star). Filled plunge pools had depths which ranged from ~ 0 – 5 cm; we make no model predictions at these depths where we observed a change in process from grain suspension to fluidization of the bed (see text for details).

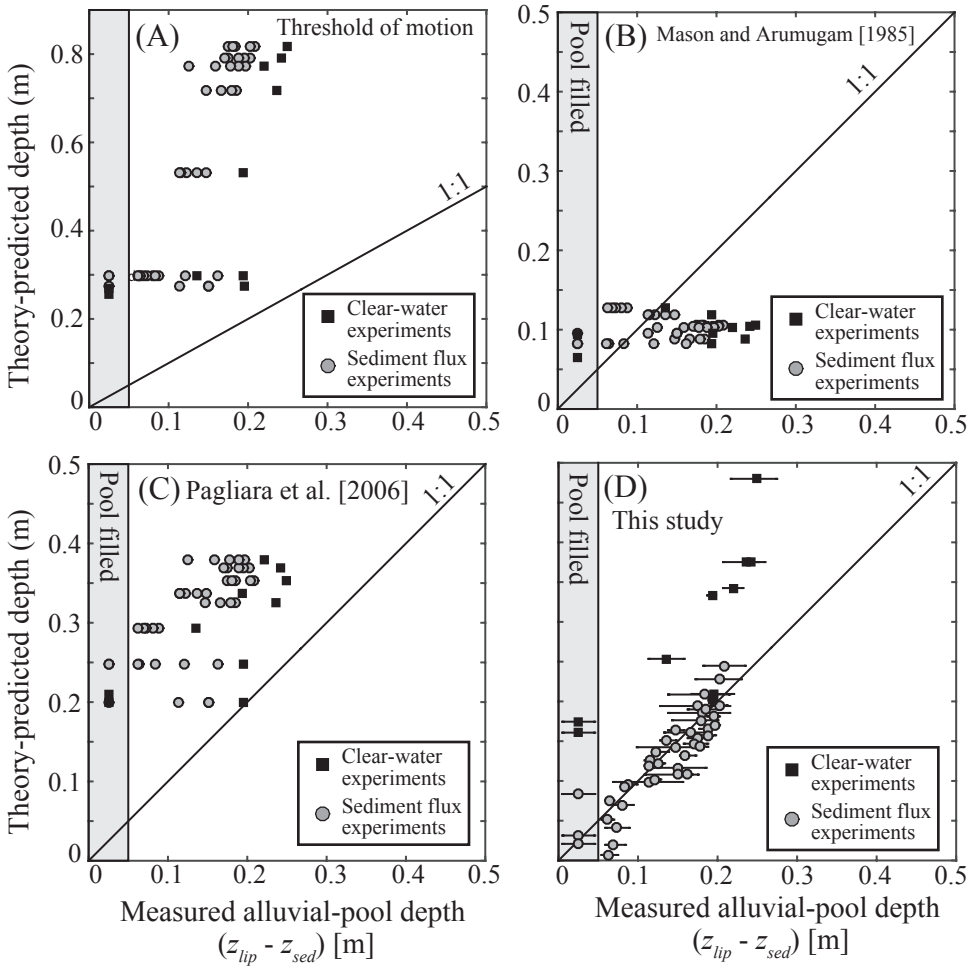

Figure 4.7: Comparison of experimentally measured alluvial-pool depth from our experiments with predictions based on (A) threshold of motion for sediment, (B) Mason and Arumugam [1985], (C) Pagliara et al. [2006], and (D) this study. Error bars in panel (D) denote topographic variability of alluvial-pool floor, identical error bars apply to panels (A) - (C) but were removed for visual clarity. Note that the threshold of motion approach, Mason and Arumugam [1985], and Pagliara et al. [2006] are not designed to handle sediment supply and therefore predict alluvial depth independent of sediment flux (causing datapoints to plot in rows). We calculate tailwater detph above the plunge-pool lip assuming Fr = 1 for both the Pagliara et al. [2006] and Manson and Arumugam [1985] predictions. The Pagliara et al. [2006] model also requires an estimate of jet air content which we did not measure in our experiments and set to 0.5. Shaded gray box in all panels marks measured depths less than 5 cm where we observed filled plunge pools with fluidized beds.

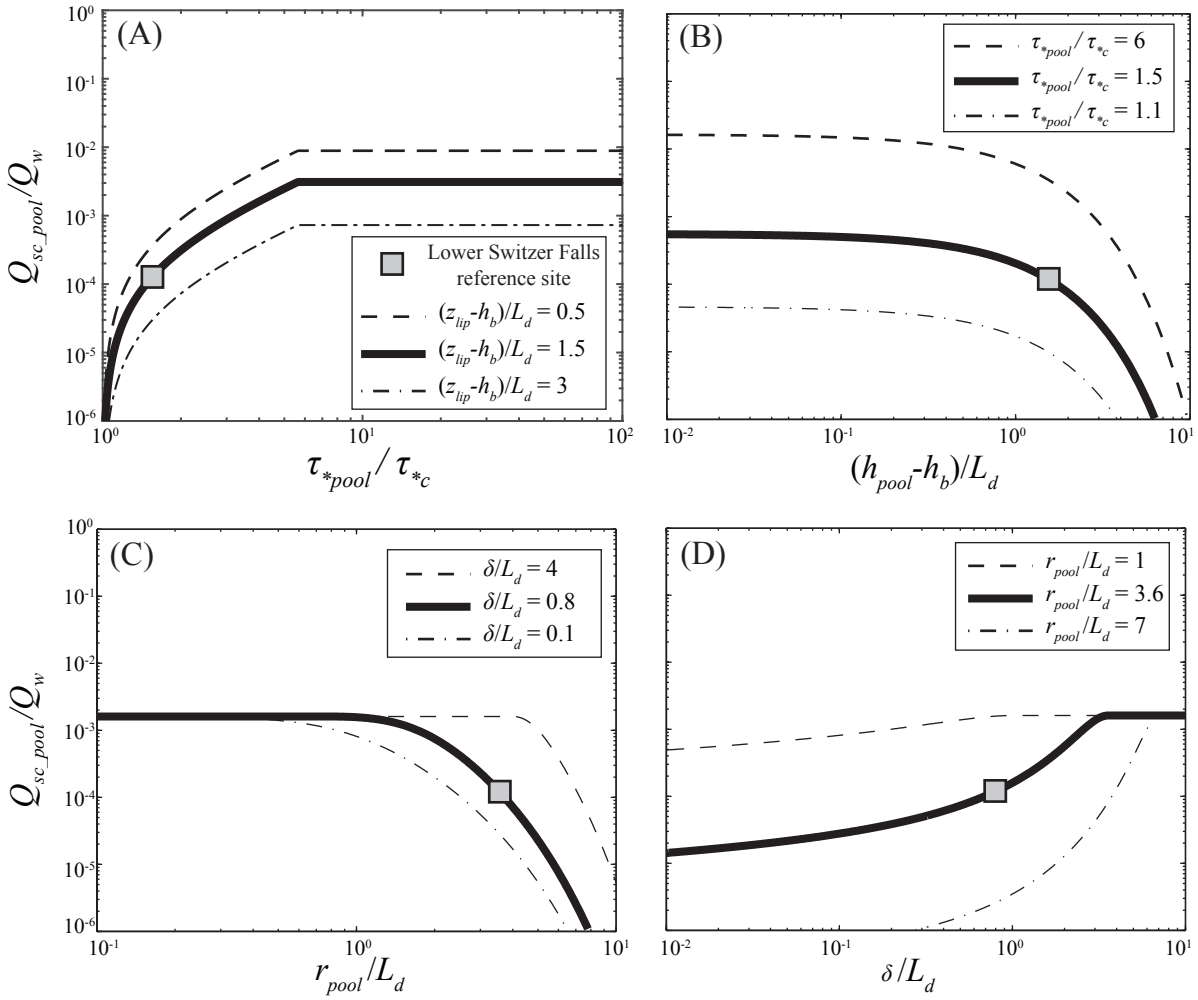

Figure 4.8: Model predictions of Q_{sc_pool} / Q_w for varying values of the four non-dimensional parameters governing plunge pool sediment concentration, (A) transport stage (τ_{*pool}/ τ_{*c}), (B), $(h_{pool} - h_b) / L_d$, (C) r_{pool}/L_d, and (D) $2b/L_d$. In each plot multiple lines show influence of varying a second non-dimensional variable and gray squares show values for the Lower Switzer Falls reference site. Non-dimensional parameters not being varied in a specific plot were held constant at their Lower Switzer Falls' values: τ_{*pool}/ τ_{*c} = 1.52, $(h_{pool} - h_b) / L_d$, = 1.55, r_{pool}/L_d = 3.58, $2b/L_d$ = 0.79. See text for details.

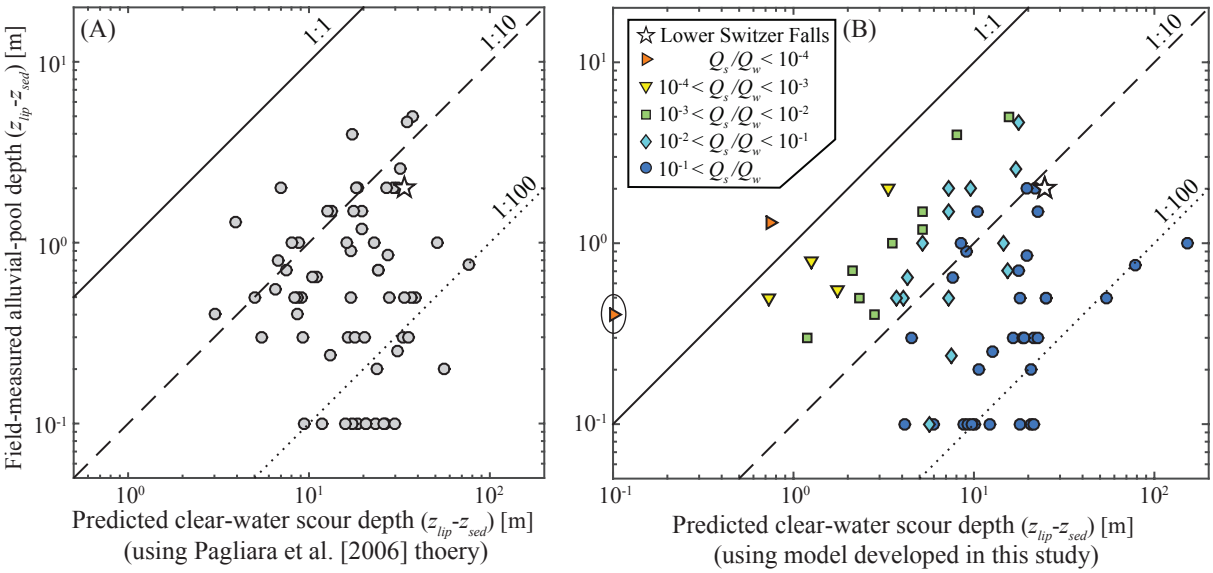

Figure 4.9: Comparison of field-measured alluvial-pool depth (z_{lip}-z_{sed}, Table S4.1) versus model-predicted clear-water depth for 2-year recurrence interval flood using (A) the Pagliara et al. [2006] empirical formula and (B) the theory developed in this study. Points below the 1:1 line represent pools shallower than predicted for clear-water flow. Points in panel (B) are color coded by the upstream sediment concentrations (Q_s/Q_w) needed to fit the observed pool depth at steady state, indicating that greater departure from the 1:1 line (i.e., partially-filled and filled pools) requires higher sediment concentration from upstream to maintain a steady-state depth. The circled point on y-axis in (B) is a plunge pool which is predicted to be completely filled with sediment under clear-water discharge. All model calculations performed with the grain size of the sediment deposited in the plunge pool. For predictions in panel (A) we assumed a jet air content of 0.5.

Supplementary material for Chapter 4

S4.1 Waterfall field survey methods

During our field surveys we measured the depth of waterfall plunge-pools using a variety of methods. All our field measurements were made at low to moderate water discharges when plunge-pools were safe to survey and accessible. For the vast majority of plunge pools surveyed, we made manual measurements of the depth to the plunge-pool floor. Most plunge-pools were alluviated during our surveys such that we report pool-alluvial depth (i.e., $z_{lip} - z_{sed}$), but for some cases (as denoted in Table S1), bedrock was exposed on the pool floor allowing measurement of plunge-pool bedrock depth (i.e., $z_{lip} - z_{BR}$). In some cases the distinction between a sediment and bedrock floor was not denoted, and we make no distinction as to whether such depths are alluvial or bedrock pool depths. We measured the vertical distance from the plunge-pool lip to the plunge-pool floor using either a stadia rod or plumb-bob attached to a tape measure.

Several plunge-pools were completely filled with sediment (i.e., $z_{lip} - z_{sed} \approx 0$) and many were partially-filled during our field surveys. These shallow alluvial depths are likely a result of our surveying at low flow and perhaps additionally due to temporal variability in sediment supply (for example, many of our measurements in the San Gabriel Mountains, California occurred within 1-3 years of the 2009 Station Fire when sediment supply was likely elevated by up to an order of magnitude compared to background levels [*Lamb et al.*, 2011]. To mitigate this effect, for 16 out of 75 of our surveyed plunge-pools we report pre-existing data indicating deeper plunge-pools measurement depths than obtained during our surveyed. This data came from three separate sources. For Wailua Falls, Hawaii ("WF" in Table S1) we use the depth

measured by Doughty [2010] when SCUBA diving in the plunge-pool. For upper Ho'opi'i Falls, Hawaii (HFU Table S1), 3 separate falls on Arroyo Seco, California (MSF, LSF, ASP4), and 1 waterfall on Fall Creek, California (FCR1) we estimate the minimum plunge-pool depth as 2 m based on countless accounts of cliff-jumping from heights > 2 m. Finally, many depth-estimates of plunge-pools within Little Santa Anita Canyon, CA and one estimate from Fox Creek, CA are unpublished data provided by Prof. Chris Brennen who assisted with field surveys. These data were collected by Prof. Brennen over countless visits to these canyons while researching a canyoneering guidebook for the San Gabriel Mountains [*Brennen*, 2000], and the measurements should be treated as estimates with up to 25% error. The measurement technique used for each surveyed plunge-pool is denoted in Table S1.

S4.2 References

Brennen, C. (2000), *Adventure hikes and canyoneering in the San Gabriels*, Dankat Publishing Company, Pasadena.

Doughty, A. (2010), *The Ultimate Kauai Guidebook*, 7th ed., Wizard Publications, Lihu'e, Hawai'i.

Lamb, M. P., J. S. Scheingross, W. H. Amidon, E. Swanson, and A. Limaye (2011), A model for fire-induced sediment yield by dry ravel in steep landscapes, *Journal of Geophysical Research-Earth Surface*, *116*, doi:10.1029/2010jf001878.

S4.3 Movie Captions

Movie S1. Video of plunge-pool sediment transport during Experiment 12 (Table S4.2). Plunge pool is 10.2 cm in diameter for scale. Movie taken with a high speed camera recording at 240 frames per second, resulting in approximately a factor of 5 slow-down compared to real time.

Table S4.1. Measurements of field-surveyed plunge pools and calculation of non-dimensional variables[a]

River	ID	S	W (m)	H (m)	r_{pool} (m)	h_{pool} (m)	D pool (m)	D river (m)	A (km^2)	Q_{2yr} (m^3/s)	Q_{sc_pool} / Q_w	τ_{*pool} / τ_{*c}	$(h_{pool} - h_b) / L_d$	r_{pool} / L_d	$2b / L_d$	UTM Easting	UTM Northing	Depth reported
Colby Canyon	CP1	0.06	5	2.5	2.3	0.9	0.01	0.15	2.62	1.03	0.12	9.17	0.54	1.45	0.29	395326	3792758	meas. (s)
Colby Canyon	CP2a	0.07	4	2	0.9	0.65	0.015	0.15	1.64	0.64	0.12	5.28	0.34	0.48	0.21	395467	3792855	meas. (s)
Colby Canyon	CP2b	0.07	4	0.6	1.9	0.4	0.015	0.15	1.64	0.64	2.1×10^{-3}	2.76	0.63	3.14	0.55	395467	3792855	meas. (s)
Colby Canyon	CP3	0.06	3	1.2	1.8	0.5	0.015	0.15	1.64	0.64	0.01	3.83	0.60	2.33	0.47	395463	3792879	meas. (s)
Colby Canyon	CP4b	0.05	3	3.2	1.5	1	0.02	0.15	1.61	0.63	0.03	5.29	0.98	1.57	0.39	395568	3792957	meas. (s)
Colby Canyon	CP4c	0.05	3	1.9	2.3	1	0.02	0.15	1.61	0.63	1.9×10^{-3}	3.54	1.28	3.06	0.52	395568	3792957	meas. (s)
Little Santa Anita	LR1	0.08	3.5	8.5	1.0	0.1	0.02	0.1	5.49	1.43	0.96	14.25	0.00	0.16	0.07	403678	3782944	meas. (s)
Little Santa Anita	LR2	0.08	5	4	2.9	0.5	0.02	0.1	5.49	1.43	0.05	7.60	0.31	2.08	0.34	403681	3782993	comm.
Little Santa Anita	LR3	0.08	4	3.5	0.7	0.3	0.02	0.1	5.54	1.44	0.32	7.30	0[b]	0[b]	0[b]	403700	3782879	meas. (br)
Little Santa Anita	LR4	0.08	5	8	2.0	1.5	0.02	0.1	5.55	1.45	0.25	13.00	0.73	1.04	0.23	403707	3782848	comm.
Little Santa Anita	LR5a	0.08	4	5.5	0.8	1.5	0.02	0.1	5.55	1.45	0.54	9.99	0[b]	0[b]	0[b]	403704	3782825	comm.
Little Santa Anita	LR5b	0.08	4	1.25	1.3	1.5	0.02	0.1	5.55	1.45	0.04	4.27	0.90	0.78	0.26	403704	3782825	comm.
Little Santa Anita	LD1a	0.08	5	1	0.6	0.24	0.02	0.1	5.59	1.46	0.08	3.59	0[b]	0[b]	0[b]	403707	3782759	meas. (br)
Little Santa Anita	LD1b	0.08	5	4	0.7	0.1	0.02	0.1	5.59	1.46	0.34	7.63	0[b]	0[b]	0[b]	403707	3782759	meas. (s)
Little Santa Anita	LR6	0.08	6	5.2	1.9	2	0.02	0.1	5.6	1.46	0.10	8.99	1.08	1.06	0.27	403719	3782712	comm.
Little Santa Anita	LR7a	0.08	6	4.5	1.0	0.3	0.02	0.1	5.6	1.46	0.36	8.05	0.03	0.13	0.07	403675	3782679	meas. (s)
Little Santa Anita	LR7b	0.08	6	0.75	1.5	1.5	0.02	0.1	5.6	1.46	0.01	3.00	1.38	1.42	0.39	403675	3782679	comm.
Little Santa Anita	LDF	0.1	6	1.5	2.1	0.1	0.02	0.1	5.7	1.48	0.04	4.71	0.04	1.99	0.40	403693	3782583	meas. (s)
Little Santa Anita	LR8	0.11	6	4.5	2.0	0.1	0.02	0.1	5.72	1.49	0.25	9.12	0.01	1.24	0.28	403699	3782457	meas. (s)
Little Santa Anita	LR9	0.11	5	2.7	2.0	2	0.02	0.1	5.76	1.50	0.03	7.11	1.44	1.50	0.31	403722	3782369	comm.
Little Santa Anita	LR10	0.09	3	3	1.5	1	0.02	0.1	5.8	1.51	0.16	7.81	0.54	0.88	0.24	403870	3782433	comm.
Little Santa Anita	LR11	0.09	2.5	4.7	2.3	4	0.02	0.1	5.82	1.52	2.1×10^{-3}	5.46	3.59	2.05	0.73	403910	3782489	comm.
Rubio Canyon	RR1	0.13	4	23	1.9	0.25	0.01	0.1	2.26	0.88	0.72	69.02	0.05	0.67	0.10	397227	3785825	meas. (s)
Rubio Canyon	RR2	0.13	3	6.5	1.6	0.2	0.01	0.1	2.26	0.88	0.72	26.07	0.06	0.72	0.15	397226	3785809	meas. (s)
Rubio Canyon	RR3	0.13	4	4.6	1.5	0.1	0.01	0.1	2.27	0.89	0.75	19.48	0.02	0.75	0.17	397223	3787590	meas. (s)
Rubio Canyon	RR4	0.15	4	6.2	2.3	0.1	0.01	0.1	2.27	0.89	0.42	25.27	0.02	1.27	0.18	397178	3785777	meas. (s)
Rubio Canyon	RR5	0.15	3	7.5	2.0	0.1	0.01	0.1	2.27	0.89	0.55	30.58	0.01	1.04	0.16	397172	3785769	meas. (s)

Rubio Canyon	RR6	0.18	4	8.5	1.4	0.1	0.01	0.1	2.28	0.89	0.87	33.84	0.01	0.51	0.11	397152	3785725	meas. (s)
Daisy Canyon	DC1	0.1	2	1.5	0.8	0.3	0.01	0.11	0.75	0.29	0.20	7.84	0.30	0.90	0.24	395633	3792897	meas. (s)
Daisy Canyon	DC2	0.1	3	2.3	1.3	0.65	0.01	0.11	0.75	0.29	0.07	9.10	0.77	1.67	0.30	395615	3792880	meas. (s)
Daisy Canyon	DC3	0.1	2	1.1	1.0	0.5	0.01	0.11	0.76	0.30	0.07	6.80	0.67	1.38	0.30	395604	3792828	meas. (s)
Daisy Canyon	DC4	0.1	2	1.5	1.0	0.1	0.01	0.11	0.8	0.31	0.18	8.01	0.08	1.28	0.28	395581	3792807	meas. (s)
Daisy Canyon	DC5	0.1	2	4	1.0	0.1	0.01	0.11	0.85	0.33	0.69	14.91	0.04	0.87	0.20	395508	3792735	meas. (s)
Arroyo Seco	USF	0.035	5	12	7.3	0.5	0.01	0.21	12.08	4.73	0.28	35.76	0.09	1.49	0.16	393659	3791349	meas. (s)
Arroyo Seco	MSF	0.035	5	3	4.0	3	0.01	0.21	12.28	4.81	0.21	11.55	0.76	1.03	0.24	393855	3791207	comm.
Arroyo Seco (Lower Switzer Falls reference site)	LSF	0.035	5	5	4.4	2	0.01	0.21	12.28	4.81	0.40	16.94	0.45	1.00	0.20	393855	3791207	comm.
Arroyo Seco	ASP1	0.014	4	1.21	3.0	0.3	0.01	0.21	12.53	4.90	0.12	4.90	0.07	0.74	0.28	394148	3790733	meas. (s)
Arroyo Seco	ASP2	0.049	3	1.45	3.0	0.5	0.01	0.21	12.51	4.90	0.43	11.41	0.13	0.84	0.18	394085	3790816	meas. (s)
Arroyo Seco	ASP3	0.052	5	2.18	3.0	0.3	0.01	0.21	12.49	4.89	0.54	11.62	0.06	0.69	0.18	394042	3790846	meas. (s)
Arroyo Seco	ASP4	0.035	5	2.32	3.0	3	0.01	0.21	12.49	4.89	0.17	7.46	0.59	0.60	0.23	394048	3790853	comm.
Arroyo Seco	ASP5	0.016	4	1.23	3.0	0.1	0.01	0.21	12.48	4.88	0.14	5.11	0.02	0.74	0.27	394066	3790866	meas. (s)
Fall Creek	FCR1	0.05	3	10.5	1.9	2	0.02	0.025	5.68	0.26	6.9×10^{-4}	7.40	3.51	3.51	0.73	392877	3796770	comm.
Fall Creek	FCR2	0.05	4	12	3.7	0.7	0.02	0.025	5.68	0.26	3.5×10^{-3}	16.62	0.75	4.71	0.25	392885	3796758	meas. (s)
Fall Creek	FCR3	0.05	3	7	3.9	0.55	0.02	0.025	5.68	0.26	7.6×10^{-4}	9.98	0.69	5.73	0.33	392890	3796746	meas. (s)
Fall Creek	FCR4	0.05	4	23	3.9	0.5	0.02	0.025	5.68	0.26	7.8×10^{-3}	31.43	0.37	4.18	0.18	392895	3796728	meas. (s)
Classic Canyon	CC1	0.12	4	1.5	1.5	0.4	0.03	0.05	1.42	0.07	0.00	1.72	2.02	8.35	0.78	392893	3796323	meas. (s)
Classic Canyon	CCR1	0.12	3	6.5	2.3	0.8	0.01	0.05	1.49	0.07	4.6×10^{-4}	13.35	1.86	5.70	0.40	392684	3796459	meas. (s)
Classic Canyon	CCR2	0.12	3	9	2.3	0.5	0.02	0.05	1.49	0.07	4.3×10^{-4}	12.83	1.09	6.18	0.29	392675	3796474	meas. (s)
Classic Canyon	CCR2a	0.12	3	2	1.4	1.3	0.02	0.05	1.49	0.07	0.00	1.76	7.23	7.80	1.47	392675	3796474	meas. (br)
Classic Canyon	CCR2b	0.12	3	2	1.6	0.3	0.01	0.05	1.49	0.07	1.3×10^{-3}	6.80	0.76	4.68	0.39	392675	3796474	meas. (s)
Fox Creek	FXR1	0.05	2	3	2.3	1	0.005	0.03	22.75	7.27	1.00	42.42	0^b	0^b	0^b	391431	3797425	meas. (br)
Fox Creek	FXR2	0.05	5	13	3.5	0.75	0.005	0.03	22.75	7.27	0.96	84.29	0.03	0.17	0.04	391467	3797391	meas. (s)
Fox Creek	FXR3	0.05	3	3.5	3.5	1	0.03	0.03	22.75	7.27	0.10	6.48	0.33	1.29	0.31	391482	3797388	meas. (s)
Fox Creek	FXR4	0.05	3.6	7.5	3.4	0.85	0.03	0.03	22.75	7.27	0.31	9.69	0.19	0.90	0.24	391495	3797399	meas. (s)
Fox Creek	FXR5	0.05	4	3.5	2.8	0.7	0.03	0.03	22.75	7.27	0.15	5.90	0.17	0.78	0.25	391501	3797420	meas. (s)
Fox Creek	FXR6	0.05	7	27	2.0	0.5	0.03	0.03	22.75	7.27	0.98	26.14	0.02	0.11	0.05	391565	3797461	meas. (s)

Fox Creek	FXR7	0.05	4	6	3.0	2	0.03	0.03	22.75	7.27	0.19	8.14	0.49	0.78	0.24	391582	3797472	comm.
Fox Creek	FXR8	0.05	4	3.5	3.5	0.7	0.03	0.03	22.75	7.27	0.10	5.90	0.22	1.26	0.32	391611	3797487	meas. (s)
Fox Creek	FXR9	0.05	5	16	3.5	0.5	0.03	0.03	24.6	7.86	0.76	16.87	0.07	0.72	0.18	391524	3796514	meas. (s)
Millard Canyon	M1	0.075	5	17	2.9	0.3	0.01	0.05	5.1	2.00	0.69	50.87	0.05	0.75	0.12	394833	3787038	meas. (s)
Wolfskill Canyon	W1	0.1	6	9	5.0	1.2	0.01	0.17	5.2	0.55	0.01	27.00	0.77	3.43	0.20	430738	3781897	meas. (s)
Dry Meadow Ck	STC1	0.05	12	2.66	6.2	3.9		0.1	93.5	3.66	-	-	-	-	-	366139	3984275	meas.
Dry Meadow Ck	STC2	0.05	12	3.74	4.8	2		0.1	93.5	3.66	-	-	-	-	-	366143	3984266	meas.
Dry Meadow Ck	STC3	0.05	12	5.34	9.2	5	0.01	0.1	93.5	3.66	0.01	13.66	1.66	3.07	0.33	366146	3984250	meas. (s)
Dry Meadow Ck	STC4	0.05	12	3.89	5.9	4.62	0.01	0.1	93.5	3.66	0.04	11.82	1.51	1.93	0.30	366155	3984237	meas. (s)
Dry Meadow Ck	STC5	0.05	12	1.24	4.9	2.21		0.1	93.5	3.66	-	-	-	-	-	366159	3984225	meas. (br)
Dry Meadow Ck	STC6	0.05	12	2.85	7.4	2.53		0.1	93.5	3.66	-	-	-	-	-	366166	3984219	meas.
Dry Meadow Ck	STC7	0.05	12	2.36	4.5	2.55	0.01	0.1	93.5	3.66	0.07	8.87	0.87	1.55	0.30	366175	3984206	meas. (s)
Dry Meadow Ck	STC8	0.05	12	11	4.4	1.35		0.1	93.5	3.66	-	-	-	-	-	366191	3984207	meas.
Dry Meadow Ck	STC9	0.05	12	13.99	6.4	3.57		0.1	93.5	3.66	-	-	-	-	-	366246	3984191	meas.
Kapaa Stream	HFU	0.007	12	6	4.0	3		0.15	16.8	111.73	-	-	-	-	-	464537	2444738	comm.
SF Wailua River	WF	0.006	12	49	40.0	10		0.1	62	412.33	-	-	-	-	-	460951	2436662	comm.
Huleia Stream	KP	0.003	10	5.6	22.3	7.5		0.2	47	177.76	-	-	-	-	-	456876	2427414	meas.
Kaulaula Valley	KA	0.13	6	39	3.7	0.2	0.01	0.3	3.2	2.31	0.66	115.27	0.01	0.75	0.08	425986	2442220	meas.
Hanakapiai Stream	HF	0.4	10	120	22.0	4.7		0.3	4.5	27.19	-	-	-	-	-	438743	2453474	meas.

[a] S and W refer to channel reach-averaged slope and width upstream of the waterfall. Plunge pool grain size measurements reported are typically from visual estimates, and reach-averaged grain sizes are a mixture of visual estimates and random-walk pebble counts. 2-year recurrence interval discharge estimates (Q_{2yr}) are made from USGS gage 11098000 for plunge pools on Arroyo Seco, Colby Canyon, Millard Canyon, and Rubio Canyon, from gage 11100500 for pools on Little Santa Anita, from gage 11095500 for pools on Classic Canyon and Fall Creek, from gage 11095000 for pools on Fox Creek, from data provided by the US Forest Service Forest San Dimas Experimental Forest for plunge pools on Wolfskill Canyon, from gage 11186000 for plunge pools on Dry Meadow Creek, from gage 16060000 for pools on Kapaa Stream and S Fork Wailua River, and from gage 16055000 for Huleia Stream, from gage 16130000 for Kaulaula Valley, and from gage 16115000 for Hanakapiai Stream. Non-dimensional variables were calculated using the median grain diameter deposited in the plunge pool, discharge equal to Q_{2yr}, and $Cf_{\_river}$ set to 0.01. We did not calculate non-dimensional variable values for streams in which we did not make a measure of the plunge pool grain size and denote such cases with '-'. Depth reported column distinguishes between our measured pool depths (meas.) versus maximum observed depths communicated to us from hikers and canyoneers (comm.), letter in parantheses refers to whether the pool bottom was filled sediment (s) or whether bedrock was exposed (br) at the time of measurement, lack of letter indicates no distinction was made at time of measurement.

[b] These are cases with large discharges relative to pool diameter and grain size such that $w_{net} < 0$ and, as a result, L_d is infinite.

Table S2. Measurements from waterfall plunge-pool sediment-transport capacity experiments and calculation of non-dimensional variables[a]

Exp #	Q_s (g/s)	Q_w (L/s)	H (cm)	r_{pool} (cm)	D (mm)	u_{brink} (m/s)	Min h_{pool} (cm)	Max h_{pool} (cm)	Average h_{pool} (cm)	Q_{sc_pool} / Q_w	τ_{*pool} / τ_{*c}	$(h_{pool} - h_b) / L_d$	r_{pool} / L_d	$2b / L_d$
1	0 ± 0	0.76	66	5.1	2.4	0.61 ± 0.1	21.7	27.4	24.9	0	3.31	3.33	0.70	0.68
1	3.14 ± 0.33	0.76	66	5.1	2.4	0.61 ± 0.1	18.2	23.4	20.8	0.0024	3.97	2.52	0.64	0.52
1	5.12 ± 0.44	0.76	66	5.1	2.4	0.61 ± 0.1	17.2	22.9	20.3	0.0039	4.06	2.43	0.63	0.50
1	8.84 ± 0.63	0.76	66	5.1	2.4	0.61 ± 0.1	13.8	21.5	18.4	0.0068	4.48	2.09	0.60	0.43
1	13.26 ± 0.93	0.76	66	5.1	2.4	0.61 ± 0.1	12.8	21.5	17.5	0.01	4.71	1.93	0.59	0.40
1	16.88 ± 1.24	0.76	66	5.1	2.4	0.61 ± 0.1	13.8	21.5	18.1	0.013	4.56	2.03	0.60	0.42
2	0 ± 0	0.58	66	5.1	2.4	0.61 ± 0.1	20.7	25.9	23.6	0	3.07	4.48	0.99	0.91
2	3.14 ± 0.33	0.58	66	5.1	2.4	0.61 ± 0.1	16.2	20.0	18.5	0.0031	3.91	3.08	0.88	0.64
2	5.12 ± 0.44	0.58	66	5.1	2.4	0.61 ± 0.1	14.3	20.0	17.9	0.0051	4.04	2.93	0.86	0.61
2	8.84 ± 0.63	0.58	66	5.1	2.4	0.61 ± 0.1	13.3	19.0	16.6	0.0088	4.36	2.60	0.83	0.54
2	16.88 ± 1.24	0.58	66	5.1	2.4	0.61 ± 0.1	9.8	17.0	14.7	0.017	4.94	2.13	0.78	0.45
3	0 ± 0	0.76	63	3.9	2.4	0.61 ± 0.1	22.2	25.4	23.5	0	3.39	1.11	0.19	0.23
3	3.14 ± 0.33	0.76	63	3.9	2.4	0.61 ± 0.1	19.2	23.0	20.9	0.0024	3.82	0.93	0.18	0.19
3	5.12 ± 0.44	0.76	63	3.9	2.4	0.61 ± 0.1	18.2	22.5	20.6	0.0039	3.86	0.91	0.18	0.19
3	8.84 ± 0.63	0.76	63	3.9	2.4	0.61 ± 0.1	17.2	22.0	19.8	0.0068	4.02	0.85	0.17	0.18
3	13.26 ± 0.93	0.76	63	3.9	2.4	0.61 ± 0.1	18.7	22.5	20.4	0.01	3.91	0.89	0.18	0.18
3	16.88 ± 1.24	0.76	63	3.9	2.4	0.61 ± 0.1	18.7	24.5	21.7	0.013	3.67	0.98	0.18	0.20
4	0 ± 0	0.76	63	7.7	2.4	0.61 ± 0.1	23.6	25.1	24.2	0	3.30	4.73	1.54	0.97
4	3.14 ± 0.33	0.76	63	7.7	2.4	0.61 ± 0.1	19.2	21.2	20.3	0.0024	3.94	3.60	1.41	0.74
4	5.12 ± 0.44	0.76	63	7.7	2.4	0.61 ± 0.1	18.7	20.2	19.5	0.0039	4.09	3.40	1.38	0.70
4	8.84 ± 0.63	0.76	63	7.7	2.4	0.61 ± 0.1	17.7	19.2	18.9	0.0068	4.23	3.22	1.36	0.67
4	13.26 ± 0.93	0.76	63	7.7	2.4	0.61 ± 0.1	16.2	18.7	17.5	0.01	4.56	2.86	1.31	0.59
4	16.88 ± 1.24	0.76	63	7.7	2.4	0.61 ± 0.1	15.8	18.7	17.0	0.013	4.70	2.73	1.29	0.57
5	0 ± 0	0.76	61	10.1	2.4	0.61 ± 0.1	20.7	23.1	22.1	0	3.53	4.56	2.15	0.94
5	3.14 ± 0.33	0.76	61	10.1	2.4	0.61 ± 0.1	18.7	20.2	19.6	0.0024	3.97	3.80	2.02	0.78
5	5.12 ± 0.44	0.76	61	10.1	2.4	0.61 ± 0.1	17.7	19.7	18.9	0.0039	4.13	3.58	1.99	0.74
5	8.84 ± 0.63	0.76	61	10.1	2.4	0.61 ± 0.1	17.2	18.7	17.8	0.0068	4.37	3.27	1.93	0.68
5	13.26 ± 0.93	0.76	61	10.1	2.4	0.61 ± 0.1	15.3	17.2	15.9	0.01	4.89	2.74	1.82	0.57
5	16.88 ± 1.24	0.76	61	10.1	2.4	0.61 ± 0.1	11.8	13.3	12.6	0.013	6.20	1.88	1.62	0.40

6	0 ± 0	0.76	37	7.7	2.4	0.61 ± 0.1	18.7	19.7	19.4	0	2.78	3.65	1.49	0.75
6	3.14 ± 0.33	0.76	37	7.7	2.4	0.61 ± 0.1	13.8	15.8	14.8	0.0024	3.64	2.40	1.30	0.50
6	5.12 ± 0.44	0.76	37	7.7	2.4	0.61 ± 0.1	12.8	14.8	13.6	0.0039	3.95	2.11	1.25	0.44
6	8.84 ± 0.63	0.76	37	7.7	2.4	0.61 ± 0.1	11.8	13.8	12.2	0.0068	4.36	1.79	1.19	0.38
6	13.26 ± 0.93	0.76	37	7.7	2.4	0.61 ± 0.1	10.8	11.8	11.5	0.01	4.36	1.67	1.19	0.38
6	16.88 ± 1.24	0.76	37	7.7	2.4	0.61 ± 0.1	10.8	12.8	11.4	0.013	4.36	1.66	1.19	0.38
7	0 ± 0	0.76	17	7.7	2.4	0.61 ± 0.1	11.3	15.8	13.5	0	2.12	2.50	1.46	0.54
7	3.14 ± 0.33	0.76	17	7.7	2.4	0.61 ± 0.1	7.9	9.8	8.8	0.0024	2.12	1.60	1.46	0.54
7	5.12 ± 0.44	0.76	17	7.7	2.4	0.61 ± 0.1	6.9	9.4	8.0	0.0039	2.12	1.46	1.46	0.54
7	8.84 ± 0.63	0.76	17	7.7	2.4	0.61 ± 0.1	5.9	8.9	7.2	0.0068	2.12	1.30	1.46	0.54
7	13.26 ± 0.93	0.76	17	7.7	2.4	0.61 ± 0.1	5.9	8.4	6.9	0.01	2.12	1.24	1.46	0.54
7	16.88 ± 1.24	0.76	17	7.7	2.4	0.61 ± 0.1	5.4	7.4	6.2	0.013	2.12	1.11	1.46	0.54
8	0 ± 0	0.76	63	3.9	7	0.61 ± 0.1	20.7	25.5	23.1	0	1.18	5.34	0.92	1.09
8	2.36 ± 0.26	0.76	63	3.9	7	0.61 ± 0.1	16.2	21.0	19.2	0.0018	1.43	3.97	0.84	0.82
8	3.75 ± 0.38	0.76	63	3.9	7	0.61 ± 0.1	15.8	17.6	17.1	0.0029	1.60	3.31	0.79	0.69
8	5.9 ± 0.43	0.76	63	3.9	7	0.61 ± 0.1	15.8	17.6	16.8	0.0045	1.63	3.21	0.78	0.67
8	9.12 ± 0.93	0.76	63	3.9	7	0.61 ± 0.1	14.8	18.1	16.5	0.007	1.66	3.11	0.77	0.65
8	16.57 ± 0.78	0.76	63	3.9	7	0.61 ± 0.1	14.3	16.1	14.9	0.013	1.84	2.65	0.74	0.56
8	27.24 ± 1.6	0.76	63	3.9	7	0.61 ± 0.1	13.7	15.1	14.6	0.021	1.88	2.55	0.73	0.55
8	35.69 ± 1.78	0.76	63	3.9	7	0.61 ± 0.1	11.8	14.0	13.1	0.027	2.09	2.14	0.69	0.46
9	0 ± 0	0.76	66	5.1	7	0.61 ± 0.1	16.7	22.0	19.6	0	1.45	5.53	1.50	1.15
9	2.36 ± 0.26	0.76	66	5.1	7	0.61 ± 0.1	11.8	18.5	15.1	0.0018	1.88	3.63	1.31	0.77
9	3.75 ± 0.38	0.76	66	5.1	7	0.61 ± 0.1	10.8	17.5	15.1	0.0029	1.88	3.63	1.31	0.77
9	5.9 ± 0.43	0.76	66	5.1	7	0.61 ± 0.1	6.9	15.6	11.4	0.0045	2.49	2.26	1.14	0.51
9	8.22 ± 0.12	0.76	66	5.1	7	0.61 ± 0.1	0.5	4.5	2.5	0.0063	2.61	0.27	1.11	0.47
10	0 ± 0	0.76	63	7.7	7	0.61 ± 0.1	0.5	4.5	2.5	0	2.50	0.33	2.03	0.58
11	0 ± 0	0.42	61.5	3.9	5.6	0.48 ± 0.12	12.3	14.8	13.5	0	1.83	4.27	1.30	0.90
11	2 ± 0.17	0.42	61.5	3.9	5.6	0.48 ± 0.12	9.4	13.3	11.3	0.0028	2.19	3.19	1.19	0.69
11	5.53 ± 0.07	0.42	61.5	3.9	5.6	0.48 ± 0.12	7.9	10.8	9.4	0.0077	2.65	2.31	1.08	0.52
11	16.87 ± 0.03	0.42	61.5	3.9	5.6	0.48 ± 0.12	0.5	4.5	2.5	0.024	3.02	0.35	1.01	0.43
11	34.27 ± 0.07	0.42	61.5	3.9	5.6	0.48 ± 0.12	0.5	4.5	2.5	0.048	3.02	0.35	1.01	0.43
12	0 ± 0	0.58	64	5.1	5.6	0.61 ± 0.12	19.2	19.7	19.4	0	1.56	6.29	1.71	1.30

12	2.32 ± 0.65	0.58	64	5.1	5.6	0.61 ± 0.12	15.8	16.7	16.2	0.0023	1.87	4.72	1.56	0.99
12	3.33 ± 0.33	0.58	64	5.1	5.6	0.61 ± 0.12	11.3	12.8	12.1	0.0033	2.52	2.91	1.34	0.63
12	5.67 ± 0.13	0.58	64	5.1	5.6	0.61 ± 0.12	7.9	8.9	8.4	0.0056	3.17	1.68	1.20	0.45
12	9.48 ± 0.2	0.58	64	5.1	5.6	0.61 ± 0.12	5.9	6.9	6.4	0.0094	3.17	1.22	1.20	0.45
12	16.77 ± 0.17	0.58	64	5.1	5.6	0.61 ± 0.12	5.4	6.9	6.2	0.017	3.17	1.16	1.20	0.45
12	26.77 ± 0.23	0.58	64	5.1	5.6	0.61 ± 0.12	0.5	4.5	2.5	0.027	3.17	0.31	1.20	0.45
12	34.23 ± 0.03	0.58	64	5.1	5.6	0.61 ± 0.12	0.5	4.5	2.5	0.034	3.17	0.31	1.20	0.45
13	0 ± 0	0.42	65.5	5.1	5.6	0.48 ± 0.12	0.5	4.5	2.5	0	3.21	0.39	1.52	0.48

[a] For all experiments, upstream flume width was 9.6 cm, and upstream water surface slope was approximately 0.007. Qs - sediment flux (mean ± standard deviation), Q_w - water discharge, H - waterfall drop height, r_{pool} - plunge pool radius, D - grain diameter, u_{brink} - water velocity at waterfall brink (calculated from conservation of mass based on discharge, channel width, and flow depth at brink, mean ± standard deviation reported), h_{pool} - plunge pool depth (minimum, maxium, and average depths reflect topographic variability)

C h a p t e r 5

BEDROCK EROSION IN WATERFALL PLUNGE POOLS: THEORY, EXPERIMENTS, AND IMPLICATIONS FOR LANDSCAPE EVOLUTION

Joel S. Scheingross, Michael P. Lamb, and Daniel Y. Lo

Division of Geological and Planetary Sciences, California Institute of Technology, Pasadena, CA, 91125, USA

* In preparation for submission to *Journal of Geophysical Research – Earth Surface*.

5.1 Abstract

Landscapes often respond to changes in climate and tectonics through the formation and upstream propagation of waterfalls. However, little work has been done on the mechanics of waterfall retreat, and instead most landscape-scale models neglect waterfalls or use stream-power rules that must be locally calibrated. Here, we combine existing waterfall sediment-transport and fluvial bedrock-incision theories to develop a physically-based model to predict waterfall plunge-pool erosion. Our model assumes erosion occurs from abrasion of particle impacts, with incision rates governed by sediment concentration, particle impact velocity, and the presence or absence of sediment cover which can act as an armor layer to inhibit erosion. The model captures the general behavior observed in plunge-pool erosion experiments where evolving plunge pools display initially high vertical erosion rates that slow and eventually cease as pools deepen and deposit sediment; however, the model does not perfectly capture the timing of the onset of sediment deposition and magnitude of erosion. Lateral erosion of the exposed plunge-pool side walls continues regardless of cover in both our experiments and model predictions, allowing for potential waterfall undercutting and retreat. Model results suggest that waterfall retreat can occur over a wider range of conditions than normal fluvial bedrock erosion, which may partly explain relatively high erosion rates of natural waterfalls.

5.2 Introduction

Waterfalls are ubiquitous in upland areas and have been documented to retreat rapidly upstream at rates up to 10^0 to 10^3 mm/yr (e.g., Gilbert, 1907; Philbrick, 1974;

Crosby and Whipple, 2006; Lamb et al., 2007; Hayakawa et al., 2008; Mackey et al., 2014), far outpacing standard fluvial incision rates into bedrock which typically range from ~ 10^{-3} to 10^{0} mm/yr (Portenga and Bierman, 2011). As waterfalls retreat upstream, local base-level lowering causes adjacent hillslopes to steepen resulting in increased erosion rates (e.g., Clark et al., 2005; Berlin and Anderson, 2009; DiBiase et al., 2015). In this way, waterfall erosion and retreat rate can set the pace and style of landscape evolution. Yet, not all waterfalls retreat rapidly. DiBiase et al. (2015) showed that waterfalls within the same drainage basin can have opposite influences on landscape scale adjustment, where some waterfalls retreat rapidly and drive landscape evolution while others appear to be fixed in place, slowing landscape response to perturbations. While DiBiase et al. (2015) suggest this difference in behavior is due to variation in rock strength and sediment supply, evaluating this hypothesis is made difficult by a lack of process-based models describing waterfall erosion and retreat.

Waterfall retreat is most commonly modeled using a generic celerity or stream power model which assumes waterfall retreat is proportional to drainage area, A, i.e.,

$$\frac{dx}{dt} = kA^{p}, \qquad (5.1)$$

where x is the waterfall position, t is time, and k and p are empirically calibrated constants which incorporate the effects of rock type, sediment supply, climate variability, waterfall geometry, retreat mechanism, and more (e.g., Seidl et al., 1994; Stock and Montgomery, 1999; Crosby and Whipple, 2006; Berlin and Anderson, 2007; Loget and Van Den Driessche, 2009). Equation (5.1) is limited in its predictive power as k and p must be calibrated individually at each site. Hayakawa and Matsukura (2003) proposed a slightly more detailed model which accounts for rock compressive strength; however

their model requires an empirically calibrated constant similar to k in Eq. (5.1) which lumps the influence of sediment supply, climate, and more.

An alternative approach is to model the erosion mechanics, allowing for the evaluation of the specific controls on waterfall retreat, such that, for example, predictions of changing waterfall retreat rate in response to changes in water discharge or sediment supply can be independently evaluated. Few process-based models for waterfall erosion and retreat exist, and those that do are limited to specific cases which are not appropriate for the vast majority of waterfalls found in mountainous environments. For example, Lamb and Dietrich (2009) proposed a model whereby waterfalls retreat via toppling of bedrock columns, and is not appropriate for waterfalls formed into massive, homogeneous rock (e.g. Fig. 5.1C). Gilbert (1890) proposed that waterfalls in layered rock retreat via undercutting of the lower, weaker layer until the point of failure of the cantilever caprock. Models describing the mechanics of failure of over-hanging caprock exist (e.g., Stein and LaTray, 2002; Haviv et al., 2010; Hayakawa and Matsukura, 2010); however, no model has been proposed for the abrasion of bedrock within the plunge-pool, which is often assumed to be the rate-limiting step to waterfall retreat in the above models.

Here we focus on erosion which occurs exclusively in waterfall plunge pools (Fig. 5.1). Deep plunge pools provide a locus for waterfall erosion where the impinging waterfall jet delivers sediment to the plunge pool floor which can abrade bedrock, and creates high shear stress capable of entraining deposited sediment which can further abrade the plunge pool floor and sidewalls. Plunge pools are commonly observed below waterfalls, and occur across a variety of rock types from massive homogenous rock (e.g.,

Fig. 5.1C), to jointed basalt (e.g., Figs. 5.1AB), to layered sedimentary rock (e.g. Niagara Falls (Gilbert, 1890)). Acceleration of flow towards the waterfall brink often causes waterfall jets to fully detach from the waterfall face during free-fall, such that plunge-pool erosion, rather than erosion of the waterfall face, is likely the dominant erosion mechanism for many waterfall systems (e.g., Gilbert, 1890; Lamb et al., 2007). While engineers have developed theories for plunge-pool erosion via plucking of bedrock blocks below dams and overspills (e.g., Robinson et al., 2001; Bollaert and Schleiss, 2003b, a), these theories cannot be applied to plunge pools formed in massive, crystalline rock where abrasion is the dominant erosion process (e.g., Fig. 5.1C). Furthermore, abrasion by sediment impacts seems to be a dominant erosion mechanism even in select cases of jointed (e.g., Fig. 5.1AB) or layered rock (e.g., Gilbert, 1890).

The only theory, to our knowledge, which describes bedrock-abrasion of waterfall plunge pools is that of Lamb et al. (2007). The Lamb et al. (2007) model is built off existing fluvial bedrock abrasion framework (Sklar and Dietrich, 2004) and predicts plunge-pool abrasion via vertical impacts from particles which accelerate during free-fall from the upstream waterfall brink to the plunge-pool floor. The model represents an incomplete description of plunge-pool erosion processes for two distinct reasons. First, the model is essentially zero-dimensional in that it describes erosion only at the center of the pool and assumes plunge-pool erosion only occurs in the vertical direction. Waterfall retreat and headwall propagation, therefore, occur via successively drilling pools in the model, the formation of which is assumed to not be a rate-limiting step. Second, while erosion in the model is reduced and eventually ceases as sediment supply approaches and exceeds sediment-transport capacity, there is no description of the controls on waterfall

plunge-pool sediment-transport capacity. Therefore, erosion predictions with the Lamb et al. (2007) model require either neglecting the sediment cover term, or developing a plunge-pool sediment-transport capacity theory (e.g., Scheingross and Lamb, in review) which can be used within the existing model framework. In addition to these two limitations, the model has yet to be tested at field or laboratory scale. While the Lamb et al. (2007) model has offered insights into the rate of waterfall lowering, predictions of waterfall retreat via plunge-pool abrasion require a complete model which can account for vertical and lateral erosion rates, as well as tracking the scour and deposition of sediment armor. This lack of a process-based model for waterfall retreat via plunge-pool abrasion represents a major knowledge gap which limits our ability to predict landscape response to external forcing from changes in climate, tectonics, and sea-level.

In this paper we develop a theory for waterfall plunge-pool erosion and retreat which is capable of tracking sediment fill and evacuation. We first describe the theory which is built off our previously developed waterfall plunge-pool sediment-transport capacity theory (Scheingross and Lamb, in review) and combined with elements of both the Lamb et al. (2007) plunge-pool erosion model as well as existing fluvial bedrock incision theory (Sklar and Dietrich, 2004; Lamb et al., 2008). Second, we present flume experiments of waterfall plunge-pool erosion and compare experimental results to theory predictions. Finally we discuss the morphodynamic evolution of waterfall plunge pools, and use our plunge-pool erosion theory to explore the controls on waterfall retreat via plunge pool lateral erosion.

5.3 Theory

5.3.1 Conceptual overview and modeling framework

Our model is designed to predict plunge-pool erosion from particle abrasion and does not account for erosion via plucking (e.g., Whipple et al., 2000; Chatanantavet and Parker, 2009; Lamb and Fonstad, 2010; Lamb et al., 2015), toppling (e.g., Weissel and Seidl, 1997; Lamb and Dietrich, 2009; Baynes et al., 2015), or other erosional processes such as bedrock weathering (e.g., Haviv et al., 2010). Observations of smooth and well-polished surfaces across a variety of waterfall plunge pools (e.g., Fig. 5.1) suggests that particle abrasion is common, and abrasion is often evoked or implied in studies of both fluvial bedrock incision (e.g., Whipple et al., 2000; Sklar and Dietrich, 2004) and waterfall plunge pool erosion (e.g., Gilbert, 1890; Young, 1985; Howard et al., 1994; Lamb et al., 2007).

We attempt to develop a flexible model which can be used to predict waterfall erosion over a wide range of timescales from individual floods lasting hours to days to landscape response to changing climate or tectonic forcing over ~10^3 – 10^6 yr periods. Accurate erosion predictions require coupling with hydrodynamics and sediment transport which drive erosion, but calculations must be simple enough to apply over the relevant geomorphic timescales over which landscapes evolve (e.g., Dietrich et al., 2003). To this end, we develop a plunge-pool abrasion theory under the constraints of a channel-spanning cylindrical plunge pool. Our theory is quasi two-dimensional in that plunge pools are allowed to erode laterally and vertically, however we force pools to maintain cylindrical geometries. This geometric constraint allows for an analytical solution, whereas more complex pool shapes would likely require a computationally expensive full

3-D simulation, which goes against the goal of developing a model capable of predicting erosion over long timescales.

Approaching a free over fall, flow experiences a spatial acceleration due to the loss of hydrostatic pressure on the downstream side (Rouse, 1936, 1937b; Hager, 1983). This accelerated water can detach from the face of the bedrock step, forming a sediment-laden jet which further accelerates during free fall to the ground below. We envision that, if no depression exists at the base of the waterfall, a plunge-pool will rapidly develop as the force of the waterfall jet scours away existing sediment cover, and particles entrained within the jet will impact the bedrock floor at high velocities producing rapid abrasion (e.g., Sklar and Dietrich, 2004; Lamb et al., 2007). Once a plunge pool is developed, subsequent erosion will be strongly coupled to the development and evolution of the pool. As pools deepen, particles slow due to drag, leading to reduced impact velocities and erosion rates. Furthermore, plunge-pool sediment-transport capacity decreases with increasing pool depth (Scheingross and Lamb, in review), such that pools which erode to sufficient depth will experience sediment supply in excess of transport-capacity, forcing deposition of sediment on the pool floor which can act as an armor layer to inhibit further vertical incision (e.g., Gilbert, 1877; Sklar and Dietrich, 2001; Lamb et al., 2007). Once alluviated, plunge-pools may still experience lateral erosion and widening via abrasion on the exposed channel sidewalls (Fig. 5.2), similar to adjustment of river width following sediment deposition (e.g., Hartshorn et al., 2002; Finnegan et al., 2007; Turowski et al., 2008; Yanites and Tucker, 2010; Nelson and Seminara, 2011). Under this conceptual model, waterfall retreat can occur via lateral abrasion and undercutting of the waterfall face, and, for waterfalls to

persist as vertical steps, the combined rate of vertical incision on the pool floor plus rate of gain in elevation from waterfall upstream retreat must outpace fluvial incision at the waterfall brink.

To explore this hypothesis quantitatively, here we develop a 1-D model for plunge pool vertical and lateral erosion rates. The model follows the framework of previously developed bedrock abrasion theory (Sklar and Dietrich, 2004; Lamb et al., 2007), where erosion rate (E) can be parameterized as the product of the volume of rock detached per particle impact (V_i), the rate of particle impacts per unit bed area per time (I_r), and the fraction of bedrock exposed (F_e), e.g.,

$$E = V_i I_r F_e \ . \tag{5.2}$$

Lamb et al. (2008) modified Eq. (5.2) to be expressed in terms of (dimensionless) near-bed sediment concentration (c_b) and particle impact velocity (w_i), e.g.,

$$E = \kappa c_b w_i^3 F_e . \tag{5.3}$$

κ in Eq. (5.3) is a dimensional constant [T^2/L^2] which accounts for bedrock material properties;

$$\kappa = \frac{A_1 \rho_s k_Y}{\sigma_T^2}, \tag{5.4}$$

where ρ_s and σ_T are rock density and tensile strength, respectively, $k_Y \sim 0.05$ MPa is an empirical constant related to the energy required to erode a unit volume of rock and rock elasticity (Lamb et al., 2015), and $A_1 < 1$ is a constant which we set equal to 0.5 reflecting the fact that grains can be advected both towards and away from the bedrock surface. Because erosion rates scale non-linearly with impact velocity, Lamb et al. (2008) replace

w_i in Eq. (5.3) with an effective impact velocity, w_{eff}, which includes non-linear averaging over particle turbulent fluctuations (see Section 5.3.3).

We modify Eq. (5.3) to predict both vertical (E_{vert}) and lateral (E_{lat}) plunge-pool abrasion rates. We replace c_b with a spatially-variable sediment concentration along the plunge-pool floor $c_{bed}(r)$ and walls $c_{wall}(z)$ (where r and z are radial and vertical coordinates with an origin at the center of the bedrock plunge-pool floor), respectively, and separately parameterize the vertical versus lateral effective particle impact velocities ($w_{vert\_eff}(r)$ and $u_{lat\_eff}(z)$, respectively), as well as the fraction of exposed bedrock on the plunge-pool floor and walls (F_{e_bed} and F_{e_wall}, respectively). Our basic equation for plunge-pool abrasion is thus

$$E_{vert} = \kappa c_{bed}(r) w_{vert\_eff}^3(r) F_{e\_bed} \ , \qquad (5.5a)$$

$$E_{lat} = \kappa c_{wall}(z) u_{lat\_eff}^3 F_{e\_wall} \ . \qquad (5.5b)$$

We devote the following three sub-sections to presentation of theory to predict sediment concentration, particle impact rates, and fraction of bedrock exposure in waterfall plunge pools. In the final sub-section, we apply the theory to an example plunge.

5.3.2: Sediment concentration

5.3.2.1: Overview and key parameters

We predict spatially-variable sediment concentration within plunge pools building off our previously-developed plunge-pool sediment-transport capacity model (Scheingross and Lamb, in review). The Scheingross and Lamb [in review] model builds on decades of work on jet hydrodynamic theory development, which we review conceptually below. As a waterfall jet impinges into a standing pool of water it travels a finite distance within the Zone of Flow Establishment (ZOFE) (e.g., Albertson et al.,

1950; Rajaratnam, 1976) where the jet maintains a constant velocity along its centerline. As the jet impinges deeper, it enters the Zone of Established Flow (ZOEF) where friction from the surrounding boundary reaches the jet-centerline, exerting a drag which results in deceleration. Within the ZOEF, the jet spreads as it decelerates such that the sediment-laden waterfall jet mixes with the surrounding fluid (e.g., Abramovich and Schindel, 1963; Giger et al., 1991). This ultimately results in the jet impinging on the plunge-pool floor over a circular area that we refer to as the "sediment source zone." The impinging jet entrains sediment from within this sediment source area into a near-bed bedload layer where sediment concentration is constant with depth, and above which sediment concentration decays, similar to standard fluvial sediment transport theory (Rouse, 1937a). In the radial direction, sediment concentration is assumed to be constant within the sediment source zone, but decays with increasing radial distance in the annulus outside of the sediment source zone, which we refer to as the "sediment transport zone" (Fig. 5.3).

Predictions of $c_{wall}(z)$ and $c_{bed}(r)$ thus depend on the bedload layer height and the radius of the sediment source zone. The bedload layer height, h_b, can be estimated using the empirical data compilation by Sklar and Dietrich (2004), where h_b is a function of transport stage. The radius of the sediment source zone depends on the rate of jet spreading within the ZOEF. Jet spreading is typically described in terms of the jet half width (b, the radial distance at which the jet velocity is half its centerline width), and increases linearly with depth in the pool (e.g., Abramovich and Schindel, 1963; Giger et al., 1991). At $r > 2b$ the jet velocity approaches that of the surrounded fluid, such that Scheingross and Lamb [in review] define the sediment source zones as $r < 2b$. For cases

when the plunge pool floor is within the ZOFE, the sediment source zone is set to $r < r_{jet}$, where r_{jet} is the waterfall jet radius at impingement with the plunge-pool water surface.

The Scheingross and Lamb (in review) model predicts spatially-variable sediment concentration assuming steady, radially uniform flow and solving an equation of conservation of mass which balances particle advection from gravitational settling and fluid flow with turbulent diffusion. This approach is similar to Rouse's (1937a) classic method predicting suspended sediment concentration in shear flows, and to more recent approaches predicting variable sediment concentration across floodplains (Pizzuto, 1987). Sediment mixing scales with a diffusive length scale, L_d, which represents a balance between turbulence (parametrized through the kinematic eddy viscosity, v_e) and net particle setting velocity, i.e.,

$$L_d = \frac{v_e}{w_s - w_{up}} , \qquad (5.6)$$

where w_s is particle gravitational settling calculated following Ferguson and Church (2004), and w_{up} is the averaged-upward velocity from the jet return flow. In general, larger positive values of L_d lead to more efficient sediment mixing, and higher sediment concentrations throughout the plunge pool.

An approach similar to that of Prandtl (1925), allows approximation of plunge pool eddy viscosity as

$$v_e = u_* \lambda , \qquad (5.7)$$

where u_* is the plunge-pool shear velocity, calculated following Stein et al. (1993) and λ is the depth of the ZOFE which varies with jet radius and angle of jet impact (Beltaos and Rajaratnam, 1973; Beltaos, 1976; Stein et al., 1993). w_{up} in Eq. (5.6) is calculated

following conservation of mass based on the water discharge (Q_w) and cross-sectional areas of the pool and jet (A_{pool} and A_{jet}, respectively), i.e.,

$$w_{up} = \frac{Q_w}{(A_{pool} - A_{jet})} \ . \qquad (5.8)$$

Note that for small plunge pools or for large discharges it is possible for the return flow to exceed the particle settling velocity (i.e., $w_{up} > w_s$). For these cases, sediment is predicted to be rapidly advected out of the pool with no mixing, and the diffusive length scale L_d goes negative, such that the Scheingross and Lamb [in review] predicts no spatial variation in sediment concentration.

5.3.2.2: Pool-floor sediment concentration

Following Scheingross and Lamb [in review], the sediment concentration along the plunge-pool floor varies with radial distance as

$$c_{bed}(r) = c_b \text{ for } r < 2b \ , \qquad (5.9a)$$

$$c_{bed}(r) = c_b \left(\frac{I_0(r/L_d) + \frac{I_1(r_{pool}/L_d)}{K_1(r_{pool}/L_d)} K_o(r/L_d)}{I_0(2b/L_d) + \frac{I_1(r_{pool}/L_d)}{K_1(r_{pool}/L_d)} K_0(2b/L_d)} \right) \text{ for } r > 2b \ , \qquad (5.9b)$$

where c_b is the bedload layer sediment concentration within the sediment source zone and r_{pool} is the plunge-pool radius. Equation (5.9a) reflects the assumption of constant sediment concentration within the sediment source zone, while Eq. (5.9b) incorporates the radial mixing of sediment, where I_0, K_0, I_1, and K_1 are the modified Bessel functions of the first and second kind of order 0 and 1, respectively, which occur in the solution due to the cylindrical geometry imposed.

5.3.2.3: Pool-wall sediment concentration

Sediment concentration along the plunge pool walls varies with height above the pool floor, and depends on whether the plunge-pool radius is greater or less than that of the sediment source zone. Thus, $c_{wall}(z)$ is defined in four separate zones, i.e.,

$$c_{wall}(z) = c_b \text{ for } r_{pool} < 2b \text{ and } z < h_b \ , \qquad (5.10a)$$

$$c_{wall}(z) = c_b \exp\left(-\frac{(z-h_b)}{L_d}\right) \text{ for } r_{pool} < 2b \text{ and } z > h_b \ , \qquad (5.10b)$$

$$c_{wall}(z) = c_b \left(\frac{I_0(r/L_d) + \frac{I_1(r_{pool}/L_d)}{K_1(r_{pool}/L_d)} K_o(r/L_d)}{I_0(2b/L_d) + \frac{I_1(r_{pool}/L_d)}{K_1(r_{pool}/L_d)} K_0(2b/L_d)} \right)$$

$$\text{for } r_{pool} > 2b \text{ and } z < h_b \ , \qquad (5.10c)$$

$$c_{wall}(z) = c_b \exp\left(-\frac{(z-h_b)}{L_d}\right) \left(\frac{I_0(r/L_d) + \frac{I_1(r_{pool}/L_d)}{K_1(r_{pool}/L_d)} K_o(r/L_d)}{I_0(2b/L_d) + \frac{I_1(r_{pool}/L_d)}{K_1(r_{pool}/L_d)} K_0(2b/L_d)} \right)$$

$$\text{for } r_{pool} > 2b \text{ and } z > h_b \ , \qquad (5.10d).$$

Equations (5.10a) and (5.10b) represent the case when the plunge-pool radius is less than that of the sediment source zone, such that there is no radial variation in sediment concentration. Therefore, the sediment concentration at the base of the pool wall is equal to the bedload layer concentration at the pool center (Eq. 5.10a), and sediment concentration decays with distance above the bedload layer height (Eq. 5.10b). Equations (10c) and (10d) are for pool radii greater than the sediment source zone, and include a radial reduction in sediment concentration moving away from the sediment source zone. Equation (5.10c) represents the bedload layer concentration at the pool

wall, whereas Eq. (5.10d) incorporates reduction of concentration with distance above the pool floor.

5.3.2.4: Estimating c_b

Solving for sediment concentration in Eqs. (5.9) and (5.10) require an estimate of c_b which we back-calculate based on the imposed sediment flux from upstream, Q_s. If the imposed sediment flux is less than the plunge pool sediment transport capacity (Q_{sc_pool}), there will be no aggradation of sediment within the plunge pool, and the sediment flux out of the pool will be equal to sediment flux in, i.e.,

$$Q_s = Q_w c_{wall}(z_{lip}), \qquad (5.11)$$

where z_{lip} is the elevation of the downstream plunge-pool lip. Inserting Eq. (5.9) or (5.10) into (5.11) and re-arranging allows solving for c_b as a function Q_s. Solving for c_b requires knowledge of the plunge pool geometry (pool depth, pool radius, and waterfall drop height), as well as the total water discharge, and flow conditions upstream of the waterfall, and is explained in detail in Scheingross and Lamb [in review].

5.3.3 Particle impact velocity

5.3.3.1: Vertical impacts

We assume vertical impacts are a mixture of low velocity impacts from grains falling out of suspension, which we estimate have velocities equal to $w_{net} = w_s - w_{up}$, and relatively high velocity impacts from particles falling from the waterfall brink above. Lamb et al. (2007) solved for vertical particle fall velocity, w_{fall}, based on the difference between acceleration from gravity and deceleration due to drag as a particle travels through both air and water when falling from the top of a waterfall to the bottom of a plunge pool,

$$w_{fall} = \sqrt{\frac{C_{1w}}{C_{2w}} + \left(w_a^2 - \frac{C_{1w}}{C_{2w}} \right) \exp(-2C_{2w} h_{pool})} \,. \quad (5.12)$$

w_a in Eq. (5.12) is the particle fall velocity at impact with the plunge-pool water-surface after falling a distance equal to the waterfall drop height, H, and

$$w_a = \sqrt{\frac{C_{1a}}{C_{2a}} \left(1 - \exp[-2C_{2w} H]\right)} \,. \quad (5.13)$$

C_1 and C_2 are given by

$$C_1 = \frac{\rho_s - \rho_f}{\rho_s} g \;, \quad (5.14a)$$

$$C_2 = \frac{1}{2} C_{drag} \frac{\rho_f}{\rho_s} \frac{A_p}{V_p} \;, \quad (5.14b)$$

where ρ_f is the fluid density (ρ_f is set equal to water density for C_{1w} and C_{2w}, and air density for C_{1a} and C_{2a}), A_p and V_p are particle cross-sectional area and volume, respectively, and C_{drag} is a drag coefficient.

We solve for the drag coefficient in still water using an empirical calibration for natural particles (Ferguson and Church, 2004). In waterfall plunge pools, the downward force of the waterfall jet exerts a drag on particles not present in still water, which we account for by reducing the drag coefficient from its still water approximation as

$$C_{drag} = C_{drag\_still} \frac{w_{fall}}{u_{jet\_impact}} \text{ for } w_{fall}/u_{jet\_impact} < 1 \,, \quad (5.15a)$$

$$C_{drag} = C_{drag\_still} \text{ for } w_{fall}/u_{jet\_impact} > 1 \,, \quad (5.15b)$$

where u_{jet_impact} is the jet velocity at impact with the plunge-pool floor and can be calculated following Stein et al. (1993) and Scheingross and Lamb (in review). Equation

5.15 represents a crude approximation but allows for reproduction of behavior observed in our experiments described below.

Where sediment is well mixed within the sediment source zone ($r < 2b$) we assume an equal mixture of grains falling out of suspension and grains falling from the top of the waterfall, whereas for $r > 2b$ we assume all impacts are due to grains falling out of suspension. Recognizing that erosion scales with impact velocity cubed (Eq. 5.5), we estimate average vertical impact velocity, w_i, as

$$w_i = \frac{(w_{net}^3 + w_{fall}^3)^{1/3}}{2} \text{ for } r < 2b \,, \qquad (5.16a)$$

$$w_i = w_{net} \text{ for } r > 2b \,. \qquad (5.16a)$$

In addition to particle fall velocity, grains can also be advected towards the bed due to turbulent fluctuations and we account for such fluctuations following Lamb et al. (2008) where the probability density of vertical velocity fluctuations, w' is given by

$$P(w') = \frac{1}{\sqrt{2\pi}\sigma_w} \exp\left(-\frac{(w')^2}{2\sigma_w^2} \right), \qquad (5.17)$$

and $\sigma_w = \sqrt{\overline{w'^2}}$ is the time-averaged standard deviation of fluctuations. In open channel flow $\sigma_w = u_*$ (Nezu and Nakagawa, 1993), and we assume this approximation holds for plunge pools. Again, recognizing that erosion scales with impact velocity cubed, we calculate an effective average vertical impact velocity, w_{vert_eff}, including turbulent fluctuations, as

$$w_{vert\_eff} = \left[\int_{-w_{fall}}^{6\sigma_w} (w' + w_i)^3 P(w') dw' \right]^{1/3} , \qquad (5.18)$$

where the limits of integration are chosen to include almost all the positive velocity fluctuations and exclude any negative impacts (i.e., turbulence advecting particles away from the bed), which can occur if $w' > w_i$.

5.3.3.2: Lateral impacts

We assume lateral impacts are driven entirely by fluid turbulence and calculate lateral impact velocity following a method similar to that outlined above for vertical impacts. Again, we assume a Gaussian probability density of horizontal velocity fluctuations, u';

$$P(u') = \frac{1}{\sqrt{2\pi}\sigma_u} \exp\left(-\frac{(u')^2}{2\sigma_u^2}\right), \qquad (5.19)$$

where $\sigma_u = \sqrt{\overline{u'^2}}$ is the time-averaged standard deviation of horizontal fluctuations. Following observations in open channel flow, we assume $\sigma_u = 2u_*$ (Nezu and Nakagawa, 1993) and calculate an effective lateral impact velocity, u_{lat_eff}, as

$$u_{lat\_eff} = \left[\int_0^{6\sigma_u} (u')^3 P(u')du'\right]^{1/3}, \qquad (5.20)$$

For simplicity, we assume that u_{lat_eff} is constant with elevation above the plunge pool floor. In actuality, u_{lat_eff} is likely set by large-scale eddies and backrollers which form within plunge pools (e.g., Robinson et al., 2000; Bennett and Alonso, 2005), the inclusion of which requires 3-D flow models which make solving for erosion over landscape evolution timescales impractical.

5.3.4 Fraction of bed exposed

As was originally hypothesized by Gilbert (1877), and more recently shown in both experimental and field studies (Sklar and Dietrich, 2001; Finnegan et al., 2007; Turowski et al., 2008; Hobley et al., 2011; Yanites et al., 2011), increases in the sediment supply

decrease erosion rates via creation of a cover layer which armors the bed from impacts. Following Sklar and Dietrich (2004), we represent the influence of increased sediment supply based on the fraction of the bed exposed to impacts, assuming a linear scaling between F_{e_bed} and the ratio of sediment supply to transport capacity, i.e.,

$$F_{e\_bed} = 1 - \frac{Q_s}{Q_{sc\_pool}} = 1 - \frac{c_b}{c_{b\_capacity}} \text{ , for } Q_s < Q_{sc\_pool} \qquad (5.21a)$$

$$F_{e\_bed} = 0 \text{ , for } Q_s > Q_{sc\_pool} \qquad (5.21b)$$

where $c_{b\_capacity}$ is the bedload layer sediment concentration at capacity and is calculated following Scheingross and Lamb [in review], i.e.,

$$c_{b\_capacity} = 0.02\left(\frac{\tau_{*\text{pool}}}{\tau_{*\text{c}}} - 1\right)^{1.5} . \qquad (5.22)$$

Note that if $c_b > c_{b\_capacity}$, the imposed sediment flux is greater than the plunge pool sediment transport capacity, and the pool should aggrade with sediment following Scheingross and Lamb [in review].

We use a linear function estimating the fraction of bedrock exposed on the plunge-pool floor to account for the fact that there may be partial alluviation across the pool diameter. The plunge-pool walls, however, cannot experience partial cover and we instead use a binary function to estimate the fraction of bedrock exposed, i.e.,

$$F_{e\_wall} = 1 \text{ for } z > z_{sed} \text{ , } \qquad (5.23a)$$

$$F_{e\_wall} = 0 \text{ for } z < z_{sed} \text{ , } \qquad (5.23b)$$

where z_{sed} is the level of sediment deposition on top of the plunge pool bedrock floor ($z_{sed} = z_{BR}$ for cases of sediment-free plunge pools, and $z_{BR} = 0$ is defined as the elevation of the plunge-pool bedrock floor).

5.3.5 Plunge-pool averaging and sample calculation

Calculation of spatially-variable erosion across the plunge-pool floor can be performed by inserting Eqs. (5.9), (5.18), and (5.21) into Eq. (5.5a); similarly, spatially-variable lateral erosion comes from inserting of Eqs. (5.10), (5.20), and (5.23) into Eq. (5.5b). We calculate radially-averaged, $\overline{E_{vert}}$, and depth-averaged, $\overline{E_{lat}}$, plunge-pool vertical and lateral erosion rate, respectively, as

$$\overline{E_{vert}} = \frac{2\pi \int_{r=0}^{r=r_{pool}} E_{vert}(r) r dr}{A_{pool}} , \qquad (5.24a)$$

$$\overline{E_{lat}} = \frac{\int_{z=z_{BR}}^{z=z_{lip}} E_{lat}(z)}{(z_{lip} - z_{BR})} , \qquad (5.24b)$$

We perform a sample calculation of plunge-pool erosion in order to illustrate how sediment concentration, impact velocity, fraction of cover, and erosion rate vary as functions of pool radius and depth (Fig. 5.4A). We use Lower Switzer Falls, a 5 m tall waterfall in the San Gabriel Mountains, California as a reference site (Scheingross and Lamb, in review). In the radial direction, $c_{bed}(r)$ is highest and maintains a constant value within the sediment source zone ($r < 2b$) when the impinging jet entrains sediment off the pool floor; for $r > 2b$, sediment concentration decays non-linearly due to turbulent diffusion. w_{vert_eff} is represented by a step function where it is high within the sediment source zone due to impacts from grains falling from the waterfall brink below, and drops to a lower value for $r > 2b$ where impacts are from grains which fall out of suspension in the water column (Eq. 5.16). F_{e_bed} is constant and non-zero for this example, representing a uniform reduction of erosion rate. The combination of near-bed sediment concentration, impact velocity, and cover result in a spatially-variable vertical erosion

rate which is constant within the sediment source zone and decays non-linearly for $r > 2b$ due to reductions in concentration and impact velocity (Fig. 5.4A).

In the vertical direction, $c_{wall}(z)$ is constant within the bedload layer ($z < h_b$) and decays with increasing height above the bed for $z < h_b$ due to the balance between gravitational settling, turbulent diffusion, and vertical advection of particles by the return jet flow (Fig. 5.4B). Unlike in the radial direction, lateral impact velocity is assumed to be constant throughout the water column, and F_{e_wall} is also constant for all depths. Thus, $E_{lat}(z)$ decreases with depth for $z < h_b$ due entirely to changes in sediment concentration (Fig. 5.4B).

5.4. Experimental setup and methods

We designed laboratory flume experiments where a sediment-laden waterfall jet eroded a plunge pool into an initially planar bed under constant forcing. Measurements of the evolving pool geometry, combined with multiple runs varying sediment size and flux, allowed for a test of our theoretical and conceptual models outlined above. In this section first we describe the basic flume set up, second we go over the individual experiments, third we present methods for calculating erosion rates from the experiment, and finally we present methods for comparing experimental versus theoretical predictions.

5.4.1 Flume setup

Experiments were carried out in a custom designed flume built specifically to study waterfall processes (Fig. 5.5). In all experiments, water was fed by a pump into a 9.6 cm wide by 2.06 m long upstream flume tilted to ~2 deg, with a fixed bed of 2.4 mm sub-rounded quartz grains. Flow at the waterfall brink was in the fully turbulent regime

(Reynolds numbers of ~6 x 10^3 and Reynolds particle numbers of ~1 x 10^3) such that the experiments should have dynamic similarity with field-scale waterfalls (Paola et al., 2009), and flow was supercritical (Fr ~ 1.1) at the upstream end of the flume, similar to mountain streams during floods. A fully-ventilated waterfall cascaded off the end of the upstream flume and fell into a lower flume (24 cm wide x 80 cm long) where we fixed an erodible polyurethane foam block (~18 cm wide by 27 cm long) in which a plunge pool could be formed. We aligned the flume such that the waterfall jet impacted the center of the block. A rotating auger position immediately above the waterfall brink fed sediment, allowing sediment transport rates to be controlled independently from the upstream flume sediment transport capacity. Sediment was entrained in the flow, and carried by the waterfall jet to impact the foam block below. We tilted the downstream flume by 10 – 14.5 deg to ensure that any sediment transported out of the plunge pool was immediately transported out of the system; therefore the influence of downstream sediment transport capacity on plunge pool evolution was minimized. In order to allow the plunge pool to develop with minimal downstream controls, experiments were designed to minimize erosion on the downstream plunge-pool lip, and the lip was protected when detectable erosion occurred. Upon exiting the downstream flume, sediment fell into a tail box and was collected for manual re-circulation.

We used a homogenous, polyurethane foam as a bedrock simulant that follows the same tensile-strength vs. erosion-rate scaling as observed in natural rock and concrete, and its low tensile strength (σ_T = 0.32 MPa) allows for observable erosion over laboratory timescales (Scheingross et al., 2014; Lamb et al., 2015). Preliminary experiments using

weak (10:1 sand to cement ratio) concrete produced plunge pools with similar morphologies to those of our subsequent experiments eroding foam.

5.4.2 Individual experiments

We performed two separate sets of waterfall plunge-pool erosion experiments (Table 5.1). Both sets of experiments were designed so that the key non-dimensional variables controlling waterfall sediment transport were within the range of natural observations (Scheingross and Lamb, in review), thus, the dynamics observed in these experiments should be similar to those observed in natural waterfalls (e.g., Lamb et al., 2015).

In Experiment 1 (Exp1) we fed 2.4 mm diameter sub-rounded grains from a waterfall drop height of 41.5 cm and allowed a plunge-pool to develop under constant sediment flux and water discharge. In Experiment 2 (Exp2) we fed 7 mm diameter sub-angular grains from a waterfall drop height of 52.5 cm. We allowed the pool to evolve under constant water discharge and (low) initial sediment flux of ~9 g/s for ~15 hours, after which we imposed an approximately five-fold increase in sediment flux to Q_s ~ 45 g/s, while holding water discharge constant, to force aggradation of the pool and increase lateral erosion rates. In this way our two experiments independently explored the influence of changing grain size and sediment flux on plunge-pool evolution.

We measured the evolving plunge pool geometry in both experiments by periodically pausing the run to make topographic measurements, during which we also noted the presence or absence of sediment deposition within the pool. We used a high-resolution laser-scanner to detect the lowest point within the plunge pool and measured the pool depth as the gravity-parallel distance from the deepest point in the pool to the

downstream plunge-pool lip. In Exp1 we used a scanner with ~1 mm lateral resolution (FARO Focus 3D); however, complications with the scanner led to inaccuracies in depth measurements by up to 20% for deep and narrow pools. In Exp2 we used a different laser scanner (E-SCAN) with sub-mm resolution in both the lateral and vertical directions. We used a ruler to make hand measurements of the average plunge-pool cross-stream width and along-stream length at the top of the foam (i.e., at the level of the water surface when flow spills out of the pool), and used the average of these measurements to estimate pool radius. Because laser scanning did not capture undercut portions of the plunge pool, we measured the total pool volume by weighing the mass of water needed to fill the pool to the point of overspill.

For cases when sediment was deposited in the pool, we measured the elevation of sediment fill by measuring the gravity-parallel distance from the downstream plunge-pool lip to top of the sediment deposit. These measurements slightly over-estimate the elevation of fill (i.e., estimate fill levels closer to the pool-lip) as they include both sediment that was deposited during the experiment, as well as sediment which fell out of suspension within the plunge pool when pausing the experiment to make measurements.

5.4.3 Erosion rate calculations

We calculated vertical erosion rates in our experiments by differencing the maximum plunge pool bedrock depth between successive measurements and dividing by the time elapsed, i.e.,

$$\overline{E_{vert}} = \frac{(z_{lip} - z_{BR})|_{t=i} - (z_{lip} - z_{BR})|_{t=i-1}}{\Delta t} \quad . \qquad (5.25)$$

While Eq. (5.25) gives a maximum erosion rate, it should be comparable to our spatially-averaged theoretical prediction (i.e., Eq. 5.24a) as both equations represent the rate of lowering of the plunge-pool floor.

We used our measurements of changing plunge-pool volume, V_{pool}, and depth to estimate lateral erosion rates in a two-step procedure. First, we back-calculated a plunge-pool averaged radius, r_{pool_avg} at each time-step by assuming a cylindrical plunge pool geometry, and solving for r_{pool_avg} based on measurements of pool volume and depth, i.e.,

$$r_{pool\_avg} = \sqrt{\frac{V_{pool}}{\pi(z_{lip} - z_{BR})}} \quad . \qquad (5.26)$$

We then calculated pool-averaged lateral erosion rates in a fashion similar to our vertical erosion rate calculations,

$$\overline{E_{lat}} = \frac{r_{pool\_avg}\,|_{t=i} - r_{pool\_avg}\,|_{t=i-1}}{\Delta t} \quad . \qquad (5.27)$$

Estimating spatially-averaged lateral erosion rate over a cylindrical surface area as in Eq. (5.27) allows for straightforward comparison with our theoretical erosion prediction using Eq. (5.24b).

5.4.4 Methods for comparing experimental and theoretical predictions

Our plunge-pool erosion model predicts erosion rates as a function of pool geometry, grain size, and flow hydraulics. We calculated theoretically-predicted average erosion rates (e.g., Eq. 5.24) at each time-step in our experiment for a cylindrical pool with dimensions equivalent to our measurements of r_{pool_avg} and either plunge-pool bedrock depth or depth to sediment depending on if the pool was free of sediment or alluviated. This represents the most simple and straightforward way to compare experiments and theory, without additional complications (e.g., the imposition of

complex pool geometry for which the theory is not designed). In Exp1, we made no measurements of pool volume for the first 20 hours of experimental run time, and instead estimate r_{pool_avg} for all Exp1 theory-predicted erosion rates using the plunge-pool radius at the pool surface. This gives radius estimates of up to ~50% larger than those from Eq. (5.26), and results in slightly lower theory predictions for both lateral and vertical erosion rates.

For cases when the sediment supply exceeded the theoretically predicted sediment transport capacity, our theory predicts the onset of alluvial cover (i.e. $F_{e\_bed} = 0$) such that vertical erosion rates go to zero. For pools partially filled with sediment, we used the Scheingross and Lamb [in review] theory to calculate $c_{wall}(z)$ at capacity (i.e., we used Eq. (5.22) to substitute $c_{b\_capacity}$ for c_b in Eq. (5.10)), and used this value of sediment concentration to drive lateral erosion predictions.

5.5 Experimental results and comparison with theory

Both experiments showed the same general behavior and evolution where the sediment-laden waterfall jet impacted an initially flat surface and rapidly developed a plunge pool which increased in planform area to approximately match the width across which vertical sediment impacts rained down from above (Fig. 5.6). As the experiment progressed, pools deepened (to maximum depths of ~20 and 15 cm in Exp1 and Exp2, respectively), and both vertical and lateral erosion rates slowed from their initial rapid values (Fig. 5.7). Following our conceptual model, continued plunge-pool deepening in Exp1 led to the onset of sediment deposition as the imposed sediment supply exceeded the plunge-pool sediment transport-capacity. Similarly, the increase in imposed sediment

flux in Exp2 also led to alluviation. In both cases, the onset of sediment deposition caused cessation of vertical erosion and focused lateral erosion around the level of sediment fill (Figs. 5.7 and 5.8). Erosion in these experiments was accomplished exclusively via abrasion from sediment impacts. A preliminary clear water experiment with conditions identical to those in Exp1 showed no erosion of foam after 24 hours of constant forcing, in contrast to observations of visible erosion in Exp1 and Exp2 within minutes of initiating sediment impacts (e.g., Fig. 5.7). Below, we describe our experimental results in terms of plunge pool deepening and vertical erosion rates separately from pool widening and lateral erosion, and make use of our plunge-pool erosion theory to compare to and help explain the observed experimental behavior.

5.5.1 Vertical erosion

Both Exp1 and Exp2 showed initially rapid rates of vertical erosion (order ~10 cm/hr) which decreased as the experiments progressed (Figs. 5.9 and 5.10). Theory predictions of area-weighted averaged plunge-pool erosion (Eq. 5.24a, gray symbols in Figs. 5.9B and 5.10B) typically matched experimental observations within less than a factor of ~3 for Exp1 and less than a factor of ~5 for Exp2 up until the point where the theory predicted the onset of sediment deposition. Decreases in erosion rate with increasing pool depth can occur in our plunge-pool erosion theory due to a reduction of sediment concentration on the plunge-pool floor (which results in fewer impacts), a decrease in vertical impact velocity, or an increase in the fraction of cover protecting the sediment bed (e.g., Eq. 5.5). Theoretical predictions for the conditions in Exp1 and Exp2 suggest that the rapid decrease in vertical erosion within the first ~ 5 hours of run time occurred primarily due to a reduction in particle vertical impact velocity (Figs. 5.9C and

5.10C). Impact velocity decreased with increasing pool depth, as drag within the plunge pool caused particles to decelerate. For deeper pools, particles reach terminal settling velocity and impact rates are not a function of depth, as may have occurred after ~10 hours of run time in Exp1 (Fig. 5.9C). Note that in the first ~5 hours of Exp1 and Exp2 our theory predicts no changes in near-bed sediment concentration or fraction of sediment cover. This occurs due to the initially shallow plunge pool depths such that the plunge pool floor remains in the ZOFE and the shear stress on the pool floor is predicted to remain constant.

After initially high rates of deepening, plunge-pool vertical incision slowed in Exp1 (Fig. 5.9B). Our erosion theory predicts this slowing is due to a reduction in vertical-impact velocity as described above, as well a progressive increase in sediment cover (Fig. 5.9C). Cover increases for deeper pools, as the waterfall jet must impinge through a deeper water column, leading to lower shear stresses on the plunge pool floor, and sediment concentrations closer to the transport capacity. Interestingly, the theory predicts the reduction in shear stress and pool deepening also leads to an increase in sediment concentration on the pool floor. This occurs due to the constant sediment flux imposed from upstream, such that holding sediment flux out of the pool constant (which must occur so long as sediment is not deposited within the pool) requires larger values of c_b to make up for the reduced transport efficiency (lower L_d) and increased length scale over which sediment must be transported to exit the pool. For both Exp1 and Exp2, our theory predicts the increase in cover outweighs the influence of the increase in sediment concentration, such that erosion rates continue to decrease with increasing pool depth (Figs. 5.9 and 5.10).

At t ~ 40 hr in Exp1 we observed the start of sediment deposition within the plunge pool. For the geometry of the Exp1 pool at t = 40 hr and all later times, our erosion theory predicts sediment supply is greater than transport capacity, forcing pool alluviation and cessation of vertical incision (Fig. 5.9B), in agreement with our experimental observations which also showed the start of sediment deposition at t = 40 hr (Fig. 5.9A). Our erosion model predicts vertical incision reduces to zero following the deposition of a single grain-layer of sediment (Fig. 5.9B); however, we observed continued deepening at lower vertical-erosion rates for Exp1 from t = ~40-60 hr (Figs. 5.9A and B), suggesting that erosion continued until the sediment deposit became 3 – 10 grain-diameters thick (Fig. 5.9A). The increasing thickness of the sediment deposit with time was likely due to continued lateral erosion after the onset of alluviation (Section 5.5.2, Fig. 5.11), such that the plunge-pool self-adjusted its alluvial depth in response to an increase in pool radius as in Scheingross and Lamb (in review).

Exp1 and Exp2 had essentially identical conditions with the exception of larger grain sizes and slightly higher drop height in Exp2. This increase in grain size and drop height had no detectable influence on plunge-pool vertical-erosion rates (Fig. 5.11). Our theory predicts Exp2 erosion rates should exceed those of Exp1 by a factor of approximately one to four, due primarily to the higher impact velocities associated with more massive grains falling a greater distance. However, this difference is probably within error of theoretical predictions, as errors already present in the underlying sediment transport theory (Scheingross and Lamb, in review) and bedrock erosion theory (Sklar and Dietrich, 2004) are compounded in our plunge-pool erosion model. An example of this can be seen in the vertical-erosion rate predictions in Exp2 which cease

after t = 5 hr as the underlying sediment transport theory predicts pool alluviation in contrast to experimental observations. Overall, we are encouraged that the erosion model presented above does a reasonable job of reproducing the trends observed in our experimental observations, despite not always matching the magnitude.

5.5.2 Lateral erosion

5.5.2.1: Depth-averaged lateral erosion

Exp1 and Exp2 showed similar trends in lateral erosion rate over the course of the experiments (Figs. 5.12 and 5.13). Plunge-pool radius increased rapidly during the first ~1-5 hours of experiment time, resulting in large initial lateral erosion rates. These high lateral erosion rates are somewhat misleading in that during this time the pool adjusted its radius to approximately match the size of the sediment-laden waterfall jet impacting the pool. As such, while pool widening occurred, the mechanism of widening was predominately vertical sediment impacts from above, as opposed to lateral impacts within the plunge pool.

After the initially rapid widening, pool lateral erosion slowed in both experiments until the onset of sediment deposition. In our theory, this can occur due to decreasing lateral impact velocities as plunge-pool radius grows (e.g., Fig. 5.12C). However, the theory predicts roughly constant lateral erosion rates, as the reduction in impact velocity is offset by an increase in the average $c_{wall}(z)$ which occurs due to pool deepening and widening as described above (Figs. 5.12 and 5.13).

Sediment deposition at t = ~40 hr in Exp1 and t = 14.75 hr in Exp2 led to temporary increases in lateral erosion rates, after which rates returned to approximately stable values (Figs. 5.12 and 5.13). While this behavior is not captured by our model

predictions, the initial increase in erosion rate following the onset of sediment deposition is consistent with our model framework. This enhanced lateral-erosion can occur from rising wall-impact velocities as the pool floor aggrades allowing higher values of u_*, as well as increased sediment concentration along the wall. The return of lateral-erosion rates to a background value after an initial pulse of widening is also not captured by our model. This likely happens due to decreases in particle-impact velocity with increasing radius, an effect not included in our model framework which predicts impact velocity is constant with changing radius (Fig. 5.4).

5.5.2.2: Spatial-variation in lateral erosion

We used topographic scans of the deposited sediment and plunge-pool bedrock evolution in Exp2 to evaluate spatial-variation in lateral erosion. Lateral erosion in both Exp1 and Exp2 tended to be concentrated at or slightly below the level of sediment deposition in our experiments (e.g., Figs. 5.7 and 5.8). From t = 14.75 to t = 17.7 hr lateral erosion was fairly uniform across the upstream plunge-pool wall (Fig. 5.8) during the period when total sediment deposition in the pool was increasing. After t = 17.7 hr, lateral erosion was focused at and up to ~10 grain diameters below the layer of sediment fill, with the plunge pool experiencing a slight undercutting of its upstream wall and a pronounced undercutting of its downstream wall (Fig. 5.8). This erosion below the level of sediment fill is consistent with observations of vertical erosion with up to ~10 grain diameters sediment fill in Exp1, and suggests that lateral erosion in our plunge-pool was concentrated in a fairly deep active-layer where sediment was likely entrained in high concentrations allowing for frequent grain impacts. A 10 grain-diameter-deep active layer would be slightly larger than the approximately three to six times the median grain size

typically observed in gravel-bedded rivers (Parker, 2004), and may reflect the influence of the vertically-directed impinging waterfall jet compared to bed-parallel shear flow in standard river transport. The presence of a deep-active layer is further supported by careful removal of grains, spray painting, and replacement between t = 43.8 and 45.7 hr, which showed grains up to ~ 10 grain diameter depth tended to be replaced, while those deeper tended to remain in place.

Erosion within the active-layer is not accounted for by our theory, which predicts no erosion following the onset of cover, but is consistent with our conceptual model where lateral retreat continues after sediment deposition. While incomplete scans due to overhangs make it difficult to evaluate the full evolution of the pool walls in Exp2, total erosion amount seemed to be approximately equal between the upstream and downstream walls. However, the style of erosion was different with upstream walls showing approximately parallel retreat, compared to distinct undercutting on the downstream wall (Fig. 5.8). These observations are counter to the Gilbert (1907) model where undercutting is focused on the upstream pool wall, perhaps reflecting the use of a homogenous substrate in our experiments compared to the hard over weak stratigraphy envisioned in the Gilbert (1907) model.

5.6 Plunge-pool morphodynamics and implications for long-profile evolution

Our experimental observations and plunge pool erosion theory suggests plunge-pool evolution generally follows our conceptual model outlined above, with rich feedbacks between the flow hydraulics, sediment transport, and evolving topography. As plunge pools increase their depth, shear stress on the pool floor decreases, and the

distance over which sediment must be suspended to escape the pool increases, both leading to a reduction in plunge-pool sediment transport capacity (Scheingross and Lamb, in review). For a given water discharge and sediment supply, pools which erode below a critical depth will no longer have the capacity to transport the sediment supplied from upstream, and will instead deposit sediment, forcing aggradation of the pool floor, allowing the pool to self-adjust its alluvial depth to reach a new equilibrium between sediment supply and plunge-pool transport capacity (e.g., Fig. 5.9A). This process of sediment deposition covers the bed and, so long as it is sufficiently thick, prevents further vertical incision, but still allows for lateral erosion. In fact, the formation of an alluvial cover can increase lateral erosion rates (e.g. Figs. 5.12 and 5.13) by increasing sediment concentration along the plunge pool wall and by raising the elevation of the sediment bed, thereby increasing shear stresses, and, in turn, particle lateral impact velocity. Once sediment is deposited, lateral erosion of the sidewalls should widen the pool, with erosion focused within the active layer where sediment concentrations are high (Fig. 5.8), further reducing sediment transport capacity, and causing further sediment aggradation. Under constant forcing, with no erosion of the upstream waterfall brink or downstream plunge-pool lip, plunge pools are expected to reach a final state where they are filled with sediment, but have bedrock topography which increases in radius with increasing distance above the pool floor.

In natural rivers, complications between variability in water discharge, sediment supply, and grain-size distribution can keep plunge pools from evolving to their expected equilibrium forms under constant forcing. However, it seems likely that, given adequate time, plunge-pool bedrock depth evolves to reflect a characteristic water discharge and

sediment flux. If this is the case, it may be possible to use field measurements of plunge-pool bedrock geometry to infer relative rates of upstream waterfall retreat to vertical incision. For example, waterfalls which retreat rapidly should have under-developed plunge pools with bedrock depths shallower than those expected for the characteristic water and sediment flux, and narrow widths. In contrast, slowly-retreating waterfalls should have fully-developed plunge-pools with bedrock-depths adjusted to the imposed conditions, and relatively wide widths with undercutting.

The relative rates of plunge-pool vertical to lateral erosion, as well as relative rates of river downcutting at the upstream waterfall brink and downstream plunge pool lip, ultimately control whether waterfalls grow or diminish in height, retreat upstream, or stall in place. Our plunge-pool erosion theory developed above, used in combination with existing theory for fluvial bedrock incision (Sklar and Dietrich, 2004; Lamb et al., 2008), allows us to evaluate the controls on waterfall plunge-pool retreat and resulting long-profile evolution from a mechanistic perspective, and to compare against predictions from commonly-used, generic stream-power or celerity models (e.g., Rosenbloom and Anderson, 1994; Seidl et al., 1994; Crosby and Whipple, 2006; Berlin and Anderson, 2007; Loget and Van Den Driessche, 2009).

We explore two simple cases for waterfall retreat and growth in height, again using conditions at Lower Switzer Falls as a reference site. Lower Switzer Falls is an ~5 m tall waterfall that discharges into a pool with a depth of at least 2 m (although the true depth to bedrock may be deeper), and which has experienced cycles of sediment fill and evacuation. We compare the relative rates of plunge-pool vertical and lateral erosion to the rate of waterfall lip lowering, E_{lip}, taking into account flow acceleration and increased

shear stress due to drawdown at the brink (Rouse, 1936, 1937b; Hager, 1983), as well as to the erosion rate under normal flow conditions, E_n, which we assume approximates fluvial incision of the downstream plunge-pool lip. We use our plunge-pool sediment transport capacity model (Scheingross and Lamb, in review) to keep track of sediment deposition in the plunge pool, and calculate river hydraulics assuming a constant friction factor, $C_{f\_river} = 0.01$, steady, uniform flow ($\tau_{river}=\rho_f g h_n S$ where h_n is the normal flow depth in the river and S is channel slope) and conservation of mass ($Q_w = u_n W h_n$ where u_n is the normal river flow velocity and W is reach-averaged channel width).

We explore the influence of changing water discharge on plunge-pool erosion and retreat by holding sediment supply and all other variables constant, while allowing Q_w to vary from 1 – 1000 m^3/s. We set $Q_s = 10^{-2}$ m^3/s to approximate average sediment flux at Lower Switzer Falls based on its 12.3 km^2 drainage area, assuming a 1% intermittency factor for periods of sediment flux, and assuming a catchment average erosion rate between 0.1 – 1 mm/yr as is typical in the San Gabriel Mountains (DiBiase et al., 2010). Relative rates of plunge pool and river erosion are predicted to be strongly modulated by the presence of sediment cover (Fig. 5.14A). At low discharges, sediment flux exceeds transport capacity for both the river and plunge pool such that there is no erosion and the plunge pool is predicted to be filled with sediment. As water discharge increases, the pool begins to partially empty, allowing lateral erosion of the plunge pool walls, but no vertical incision. For these discharges, sediment supply is still greater than river transport capacity, such that fluvial erosion is prevented by cover on the river bed. Further increases in discharge approaching the two-year recurrence interval (Q_{2yr}) value cause the pool to empty of sediment, allowing plunge-pool vertical incision, but with cover still

preventing erosion in the fluvial reaches above and below. Under these conditions, plunge-pool vertical incision outpaces lateral erosion by over an order of magnitude, and the pool should deepen. As water discharges continue to increase river sediment transport capacity exceeds sediment supply (first at the waterfall brink where flow is accelerated, and later for normal flow conditions) such that river incision can occur; however, plunge-pool vertical incision outpaces river incision such that the waterfall should persist.

While stream-power and celerity based waterfall retreat models predict that increases in drainage area, a proxy for water discharge, result in faster retreat rates, our simple modeling exercise does not show this trend. Assuming that plunge-pool lateral erosion is the rate-limiting step to waterfall retreat, retreat is maximized at relatively modest discharges when cover prevents fluvial erosion and vertical waterfall incision. Furthermore, because these low-discharge periods occur more frequently than large-flood events, the combination of high lateral erosion rates and long time periods may lead to large retreat distances. As water discharges increase under constant sediment flux, plunge-pool lateral erosion rates decrease by almost two orders of magnitude, in contrast to standard stream-power predictions. A paucity of field data documenting waterfall retreat makes it difficult to compare these predictions to natural examples; however, it is possible that increases in waterfall retreat with increasing drainage area could occur through increases in sediment supply rather than increases in water discharge.

We explore the influence of sediment supply on plunge and river evolution by predicting erosion rates under varying sediment supply from 10^{-4} $m^3/s < Q_s < 10^0$ m^3/s while setting water discharge to its two-year recurrence interval value ($Q_{2yr} = 4.8$ m^3/s) and holding all other parameters constant. For these conditions, both fluvial and plunge-

pool erosion rates increase with increasing sediment flux, up until the point that sediment flux exceeds sediment transport capacity causing cover (Fig. 5.14B). For conditions at the Lower Switzer Falls reference site, our modeling predicts that increasing sediment supply will lead first to the cessation of fluvial erosion due to the onset of cover, then to cessation of plunge-pool vertical incision, and finally to the cessation of plunge-pool lateral erosion. Unlike the behavior predicted for increasing water discharge, lateral erosion is predicted to continually increase with increasing sediment flux, and relative rates of lateral erosion will be maximized for high sediment supplies when all other erosion ceases due to cover effects.

In natural rivers, discharge and sediment supply often co-vary, such that larger sediment fluxes at larger drainage areas may lead to increased rates of waterfall retreat as predicted by stream-power models. Determining the full controls on when plunge pool retreat and resulting long-profile evolution requires modeling the co-evolution of plunge-pool and river long-profile geometry, as changes in plunge pool depth, radius, waterfall drop height, and channel slope all feedback on resulting erosion rates in complicated ways. While such a modeling task is beyond the scope of this paper, the theory developed here provides the basis for such models to be made and predictions to be explored.

5.7 Conclusions

We have developed a model to predict plunge-pool erosion via particle abrasion, building off previously developed plunge-pool sediment transport capacity (Scheingross and Lamb, in review) and fluvial bedrock incision (Sklar and Dietrich, 2004; Lamb et al.,

2007; Lamb et al., 2008) models. Our model and flume experiments show similar behavior for plunge pool evolution where pools have initially rapid rates of vertical incision, which slow as pools deepen and particle impact velocities decrease. Pools deepen until the point of sediment deposition, after which lateral erosion can continue, and in certain cases, may increase in rate. Comparing model-predictions of plunge pool erosion to existing fluvial incision shows that the onset of sediment cover strongly modulates relative rates of plunge pool versus fluvial erosion, suggesting sediment supply may control when waterfalls grow or decrease in height, retreat upstream, or stall in place.

5.8 Acknowledgements

A MATLAB script to calculate plunge-pool erosion is available by contacting the lead author. We are grateful to Brian Fuller and Conor O'Toole for assistance with laboratory experiments and to Jeff Prancevic and Roman DiBiase for stimulating discussions. We thank Guillermo Vergara Muñoz and Juan Francisco Bustos for sharing photos from Radal Siete Tazas National Park and acknowledge funding from the National Science Foundation via grant EAR-1147381 to M.P.L and a Graduate Research Fellowship to J.S.S, as well as funding from NASA grant 12PGG120107.

5.9 Notation

A	drainage area [L^2]
A_1	constant indicating fraction of particle concentration which impacts bedrock surfaces [dimensionless]
A_{jet}	waterfall jet area [L^2]
A_p	particle cross-sectional area [L^2]
A_{pool}	plunge pool area [L^2]
C_{1a}	constant in particle acceleration for grains falling through air [$M\ L^{-2}\ T^{-2}$]
C_{1w}	constant in particle acceleration for grains falling through water [$M\ L^{-2}\ T^{-2}$]
C_{2a}	parameter in particle acceleration for grains falling through air [L]
C_{2w}	parameter in particle acceleration for grains falling through water [L]
C_{drag}	drag coefficient for non-still water [dimensionless]
C_{drag_still}	drag coefficient for still water [dimensionless]
C_{f_river}	river friction factor [dimensionless]
E	river vertical erosion rate [L/T]
E_{lat}	plunge-pool lateral erosion rate [L/T]
$\overline{E_{lat}}$	depth-averaged plunge-pool lateral erosion rate [L/T]

E_{lip} waterfall brink erosion rate from fluvial incision [L/T]
E_n river normal flow erosion rate [L/T]
E_{vert} plunge-pool vertical erosion rate [L/T]
$\overline{E_{vert}}$ area-averaged plunge-pool vertical erosion rate [L/T]
F_e fraction of bedrock exposed in river bed [dimensionless]
F_{e_bed} fraction of bedrock exposed on plunge-pool floor [dimensionless]
F_{e_wall} fraction of bedrock exposed in plunge-pool walls [dimensionless]
H waterfall drop height [L]
I_r particle impact rate [impacts / L^2T]
L_d characteristic length scale over which turbulence mixes sediment [L]
Q_s sediment supply [L/T^3]
Q_{sc_pool} plunge-pool sediment-transport capacity [L/T^3]
Q_w water discharge [L/T^3]
Q_{2yr} water discharge for two-year recurrence interval flood [L/T^3]
S channel slope [dimensionless]
V_i Volume of bedrock eroded for particle impact [L^3]
V_p particle volume [L^3]
V_{pool} plunge pool volume [L^3]
W reach-averaged channel width [L]
b jet half width [L]
c sediment concentration [dimensionless]
c_b bedload layer sediment concentration in the sediment source zone [dimensionless]
$c_{b\_capacity}$ bedload layer sediment concentration in the sediment source zone at transport capacity [dimensionless]
$c_{bed}(r)$ sediment concentration along the plunge-pool floor [dimensionless]
$c_{wall}(z)$ sediment concentration along the plunge-pool wall [dimensionless]
g gravitational acceleration [L/T^2]
h_b bedload layer height [L]
h_n river normal flow depth [L]
k empirical constant in stream power waterfall retreat model [dimensionless]
k_Y empirical constant relating energy transfer and elasticity [$M/(LT^2)$]
p empirical constant in stream power waterfall retreat model [dimensionless]
r radial coordinate [L]
r_{jet} waterfall jet radius at point of impact with water surface [L]
r_{pool} plunge pool radius [L]
r_{pool_avg} average plunge pool radius for non-cylindrical pools [L]
t time [T]
u_{jet_impact} jet velocity upon impact with the plunge-pool floor [L/T]
u_{lat_eff} effective particle lateral impact velocity for erosion [L/T]
u_n normal river flow velocity [L/T]
u_* shear velocity at the plunge-pool bed [L/T]
u' lateral turbulent velocity fluctuations [L/T]
w_a vertical particle velocity at impact with water surface [L/T]
w_{fall} vertical particle impact velocity when falling from the waterfall brink [L/T]

w_i	average vertical particle impact velocity without turbulence [L/T]
w_{net}	net particle settling velocity [L/T]
w_s	terminal particle gravitational settling velocity [L/T]
w_{up}	vertical velocity of the jet return flow [L/T]
w_{vert_eff}	effective particle vertical impact velocity for erosion [L/T]
w'	vertical turbulent velocity fluctuations [L/T]
z	vertical coordinate [L]
z_{BR}	vertical coordinate of the plunge-pool bedrock-floor [L]
z_{lip}	vertical coordinate of the plunge-pool downstream lip [L]
z_{sed}	vertical coordinate of the plunge-pool alluvial-floor [L]
κ	constant in bedrock erosion theory [T^2/L^2]
λ	length of ZOFE [L]
ν_e	kinematic eddy diffusivity [L^2/T]
ρ_f	fluid density [M/L^3]
ρ_s	sediment density [M/L^3]
σ_T	tensile strength [$M/(LT^2)$]
σ_u	standard deviation of lateral turbulent velocity fluctuations [L/T]
σ_w	standard deviation of vertical turbulent velocity fluctuations [L/T]
τ_{river}	river bed shear stress [$M\ L^{-1}\ T^{-2}$]
τ_{*c}	critical Shields stress for grain motion [dimensionless]
τ_{*pool}	plunge-pool bed Shields stress [dimensionless]

5.10 References

Abramovich, G., and L. Schindel (1963), *The theory of turbulent jets*, 671 pp., MIT Press, Cambridge, MA.

Albertson, M. L., Y. B. Dai, R. A. Jensen, and H. Rouse (1950), Diffusion of submerged jets, *Transactions of the American Society of Civil Engineers*, *115*, 639-664.

Baynes, E. R. C., M. Attal, S. Niedermann, L. A. Kirstein, A. J. Dugmore, and M. Naylor (2015), Erosion during extreme flood events dominates Holocene canyon evolution in northeast Iceland, *Proceedings of the National Academy of Sciences of the United States of America*, *112*(8), 2355-2360, doi:10.1073/pnas.1415443112.

Beltaos, S. (1976), Oblique impingement of plane turbulent jets, *Journal of the Hydraulics Division-Asce*, *102*(9), 1177-1192.

Beltaos, S., and N. Rajaratnam (1973), Plane turbulent impinging jets, *Journal of Hydraulic Research*, *11*(1), 29-59, doi:10.1080/00221687309499789.

Bennett, S. J., and C. V. Alonso (2005), Kinematics of flow within headcut scour holes on hillslopes, *Water Resources Research*, *41*(9), doi:10.1029/2004wr003752.

Berlin, M. M., and R. S. Anderson (2007), Modeling of knickpoint retreat on the Roan Plateau, western Colorado, *Journal of Geophysical Research-Earth Surface*, *112*(F3), doi:10.1029/2006jf000553.

Berlin, M. M., and R. S. Anderson (2009), Steepened channels upstream of knickpoints: Controls on relict landscape response, *Journal of Geophysical Research-Earth Surface*, *114*, doi:10.1029/2008jf001148.

Bollaert, E., and A. Schleiss (2003a), Scour of rock due to the impact of plunging high velocity jets Part I: A state-of-the-art review, *Journal of Hydraulic Research*, *41*(5), 451-464, doi:10.1080/00221680309499991.

Bollaert, E., and A. Schleiss (2003b), Scour of rock due to the impact of plunging high velocity jets Part II: Experimental results of dynamic pressures at pool bottoms and in one- and two-dimensional closed end rock joints, *Journal of Hydraulic Research*, *41*(5), 465-480.

Chatanantavet, P., and G. Parker (2009), Physically based modeling of bedrock incision by abrasion, plucking, and macroabrasion, *Journal of Geophysical Research-Earth Surface*, *114*, doi:10.1029/2008jf001044.

Clark, M. K., G. Maheo, J. Saleeby, and K. A. Farley (2005), The non-equilibrium landscape of the southern Sierra Nevada, California, *GSA Today*, *15*(9), doi:10:1130/1052-5173(2005)015<4:TNELOT>2.0.CO;2.

Crosby, B. T., and K. X. Whipple (2006), Knickpoint initiation and distribution within fluvial networks: 236 waterfalls in the Waipaoa River, North Island, New Zealand, *Geomorphology*, *82*(1-2), 16-38, doi:10.1016/j.geomorph.2005.08.023.

DiBiase, R. A., K. X. Whipple, A. M. Heimsath, and W. B. Ouimet (2010), Landscape form and millennial erosion rates in the San Gabriel Mountains, CA, *Earth and Planetary Science Letters*, *289*(1-2), 134-144, doi:10.1016/j.epsl.2009.10.036.

DiBiase, R. A., K. X. Whipple, M. P. Lamb, and A. M. Heimsath (2015), The role of waterfalls and knickzones in controlling the style and pace of landscape adjustment in the western San Gabriel Mountains, California, *Geological Society of America Bulletin*, *127*(3-4), 539-559, doi:10.1130/B31113.1.

Dietrich, W. E., D. Bellugi, A. M. Heimsath, J. J. Roering, L. Sklar, and J. D. Stock (2003), Geomorphic transport laws for predicting the form and evolution of landscapes, in *Geophysical Monograph Series*, edited by P. R. Wilcock and R. M. Iverson, pp. 103-132, American Geophysical Union, doi:10.1029/GM135.

Ferguson, R. I., and M. Church (2004), A simple universal equation for grain settling velocity, *Journal of Sedimentary Research*, *74*(6), 933-937, doi:10.1306/051204740933.

Fernandez-Luque, R., and R. van Beek (1976), Erosion and transport of bedload sediment, *Journal of Hydrualic Research*, *14*, pp. 127-144, doi:10.1080/00221687609499677.

Finnegan, N. J., L. S. Sklar, and T. K. Fuller (2007), Interplay of sediment supply, river incision, and channel morphology revealed by the transient evolution of an experimental bedrock channel, *Journal of Geophysical Research-Earth Surface*, *112*(F3), doi:10.1029/2006jf000569.

Giger, M., T. Dracos, and G. H. Jirka (1991), Entrainment and mixing in plane turbulent jets in shallow-water, *Journal of Hydraulic Research*, *29*(5), 615-642, doi:10.1080/00221689109498980.

Gilbert, G. K. (1877), *Report on the Geology of the Henry Mountains: Geographical and Geological Survey of the Rocky Mountain Region*, 160 pp., U.S. Government Print Office, Washington, D.C.

Gilbert, G. K. (1890), The history of the Niagara River, extracted from the sixth annual report to the commissioners of the state reservation at Niagara, Albany, NY.

Gilbert, G. K. (1907), The rate of recession of Niagara Falls, *US Geological Survey Bulletin*, *306*, 1-31.

Hager, W. H. (1983), Hydraulics of plane free overfall, *Journal of Hydraulic Engineering-Asce*, *109*(12), 1683-1697, doi:10.1061/(ASCE)0733-9429(1983)109:12(1683).

Hartshorn, K., N. Hovius, W. B. Dade, and R. L. Slingerland (2002), Climate-driven bedrock incision in an active mountain belt, *Science*, *297*(5589), 2036-2038, doi:10.1126/science.1075078.

Haviv, I., Y. Enzel, K. X. Whipple, E. Zilberman, A. Matmon, J. Stone, and K. L. Fifield (2010), Evolution of vertical knickpoints (waterfalls) with resistant caprock: Insights from numerical modeling, *Journal of Geophysical Research-Earth Surface*, *115*, doi:10.1029/2008jf001187.

Hayakawa, Y. S., and Y. Matsukura (2003), Recession rates of waterfalls in Boso Peninsula, Japan, and a predictive equation, *Earth Surface Processes and Landforms*, *28*(6), 675-684, doi:10.1002/esp.519.

Hayakawa, Y. S., and Y. Matsukura (2010), Stability analysis of waterfall cliff face at Niagara Falls: An implication to erosional mechanism of waterfall, *Engineering Geology*, *116*(1-2), 178-183, doi:10.1016/j.enggeo.2010.08.004.

Hayakawa, Y. S., S. Yokoyama, and Y. Matsukura (2008), Erosion rates of waterfalls in post-volcanic fluvial systems around Aso volcano, southwestern Japan, *Earth Surface Processes and Landforms*, *33*(5), 801-812, doi:10.1002/esp.1615.

Hobley, D. E. J., H. D. Sinclair, S. M. Mudd, and P. A. Cowie (2011), Field calibration of sediment flux dependent river incision, *Journal of Geophysical Research-Earth Surface*, *116*, doi:10.1029/2010jf001935.

Howard, A. D., W. E. Dietrich, and M. A. Seidl (1994), Modeling fluvial erosion on regional to continental scales, *Journal of Geophysical Research-Solid Earth*, *99*(B7), 13971-13986, doi:10.1029/94JB00744.

Lamb, M. P., and W. E. Dietrich (2009), The persistence of waterfalls in fractured rock, *Geological Society of America Bulletin*, *121*(7-8), 1123-1134, doi:10.1130/b26482.1.

Lamb, M. P., W. E. Dietrich, and L. S. Sklar (2008), A model for fluvial bedrock incision by impacting suspended and bed load sediment, *Journal of Geophysical Research-Earth Surface*, *113*(F3), doi:10.1029/2007jf000915.

Lamb, M. P., N. J. Finnegan, J. S. Scheingross, and L. S. Sklar (2015), New insights into the mechanics of fluvial bedrock erosion through flume experiments and theory, *Geomorphology*, *244*, 33-55, doi:10.1016/j.geomorph.2015.03.003.

Lamb, M. P., and M. A. Fonstad (2010), Rapid formation of a modern bedrock canyon by a single flood event, *Nature Geoscience*, *3*(7), 477-481, doi:10.1038/ngeo894.

Lamb, M. P., A. D. Howard, W. E. Dietrich, and J. T. Perron (2007), Formation of amphitheater-headed valleys by waterfall erosion after large-scale slumping on Hawai'i, *Geological Society of America Bulletin*, *119*(7-8), 805-822, doi:10.1130/b25986.1.

Loget, N., and J. Van Den Driessche (2009), Wave train model for knickpoint migration, *Geomorphology*, *106*(3-4), 376-382, doi:10.1016/j.geomorph.2008.10.017.

Mackey, B. H., J. S. Scheingross, M. P. Lamb, and K. A. Farley (2014), Knickpoint formation, rapid propagation, and landscape response following coastal cliff retreat at the last interglacial sea-level highstand: Kaua'i, Hawai'i, *Geological Society of America Bulletin*, *126*(7-8), 925-942, doi:10.1130/b30930.1.

Nelson, P. A., and G. Seminara (2011), Modeling the evolution of bedrock channel shape with erosion from saltating bed load, *Geophysical Research Letters*, *38*, doi:10.1029/2011gl048628.

Nezu, L., and H. Nakagawa (1993), *Turbulence in open channel flows*, 281 pp., Rotterdam, Netherlands.

Nitsche, M., D. Rickenmann, J. M. Turowski, A. Badoux, and J. W. Kirchner (2011), Evaluation of bedload transport predictions using flow resistance equations to account for macro-roughness in steep mountain streams, *Water Resources Research*, *47*, doi:10.1029/2011wr010645.

Paola, C., K. Straub, D. Mohrig, and L. Reinhardt (2009), The "unreasonable effectiveness" of stratigraphic and geomorphic experiments, *Earth-Sci Rev*, *97*(1-4), 1-43, doi:10.1016/j.earscirev.2009.05.003.

Parker, G. (2004), 1D Sediment transport morphodynamics with applications to rivers and turbidity currents, available at: *http://hydrolab.illinois.edu/people/parkerg/morphodynamics_e-book.htm* (accessed 16 Aug 2015).

Philbrick, S. S. (1974), What Future for Niagara Falls, *Geological Society of America Bulletin*, *85*(1), 91-98, doi:Doi 10.1130/0016-7606(1974)85<91:Wffnf>2.0.Co;2.

Pizzuto, J. E. (1987), Sediment diffusion during overbank flows, *Sedimentology*, *34*(2), 301-317, doi:10.1111/j.1365-3091.1987.tb00779.x.

Portenga, E. W., and P. R. Bierman (2011), Understanding Earth's eroding surface with 10-Be, *GSA Today*, *21*(8), doi:10.1130/G111A.1.

Prandtl, L. (1925), A report on testing for built-up turbulence, *Zeitschrift Fur Angewandte Mathematik Und Mechanik*, *5*, 136-139.

Rajaratnam, N. (1976), *Turbulent Jets*, Elsevier, Amsterdam.

Recking, A. (2010), A comparison between flume and field bed load transport data and consequences for surface-based bed load transport prediction, *Water Resources Research*, *46*, doi:10.1029/2009wr008007.

Robinson, K. M., K. R. Cook, and G. J. Hanson (2000), Velocity field measurements at an overfall, *Transactions of the ASAE*, *43*(3), 665-670.

Robinson, K. M., G. J. Hanson, K. R. Cook, and K. C. Kadavy (2001), Erosion of fractured materials, *Transactions of the Asae*, *44*(4), 819-823.

Rosenbloom, N. A., and R. S. Anderson (1994), Hillslope and Channel Evolution in a Marine Terraced Landscape, Santa-Cruz, California, *Journal of Geophysical Research-Solid Earth*, *99*(B7), 14013-14029, doi:Doi 10.1029/94jb00048.

Rouse, H. R. (1936), Discharge characteristics of the free overfall, *Civil Engineering*, *6*, 257-260.

Rouse, H. R. (1937a), Modern conceptions of the mechanics of turbulence, *Trans. Am. Soc. Civ. Eng.*, *102*(1), 463-543.

Rouse, H. R. (1937b), Pressure distribution and acceleration at the free overfall, *Civil Engineering*, *7*, 518.

Scheingross, J. S., F. Brun, D. Y. Lo, K. Omerdin, and M. P. Lamb (2014), Experimental evidence for fluvial bedrock incision by suspended and bedload sediment, *Geology*, doi:doi:10.1130/G35432.1.

Scheingross, J. S., and M. P. Lamb (in review), Sediment transport through waterfall plunge pools.

Seidl, M. A., W. E. Dietrich, and J. W. Kirchner (1994), Longitudinal profile development into bedrock - an analysis of Hawaiian channels, *Journal of Geology*, *102*(4), 457-474.

Sklar, L. S., and W. E. Dietrich (2001), Sediment and rock strength controls on river incision into bedrock, *Geology*, *29*(12), 1087-1090, doi:10.1130/0091-7613(2001)029<1087:sarsco>2.0.co;2.

Sklar, L. S., and W. E. Dietrich (2004), A mechanistic model for river incision into bedrock by saltating bed load, *Water Resources Research*, *40*(6), doi:10.1029/2003wr002496.

Stein, O. R., C. V. Alonso, and P. Y. Julien (1993), Mechanics of jet scour downstream of a headcut, *Journal of Hydraulic Research*, *31*(6), 723-738, doi:10.1080/00221689309498814.

Stein, O. R., and D. A. LaTray (2002), Experiments and modeling of head cut migration in stratified soils, *Water Resources Research*, *38*(12), doi:10.1029/2001wr001166.

Stock, J. D., and D. R. Montgomery (1999), Geologic constraints on bedrock river incision using the stream power law, *Journal of Geophysical Research-Solid Earth*, *104*(B3), 4983-4993, doi:Doi 10.1029/98jb02139.

Turowski, J. M., N. Hovius, M.-L. Hsieh, D. Lague, and M.-C. Chen (2008), Distribution of erosion across bedrock channels, *Earth Surface Processes and Landforms*, *33*(3), 353-363, doi:10.1002/esp.1559.

Weissel, J. K., and M. A. Seidl (1997), Influence of rock strength properties on escarpment retreat across passive continental margins, *Geology*, *25*(7), 631-634, doi:10.1130/0091-7613(1997)025<0631:iorspo>2.3.co;2.

Whipple, K. X., G. S. Hancock, and R. S. Anderson (2000), River incision into bedrock: Mechanics and relative efficacy of plucking, abrasion, and cavitation, *Geological Society of America Bulletin*, *112*(3), 490-503, doi:10.1130/0016-7606(2000)112<0490:riibma>2.3.co;2.

Yager, E. M., W. E. Dietrich, J. W. Kirchner, and B. W. McArdell (2012), Prediction of sediment transport in step-pool channels, *Water Resources Research*, *48*, doi:10.1029/2011WR010829.

Yanites, B. J., and G. E. Tucker (2010), Controls and limits on bedrock channel geometry, *Journal of Geophysical Research-Earth Surface*, *115*, doi:10.1029/2009jf001601.

Yanites, B. J., G. E. Tucker, H.-L. Hsu, C.-c. Chen, Y.-G. Chen, and K. J. Mueller (2011), The influence of sediment cover variability on long-term river incision rates: An example from the Peikang River, central Taiwan, *Journal of Geophysical Research-Earth Surface*, *116*, doi:10.1029/2010jf001933.

Young, R. (1985), Waterfalls: Form and process, *Zeitschrift fur Geomorphologie*(Supplementband 55), 81-95.

Table 5.1. Summary of parameters for waterfall plunge-pool erosion experiments[a]

Experiment ID	Water Discharge (L/s)	Waterfall drop height (m)	Grain diameter (mm)	Sediment flux (g/s)	Flow depth at brink (cm)	Upstream flume slope (deg)	Downstream flume slope (deg)	Total run time (hr)
Exp1	0.58	0.42	2.4	9	1.3	2	10	113
Exp2	0.58	0.53	7	9 - 45	1.3	2	14.5	51

[a] All experiments used a commercially available, closed-cell polyurethane foam bedrock simulant (http://www.precisionboard.com), with 0.32 MPa tensile strength.

Figure 5.1: Examples of waterfall plunge pools. A) An unnamed waterfall in Radal Siete Tazas National Park, Chile carved into basalt pictured at low water flow and (B) shortly after the 2010 Maule Earthquake (M_w = 8.8) which temporarily caused the river to run dry as flow upstream was diverted into groundwater; note person in foreground for scale. Yellow dashed line in (B) denotes contact between exposed bedrock and sediment deposit. Pronounced undercutting is visible in (B) which is hidden below the water surface (A), highlighting the role of plunge-pool erosion. C) Successive plunge pools carved into massive granite on Dry Meadow Creek, California (commonly referred to as the Seven Tea Cups), large waterfall in center of photo has surveyed drop height of 5.3 m for scale. Photograph credits: (A) - Juan Francisco Bustos, (B) - Guillermo Vergara Muñoz, (C) - Devon Santy.

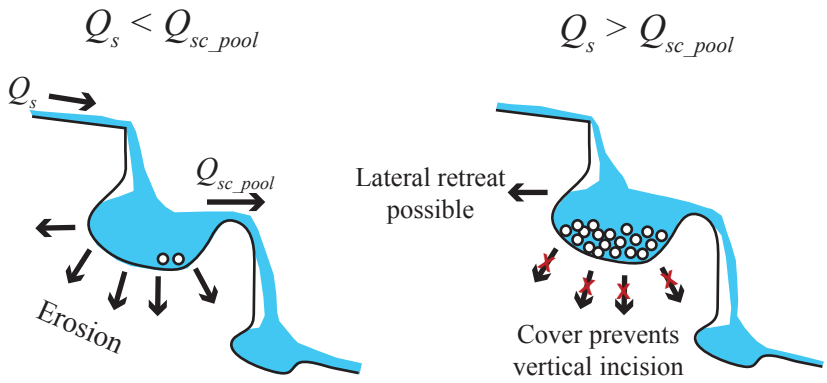

Figure 5.2: Conceptual model showing feedback between sediment supply, transport capacity, and plunge pool lateral versus vertical erosion. When sediment supply (Q_s) is less than plunge-pool sediment transport capacity (Q_{sc_pool}), pools flush out all sediment, exposing bedrock floors and walls, and allowing for both lateral and vertical erosion. When $Q_s > Q_{sc\_pool}$, pools deposit sediment to reach an equilibrium alluvial depth, covering the bedrock bed to prevent vertical incision, but still allowing for lateral erosion.

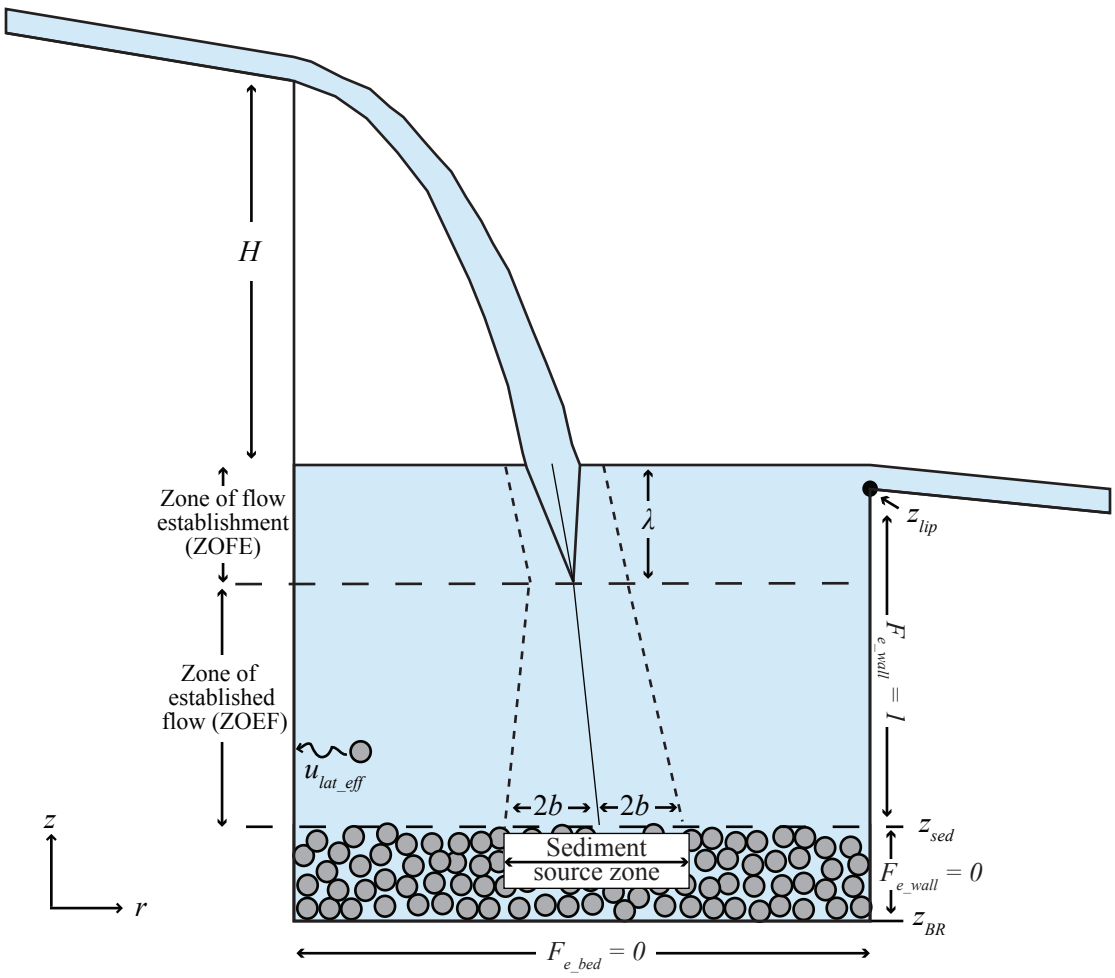

Figure 5.3: Schematic of partially-filled waterfall plunge-pool system with key variables labeled.

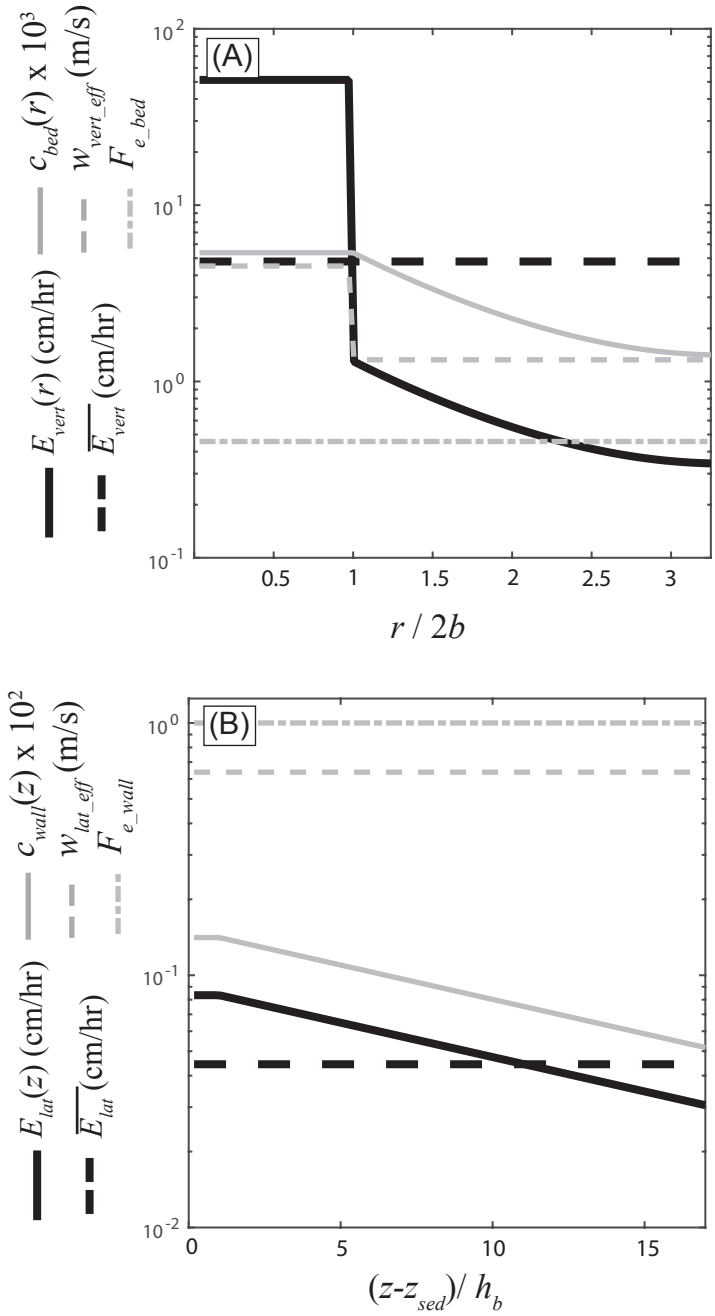

Figure 5.4: Example calculation of variation in erosion rate, sediment concentration, particle impact velocity, and sediment cover. (A) Variables plotted against radial distance (r) from the center of the plunge pool normalized by the radius of the sediment source zone ($2b$). (B) Variables plotted against vertical distance (z) above the plunge-pool floor normalized by bedload layer height (h_b). We used parameters from the Lower Switzer Falls reference site [Scheingross and Lamb, in review] for this calculation (H = 5 m, (z_{lip} - z_{BR}) = 2 m, r_{pool} = 4.4 m, Q_s = 4.8 x 10^{-3} m^3/s, Q_w = 9.6 m^3/s).

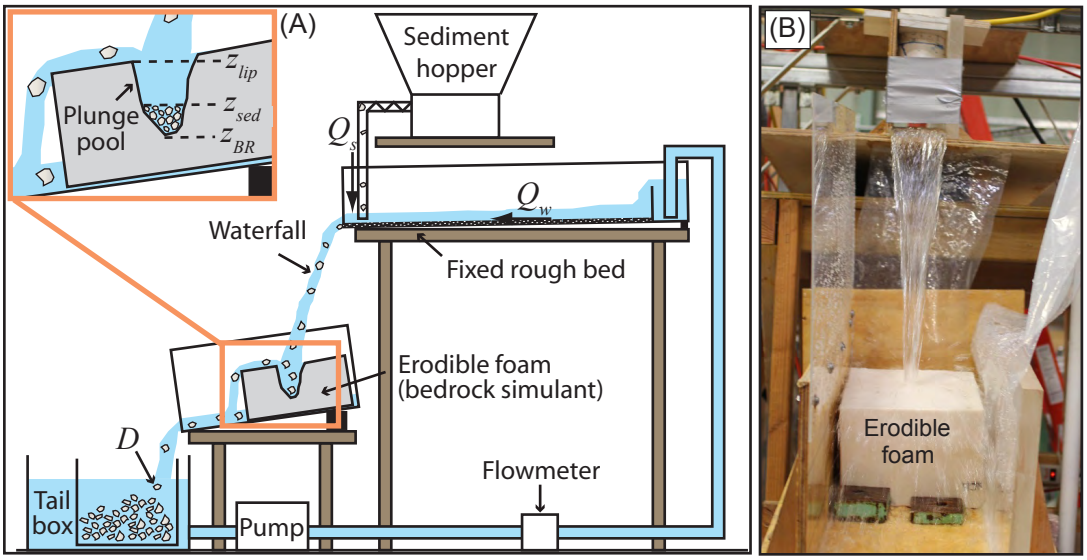

Figure 5.5: (A) Cartoon schematic of experimental set up and (B) photograph of Exp1 at start of experimental run.

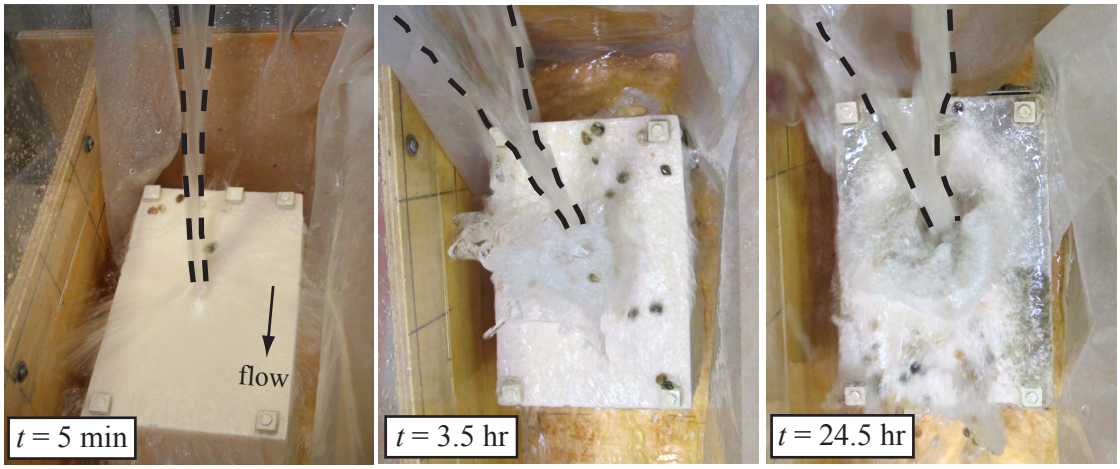

Figure 5.6: Photos showing progressive evolution of Exp2. Flow is from top to bottom in all photos, and dashed-line highlights waterfall jet.

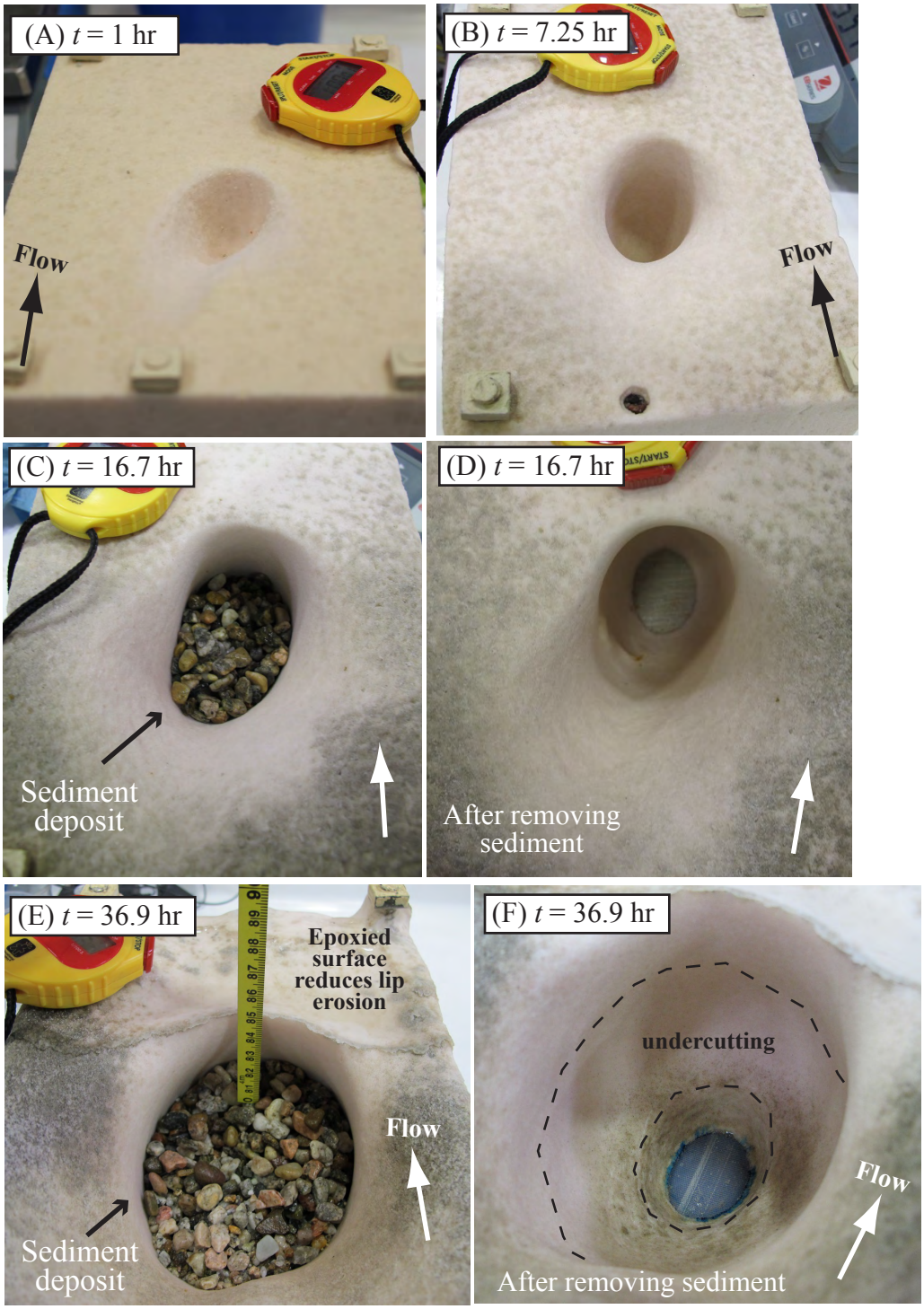

Figure 5.7: Photos showing progressive plunge-pool erosion during Exp2. (A and B) Show erosion during the first portion of the experiment with low sediment flux and prior to pool alluviation. (C and E) Show pools with sediment deposit and (D and F) after manual removal of sediment at t = 16.7 hr and 36.9 hr, respectively. Undercutting and widening of the pool is visible in (F). Flow is from bottom to top in all photos. Portion where pool eroded through bottom of foam block is visible in (D) and (F).

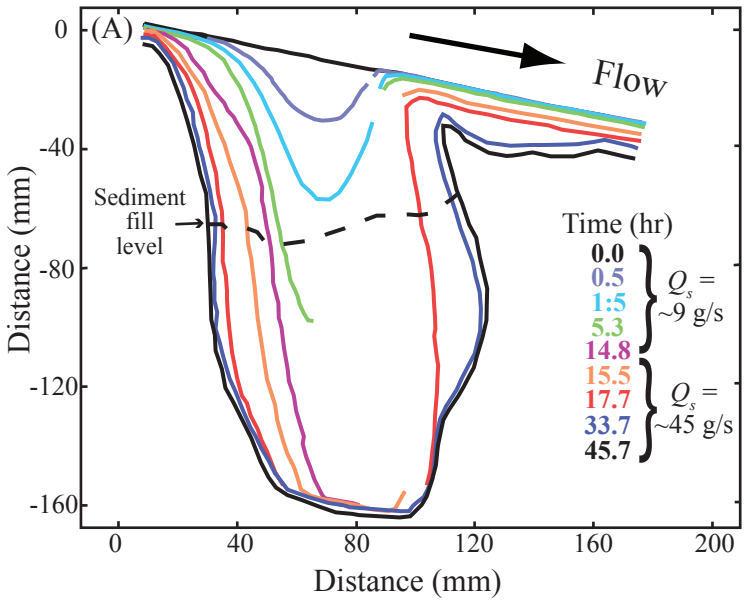

Figure 5.8: Long-profiles from high-resolution laser-scans showing plunge-pool evolution and sediment deposition during Exp2. Gaps in profile lines are from overhangs which limited laser-scanner line of sight. Some overhangs were partially captured by merging multiple scans in post-processing using open-source software (CloudCompare [http://www.danielgm.net/cc/]).

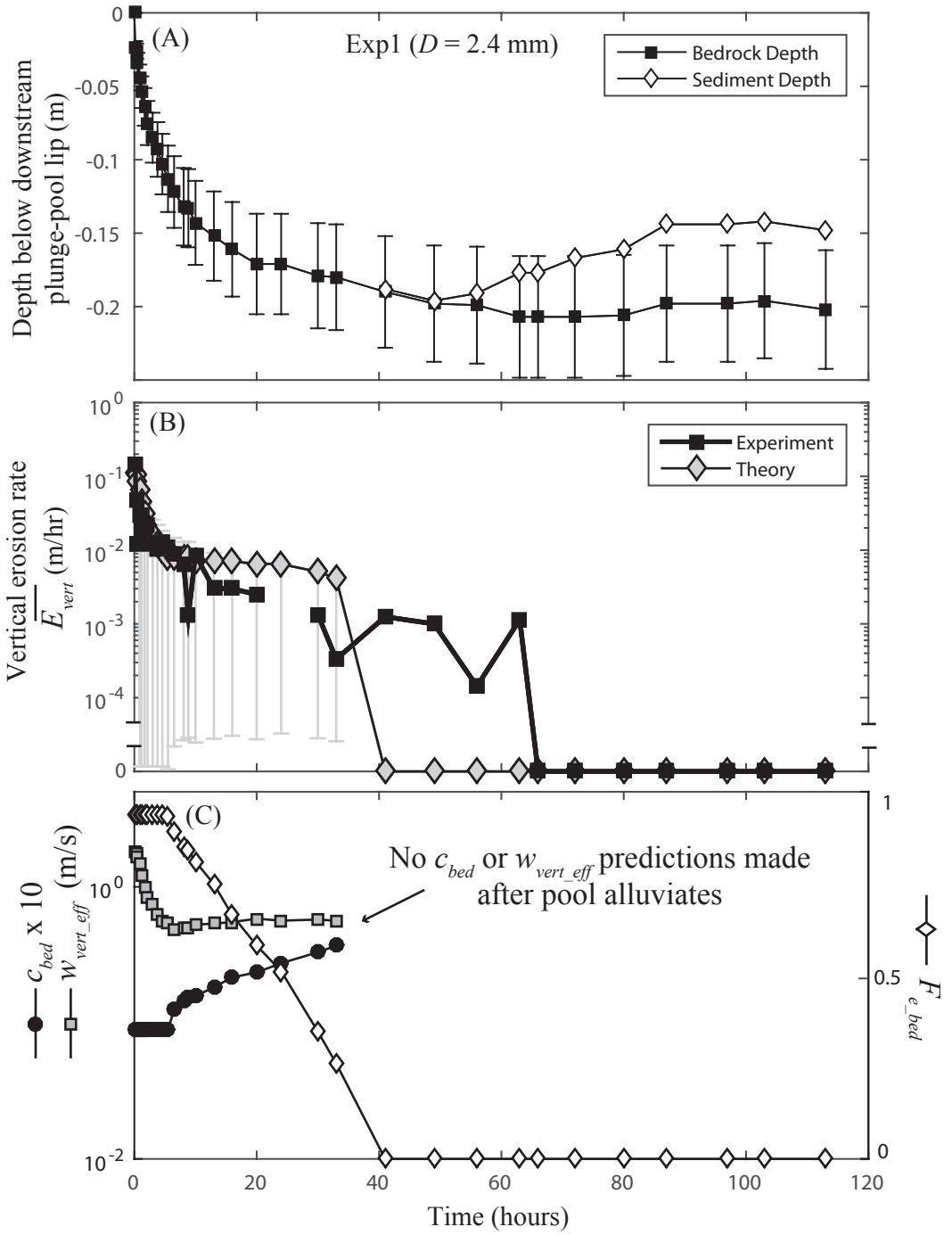

Figure 5.9: (A) Evolution of experimentally measured bedrock depth (black squares) and elevation of sediment cover (white diamonds) for Exp1. Error bars on bedrock depth reflect ~20% uncertainty in laser-scanner measurements. (B) Measured experimental (black squares) and theoretically predicted (gray diamond) vertical erosion rates in Exp1. Error bars on theory prediction depict the range of predicted erosion rates as a function of radial distance from the plunge pool center (e.g., Fig. 5.4, Eq. 5.5a), with the data points plotted for the area-weighted mean erosion rate (Eq. 5.24a). (C) Theoretical predictions of area-weighted mean sediment concentration on the plunge pool floor (black circles), particle effective vertical impact velocity (gray squares) and fraction of bedrock exposed (white diamonds).

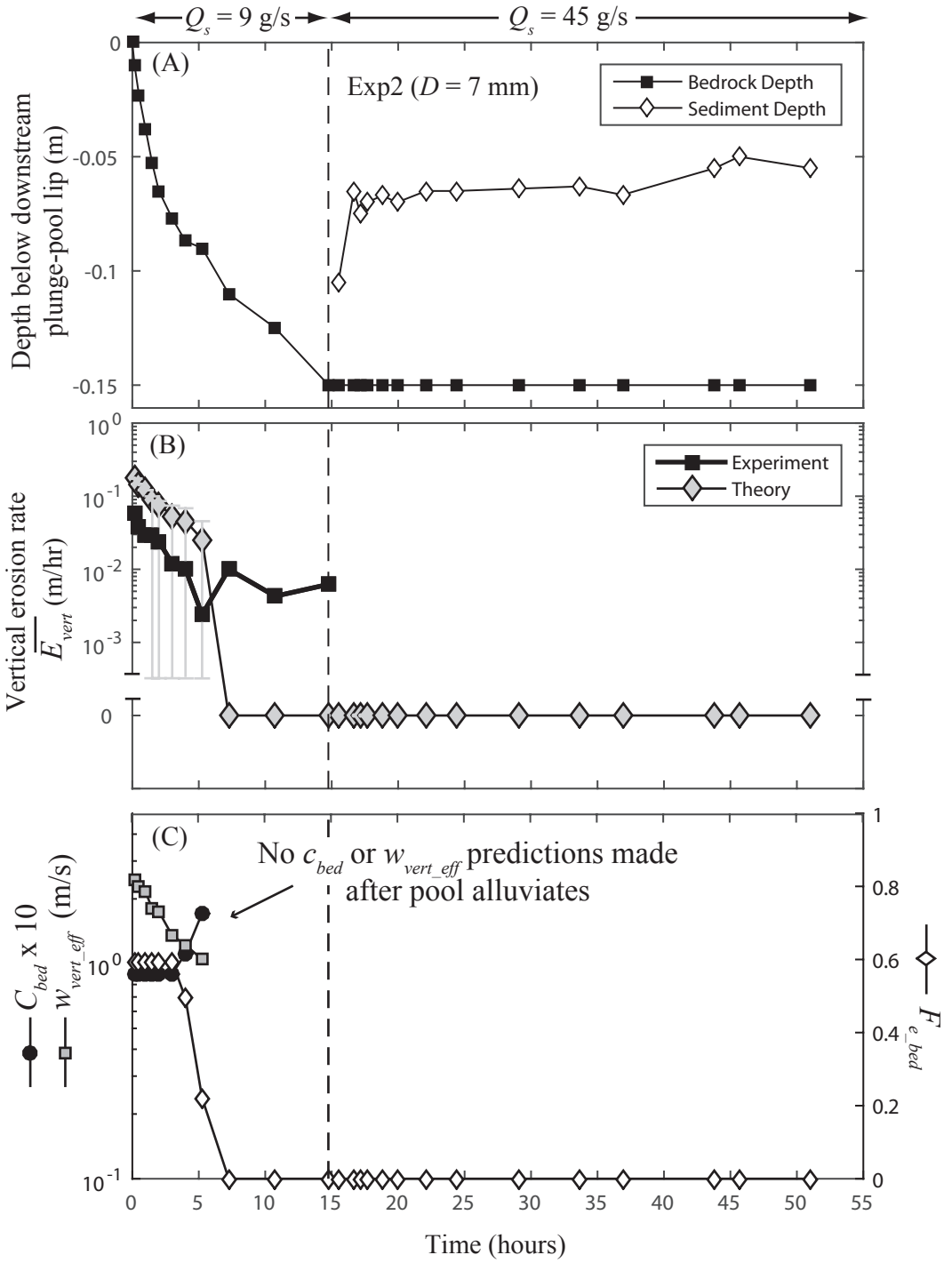

Figure 5.10: (A) Evolution of Exp2 bedrock depth (black squares) and elevation of sediment deposit (white diamonds). (B) Measured experimental (black squares) and theoretically predicted (gray diamond) vertical erosion rates in Exp2. Error bars on theory prediction depict the range of predicted erosion rates as a function of radial distance from the plunge pool center (e.g., Fig. 5.4, Eq. 5.5a), with the data points plotted for the area-weighted mean erosion rate (Eq. 5.24a). (C) Theoretical predictions of area-weighted mean sediment concentration on the plunge pool floor (black circles), particle effective vertical impact velocity (gray squares) and fraction of bedrock exposed (white diamonds). Dashed line at t = 14.75 hr in all panels denotes timing of increase in sediment supply (Q_s) from Q_s = 9 g/s (t < 14.75 hr) to Q_s = 45 g/s (t > 14.75 hr).

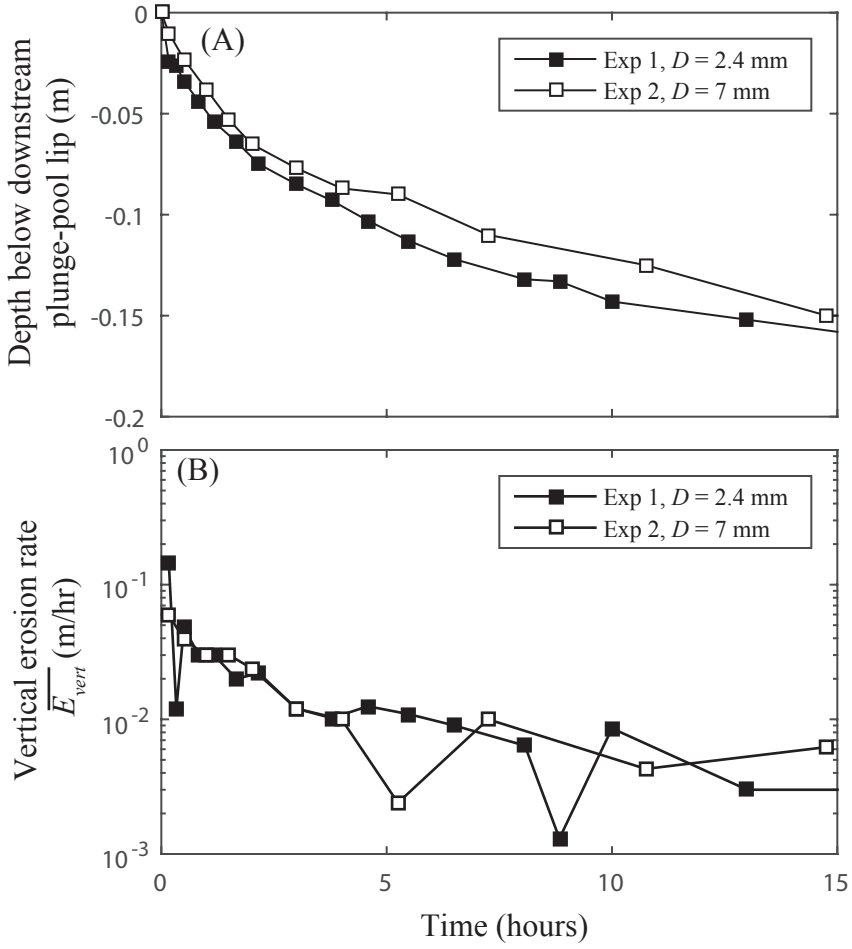

Figure 5.11: (A) Comparison of plunge-pool bedrock depth and (B) experimentally measured vertical erosion rates in Exp1 versus Exp2.

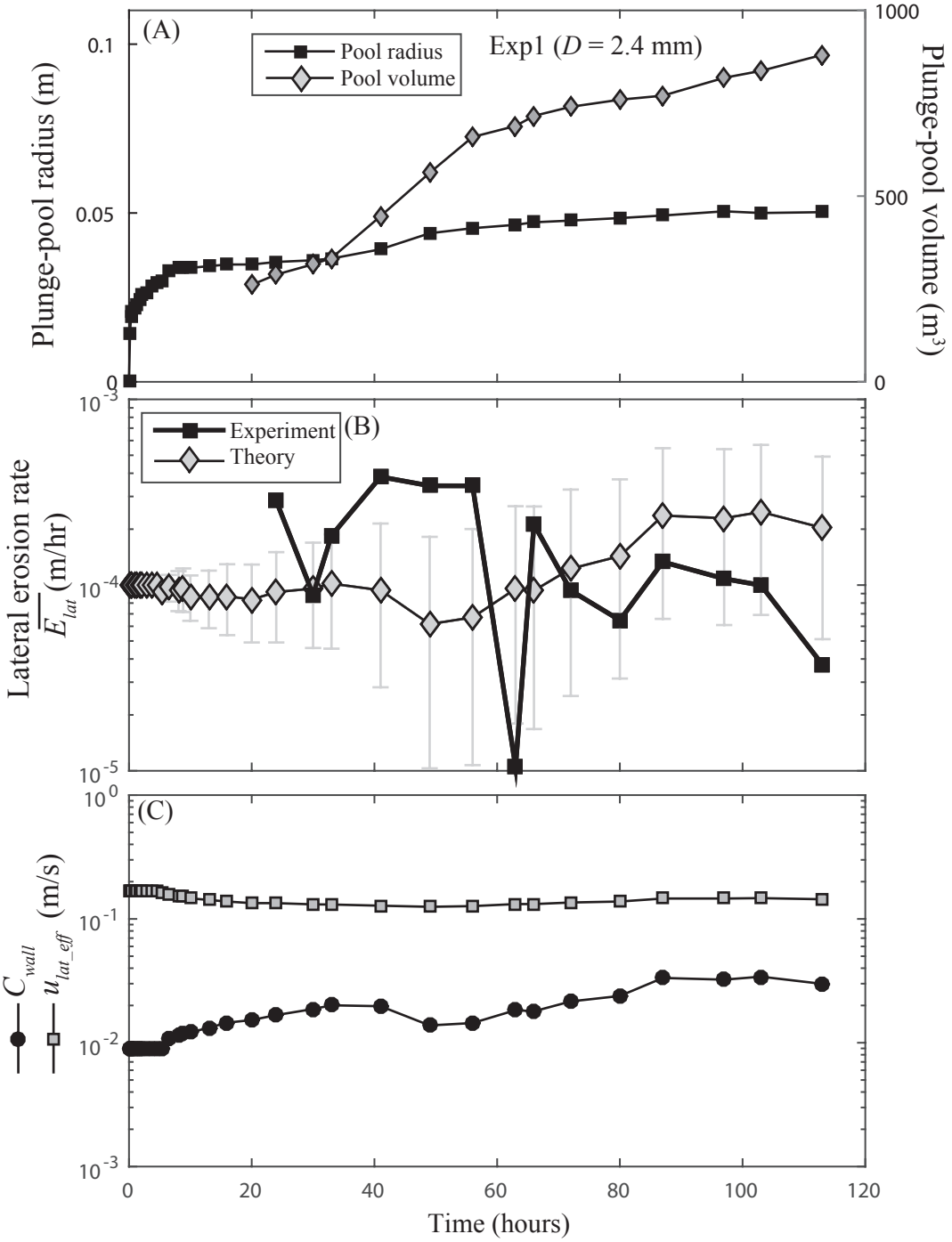

Figure 5.12: (A) Experimentally measured total pool volume (gray diamonds) as well as average pool radius measured at the top of the plunge pool (i.e., in the plane of $z = z_{lip}$) for Exp1. (B) Experimentally measured (black squares, Eq. 5.27) and theoretically predicted (gray diamonds, Eq. 5.24b) plunge-pool lateral erosion rates. Error bars on theory prediction show the range of predicted erosion rates as a function of vertical distance above the plunge pool floor (e.g., Fig. 5.4, Eq. 5.5b). (C) Theoretical predictions of depth-averaged sediment concentration along the plunge-pool wall (black circles) and particle effective lateral impact velocity (gray squares).

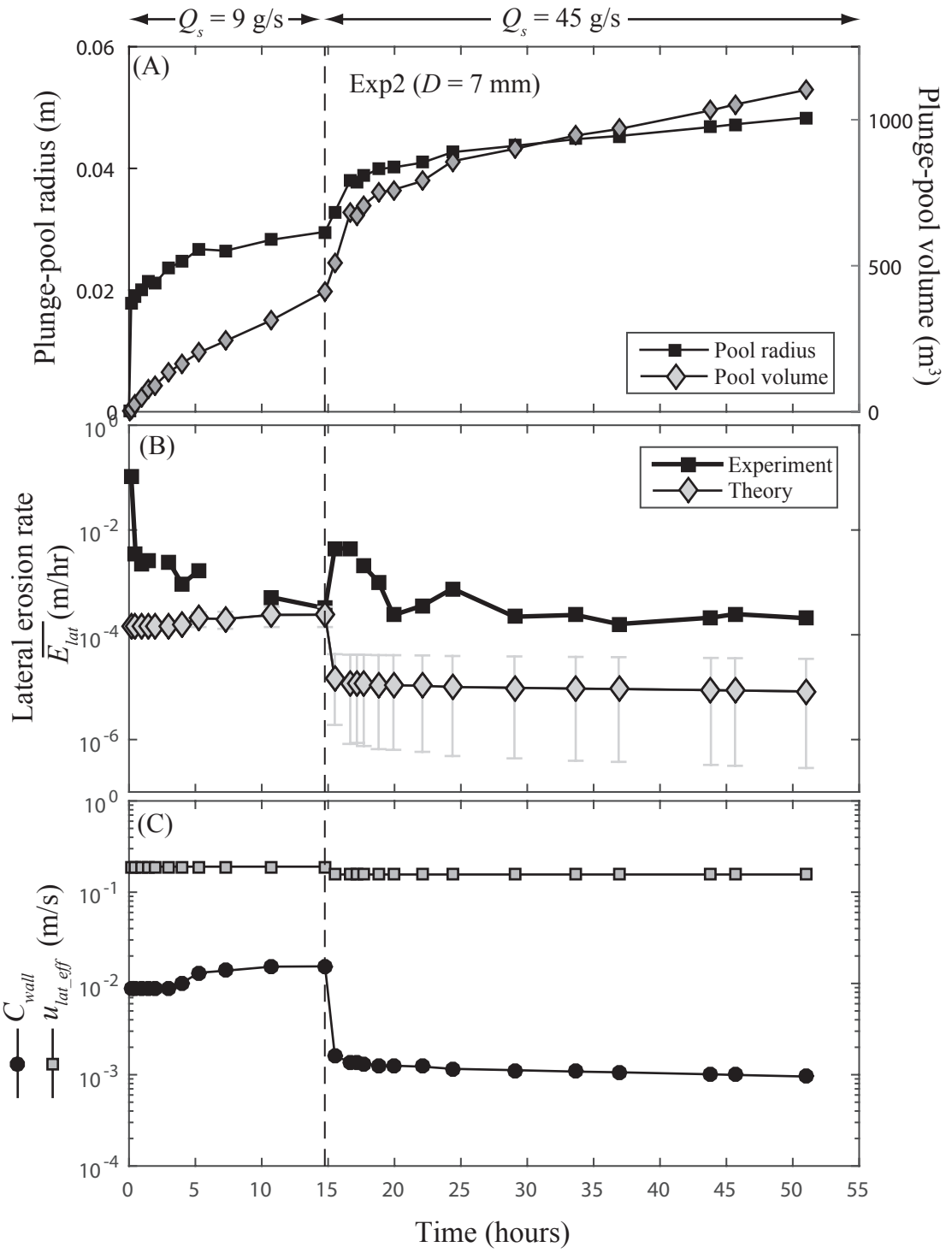

Figure 5.13: (A) Experimentally measured total pool volume (gray diamonds) as well as plunge pool radius measured at the top of the plunge pool (i.e., in the plane of $z = z_{lip}$) for Exp2. (B) Experimentally measured (black squares, Eq. 5.27) and theoretically predicted (gray diamond, Eq. 5.24b) plunge-pool lateral-erosion rates. Error bars on theory prediction show the range of predicted erosion rates as a function of vertical distance above the plunge pool floor (e.g., Fig. 5.4, Eq. 5.5b) and are smaller than the symbol where not shown. (C) Theoretical predictions of depth-averaged sediment concentration along the plunge-pool wall (black circles) and particle effective lateral impact velocity (gray squares). Dashed line at t = 14.75 hr in all panels denotes timing of increase in sediment supply (Q_s) from Q_s = 9 g/s (t < 14.75 hr) to Q_s = 45 g/s (t > 14.75 hr).

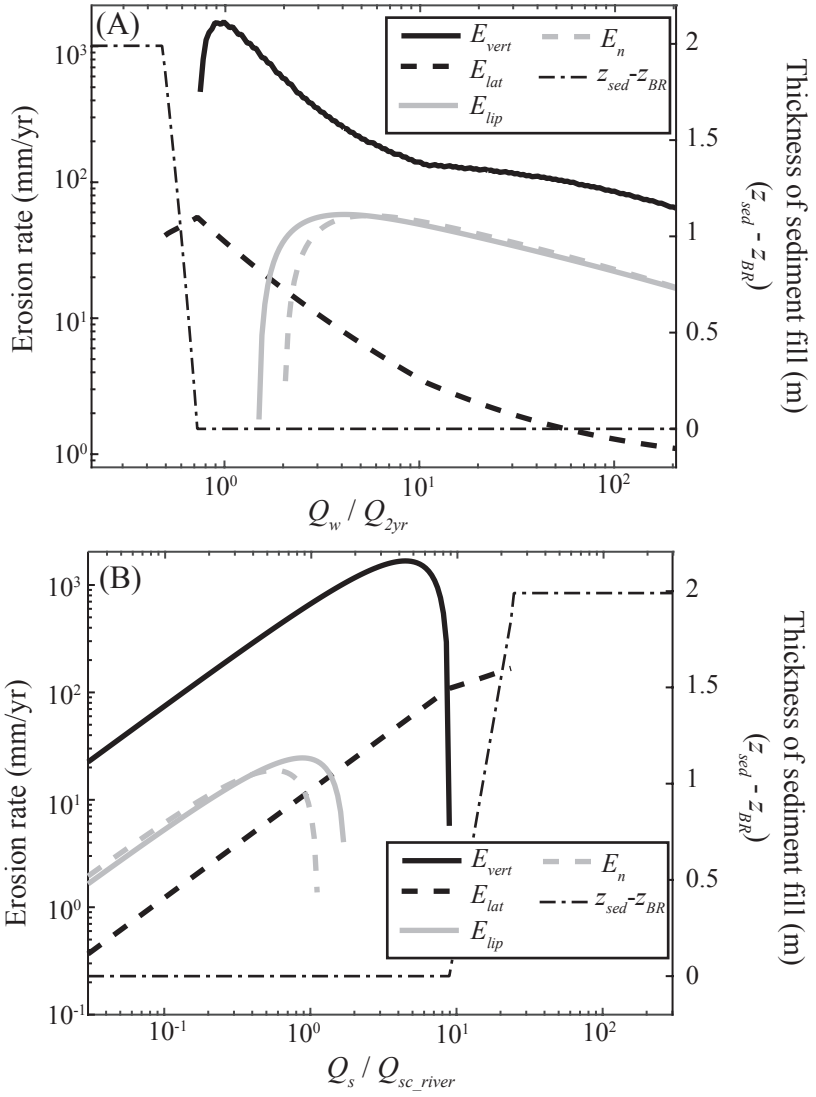

Figure 5.14 : Example calculations of average plunge-pool vertical (E_{vert}) and lateral erosion (E_{lat}), versus fluvial erosion under normal flow conditions (E_n) and at the water-fall brink (E_{lip}) for (A) variable water discharge (Q_w) normalized by 2-year recurrence interval discharge (Q_{2yr}) and (B) variable sediment supply normalized by plunge-pool sediment transport-capacity. Also shown is a prediction of the thickness of sediment fill ($z_{sed} - z_{BR}$) above the plunge pool bedrock floor. All calculations use base values for the Lower Switzer Falls reference site [Scheingross and Lamb, *in review*], (H = 5 m, (z_{lip} – z_{BR}) = 2 m, r_{pool} = 4.4 m, Q_{2yr} = 4.8 m^3/s, D = 4.4 cm, S = 0.035). River sediment transport capacity is calculated using the empiricism of Fernandez-Luque and van Beek [1976] based on the normal river flow, where we have reduced total transport capacity by an order of magnitude reflecting the fact that such predictions tend to greatly over-predict sediment fluxes in mountain rivers [e.g., Recking, 2010; Nitsche et al., 2011; Yager et al., 2012].

Chapter 6

FORMATION AND EVOLUTION OF AN EXPERIMENTAL SLOT CANYON THROUGH BEDROCK STEP-POOL AND WATERFALL DYNAMICS

Joel S. Scheingross, Brian M. Fuller, Juliane Preimesberger, and Michael P. Lamb

Division of Geological and Planetary Sciences, California Institute of Technology, Pasadena, CA, 91125, USA

* In preparation for submission to *Journal of Geophysical Research – Earth Surface*.

6.1 Abstract

Fluvial bedrock incision sets the pace of landscape evolution, but little is known about the mechanics of bedrock erosion in steep streams where channels commonly display bedrock steps, pools, and waterfalls, which can retreat upstream. We performed a controlled laboratory experiment designed specifically to examine bedrock incision processes at steep slopes under constant forcing. Under low sediment supply, a deep inner slot was rapidly incised into the initially planar, 19.5% sloping channel. Small-wavelength spatial variation in vertical incision rate led to the development of bedrock crests and troughs, which migrated downstream and grew into distinct step-pool topography, and at times, waterfalls. Pools deepened to the point of sediment deposition, after which selective erosion of adjacently exposed bedrock caused upstream propagation of the bedrock step, formation of a new upstream pool, and destruction of the original pool. While step-pool dynamics dominated the total incision within the flume, reach-average erosion rates were well predicted by mechanistic bedrock incision theory which assumes a planar bed. Our experimental results highlight the importance of bedrock step-pool dynamics in setting the rate and style of bedrock incision in steep streams. While waterfalls and bedrock steps are often assumed to form from changes in climatic or tectonic forcing, autogenic formation of these features in our experiment suggests care must be taken to distinguish between waterfalls and knickpoints formed by internal dynamics versus external forcing.

6.2 Introduction

River incision into bedrock drives landscape evolution and sets the flux of sediment delivered from mountain ranges to sediment basins downstream (e.g., Whipple et al., 2013). A process-based understanding of the controls on river incision allows predictions of landscape response to changes in climate and tectonics over geologic timescales, as well as predictions of sediment yield and reach-scale erosion over timescales of a single storm to multiple years. In mountainous areas where erosion is concentrated (e.g., Larsen et al., 2014), steep streams (slope, $S > 10\%$) often make up the majority of the channel network in terms of total channel length (e.g., Benda et al., 2005). Yet, despite over a century of work on river incision into bedrock (e.g., Gilbert, 1877; Shepherd and Schumm, 1974; Howard and Kerby, 1983; Whipple et al., 2000a; Sklar and Dietrich, 2004), most workers have focused on relatively low to moderate gradient reaches ($S < 10\%$), while those working in steep reaches often assume erosion is dominated by debris flow processes (e.g., Stock and Dietrich, 2006).

The mechanics of channel incision in steep channels is further complicated by the presence of bedrock steps, pools, and waterfalls, which can retreat upstream at rates far outpacing standard fluvial incision rates (e.g., Mackey et al., 2014). Predictions of landscape evolution in steep areas thus require descriptions of both waterfall and standard fluvial incision, as well as interactions between the two. While mechanisms have been proposed for waterfall retreat via undercutting in layered sedimentary rock (e.g., Gilbert, 1890; Holland and Pickup, 1976; Haviv et al., 2010; Hayakawa and Matsukura, 2010), vertical plunge-pool drilling (Howard et al., 1994; Lamb et al., 2007), and toppling of columns in jointed rock (e.g., Weissel and Seidl, 1997; Lamb and Dietrich, 2009), it is

unclear what drives waterfall retreat in massive, crystalline rock such as that commonly found in granitic batholiths.

Investigating the mechanics of river incision in the field is made difficult by the slow rates involved (~10^{-3} to 10^{0} mm/yr (Portenga and Bierman, 2011)) and the fact that erosion occurs during floods when it is difficult and dangerous to make observations. Despite some natural experiments (e.g., Whipple et al., 2000b; Snyder and Kammer, 2008) and extreme events (e.g., Lamb and Fonstad, 2010; Cook et al., 2012), field measurements of bedrock incision come mostly from small scale measurements which are limited in spatial and temporal extent (e.g., Hartshorn et al., 2002; Stock et al., 2005; Johnson et al., 2010), or are inferred from geochemical measurements which average over thousands of years making it difficult to infer process (e.g., Burbank et al., 1996; DiBiase et al., 2010). In contrast, recent advances in simulating bedrock erosion in flume experiments has allowed studies of erosion over laboratory timescales where independent control of water discharge, grain size, sediment flux, and more has led to the development and testing of mechanistically-based bedrock erosion theories (Lamb et al., 2015).

Most laboratory experiments examining bedrock incision have focused on incision at moderate slopes (e.g., Shepherd and Schumm, 1974; Finnegan et al., 2007; Johnson and Whipple, 2010). Similarly, waterfall retreat experiments, which have also been limited to moderate slopes, have focused on waterfalls formed in layered sedimentary rock and have used cohesive substrates as bedrock analogs that make scaling between laboratory and field scales difficult (e.g., Holland and Pickup, 1976; Gardner, 1983; Frankel et al., 2007). Wohl and Ikeda (1997) and Johnson and Whipple (2007)

replicated experiments across a range of slopes of up to 20% and 10%, respectively. These experiments documented a slope-dependence in the mechanics and style of bedrock incision, where channels tended to narrow and form incised slots, potholes, and pools as channel slope increased.

Slope-driven changes in channel morphology in the absence of external forcing, such as those observed by Wohl and Ikeda (1997) and Johnson and Whipple (2007), suggest that the internal dynamics of water flow, sediment transport, and abrasion may lead to autogenic formation of steps and waterfalls in natural channels, and are supported by preliminary observations of the formation of cyclic steps in an experimental bedrock channel (Yokokawa et al., 2013). In contrast, steepened channel sections (e.g., knickpoints) composed of bedrock steps and waterfalls are frequently assumed to form in response to external forcing, and waterfall retreat models are often applied in inverse to estimate the timing of changes in climate, tectonics, or sea-level (e.g., Howard et al., 1994; Whipple and Tucker, 1999; Reinhardt et al., 2007; Whittaker and Boulton, 2012; Ye et al., 2013; Mackey et al., 2014; DiBiase et al., 2015). Thus, if such features form autogenically, they must be distinguished from those formed via external forcing to avoid bias in estimates of past changes.

Taken together, the lack of knowledge on the mechanics and processes of bedrock incision at steep slopes, including the formation and retreat of bedrock steps, pools, and waterfalls, limits our ability to predict erosion rates in mountainous areas and drive landscape evolution models. To address this knowledge gap, we performed a controlled laboratory flume experiment specifically designed to examine the processes of channel incision into bedrock and the formation and propagation of steps and waterfalls at steep

slopes. In this paper we first describe our experimental setup and methods. Second we present our experimental results providing an overview of the channel evolution, and analysis of channel width, slope, step-pool development, alluvial cover, and reach-averaged erosion rates. Third we discuss our results in terms of controls on channel width, interactions between bedrock step-pools and alluvial cover which lead to development of short-lived waterfalls and upstream plunge-pool retreat, and reach-averaged incision rates. We conclude by discussing the implication of our findings for natural rivers.

6.3. Experimental methods

6.3.1 Experiment design and scaling

We conducted our experiment using a 12 m long by 30.5 cm wide by 1 m deep flume tilted to 19.5%, within which we installed a 0.76 m thick floor of polyurethane foam blocks to serve as a bedrock simulant. Similar to previous experiments investigating fluvial bedrock incision (e.g., Finnegan et al., 2007; Johnson and Whipple, 2007, 2010), we selected water discharge, sediment flux, and grain size in an attempt to maximize incision rates while having sediment flux well below the reach-averaged transport capacity. We fed unimodal, siliciclastic sediment with median diameter (D) of 2.4 cm at a constant rate of approximately 0.5 ± 0.02 kg/s (mean ± standard deviation). We selected large grains to maximize erosion via high kinetic impact energy, and chose an initial water discharge (Q_w = 14.2 L/s) such that reach-averaged Shields stress ($\tau_* \sim 0.11$) would be well in excess of the threshold of motion (Chatanantavet et al., 2013), ensuring minimal sediment deposition on our initially smooth foam-bed. We also attempted to

achieve dynamic similarity with natural bedrock channels by starting the experiment with supercritical flow and fully turbulent flow (e.g., Paola et al., 2009); over the initially planar bed, Froude numbers were ~4.5, and Reynolds numbers and Reynolds particle numbers were 4.6×10^4 and 5.0×10^4, respectively.

We divided the flume into two separate sections in order to investigate both channel incision into a planar bed, as well as interactions between waterfall and lower-gradient fluvial incision. The upstream ~7.3 m of foam consisted of an initially planar bed with constant slope of 19.5%. In the downstream ~2.2 m of the experiment we cut two 21 cm waterfall steps. These steps were separated by ~1% sloping treads of ~1.1 m length such that average slope from the top of the first waterfall to the downstream end of the flume remained 19.5% (Fig. 6.1). We protected the foam at the downstream end to hold base-level constant. This had the effect of creating two separate waterfall-tread systems; the downstream of the two waterfalls was subjected to a fixed base-level which promoted alluviation of the channel floor, while the upstream waterfall-tread system was free to adjust its base-level via incision at the waterfall step below.

For the first 3.7 hours of run time ("Phase 1") we allowed the channel to evolve under a constant water flux of 14.2 L/s and fixed base-level. After 3.7 hours of experiment run time, the upstream channel had incised deeply enough to feel the downstream base-level control. At this point, we removed the fixed base-level control and simultaneously reduced water discharge by ~40%. This allowed for the channel to set its own base-level, while the reduced water discharge promoted sediment deposition allowing observations of feedbacks between alluvial cover and channel incision. We continued the experiment holding water discharge approximately constant at ~8.3 L/s for

an additional ~5.6 hours of run time ("Phase 2"), ending the experiment after the channel had eroded through the available foam substrate.

6.3.2 Experiment setup

We installed four 2.44 m long by 0.76 m tall by 0.3 m wide polyurethane foam blocks in succession on the flume floor to make a 9.75 m long erodible test section. Foam blocks were glued to the flume floor and pressed together to minimize void space. We used a low tensile strength (σ_T = 0.32 MPa) commercially available polyurethane foam as a bedrock analog. This foam has been shown to follow the same tensile-strength scaling with erosion rate as natural rock and concrete, and erodes orders of magnitude faster than natural rock allowing for measureable bedrock erosion and topographic evolution over experiment timescales (Scheingross et al., 2014; Lamb et al., 2015).

Water and sediment entered the flume at the upstream end (Fig. 6.1). A series of conveyor belts re-circulated unimodal gravel from the downstream end of the flume into a sediment feeder which held sediment flux into the upstream end of the flume constant. Water filled in a headbox before overspilling onto a false floor approximately ~1.5 m upstream of the foam. The false floor was lowered ~12 cm below the foam surface, allowing a gravel wedge to form upstream of the start of the bedrock reach to aid in flow and sediment transport conditioning before entering the test section. We protected the upstream edge of the foam to prevent erosion, thus fixing the upstream bedrock elevation and creating a system similar to an alluvial-bedrock transition. Within the test section sidewalls extended 10 cm above the foam surface and were epoxied with fine sand to provide roughness.

We ran the experiment with sediment and water flux for periods ranging from 3 – 60 minutes, before pausing to take topographic measurements. We used instruments affixed to a motorized cart that were capable of taking measurements throughout the test section. While the experiment was running, we measured the water-surface profile along the channel thalweg at 1 mm intervals using either an ultrasound probe or laser scanner (both with sub-mm resolution), depending on the flow width and water aeration. While the experiment was paused, we used the laser scanner to measure the channel topography at 1 mm resolution in the along-stream direction and 2 – 10 mm resolution in the cross-stream direction. We first scanned the bed with deposited sediment in place, we then manually removed all deposited sediment and performed a second scan to measure the previously-covered bedrock topography before manually replacing the sediment. We paused the experiment by simultaneously cutting power to the water pump and sediment re-circulation system, such that grains in active transport at the time of pausing were often deposited on the channel-bed, but were not part of a static alluvial cover. To avoid bias from including these grains, we considered an area to be alluviated only if the sediment thickness was greater than 5 cm (~2 grain diameters).

We used our topographic scans of the channel bedrock and sediment elevations to extract longitudinal profiles showing the evolution of the channel bed and sediment cover. We marked the thalweg as the minimum elevation at each channel cross-section, and estimated reach-averaged channel slope from the best-fit line to the thalweg versus distance data. This method slightly over-estimates slopes where planform sinuosity develops, but the effect should be minimal here as the incised channel was essentially one-dimensional. We made topographic measurements parallel to the overall flume slope

of 19.5%, and rotated all profiles to make the *x* and *z* directions perpendicular and parallel to gravity, respectively.

6.4 Results

6.4.1: Overview

We describe channel erosion and evolution for the downstream section with pre-formed waterfalls separately to the planar upstream section as these two channel segments exhibited different behavior over the course of the experiment. In the downstream section, channel-spanning plunge pools rapidly developed beneath the existing waterfalls (Fig. 6.2). Incision was limited to ~7 cm on the downstream of the two waterfalls as the fixed base-level resulted in alluviation of the lower tread within the first hour of experiment run time, providing an armor layer which protected the pool from further erosion. In contrast, the upper pool incised to ~23 cm before sediment deposition prevented further incision. Fluvial incision at the waterfall lips outpaced plunge-pool incision such that the channel thalweg cut completely through the waterfall face within the first ~3 hours of experiment run time. Following removal of the fixed-base level control at the start of Phase 2, alluvial cover at the downstream tread was progressively stripped away, and the downstream end of the flume developed an over-steepened channel segment (i.e., knickpoint) which translated upstream (Fig. 6.3).

In the upstream section an ~8-10 cm wide thalweg was cut into the center of the foam within the first hour of experiment time. This topographic low quickly captured the available water and sediment flux, effectively stranding the channel margins and resulting in the formation of a deeply incised inner channel resembling a natural slot

canyon (Figs. 6.4 and 6.5). As the slot was incised, small spatial-variation in erosion rate led to the formation of a series of repeating steps and pools which grew in amplitude as the experiment progressed (Figs. 6.3-6.5). Initially, these pools migrated downstream as sediment impacts were focused on the upstream-facing surface that comprised the downstream pool wall (Fig. 6.3). In Phase 2 of the experiment, the combination of reduced water discharge and deepening pools led to sediment deposition, and feedbacks between erosion and sediment cover caused upstream pool retreat described in more detail below (Section 6.5.2).

6.4.2 Channel width and planform sinuosity

Plunge-pools incised into the downstream section were initially channel-spanning as water and sediment cascaded across the entire channel reach upstream. Subsequent incision and deepening of pools occurred over a narrower area (~10-20 cm) as slot-incision at the waterfall brink focused the sediment-laden jet (Fig. 6.2). An incised slot with a small degree of sinuosity emerged downstream of the upper plunge-pool as water and sediment were focused towards the channel's right bank before impacting the channel wall and being pushed back towards the center (Figs. 6.2bc). A similar slot developed downstream of the lower plunge-pool following removal of the fixed base-level (Fig. 6.2c).

Incision in the upstream section was focused in an ~8-10 cm wide slot which was slightly wider (widths from ~10 – 17 cm) at pools (Figs. 6.4 – 6.6). Widening at pools occurred as water was shot into the air as 'rooster tails' when exiting upstream pools, such that the upward moving jet could in some cases escape the confinement of the incised slot allowing expansion of the flow and sediment impacts over a wider area (Fig.

6.7). The initial slot was straight and centered in the channel, with no obvious bends or sinuosity in the channel path (Figs. 6.4 and 6.5). As the experiment progressed, small perturbations in channel sinuosity developed which caused the formation of low-amplitude bends within the channel (Fig. 6.4).

6.4.3: Slope evolution

We estimated reach-averaged channel gradient as the slope of the best-fit line to the extracted bedrock long-profiles. We fit the upstream slope using the profile from $1015 < x < 8110$ mm to avoid inclusion of both the steep waterfall face which formed at the upstream end of the flume, as well as the initial waterfalls in the downstream section. The downstream slope was fit to the profile for $x > 8110$ mm in order to capture the relief from the pre-cut waterfalls.

In the downstream section, channel slope decreased rapidly from ~17% at the start of the experiment to ~4% at the end of Phase 1 (Fig. 6.8b). This occurred as fluvial incision at the waterfall lips outpaced plunge pool incision, effectively erasing the waterfalls (Figs. 6.2 and 6.3), and the fixed base-level prevented further lowering at the downstream end, such that by $t \approx 3.4$ hr (where t is the cumulative water and sediment run time) the downstream bed had almost completely alluviated. Following removal of the fixed base-level at the start of Phase 2, downstream slope slowly increased from $t =$ 3.7 to ~6 hr as alluvial cover was progressively stripped from the channel bed (Fig. 6.8d). After $t \approx 6$ hr a small steepened section developed at the end of the flume and propagated upstream allowing rapid increases in the reach-averaged slope of up to ~17.5% by the end of the experiment (Figs. 6.3 and 6.8b).

Changes in channel slope were much less dramatic in the upstream section. Reach-averaged upstream slope remained roughly constant at ~19.5% for the first ~1 hour of experiment run time, slowly decreasing to ~17.5% at the end of Phase 1 (Fig. 6.8b). At $t \approx 3.4$ hr, the upstream section had lowered close to the elevation of fixed base-level such that this constraint was felt upstream (Fig. 6.3). After removing the fixed base-level at the start of Phase 2, the slope along the upstream section continued to decrease, indicating a delayed response to the change of base-level control. Starting at approximately $t = 5$ hr, a break in slope can be seen in the channel long-profiles at $x \approx 5500$ mm separating the steeper channel upstream (which had not felt the effects of fixed base-level) from the lower-gradient channel downstream (which had) (Fig. 6.3).

6.4.4. Development of bedrock step-pools

We used a measure of bedrock-step relief to quantify the rate at which the channel evolved from an initially planar bed to a series of bedrock step-pools. We estimated reach-averaged step-relief as the standard deviation of the residuals to our best fit slope lines, and calculated step relief along the channel-thalweg only, due to the 1D nature of the evolved slot canyon.

In the downstream section, reach-averaged step-relief was initially high due to the presence of the pre-cut waterfalls (Fig. 6.8c). As the experiment progressed, destruction of these waterfalls combined with plunge-pool alluviation resulted in a decrease in step relief from $t \sim 3 – 6$ hr. After $t = 7$ hr, we induced base-level fall which led to the development of a series of bedrock step-pools in the downstream reach, increasing reach-averaged step-relief once again.

The evolution of step relief in the upstream section was out of phase with that of the downstream section (Fig. 6.8c). Step relief rapidly increased from 0 mm over the planar channel bed to values of up to ~70 mm as bedrock step-pools developed. As the fixed base-level downstream began to be felt in the upstream section, the decrease in channel slope and deposition of sediment led to destruction of step-pools and an overall lowering of reach-averaged step-relief down to values of ~35 mm by the end of the experiment. Visual comparison of long-profiles for the channel upstream and downstream of $x \sim 5500$ shows overall lower step-relief for the downstream areas where the influence of fixed base-level was most pronounced.

6.4.5 Sediment cover

As reach-averaged step-relief increased over the course of the experiment, alluvial cover developed providing an armor layer which limited vertical incision. We measured the thickness and extent of alluvial cover by differencing long-profiles of bare bedrock from those which included deposited sediment. As sediment cover tended to be uniform across the active channel width, these 1D measurements are representative of the entire channel.

In the downstream section, sediment cover developed as waterfall plunge-pools increased in depth due to the fixed base-level at the downstream end. The initially cover-free surface experienced near complete alluviation by the end of Phase 1, after which sediment was progressively stripped away following removal of the base-level control (Fig. 6.8d). The upstream section experienced progressive alluviation during Phase 1 as sediment deposited in deepening bedrock step pools. From the end of Phase 1 until $t \sim 7$

hr, sediment cover stayed roughly constant with ~30% of the bed alluviated, and then increased to ~65% by the end of the experiment (Fig. 6.8d).

6.4.6 Reach-averaged vertical incision rates

Bedrock incision rates varied over the course of the experiment due to interactions between evolving sediment cover and bedrock step-pools. We calculated reach-averaged vertical incision rates by differencing successive long-profiles and taking spatial averages. In the downstream section, vertical incision rates were initially high (~50 mm/hr), progressively slowing to zero erosion as the bed almost completely alluviated (Fig. 6.8e). After removal of the fixed base-level, vertical erosion rates remained low until the alluvial cover was removed at $t \sim 6$ hr. In the final four hours of the experiment, knickpoint development and upstream retreat at the downstream end of the flume caused vertical erosion rates to increase to 67 mm/hr. In the upstream section vertical incision rates peaked near ~120 mm/hr at the start of the experiment when there was no bedrock cover and low bedrock-step relief. As pools developed and step-relief increased, sediment deposition caused erosion rates to drop to ~65-70 mm/hr at the end of Phase 1, and rates remained roughly constant at 50-75 mm/hr for the remainder of the experiment (Fig. 6.8e).

6.5 Analysis and comparison to theory

6.5.1 Controls on channel width

Repeated experiments have shown that narrow slots tend to incise into bedrock when sediment is supplied at low rates over an initially planar bed (e.g., Wohl and Ikeda, 1997; Finnegan et al., 2007; Johnson and Whipple, 2007, 2010). While the controls on

bedrock channel width are poorly understood, Nelson and Seminara (2011) proposed a model whereby channels self-adjust their width of active bedload transport in response to changes in sediment supply. This assumption is based, in part, on observations of changing active bedload transport width in response to changes in sediment supply in alluvial flume experiments (Dietrich et al., 1989), and allowed Nelson and Seminara (2011) to reproduce the evolving channel geometry observed in previous bedrock erosion experiments (Finnegan et al., 2007).

The cutting of an ~8-10 cm wide slot in our experiment allows for testing of the Nelson and Seminara (2011) framework. Nelson and Seminara (2011) assume that the width over which sediment is transported self-adjusts such that the imposed sediment supply is always transported at its transport capacity. Employing a standard bedload transport capacity empirical formula (e.g., Fernandez Luque and van Beek, 1976), the active channel width (W_{ac}) can be solved for as

$$W_{ac} = \frac{Q_s}{5.7(\tau_* - \tau_{*_c})^{3/2}(RgD^3)^{1/2}}, \qquad (6.1)$$

where Q_s is the volumetric sediment flux, τ_{*c} is the critical Shields stress for grain motion, R is submerged sediment density, and g is acceleration due to gravity. We solved Eq. (61) for conditions at the start of our experiment when we had thin flow spread over the initially 30.5 cm wide channel. Using a reduced value of $\tau_{*c} = 0.01$ to reflect the initially smooth bed (Chatanantavet et al., 2013), we calculate $W_{ac} = 11$ cm, in good agreement with our observations of the resulting 8-10 cm slot which was subsequently incised, and consistent with the model of Nelson and Seminara (2011). This finding suggests that channels self-adjust their geometry to the minimum possible width to allow transport of

the imposed sediment supply, and implies that models such as those proposed by Nelson and Seminara (2011) accurately capture the controls on evolving bedrock channel width.

6.5.2 Comparison with reach-averaged prediction of alluvial cover and erosion rate

Creation of bedrock step-pool topography in our experiment dominated channel roughness, and pool incision appeared to be the primary erosional mechanism. This step-pool morphology represents local conditions that are not often accounted for in theoretical predictions based on reach-average measurements. Here, we compare our measurements of extent of alluvial cover and average erosion rate with model predictions to explore how much local variability may influence our reach-averaged estimates.

Alluvial cover armors bedrock floors and prevents vertical incision and the fraction of cover (F_c) is commonly estimated as being linearly proportional to the ratio of sediment supply to transport capacity (Q_{sc}), i.e., $F_c = Q_s / Q_{sc}$ (Sklar and Dietrich, 2004). We solved for F_c using our imposed sediment flux of 0.5 kg/s and our measurements of reach-averaged flow depth (h) and channel slope (S). Assuming steady uniform flow and a commonly used empirical formula for sediment transport capacity (Fernandez Luque and van Beek, 1976), the fraction of cover can be solved for as

$$F_c = \frac{Q_s}{5.7W([hS/RD]-\tau_{*c})^{3/2}(RgD^3)^{1/2}}, \qquad (6.2)$$

where we once again set $\tau_{*c} = 0.01$ to reflect the smooth bed in areas without sediment cover (Chatanantavet et al., 2013). Estimates of alluvial cover using Eq. (6.2) are generally constant despite a factor two change in F_c over the course of the experiment (Fig. 6.8D), supporting the idea that the formation of cover is largely controlled by local variability in flow conditions as opposed to reach-averaged assessments (e.g., Johnson and Whipple, 2010). Note that estimating F_c with an exponential instead of a linear

model (Turowski et al., 2007) yields essentially equivalent predictions for the low values of Q_s / Q_{sc} in our experiment. Part of the error in estimating alluvial cover with Eq. (6.2) likely comes from our (commonly used) assumptions of uniform flow as well as shear stress proportional to flow depth (which likely over-estimates shear stress on the channel floor (Nelson and Seminara, 2011)). Using a more sophisticated model to calculate shear stresses (e.g., Kean and Smith, 2004) could reduce this error while still being based on reach-averaged measurements.

We compared our measurements of reach-averaged vertical incision to those predicted from the Lamb et al. (2008b) total load erosion model. The total load model is a modified version of the Sklar and Dietrich (2004) saltation-abrasion model whereby erosion is predicted to occur from impacting sediment. Unlike the saltation-abrasion model which assumes sediment impacts occur only from saltating bedload particles, the total load model is based on near-bed sediment concentration and allows for prediction of erosion rates at high transport stages when sediment may be suspended and for which the saltation-abrasion predicts zero erosion (Scheingross et al., 2014). The saltation-abrasion and total-load model both express vertical erosion rate (E) as

$$E = V_i I_r (1 - F_c) \ , \qquad (6.3)$$

where V_i and I_r are the volume of rock eroded for a given particle impact and impact rate, respectively, and (1-F_c) represents the fraction of bedrock exposed on the channel bed. Equation (6.3) is equivalently expressed in the total load model as

$$E = \kappa c_b w_i^3 (1 - F_c) \ , \quad (6.4)$$

where c_b is near-bed sediment concentration and w_i is particle impact velocity. κ in Eq. (64) is a dimensional constant which accounts for bedrock material properties,

$$\kappa = \frac{A_1 \rho_s k_Y}{\sigma_T^2} \quad , \qquad (6.5)$$

where ρ_s is rock density and A_1 is a constant which we set equal to 0.5 reflecting the fact that grains can be advected both towards and away from the bedrock surface. k_Y is an empirical constant related to the energy required to erode a unit volume of rock, rock elasticity, and material properties of the impacting particle (Lamb et al., 2015). k_Y is approximately 0.05 when the sediment load and bedrock have similar material properties, but, following Sklar and Dietrich (2004), we set $k_Y = 0.17$ to account for the siliciclastic sediment load impacting weak polyurethane foam in our experiments. We calculated total-load model predictions two separate ways using both Eq. (62) and our experimental measurements of F_c.

Total-load erosion rates generally agree with our measured incision rates within a factor of ~2-3 (Fig. 6.8E); a similar degree of error as observed in previous zero-dimensional abrasion-mill erosion experiments (Sklar and Dietrich, 2004; Scheingross et al., 2014). The total-load model under-predicts erosion rates by factor of ~2.5 in Phase 1 of the experiment before substantial deposition of sediment. This may reflect enhanced erosion of the upstream-facing surfaces of laterally migrating plunge-pools (Section 6.5.2), which is not accounted for in the model framework which assumes a planar bed (e.g., Huda and Small, 2014). In Phase 2 of the experiment when sediment cover increases, the total-load model more closely matches the observed measurements, but still tends to under-predict the total erosion rate. Again, this under-prediction could represent enhanced erosion from bedrock step-pool dynamics not included in the model. It is further encouraging that errors in predicting F_c do not drastically change the model predictions. Note that using the saltation-abrasion model in place of the total-load model

leads to further under-prediction and predictions of zero reach-averaged erosion rates as the high transport stage in the experiment causes artificially low predictions of erosion rates in the saltation-abrasion model (e.g., Scheingross et al., 2014).

6.6 Discussion

6.6.1 Interactions between bedrock step-pool dynamics and sediment cover

While waterfalls and bedrock-steps are frequently observed to retreat upstream (e.g., Gilbert, 1907; Seidl et al., 1994; Hayakawa and Matsukura, 2003; Crosby and Whipple, 2006; Cook et al., 2012; Mackey et al., 2014), we observed pools tended to initially propagate downstream, and retreated upstream following the onset of alluvial cover. Downstream propagation occurred primarily for shallow pools, due to sediment impacts concentrated on the upstream facing surfaces (Fig. 6.3 (e.g., Wilson et al., 2013; Huda and Small, 2014; Wilson and Lave, 2014)). Similar behavior has been observed in other bedrock erosion experiments (Finnegan et al., 2007; Johnson and Whipple, 2010), although in our study the relative rates of vertical incision on the pool floor compared to lateral migration of the downstream pool lip were similar (vertical to lateral rates of ~0.5 – 1), compared to lateral migration that outpaced vertical incision by a factor of ~5 in the lower sloping (channel slope of ~6.5%) experiments of Johnson and Whipple (2010). As pools migrated downstream in our experiment, they left distinct grooves in the slot sidewall recording their passage (Fig. 6.9). These grooves are similar to features observed in natural slot canyons (Fig. 6.9) and led to the development of in-phase undulating walls (e.g., Wohl et al., 1999). Examining the frequency and spacing of such

grooves in natural channels may provide a metric to determine relative amount of vertical incision from plunge-pool erosion versus standard fluvial lowering.

Pools deepened during downstream migration and eventually trapped sediment, developing an alluvial cover (Fig. 6.10). This behavior is analogous to that proposed by Scheingross and Lamb (in review) where waterfall plunge pools are expected to self-adjust their alluvial depth via sediment deposition. Sediment deposits tended to form initially on the downstream pool face, limiting further lateral migration, and later covered the pool floor, preventing vertical incision (Fig. 6.10). Exposed bedrock upstream and downstream of the alluviated pool continued to erode resulting in destruction of the upstream step and a reduction in the thickness of deposited sediment as the downstream lip incised below the level of sediment aggradation. Continued incision reduced overall pool-relief, thus reducing the transport efficiency of the impinging jet and allowing sediment deposits to persist on the pool floor, ultimately leading to the complete destruction of the pool (Fig. 6.10).

In at least two cases in our experiment, the above cover and erosion interactions led to the generation of short-lived waterfalls which promoted plunge-pool retreat (Fig. 6.11). Waterfalls formed at bedrock steps between successive pools when cover in the upstream pool caused a beveling of the bedrock surface immediately downstream (Fig. 6.11A and D). A sharp break in slope developed where the beveled surface met the pool walls below such that flow accelerated over the beveled surface, and detached from the bed in the form of a ventilated-waterfall jet when passing this break in slope (Fig. 6.11C). This led to a reduction in erosion on the newly formed waterfall face due to the lack of sediment impacts; however, fluvial incision at the waterfall lip continued and was likely

amplified by flow acceleration towards the brink (Rouse, 1936; Hager, 1983). This amplified erosion created a steepened channel reach immediately upstream of the waterfall (e.g., Haviv et al., 2006) ultimately eroding through the existing waterfall, developing a new plunge-pool upstream, and typically causing the original waterfall plunge-pool to alluviate as the energy from the jet upstream was instead focused in the newly formed upstream pool. In this way sediment cover and erosion dynamics led to the formation, destruction, and retreat of waterfall plunge-pool systems in our experimental set up. While we choose to highlight two cases where distinct waterfalls formed in Figure 6.11, inspection of the evolution of the thalweg long-profile (Fig. 6.3) shows that plunge-pools retreated upstream throughout the experiment, and this generally occurred by a process similar to that described above.

6.6.2 Implications for waterfall formation, retreat, and evolution in natural channels

While waterfalls are often associated with rapid rates of upstream retreat (e.g., Gilbert, 1907; Mackey et al., 2014), not all waterfalls are fast retreating. DiBiase et al. (2015) recently showed that waterfalls within the same drainage basin can have markedly different retreat rates, with some waterfalls propagating upstream, while others appear to be fixed in place and stalled out. Similarly, waterfalls formed along fault scarps have been observed to decrease in height and 'diffuse out' during upstream retreat (e.g., Sklar et al., 2005; Cook et al., 2012), and others have suggested the dip of sedimentary bed can control relative changes in waterfall height during upstream retreat (e.g., Berlin and Anderson, 2009). Determining the formation mechanism for waterfalls and bedrock steps, and whether, once formed, waterfalls will retreat while maintaining a vertical face,

retreat while diminishing in height, or erode in place has important implications for the rate and style of fluvial incision and subsequent landscape adjustment.

In our experiment, waterfalls which we imposed on the system by pre-cutting steps into the bedrock profile were rapidly diminished in height and were destroyed (Fig. 6.3). The vertical face of the pre-cut waterfalls combined with high velocity flows upstream caused waterfall jets to shoot out from the brink, with plunge pools forming downstream of the waterfall base. The absence of sediment impacts on the waterfall face, combined with the inability of plunge pools to undercut the waterfall face due to their position sufficiently far downstream resulted in no net lateral migration of these features. Instead, rapid vertical fluvial incision at the waterfall brink led to the erosion of the waterfall face, with no remaining steepened reaches within the long-profile to suggest a waterfall had ever existed.

In contrast, waterfalls and bedrock step-pool systems which formed autogenically promoted upstream plunge-pool retreat such that the channel long-profile remained dominated by bedrock step-pool morphology as described in Section 6.5.2. It is interesting to note that amplified erosion at the upstream waterfall brink appeared to destroy our pre-cut waterfalls, yet acted as the key mechanism to promote formation of new upstream-retreating plunge-pools in our autogenically formed step-pools. The difference in this behavior may be partially explained by alluvial cover dynamics. Autogenically formed waterfalls were typically part of a series of step-pool systems in which alluvial cover in upstream steps promoted bedrock beveling, waterfall formation, and eventual plunge pool retreat. In contrast, the upstream-most of our pre-cut waterfalls

was fluvially eroded through prior to the formation of well-developed step-pools (Fig. 6.3).

These observations suggest that upstream-driven controls on alluvial cover or lack thereof (i.e., 'tools/cover dynamics' (Sklar and Dietrich, 2004)) can play an important role in setting waterfall retreat or lack thereof. And that, in certain landscapes, it is likely upstream fluvial incision processes, as opposed to waterfall processes, which act as the rate limiting step to waterfall retreat. Steepened channel-reaches, bedrock steps, and potholes are often observed upstream of large waterfalls in the field (e.g., Bishop and Goldrick, 1992; Haviv et al., 2006), and we suggest that these may represent the start of newly forming plunge-pools which can promote upstream retreat by successively 'drilling' plunge-pools which erode vertically but do not appear to undercut the waterfall face (e.g., Howard et al., 1994; Lamb et al., 2007). Assuming that such waterfall retreat is driven by tools/cover dynamics, this suggests that changes in sediment supply can lead to greater influence on the rate and style of channel evolution than previously appreciated.

Finally, while waterfall formation is often associated with changes in external forcing (Howard, 1994; Crosby and Whipple, 2006; Reinhardt et al., 2007; Whittaker and Boulton, 2012) or variation in rock resistance to erosion (e.g., Gilbert, 1890; Haviv et al., 2010), our results suggest waterfalls can form autogenically in response to evolving channel morphodynamics. While the autogenic formation of waterfalls has been theoretically predicted (Chatanantavet and Parker, 2006), there has been limited experimental evidence documenting the formation of waterfalls via abrasion of competent bedrock (e.g., Yokokawa et al., 2013). The presence of waterfalls and

knickpoints, and their upstream retreat rates, are often used in inverse to determine the timing of past changes in climate or tectonics (e.g., Lamb et al., 2008a; Ye et al., 2013; Mackey et al., 2014; DiBiase et al., 2015). The possibility of autogenic waterfall formation means that both internally and externally forced waterfalls can co-exist and that careful analysis should be performed to distinguish between the two prior to making interpretations about past events.

6.7 Conclusions

We used a controlled laboratory experiment to examine the processes of channel incision into bedrock at steep slopes. Our experiment showed that under low sediment supply, a narrow slot is rapidly formed, the width of which is likely set so that the imposed supply matches the sediment transport capacity. Measured reach-averaged erosion rates were well predicted by a one-dimensional theoretical model despite the complex bedrock topography which developed over the course of the experiment. Spatial variation in erosion rates led to the development of bedrock step-pools which increased in amplitude until sediment was deposited, and interaction between flows hydraulics, alluvial cover, and evolving bedrock topography allowed generation of short-lived waterfalls and upstream plunge-pool retreat. Overall, our experiment suggests that bedrock step-pools can be the dominant erosion mechanism in steep channels.

6.8 Acknowledgements

Jeff Prancevic, Roman DiBiase, Noah Finnegan, and Joel Johnson provided insightful discussions. We acknowledge funding from the National Science Foundation via grant EAR-1147381 to M.P.L and a Graduate Research Fellowship to J.S.S, as well as funding from NASA grant 12PGG120107, and a Caltech Summer Undergraduate Research Fellowship to J.P.

6.9 References

Benda, L., Hassan, M. A., Church, M., and May, C. L., 2005, Geomorphology of steepland headwaters: The transition from hillslopes to channels: Journal of the American Water Resources Association, v. 41, no. 4, p. 835-851.

Berlin, M. M., and Anderson, R. S., 2009, Steepened channels upstream of knickpoints: Controls on relict landscape response: Journal of Geophysical Research-Earth Surface, v. 114.

Bishop, P., and Goldrick, G., 1992, Morphology, processes and evolution of two waterfalls near Cowra, New South Wales: Australian Geographer, v. 23, no. 2, p. 116-121.

Burbank, D. W., Leland, J., Fielding, E., Anderson, R. S., Brozovic, N., Reid, M. R., and Duncan, C., 1996, Bedrock incision, rock uplift and threshold hillslopes in the northwestern Himalayas: Nature, v. 379, no. 6565, p. 505-510.

Chatanantavet, P., and Parker, G., 2006, Modeling the bedrock river evolution of western Kaua'i, Hawai'i, by a physically-based incision model based on abrasion, *in* Parker, G., and Garcia, M., eds., River, Coastal and Estuarine Morphodynamics 2005, Taylor and Francis Group.

Chatanantavet, P., Whipple, K. X., Adams, M. A., and Lamb, M. P., 2013, Experimental study on coarse grain saltation dynamics in bedrock channels: Journal of Geophysical Research-Earth Surface, v. 118, no. 2, p. 1161-1176.

Cook, K. L., Turowski, J. M., and Hovius, N., 2012, A demonstration of the importance of bedload transport for fluvial bedrock erosion and knickpoint propagation: Earth Surface Processes and Landforms, v. 38, no. 7, p. 683-695.

Crosby, B. T., and Whipple, K. X., 2006, Knickpoint initiation and distribution within fluvial networks: 236 waterfalls in the Waipaoa River, North Island, New Zealand: Geomorphology, v. 82, no. 1-2, p. 16-38.

DiBiase, R. A., Whipple, K. X., Heimsath, A. M., and Ouimet, W. B., 2010, Landscape form and millennial erosion rates in the San Gabriel Mountains, CA: Earth and Planetary Science Letters, v. 289, no. 1-2, p. 134-144.

DiBiase, R. A., Whipple, K. X., Lamb, M. P., and Heimsath, A. M., 2015, The role of waterfalls and knickzones in controlling the style and pace of landscape adjustment in the western San Gabriel Mountains, California: Geological Society of America Bulletin, v. 127, no. 3-4, p. 539-559.

Dietrich, W. E., Kirchner, J. W., Ikeda, H., and Iseya, F., 1989, Sediment supply and the development of the coarse surface-layer in gravel-bedded rivers: Nature, v. 340, no. 6230, p. 215-217.

Fernandez Luque, R., and van Beek, R., 1976, Erosion and transport of bed-load sediment: Journal of Hydraulic Research, v. 14, p. 127-144.

Finnegan, N. J., Sklar, L. S., and Fuller, T. K., 2007, Interplay of sediment supply, river incision, and channel morphology revealed by the transient evolution of an experimental bedrock channel: Journal of Geophysical Research-Earth Surface, v. 112, no. F3.

Frankel, K. L., Pazzaglia, F. J., and Vaughn, J. D., 2007, Knickpoint evolution in a vertically bedded substrate, upstream-dipping terraces, and Atlantic slope bedrock channels: Geological Society of America Bulletin, v. 119, no. 3-4, p. 476-486.

Gardner, T. W., 1983, Experimental study of knickpoint and longitudinal profile evolution in cohesive, homogenous material: Geological Society of America Bulletin, v. 94, no. 5, p. 664-672.

Gilbert, G. K., 1877, Report on the Geology of the Henry Mountains: Geographical and Geological Survey of the Rocky Mountain Region, Washington, D.C., U.S. Government Print Office, 160 p.:

-, 1890, The history of the Niagara River, extracted from the sixth annual report to the commissioners of the state reservation at Niagara, Albany, NY.

-, 1907, The rate of recession of Niagara Falls: US Geological Survey Bulletin, v. 306, p. 1-31.

Hager, W. H., 1983, Hydraulics of plane free overfall: Journal of Hydraulic Engineering-Asce, v. 109, no. 12, p. 1683-1697.

Hartshorn, K., Hovius, N., Dade, W. B., and Slingerland, R. L., 2002, Climate-driven bedrock incision in an active mountain belt: Science, v. 297, no. 5589, p. 2036-2038.

Haviv, I., Enzel, Y., Whipple, K. X., Zilberman, E., Matmon, A., Stone, J., and Fifield, K. L., 2010, Evolution of vertical knickpoints (waterfalls) with resistant caprock: Insights from numerical modeling: Journal of Geophysical Research-Earth Surface, v. 115.

Haviv, I., Enzel, Y., Whipple, K. X., Zilberman, E., Stone, J., Matmon, A., and Fifield, L. K., 2006, Amplified erosion above waterfalls and oversteepened bedrock reaches: Journal of Geophysical Research-Earth Surface, v. 111, no. F4.

Hayakawa, Y. S., and Matsukura, Y., 2003, Recession rates of waterfalls in Boso Peninsula, Japan, and a predictive equation: Earth Surface Processes and Landforms, v. 28, no. 6, p. 675-684.
Hayakawa, Y. S., and Matsukura, Y., 2010, Stability analysis of waterfall cliff face at Niagara Falls: An implication to erosional mechanism of waterfall: Engineering Geology, v. 116, no. 1-2, p. 178-183.
Holland, W. N., and Pickup, G., 1976, Flume study of knickpoint development in stratified sediment: Geological Society of America Bulletin, v. 87, no. 1, p. 76-82.
Howard, A. D., 1994, A detachment-limited model of drainage-basin evolution: Water Resources Research, v. 30, no. 7, p. 2261-2285.
Howard, A. D., Dietrich, W. E., and Seidl, M. A., 1994, Modeling fluvial erosion on regional to continental scales: Journal of Geophysical Research-Solid Earth, v. 99, no. B7, p. 13971-13986.
Howard, A. D., and Kerby, G., 1983, Channel changes in badlands: Geological Society of America Bulletin, v. 94, no. 6, p. 739-752.
Huda, S. A., and Small, E. E., 2014, Modeling the effects of bed topography on fluvial bedrock erosion by saltating bed load: Journal of Geophysical Research-Earth Surface, v. 119, no. 6, p. 1222-1239.
Johnson, J. P., and Whipple, K. X., 2007, Feedbacks between erosion and sediment transport in experimental bedrock channels: Earth Surface Processes and Landforms, v. 32, no. 7, p. 1048-1062.
-, 2010, Evaluating the controls of shear stress, sediment supply, alluvial cover, and channel morphology on experimental bedrock incision rate: Journal of Geophysical Research-Earth Surface, v. 115.
Johnson, J. P., Whipple, K. X., and Sklar, L. S., 2010, Contrasting bedrock incision rates from snowmelt and flash floods in the Henry Mountains, Utah: Geological Society of America Bulletin, v. 122, no. 9-10, p. 1600-1615.
Kean, J. W., and Smith, J. D., 2004, Flow and boundary shear stress in channels with woody bank vegetation: Riparian Vegetation and Fluvial Geomorphology, v. 8, p. 237-252.
Lamb, M. P., and Dietrich, W. E., 2009, The persistence of waterfalls in fractured rock: Geological Society of America Bulletin, v. 121, no. 7-8, p. 1123-1134.
Lamb, M. P., Dietrich, W. E., Aciego, S. M., DePaolo, D. J., and Manga, M., 2008a, Formation of Box Canyon, Idaho, by megaflood: Implications for seepage erosion on Earth and Mars: Science, v. 320, no. 5879, p. 1067-1070.
Lamb, M. P., Dietrich, W. E., and Sklar, L. S., 2008b, A model for fluvial bedrock incision by impacting suspended and bed load sediment: Journal of Geophysical Research-Earth Surface, v. 113, no. F3.
Lamb, M. P., Finnegan, N. J., Scheingross, J. S., and Sklar, L. S., 2015, New insights into the mechanics of fluvial bedrock erosion through flume experiments and theory: Geomorphology, v. 244, p. 33-55.
Lamb, M. P., and Fonstad, M. A., 2010, Rapid formation of a modern bedrock canyon by a single flood event: Nature Geoscience, v. 3, no. 7, p. 477-481.
Lamb, M. P., Howard, A. D., Dietrich, W. E., and Perron, J. T., 2007, Formation of amphitheater-headed valleys by waterfall erosion after large-scale slumping on Hawai'i: Geological Society of America Bulletin, v. 119, no. 7-8, p. 805-822.
Larsen, I. J., Montgomery, D. R., and Greenberg, H. M., 2014, The contribution of mountains to global denudation: Geology, v. 42, no. 6, p. 527-530.
Mackey, B. H., Scheingross, J. S., Lamb, M. P., and Farley, K. A., 2014, Knickpoint formation, rapid propagation, and landscape response following coastal cliff retreat at the last interglacial sea-level highstand: Kaua'i, Hawai'i: Geological Society of America Bulletin, v. 126, no. 7-8, p. 925-942.
Nelson, P. A., and Seminara, G., 2011, Modeling the evolution of bedrock channel shape with erosion from saltating bed load: Geophysical Research Letters, v. 38.
Paola, C., Straub, K., Mohrig, D., and Reinhardt, L., 2009, The "unreasonable effectiveness" of stratigraphic and geomorphic experiments: Earth-Science Reviews, v. 97, no. 1-4, p. 1-43.
Portenga, E. W., and Bierman, P. R., 2011, Understanding Earth's eroding surface with 10-Be: GSA Today, v. 21, no. 8.
Reinhardt, L. J., Bishop, P., Hoey, T. B., Dempster, T. J., and Sanderson, D. C. W., 2007, Quantification of the transient response to base-level fall in a small mountain catchment: Sierra Nevada, southern Spain: Journal of Geophysical Research-Earth Surface, v. 112, no. F3.
Rouse, H. R., 1936, Discharge characteristics of the free overfall: Civil Engineering, v. 6, p. 257-260.
Scheingross, J. S., Brun, F., Lo, D. Y., Omerdin, K., and Lamb, M. P., 2014, Experimental evidence for fluvial bedrock incision by suspended and bedload sediment: Geology.

Scheingross, J. S., and Lamb, M. P., in review, Sediment transport through waterfall plunge pools.
Seidl, M. A., Dietrich, W. E., and Kirchner, J. W., 1994, Longitudinal profile development into bedrock - an analysis of Hawaiian channels: Journal of Geology, v. 102, no. 4, p. 457-474.
Shepherd, R. G., and Schumm, S. A., 1974, Experimental Study of River Incision: Geological Society of America Bulletin, v. 85, no. 2, p. 257-268.
Sklar, L. S., and Dietrich, W. E., 2004, A mechanistic model for river incision into bedrock by saltating bed load: Water Resources Research, v. 40, no. 6.
Sklar, L. S., Stock, J. D., Roering, J. J., Kirchner, J. W., Dietrich, W. E., Chi, W., Hsu, L., Hsieh, M., Tsao, S., and Chen, M., 2005, Evolution of fault scarp knickpoints following 1999 Chi-Chi earthquake in West-Central Taiwan: Presented at AGU Fall Meeting 2005, Abstract H34A-06S.
Snyder, N. P., and Kammer, L. L., 2008, Dynamic adjustments in channel width in response to a forced diversion: Gower Gulch, Death Valley National Park, California: Geology, v. 36, no. 2, p. 187-190.
Stock, J. D., and Dietrich, W. E., 2006, Erosion of steepland valleys by debris flows: Geological Society of America Bulletin, v. 118, no. 9-10, p. 1125-1148.
Stock, J. D., Montgomery, D. R., Collins, B. D., Dietrich, W. E., and Sklar, L., 2005, Field measurements of incision rates following bedrock exposure: Implications for process controls on the long profiles of valleys cut by rivers and debris flows: Geological Society of America Bulletin, v. 117, no. 1-2, p. 174-194.
Turowski, J. M., Lague, D., and Hovius, N., 2007, Cover effect in bedrock abrasion: A new derivation and its implications for the modeling of bedrock channel morphology: Journal of Geophysical Research-Earth Surface, v. 112, no. F4.
Weissel, J. K., and Seidl, M. A., 1997, Influence of rock strength properties on escarpment retreat across passive continental margins: Geology, v. 25, no. 7, p. 631-634.
Whipple, K. X., DiBiase, R. A., and Crosby, B. T., 2013, Bedrock Rivers, *in* Shroder, J., Jr., and Wohl, E. E., eds., Treatise on Geomorphology, Volume 9: San Diego, Academic Press.
Whipple, K. X., Hancock, G. S., and Anderson, R. S., 2000a, River incision into bedrock: Mechanics and relative efficacy of plucking, abrasion, and cavitation: Geological Society of America Bulletin, v. 112, no. 3, p. 490-503.
Whipple, K. X., Snyder, N. P., and Dollenmayer, K., 2000b, Rates and processes of bedrock incision by the Upper Ukak River since the 1912 Novarupta ash flow in the Valley of Ten Thousand Smokes, Alaska: Geology, v. 28, no. 9, p. 835-838.
Whipple, K. X., and Tucker, G. E., 1999, Dynamics of the stream-power river incision model: Implications for height limits of mountain ranges, landscape response timescales, and research needs: Journal of Geophysical Research-Solid Earth, v. 104, no. B8, p. 17661-17674.
Whittaker, A. C., and Boulton, S. J., 2012, Tectonic and climatic controls on knickpoint retreat rates and landscape response times: Journal of Geophysical Research-Earth Surface, v. 117.
Wilson, A., Hovius, N., and Turowski, J. M., 2013, Upstream-facing convex surfaces: Bedrock bedforms produced by fluvial bedload abrasion: Geomorphology, v. 180, p. 187-204.
Wilson, A., and Lave, J., 2014, Convergent evolution of abrading flow obstacles: Insights from analogue modelling of fluvial bedrock abrasion by coarse bedload: Geomorphology, v. 208, p. 207-224.
Wohl, E. E., and Ikeda, H., 1997, Experimental simulation of channel incision into a cohesive substrate at varying gradients: Geology, v. 25, no. 4, p. 295-298.
Wohl, E. E., Thompson, D. M., and Miller, A. J., 1999, Canyons with undulating walls: Geological Society of America Bulletin, v. 111, no. 7, p. 949-959.
Ye, F. Y., Barriot, J. P., and Carretier, S., 2013, Initiation and recession of the fluvial knickpoints of the Island of Tahiti (French Polynesia): Geomorphology, v. 186, p. 162-173.
Yokokawa, M., Kyogoku, A., Kotera, A., and Izumi, N., Cyclic steps incised on experimental bedrock, *in* Proceedings American Geophysical Union Fall Meeting, abstract EP24B-062013.

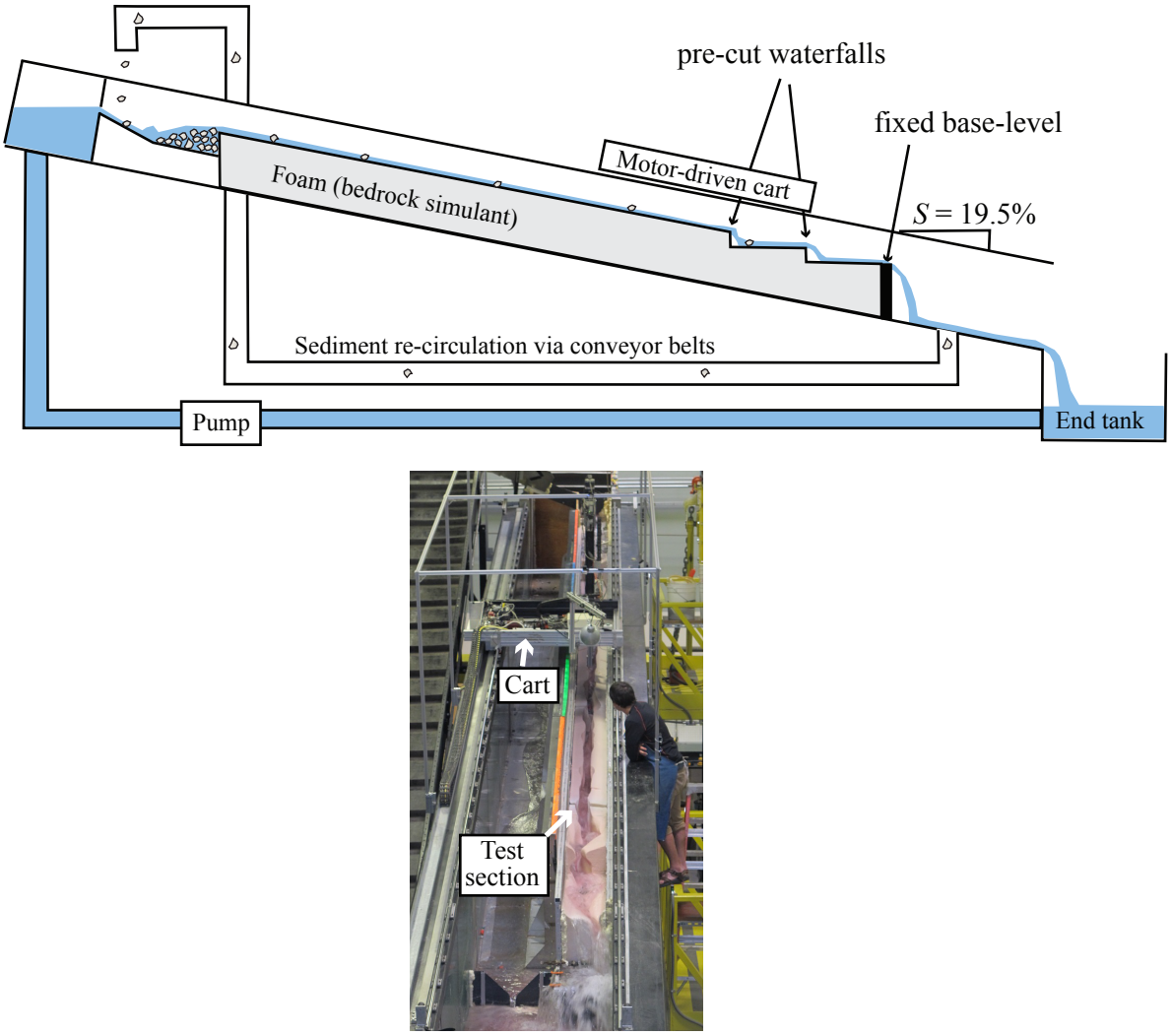

Figure. 6.1: Flume schematic (top) and photo (bottom) showing experimental set up.

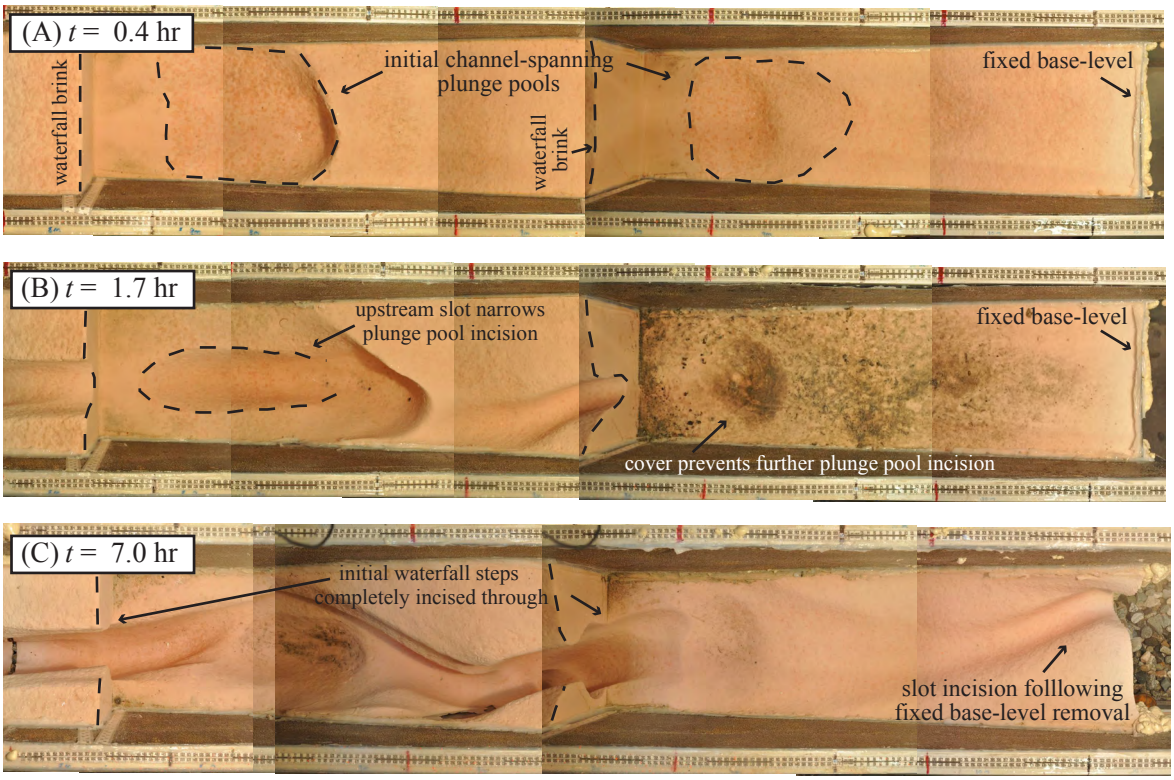

Figure 6.2: Overhead photos showing the downstream flume section at t = 0.4 hr (A), t = 1.7 hr (B), and t = 7.0 hr (C). Dark mud and silt deposited on downstream tread in panel (B) and at the center of pool on upstream tread in panel (C) are from coarse sediment deposits which were manually removed prior to photographing to allow for topographic measurements. Flume width is 30.5 cm for scale, all photographs taken when experiment was paused for topographic measurements.

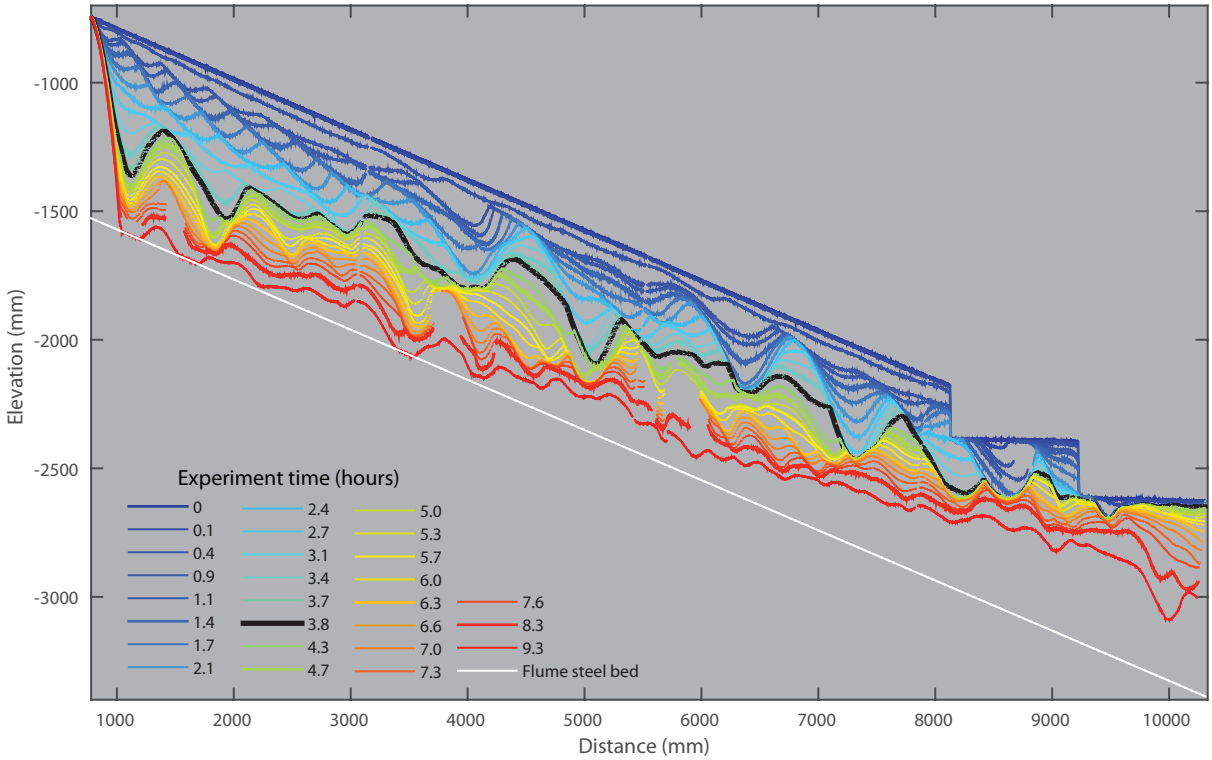

Figure 6.3: Time-series of long-profile evolution for the course of the experiment. All profiles show foam bedrock elevations (sediment deposits, when present, were removed prior to scanning, see methods). Gaps in profiles occur in locations where overhanging sidewalls prevented measurements of the channel thalweg. Bold black line shows first profile from Phase 2, after reducing water discharge and removing the fixed base-level.

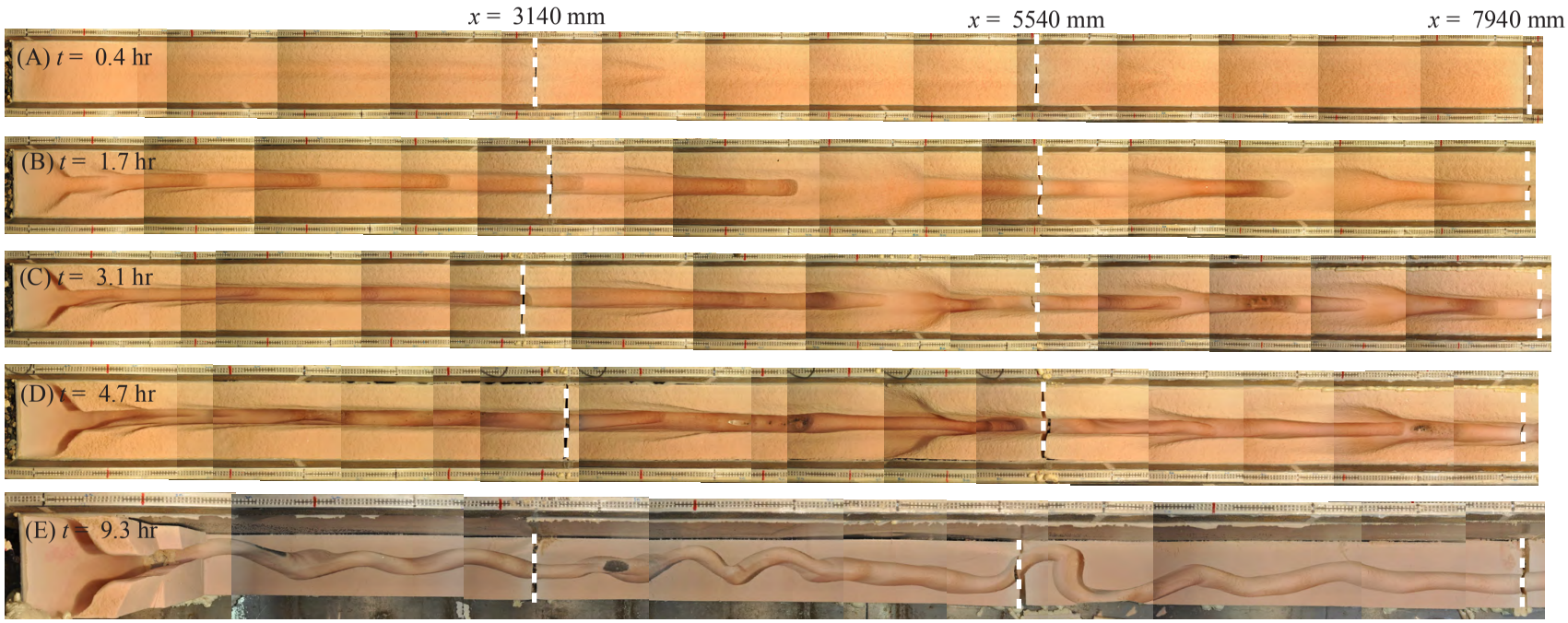

Figure 6.4: Overhead photos showing the progressive incision of the slot canyon in the upstream flume section. White dashed lines denote common cross-sections at seams between foam blocks in each photo. Channel thalweg in (C) and (D) is partially obscured by overhanging sidewalls whereas (E) shows complete thalweg trace after removal of the abandoned slot walls at the end of the experiment. Flume width is 30.5 cm for scale, all photographs taken with experiment paused and deposited sediment was manually removed to reveal bedrock topography.

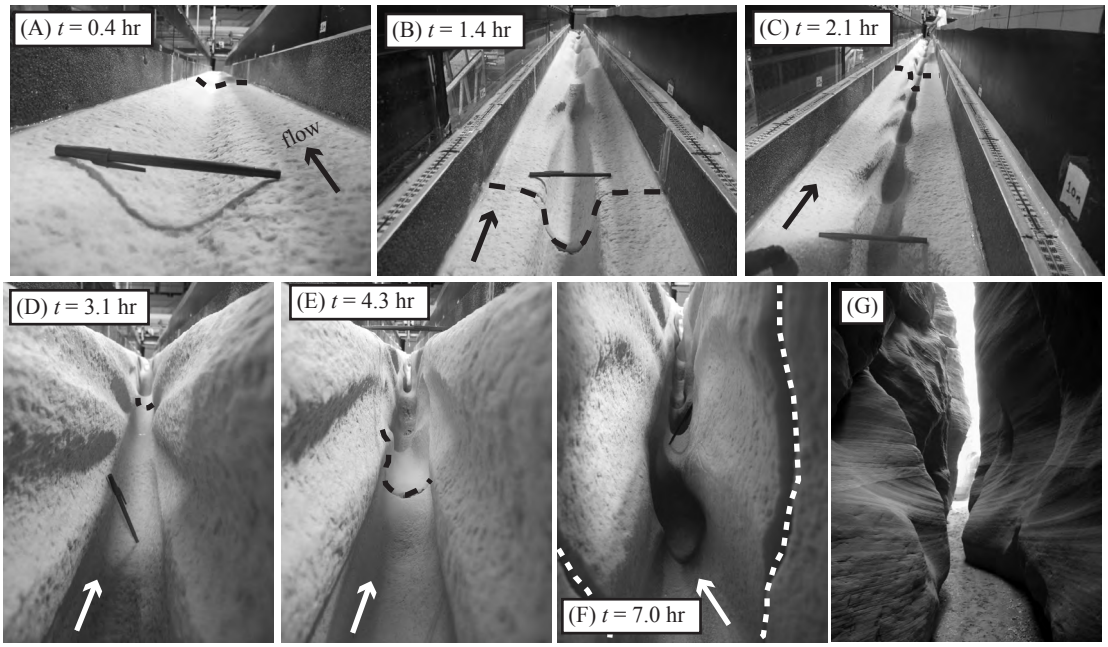

Figure 6.5: (A – F) Experiment photographs showing evolving topography and slot canyon incision in the upstream flume section. Dashed lines highlight the x = 3150 mm cross-section to provide a common tie-point between photos, and arrows point downstream. Note 15 cm long pen for scale in all images. All photos taken with experiment paused and after manual removal of deposited sediment to show bedrock topography. (G) Field photograph of Wire Pass, Utah, USA showing similar morphology to our experimentally carved canyon (credit J.J. Corneveaux, released under CC BY-SA 3.0).

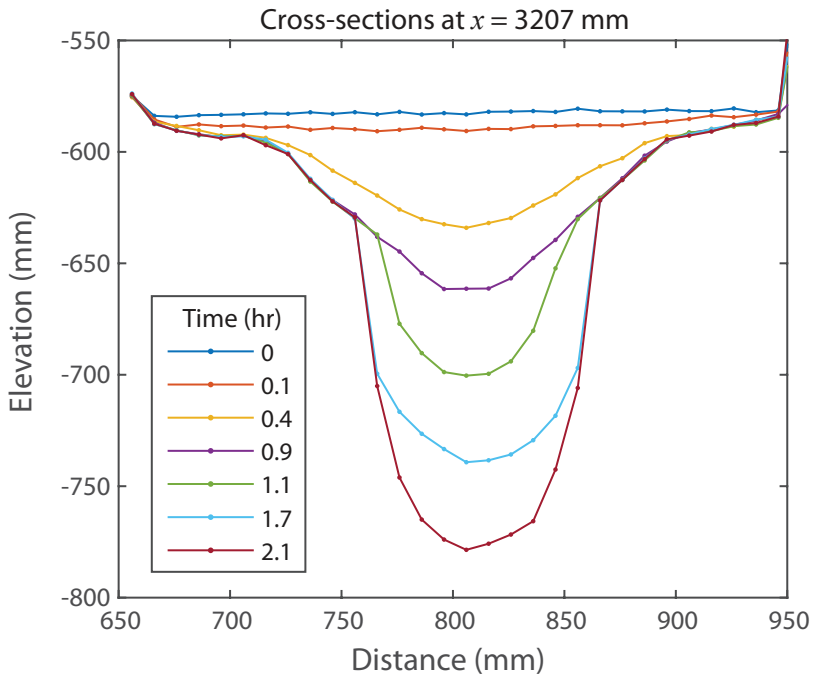

Figure 6.6: Successive cross-sections at x = 3207 mm showing the rapid carving of a slot within the first 2 hours of experiment time.

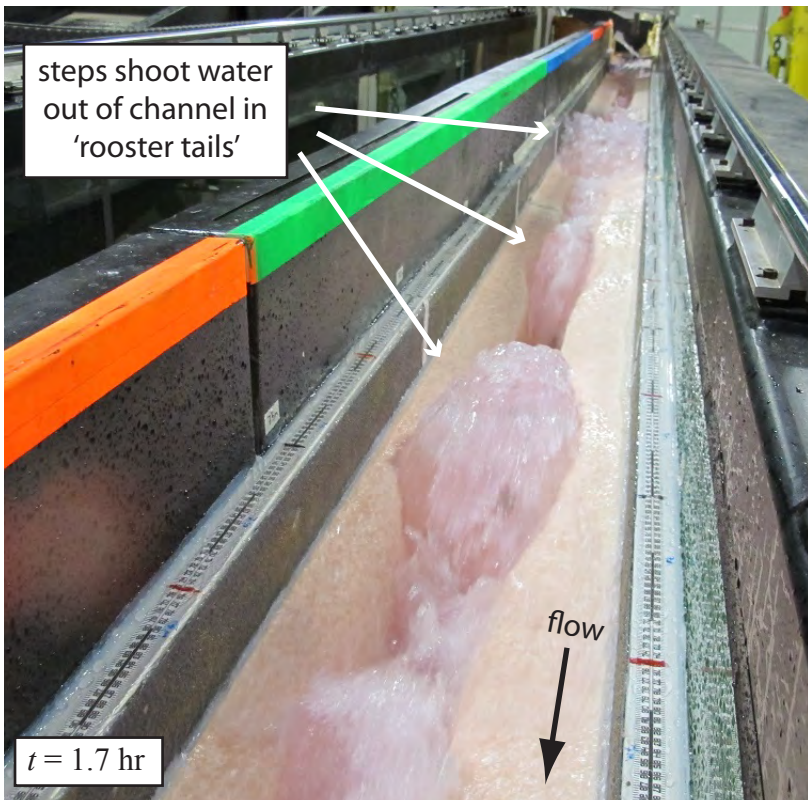

Figure 6.7: Photo showing water shooting out of channel as 'rooster tails' when exiting pools.

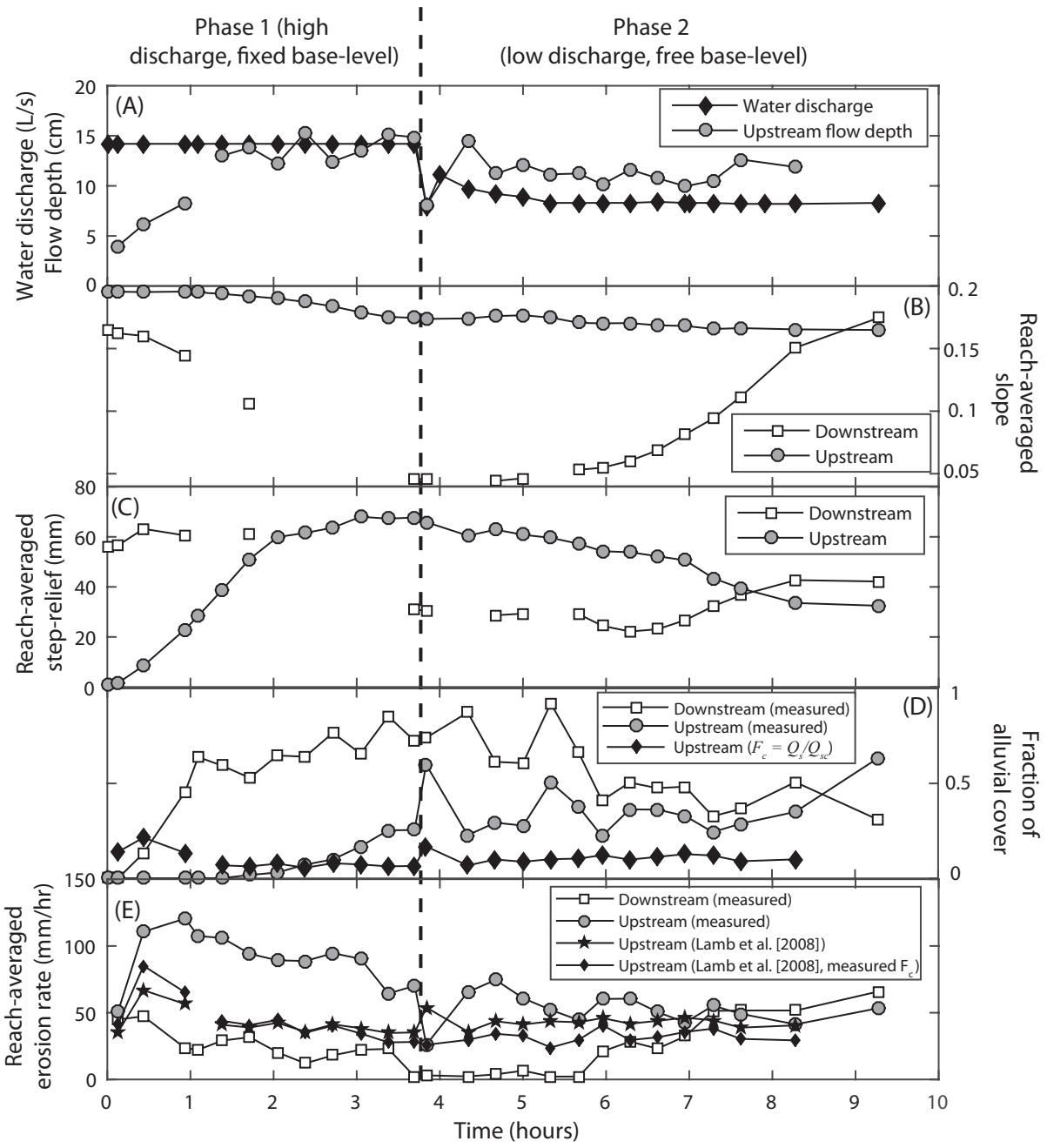

Figure 8: (A) Water discharge and upstream-section reach-averaged flow depth over the course of the experiment. (B-D) Reach-averaged slope (B), reach-averaged bedrock-step relief (C), and fraction of alluvial cover (F_c) within the slot (D) for the upstream and downstream flume sections. Also shown in (D) are theoretical predictions of F_c. (E) Measured reach-averaged erosion rates for the upstream and downstream sections from differencing successive long-profiles. Also shown are theoretical predictions (Lamb et al. [2008]) of reach-averaged erosion for the upstream flume section calculated with the fraction of exposed bedrock either calculated from theory (black stars) or input from manual measurements (black diamonds).

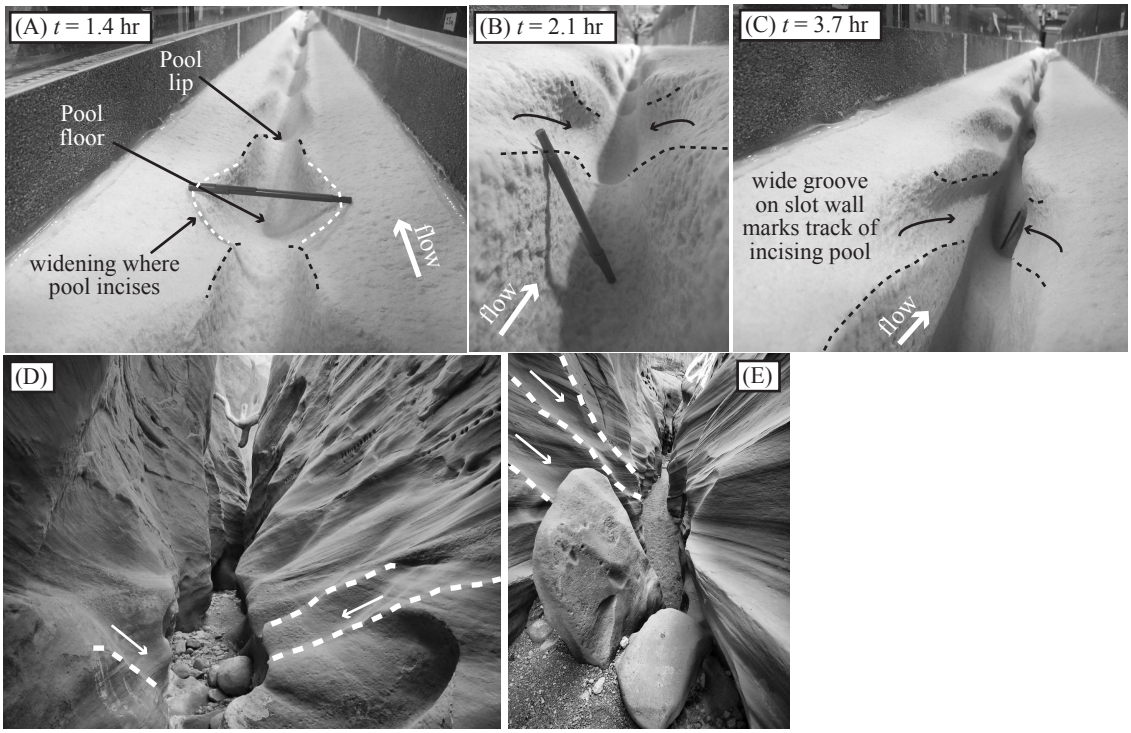

Figure 6.9: (A – C) Photos from upstream flume section showing downstream migration of step-pools which leave distinct grove morphology in the slot sidewalls. Photographs taken when experiment was paused for topographic measurements. (D and E) Field photographs from Little Death Hollow Canyon, Utah, USA where canyon sidewalls exhibit similar morphology.

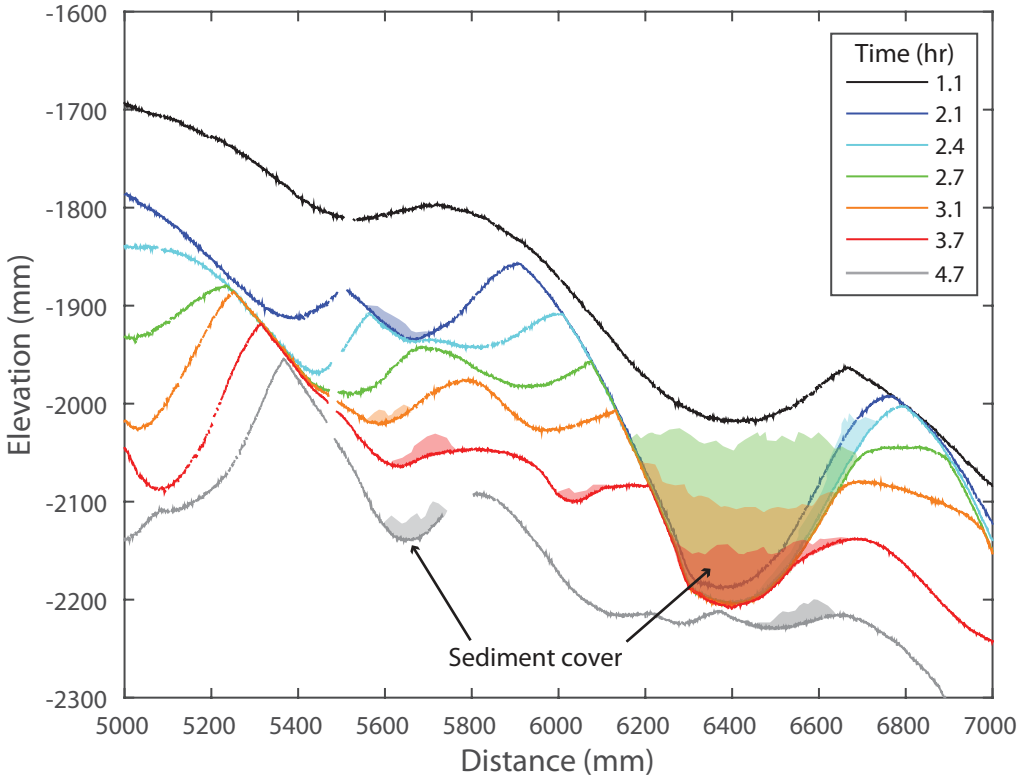

Figure 6.10: Long-profiles showing formation and destruction of a step-pool, solid lines shows bedrock topography while shaded areas mark extent of sediment cover. Note how plunge pool at $x = 6400$ mm deepens until the point of sediment deposition at $t = 2.4$ hours, after which vertical incision within the pool ceases and beveling of the channel upstream reduces the force of the impacting jet, allowing the thickness of sediment cover to extend to the height of the downstream pool lip ($t = 2.7 – 3.7$ hr). Continued erosion of exposed bedrock both upstream and downstream of the sediment cover results in the destruction of the original pool by $t = 4.7$ hr.

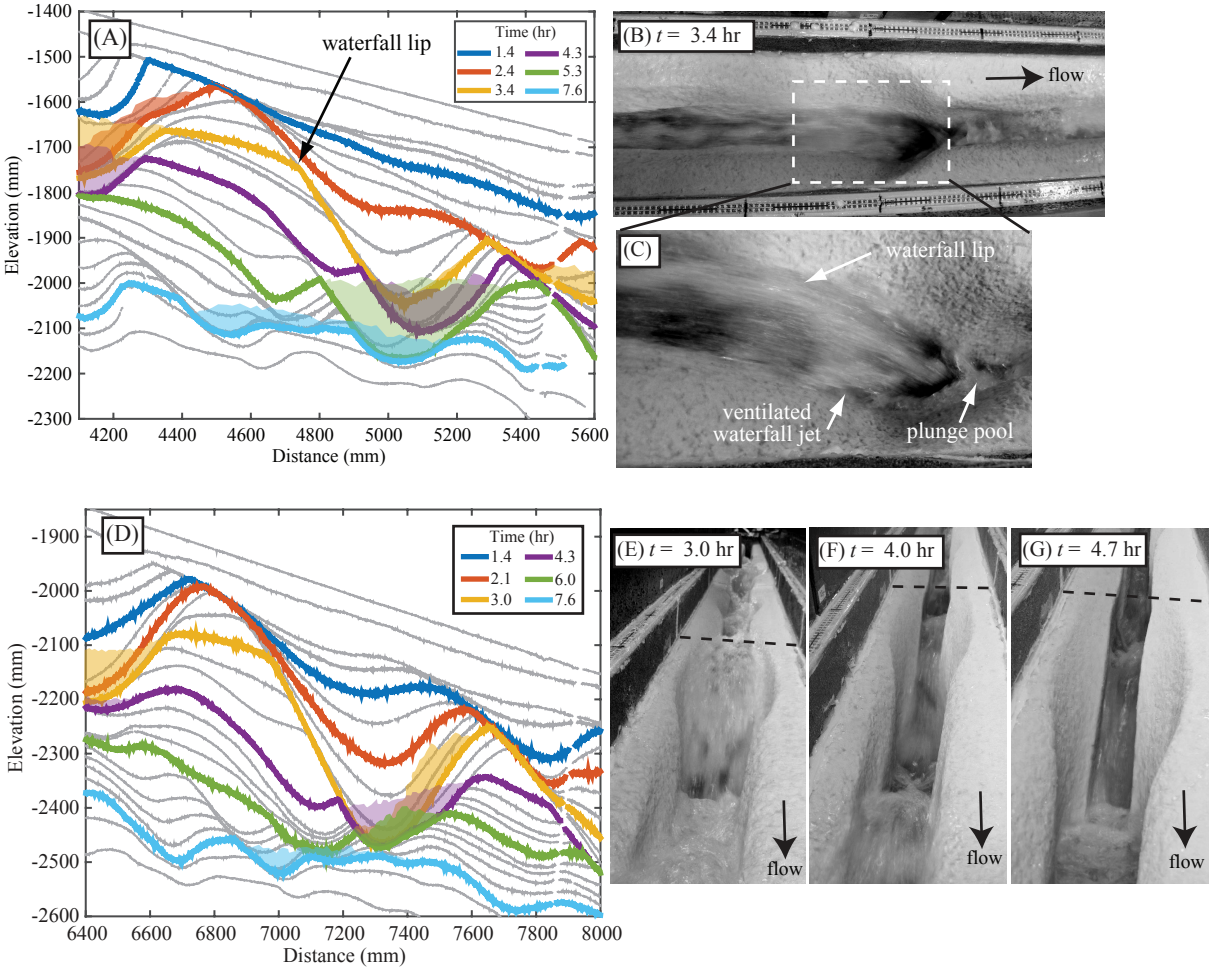

Figure 6.11: Time-series of long-profiles showing waterfall plunge-pool formation, destruction, and retreat at $x \sim$ 4700 mm (A) and $x \sim 6900$ mm (D). Colored lines show highlighted bedrock topography, and shaded areas denote sediment deposits. Gray lines show bedrock topography at other times during the experiment. (B) Photograph showing waterfall plunge-pool system at $x \sim$ 4700 mm at $t = 3.4$ mm and (C) detailed view of (B) where the ventilated waterfall jet is clearly visible. (E – F) Show formation and evolution of the waterfall plunge pool system at $x \sim$ 6900 mm. Note how flow over the step is initially wide (E) and narrows as a slot is cut and the former channel surface is progressively abandoned (F and G). Black dashed line in (E – F) indicates channel cross section at $x \sim 6800$ mm in for comparison with profiles in (D).